Doctoral Dissertation
博士論文

Physical and Chemical Structures of Young Low-Mass Protostellar Sources in Isolated Condition
(孤立領域における低質量原始星天体の物理・化学構造)

A Dissertation Submitted for the Degree of Doctor of Science
December 2019
令和元年 12 月博士 (理学) 申請

Department of Physics, Graduate School of Science,
The University of Tokyo
東京大学大学院 理学系研究科
物理学専攻

Muneaki Imai
今井 宗明

Abstract

A thorough understanding of chemical evolution in star and planet formation is an important topic in astrochemistry and astrophysics, and is deeply related to an understanding of the origin of the Solar System. In this relation, it is of fundamental importance to explore chemical compositions of protostellar cores, because they actually determine the initial condition in the evolution toward planetary systems.

During the last decade, it has been established that chemical compositions of low-mass protostellar cores show significant diversity. Examples are 'hot corino chemistry' characterized by rich existence of saturated complex organic molecules and 'warm-carbon-chain chemistry' (WCCC) characterized by abundant carbon-chain molecules. In spite of several observational attempts to reveal the origin of the chemical diversity, the definitive environmental factor causing the chemical diversity is still controversial. To approach this problem, I focus on the three isolated sources B335, CB68, and CB244, which can be regarded as a standard source without external effect and investigated their physical and chemical structures.

We conducted the interferometric observation to probe envelope structure on a few 10 to 100 au scale at almost same sensitivity among the sources. Although the isolated molecular cloud is not thought to be an active star-forming region, various rotational spectral lines of molecules are detected in the envelopes of the above three sources.

The physical and chemical characteristics of B335 and CB68 are similar to each other. Hot corno chemistry is seen at <100 au scale around the protostar and WCCC are seen at about 1000 au scale around the protostar. Moreover, their physical structures are also similar to each other. They are found to have a small rotation structure in the vicinity of the protostar. The rotation motion is explained by the infalling-rotating envelope model, which has been applied for several low-mass sources, and the radius of the centrifugal barrier is estimated to be < 4 au and < 30 au for B335 and CB68, respectively. These sizes are smaller than the typical value of low-mass sources by one order of magnitude. The complex organic molecules are enhanced around the centrifugal barrier. Such a hybrid chemical characteristic (WCCC at the outer part of the envelope and hot corino in the vicinity of the protostar) is consistent with the prediction by the chemical model calculation.

On the other hand, chemical characteristics of CB244 is different from those of B335 and CB68. Only WCCC can be seen in the scale of 1000 au in this source, and hot corino chemistry is not prominent. The physical structure of this source is also different from those of B335 and CB68. The radius of the centrifugal barrier is < 300 au, being larger than those of B335 and CB68 by about 2 orders of magnitude. Besides, an obvious asymmetric distribution of the gas is confirmed in this source, which may be caused by the existence of a nearby starless core.

These results stand for the first characterization of the physical and chemical structures of the isolated sources on a few 10 to 1000 au scale. A physical and chemical diversities among the isolated sources is revealed. The different chemical characteristics among the isolated sources suggests that the external effects by star-formation activities of nearby protostellar sources are not always necessary for the chemical diversity. The physical structure of the parent molecular cloud would cause the diversity. Although the sample is limited at the present stage, the sources with the similar cloud structure seems to have similar physical and chemical structures for the observed three cases.

Contents

1 Introduction **4**
- 1.1 Star Formation . . . 5
  - 1.1.1 Protostellar Evolution . . . 5
  - 1.1.2 Classification of Protostellar Evolution . . . 6
- 1.2 Chemical Diversity of the Protostellar Sources . . . 7
  - 1.2.1 Core-Scale Chemistry (∼1000 au) . . . 7
  - 1.2.2 Envelope Scale Chemistry (10-100 au) . . . 12
- 1.3 Motivation for the Isolated Sources . . . 15
- 1.4 Outline of This Thesis . . . 16

2 Basic Theory of Molecular Line Observations **17**
- 2.1 Intensity . . . 17
- 2.2 Brightness Temperature . . . 17
- 2.3 Radiative Transfer . . . 18
- 2.4 Optical Depth and Column Density . . . 19

3 Instruments **21**
- 3.1 Single-Dish Telescope . . . 21
  - 3.1.1 Components of the Single-Dish Telescope . . . 21
  - 3.1.2 Observation with Single Dish Telescope . . . 22
  - 3.1.3 IRAM 30 m . . . 23
- 3.2 Interferometer . . . 24
  - 3.2.1 Principles of Interferometers . . . 24
  - 3.2.2 Observation with Interferometer . . . 28
  - 3.2.3 ALMA . . . 31
  - 3.2.4 NOEMA . . . 33

4 Kinematic Model of the Infalling-Rotating Envelope **36**
- 4.1 Configuration of the IRE Model . . . 36
- 4.2 Evaluation of the Similarity of the Observation and the Model . . . 38
  - 4.2.1 Methodology . . . 39
  - 4.2.2 Effect of Noise . . . 42
  - 4.2.3 Comparison of the Model Similarity Indexes . . . 45
  - 4.2.4 Application to the Previous Observation Data . . . 45

5 Chemical Structure of B335 **48**
- 5.1 Introduction . . . 48
- 5.2 Observation . . . 49
- 5.3 Results . . . 49

5.3.1 Dust Continuum . . . 49
5.3.2 Detected Molecules and Their Distribution . . . 49
5.3.3 Derivation of Column Density and Fractional Abundance . . . 54
5.4 Discussion . . . 56
5.5 Summary . . . 58

6 Physical Structure of B335 **59**
6.1 Introduction . . . 59
6.2 Observation . . . 60
6.3 Results & Discussion . . . 60
6.3.1 Detection of 10 au Scale Velocity Gradient . . . 60
6.3.2 Existence of CH_3OH and HCOOH in Infalling-Rotating Envelope . . . 63
6.3.3 Error Estimation of the Physical Parameters . . . 65
6.3.4 Different Distribution among COMs . . . 69
6.3.5 SiO Emission Tracing the Inside of the Centrifugal Barrier . . . 69
6.3.6 Summary . . . 71

7 Physical and Chemical Structures of CB68 **73**
7.1 Introduction . . . 73
7.2 Observation . . . 74
7.3 Results & Discussion . . . 76
7.3.1 Distributions . . . 76
7.3.2 COM abundance . . . 80
7.3.3 Envelope Kinematics . . . 83
7.3.4 Evaluation of the Model Parameters . . . 84
7.3.5 Summary . . . 91

8 Physical and Chemical Structures of CB244 **93**
8.1 Introduction . . . 93
8.2 Observation . . . 95
8.3 Results . . . 95
8.3.1 Distributions . . . 95
8.3.2 Velocity Gradient Revealed by Molecular Emissions . . . 96
8.4 Discussion . . . 98
8.4.1 Chemical Composition . . . 98
8.4.2 Envelope Kinematics . . . 102
8.4.3 Evaluation of the Model Parameters . . . 105
8.4.4 Diversity of Isolated Sources . . . 110
8.5 Summary . . . 111

9 Discussion **112**
9.1 Comparison among the Isolated Sources . . . 112
9.1.1 Physical Structure . . . 112
9.1.2 Chemical Characteristics . . . 113
9.2 Comparison with Other Protostellar Sources . . . 116

10 Conclusion and Future Prospect **120**

A Error Estimate of $KL(p, q)$ **124**

Chapter 1

Introduction

It is known that the Universe consists of dark energy, dark matter, and baryons. Most of the mass in the Universe is composed of dark energy and dark matter, and the mass of baryons is only 4.6 % of the total mass of the Universe (Spergel et al. 2007). Nevertheless, baryons form rich structures in the Universe from large scales (galaxies) to small scales (stars and planets). Among such hierarchical structures, stars are the most fundamental elements in the Universe and play important roles in chemical evolution of the Universe through nucleosyntheses. In many cases, they harbor planets where the life can emerge. Thus, understanding of star formation is one of the major topics of the astrophysics and astrochemistry. Toward this goal, radio-wave observations, which usually trace low-temperature astronomical phenomena, have been making significant contributions to this issue.

Radio wave is the electromagnetic wave, whose wavelength is longer than those of visible and infrared radiation. The boundary between the radio wave and the infrared radiation is arbitrary, which is often set at 100 μm (3 THz). Radio observations plays an important role in studies of star formation for the following two reasons. The first reason is its strong penetration power relative to visible light, X ray, and infrared wave. Due to its long wavelength, radio waves are less scattered and absorbed by gas and dust. The strong penetration feature enables us to observe structures around the protostar without influenced by surrounding interstellar clouds. In addition to large-scale structures of protostellar cores, disk/envelope and outflow structures around protostars can thus be observed with radio observations. The second reason is that rotational spectral lines of various molecular species are in this energy range. Rotational spectral lines of fundamental molecules such as CO, H_2O, H_2CO, and NH_3 were detected from late 1960s' to the early 1970s' (Cheung et al. 1968; 1969; Snyder et al. 1969; Wilson et al. 1970). Since then, many other molecules have been detected in diverse regions in the Universe. The matter widely distributed in interstellar space is called "Interstellar Matter" (ISM). Now we can observe not only the above simple species but also relatively complex molecules such as NH_2CHO, CH_3COCH_3, and C_2H_5OH which are typically produced in protostellar cores. So far, more than 200 molecular species have been detected (McGuire et al. 2018). Taking this advantage, we can explorer both physical and chemical characteristics of protostellar sources.

On the other hand, the angular resolution of the radio observation is usually low, because of its long wave length. To overcome this disadvantage, large aperture telescopes were developed (*e.g.*, IRAM 30 m and NRO 45 m). However, their angular resolution (typically $\sim$ a few $10''$ at 1 mm) is still too low to probe innermost structures of the gas around protostars. This situation was drastically improved by interferometers. Interferometers uses many small antennas distributed over a few hundreds to thousands meters, and realize the high spatial resolution that almost corresponds to the resolution obtained by a single-dish telescope with an aperture size of the extent of the maximum antenna separation. Very Large Array (VLA) situated at Socorro

in USA started its operation in 1976, Nobeyama Millimeter Array (NMA) at Nobeyama in 1988, and Plateau de Bure Interferometer (PdBI: now renamed as NOEMA) in the French Alps in 1988. These telescopes realized more than 10 times better angular resolution than single dish telescopes, and they have been used for the mapping observation of the protostellar cores. The current largest radio interferometer is ALMA, which started its operation in 2011. ALMA comprises 66 antennas and realizes more than 100 times better angular resolution than single dish telescopes. Thanks to its outstanding capability of high angular resolution and high sensitivity, the innermost structure around the protostellar source can now be studied. Under this background, this thesis focuses on the relation between the chemical and physical structure in the vicinity of the protostar.

1.1 Star Formation

Stars are roughly classified into 2 categories according to their mass: low-mass stars (sun-like stars) whose mass is lower than 8 $M_{\odot}$ and high-mass stars whose mass is higher than 8 $M_{\odot}$. The time scale from the birth of a protostar to the start of the H burning as a main-sequence star strongly depends on its mass. The time scale for low-mass stars is around 10^7-10^8 yr, while that for high-mass stars is around 10^5 yr or even shorter (*e.g.*, Zinnecker & Yorke 2007). The time scale for high-mass stars is so short that they start to shine as main-sequence stars before parent molecular clouds are dissipated, and hence, physical and chemical structures of high-mass protostellar cores are significantly affected by newly born stars. For example, high-mass stars radiate intense UV radiation, which ionizes the surrounding gas to form H II regions (*e.g.*, Wood & Churchwell 1989). Furthermore, the surfaces of nearby clouds illuminated by the intense UV radiation forms dense photodissociation regions (PDRs) (*e.g.*, Tielens, & Hollenbach 1985). The evolution process of high-mass stars is poorly understood because of such complex environments. On the other hand, physical and chemical structures of low-mass protostellar cores are less affected by protostellar activities, and their structures have been intensively studied. H II regions are not usually formed, although a very small PDR sometimes appears around the protostar. In this Section, the evolutionary process of low-mass protostars revealed by theoretical and observational studies are overviewed.

1.1.1 Protostellar Evolution

Starlesscore

Stars are born in interstellar molecular clouds. Once density fluctuation develops in the interstellar molecular cloud due to Jeans instability (Jeans 1902), gravitational contraction continues in the dense part of a cloud by self gravity. Dense molecular cloud cores before the onset of the star formation are called starless core. A typical H_2 density of starless cores is around 10^4-10^6 cm^{-3}. A starless core is usually in a complex structure of a large molecular cloud, but isolated cores such as Bok globules also exist. The temperature of the core is kept to around 10 K due to a balance between gravitational energy release and radiation cooling (*e.g.*, Benson & Myers 1989). This temperature is much lower than that of a diffuse cloud (100 K). A typical mass and extent of starless cores is around 10 $M_{\odot}$ and 0.1 pc (Benson & Myers 1989), respectively, and the typical time scale of the gravitational contraction is around 10^5-10^6 yr (*e.g.*, Evans et al. 2009).

Protostar (Class 0/I)

When the central density of the core exceeds the 10^{11} cm^{-3}, the dust continuum emission becomes optically thick resulting in less cooling efficiency. This causes rapid temperature rise at the center part, which is called 'first core' (*e.g.*, Larson et al. 1969; Masunaga et al. 1998). A typical size of the first core is a few au. When the temperature rises as high as 1500 K after 100 yr from the formation of the first core, thermal dissociation of H_2 starts to occur. Dissociation of H_2 absorbs a huge energy and cools the core to trigger the second gravitational collapse. The collapse propagates outward with sound speed (Shu 1977). This collapse is recognized as the birth of the protostar.

After the birth of the protostar, the ambient gas is falling onto the protostar, and the protostar continues to grow up (main accretion phase). Generally, the ambient gas has some angular momentum, and hence, flattened envelope and disk structures are formed around the protostar. At this stage, the protostellar source is no longer spherically symmetric. The gas falls onto the protostar through the disk/envelope structure, whose gravitational energy is the source of the radiation from the protostar. The radiation is observable in the infrared and/or radio wavelengths. At the same time, the protostar drives bipolar outflow perpendicular to the disk direction (*e.g.*, Bachiller 1996; Tomisaka et al. 2000; Tomisaka et al. 2002; Machida et al. 2004). Outflow is thought to deprive the angular momentum of the infalling gas, and allows the protostar to grow further. Its velocity is as high as 10-100 km s^{-1}.

T Tauri Stars (Class II/III)

The protostar starts to shrink quasi-statically after dissipation of the surrounding envelope gas by protostellar activities such as outflows. Since most of the surrounding gas is dissipated, the accretion of the gas onto the protostar gets almost settled. The star at this stage is called 'T Tauri star'. The heat produced in the central part of the star is delivered to its surface mainly by convection ('*Hayashi phase*'; Hayashi 1961). When the temperature of the central part of the star becomes high enough, the heat is transported by radiation ('*Henyey Track*'; Henyey et al. 1955). Then the T Tauri stars evolve to the main-sequence stars with a time scale of 10^7-10^8 yr. When the central temperature becomes as high as $\sim 10^7$ K, thermonuclear reaction of hydrogen starts to proceed. During the T Tauri phase, a planetary system is thought to be formed.

1.1.2 Classification of Protostellar Evolution

Evolutionary stages of protostars are classified into Class I - Class III based on their spectral energy distribution (SED) in the infrared region (*e.g.*, Andre et al. 1993). The spectrum index α is used for the classification, where α is defined as:

$$\alpha = \frac{\mathrm{d}\log(\lambda F_\lambda)}{\mathrm{d}\log(\lambda)}. \tag{1.1}$$

The criterion for each class is defined as follows:

$$\begin{aligned} \text{Class I} &: 0 < \alpha < 3 \\ \text{Class II} &: -2 < \alpha < 0 \\ \text{Class III} &: -3 < \alpha < -2. \end{aligned}$$

The stage before Class I is called Class 0 (Andre et al. 1993). In the Class 0 stage, the protostar has just being formed, so that the peak stellar emission is in the submillimeter wave range. The SED of each stage is schematically shown in Figure 1.1. The Class I sources are

embedded in the envelope gas, which attenuates the infrared emission, and the emission peak appears in the far infrared region. On the other hand, the near infrared emission from the star as well as far infrared emission from the disk can be observed for the Class II sources. The emission peak is thus in the near infrared region. The emission is almost dominated by the black body radiation of the photosphere for the Class III sources without the far infrared excess from the disk.

The classification with the SED is sometimes difficult because the structure of the envelope/disk system is different from source to source (*e.g.,* the inclination angle of the source, multiplicity of the source, and so on). Especially, the distinction between Class 0 and Class I is often difficult, because they are surrounded by the thick envelope gas. Hence, the bolometric temperature ($T_{\rm bol}$) is sometimes used as an alternative index of the evolutionary stage of protostars (*e.g.*, Myers & Ladd 1993; Chen et al. 1995; Evans et al. 2009).

The bolometric temperature is calculated by the weighted average of frequency ($\overline{\nu}$) of the continuum emission from the source. It is defined as the temperature of the black body which gives the same weighted average of frequency ($\overline{\nu}_{\rm b}$) of the emission: $\overline{\nu}_{\rm b} = \overline{\nu}$ (Myers & Ladd 1993). Here, $\overline{\nu}$ and $\overline{\nu}_{\rm b}$ are calculated as follows:

$$\overline{\nu} \equiv \frac{I_1}{I_0}, \tag{1.2}$$

where

$$I_m = \int_0^\infty {\rm d}\nu \ \nu^m F(\nu), \tag{1.3}$$

and

$$\overline{\nu}_{\rm b} \equiv \frac{\displaystyle\int_0^\infty {\rm d}\nu \ \nu B_\nu(T_{\rm bol})}{\displaystyle\int_0^\infty {\rm d}\nu \ B_\nu(T_{\rm bol})}. \tag{1.4}$$

Here, $B_\nu(T)$ represents the intensity of the block body radiation of temperature T at the frequency of ν. The relation between $T_{\rm bol}$ and $\overline{\nu}$ is calculated as follows:

$$T_{\rm bol} = \frac{\zeta(4)}{4\zeta(5)} \frac{h\overline{\nu}}{k_{\rm B}} = 1.25 \times 10^{-11} \ \frac{\overline{\nu}}{\rm Hz} \ {\rm K}, \tag{1.5}$$

where $\zeta(n)$ is Riemann zeta function as:

$$\zeta(n) = \frac{1}{\Gamma(n)} \int_0^\infty \frac{t^{n-1}}{e^t - 1} {\rm d}t. \tag{1.6}$$

$T_{\rm bol}$ of 70 K is typically used as the threshold between Class 0 and Class I (Chen et al. 1995). Figure 1.2 shows the correlation between $T_{\rm bol}$ and α observed for protostars.

1.2 Chemical Diversity of the Protostellar Sources

1.2.1 Core-Scale Chemistry (∼1000 au)

The core-scale chemistry of low mass protostellar sources have been investigated by single dish observations. During the last decade, it has been established that chemical compositions of low-mass protostellar cores show significant diversity on a 1000 au scale (Sakai & Yamamoto 2013). The representative chemical features seen in the protostellar phase are hot corino chemistry and warm carbon-chain chemistry. Recent studies on these chemical characteristics are summarized below.

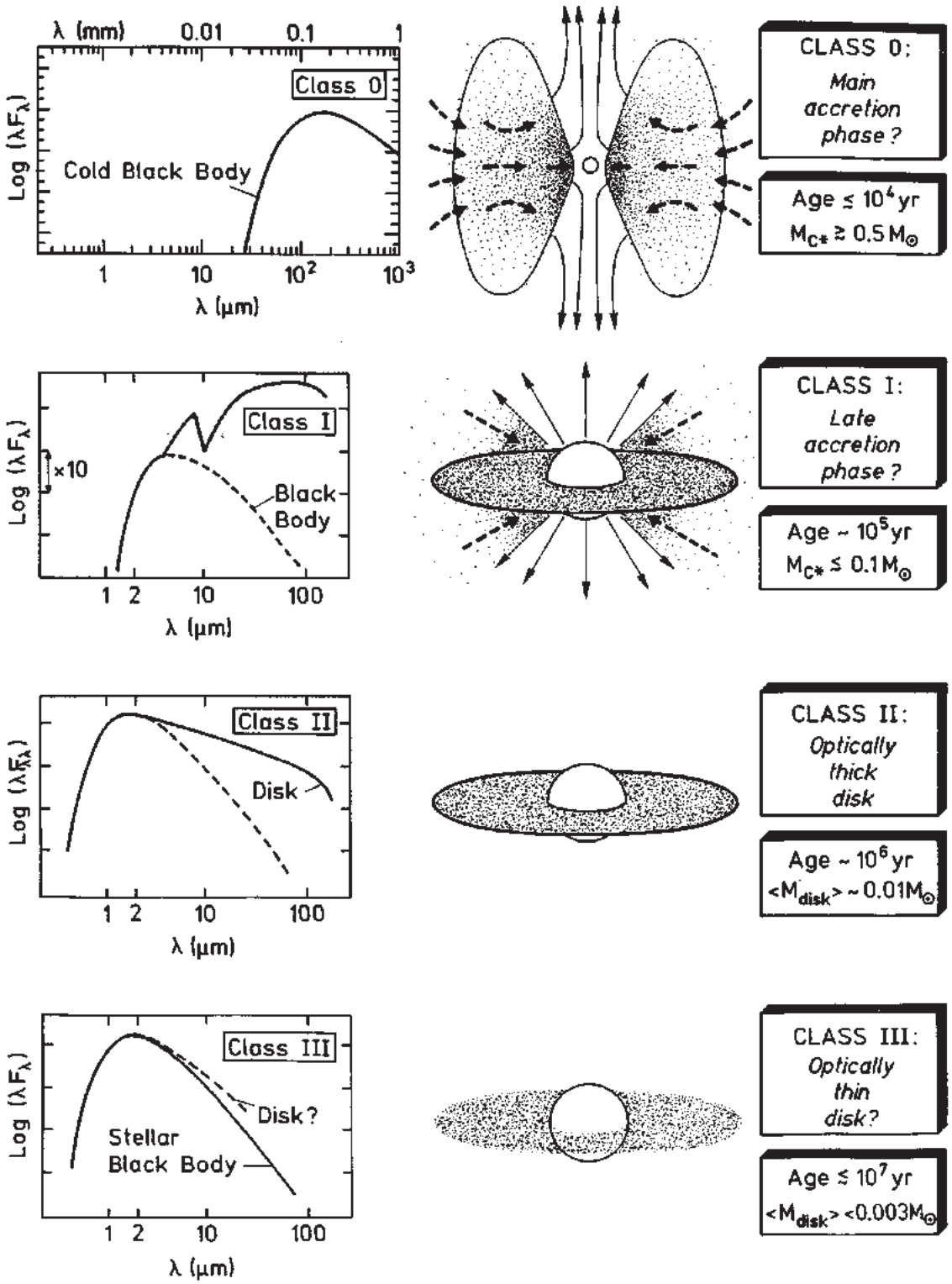

Figure 1.1: Classification of the evolutionary stage of the low-mass protostar by SED (Bachiller 1996).

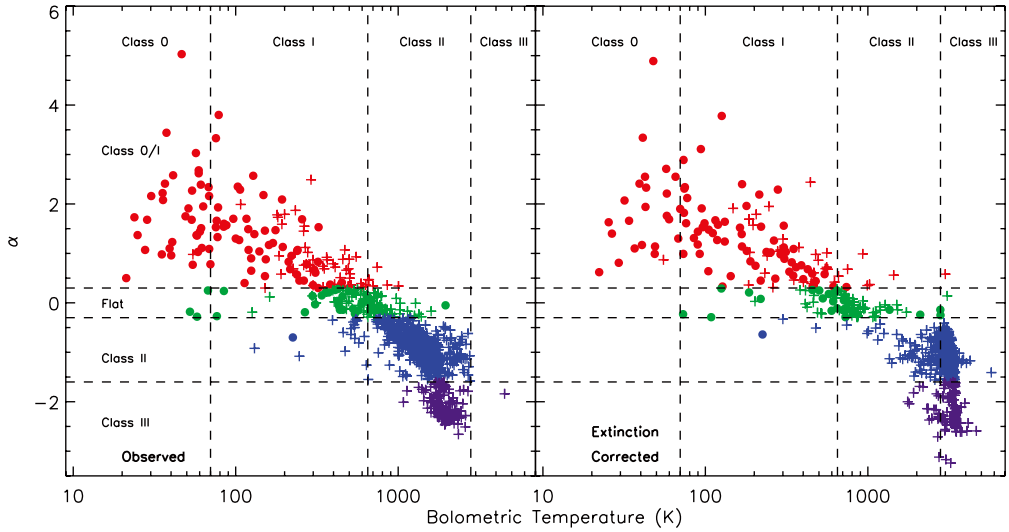

Figure 1.2: The correlation between the spectral index α and the bolometric temperature (Evans et al. 2009).

Hot Corino Chemistry and Warm Carbon Chain Chemistry

Hot corino chemistry is characterized by the rich existence of saturated complex organic molecules (COMs) such as $HCOOCH_3$ and CH_3OCH_3, and deficient carbon-chain molecules such as CCH, c-C_3H_2, and C_4H. Blake et al. (1994) and van Dishoeck et al. (1995) carried out the spectral line survey toward the IRAS 16293-2422 and detected bright emission lines of CH_3OH and CH_3CN. These molecules are not very bright in cold starless cores and usually reside in hot and dense regions, which suggests their emissions come from the vicinity of the protostar. In addition, Cazaux et al. (2003) detected spectral lines of complex organic molecules such as $HCOOCH_3$, CH_3OCH_3, C_2H_5OH, and C_2H_5CN, which also trace the hot and dense region. These results suggest that IRAS 16293-2422 harbors a hot and dence core where saturated complex organic molecules are abundant. Such a hot and dense core in low-mass sources are named as '*hot corino*', and the chemistry characterized by such rich existence of COMs are called hot corino chemistry. CH_3OH and other organic molecules are thought to be liberated from dust grains due to the high temperature (> 100 K) conditions. Later, high spatial resolution observations of complex organic molecules with interferometers revealed that the emission of these molecules indeed comes from the hot and dense region within a few 100 au from the protostar (*e.g.*, Bottinelli et al. 2004; Jørgensen et al. 2011). Examples of the hot corino sources are IRAS 16293-2422, NGC1333 IRAS 4A, NGC1333 IRAS 4B, NGC1333 IRAS 2, Serpens SMM1, Serpens SMM4, and HH212 (Cazaux et al. 2003; Bottinelli et al. 2004; Sakai et al. 2006; Öberg et al. 2011; Codella et al. 2016).

In contrast to hot corino chemistry, warm carbon-chain chemistry (WCCC) is characterized by abundant carbon-chain molecules and deficient COMs. Sakai et al. (2008) carried out the molecular line observation toward IRAS 04368+2557 in L1527 and found that the chemical composition of this source is completely different from that of hot corino sources. In spite of very sensitive observations, the spectral lines of the complex organic molecule $HCOOCH_3$ were not detected. The CH_3OH emission is not as bright as that in hot corino sources. Instead, the high excitation lines of carbon-chain molecules such as C_4H_2, C_4H, l-C_3H_2 were detected. Even long carbon-chain molecules such as HC_5N, HC_7N, C_6H, and C_6H_2 were found to be relatively abundant in this source. These unsaturated carbon-chain molecules are generally deficient in

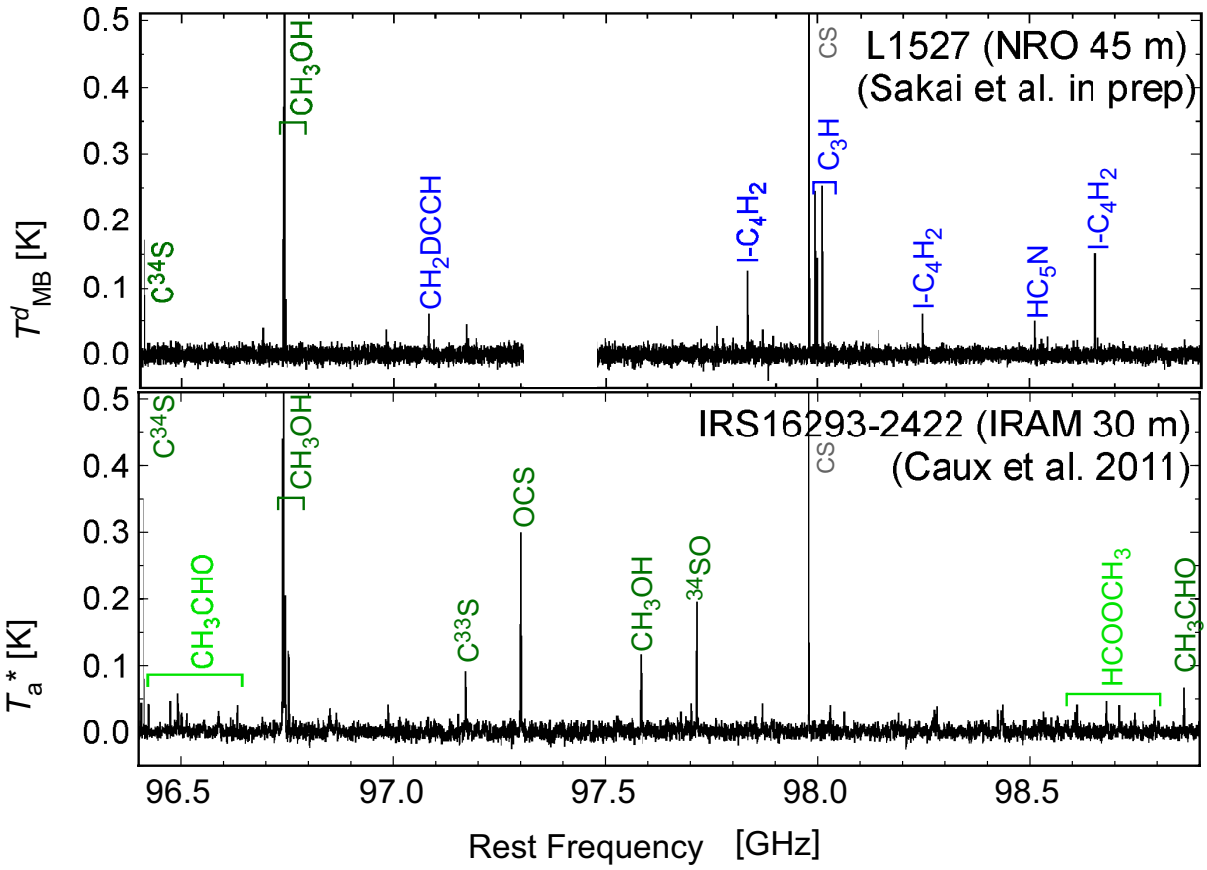

Figure 1.3: The spectra observed for the WCCC source L1527 with the Nobeyama 45 m telescope and the hot corino source IRAS 16293-2422 with the IRAM 30 m.

hot and dense regions around the protostars (Suzuki et al. 1992), and this discovery was very surprising. The rotation temperatures of C_4H_2 and CH_3CCH were derived to be 12.8 and 13.9 K, respectively. Although these temperatures are beam-averaged values, they are higher than the typical temperature of the ambient cloud (10 K). Moreover, the detection of high excitation lines with a critical density of about 10^6 cm^{-3} or higher suggests that the carbon-chain molecules reside in the warm and dense region around the protostar. In fact, the high spatial resolution observation with interferometer revealed that these carbon-chain molecules are associated to the protostar with a scale of about 1000 au (Sakai et al. 2010a). They reported that these carbon-chain molecules are efficiently produced by evaporation of CH_4 from dust grain in a warm region ($\sim$ 25 K) around the protostar. Such chemical characteristics are not seen in the hot corino sources and are named as warm carbon-chain chemistry. A prototypical sources are IRAS 04368+2557 in L1527 (Sakai et al. 2008; 2010a) and IRAS 15398-3359 in the Lupus molecular cloud.

The Figure 1.3 shows the spectra observed for WCCC source IRAS 04368+2557 in L1527 with the Nobeyama 45 m telescope (Sakai et al. in prep) and hot corino source IRAS 16293-2422 with the IRAM 30 m (Caux et al. 2011). Although they are in the similar evolutionary stage (Class 0), the spectral patterns are completely different from each other. In L1527, various carbon-chain molecules such as C_3H, l-C_4H_2 are detected, while saturated complex organic molecules except for CH_3OH are detected. On the other hand, carbon-chain molecules are deficient in IRAS16293-2422, while complex organic molecules such as CH_3OH, CH_3CHO, and $HCOOCH_3$ are detected.

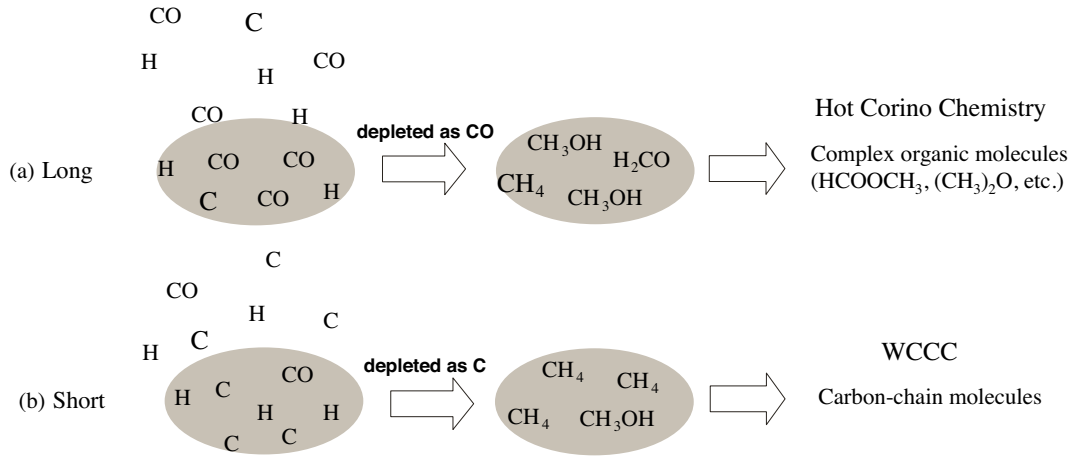

Figure 1.4: The proposed scenario to explain the difference of hot corino chemistry and WCCC (Sakai et al. 2009). See text for details.

Sakai et al. (2009) proposed that the origin of the above diversity is the duration time of the starless core phase after the shielding of the interstellar UV radiation. After the UV shielding, the formation of molecules starts both in the gas-phase and on dust grains, whose timescale is comparable to the dynamical timescale of a parent cloud ($\sim 10^5$ yr). A longer duration time of the starless core phase tends to result in hot corino chemistry, while a shorter duration time of the starless core time leads to WCCC. In the longer duration time case, most of C atoms are converted to CO molecules in the gas phase, and then CO molecules are depleted onto dust grains. They then form CH_3OH, H_2CO, and more complex organic molecules through hydrogenation reactions and radical reactions on the dust grain surfaces, before being evaporated in to the gas phase. Complex organic molecules such as $HCOOCH_3$ may also be produced from CH_3OH and H_2CO in the gas phase after their evaporation (Balucani et al. 2015). On the other hand, in the shorter duration time case, most of C atoms are depleted directly onto the dust grains before being converted to CO molecule, and then form CH_4 through hydrogenation. This favors WCCC, with the long carbon-chain molecules built up in the gas phase after evaporation of CH_4 from dust grains. This mechanism can explain the various observational results obtained so far. However, other mechanisms such as shocks (outflow, cloud-cloud/filament-filament collision) and UV radiation from nearby OB stars may also contribute to chemical diversity (*e.g.*, Buckle & Fuller 2002, Higuchi et al. 2010; 2014; Lindberg & Jørgensen 2012; Watanabe et al. 2012; Fukui et al. 2015; Spezzano et al. 2016a; 2016b). To explore the origin of the above chemical diversity, systematic observational studies have been performed by Higuchi et al. (2018) and Imai et at. (2018).

Higuchi et al. (2018) conducted the statistical survey to identify the chemical properties of many protostars located in the same molecular cloud complex in Perseus. They used the CCH/CH_3OH column density ratio as the criterion of the WCCC/hot corino chemistry, and found that the majority of the sources have intermediate character between the two distinct chemistries, hot corino chemistry and WCCC. They also investigated the correlation between physical parameters (the evolutionary indicator and the location of the protostar) and the CCH/CH_3OH ratio. They found the tendency that the sources located near cloud edges or in isolated clouds tend to have a high CCH/CH_3OH ratio, suggesting that WCCC sources tend to reside in the cloud periphery (Figure 1.5d). They also report no correlation between the evolutionary indicator and the CCH/CH_3OH ratio (Figure 1.5b-c). Based on this result, they argue that the chemical diversity is independent of the protostellar age and is more related to

the environmental effects.

On the other hand, I conducted the statistical survey to examine the relation between chemical properties and the duration time of the starless core phase by using the deuterium fractionation ratio (Imai et al. 2018). Deuterium fractionation is a phenomenon that deuterium atoms are preferentially stored in molecules in a cold and dense environment. Although the elemental D/H ratio is $\sim 10^5$ (Sonneborn et al. 2000; Wood et al. 2004; Prodanović et al. 2010), the molecular D/H ratio is often as high as 10^{-3}-10^{-1} (Howe et al. 1994; van Dishoeck et al. 1995; Hirota et al. 2001). The deuterium fractionation ratio increases during the starless core phase in the cold condition ($T < 20$ K). The ratio could therefore have the information on the duration time of the starless core phase even after the onset of star formation. However, no relation between the deuterium fractionation ratio ($DNC/HN^{13}C$) and the CCH/CH_3OH ratio (an indicator of the chemical diversity) is found (Figures 1.6 a-b). Rather, the fractionation ratio has a negative correlation with a bolometric temperature, which is an evolutionary indicator of the protostar (Figures 1.6 c-d). Based on the result, it is concluded that the decrease of the deuterium fractionation ratio due to the temperature rise after the onset of the protostar overwhelms the variation of the deuterium fractionation ratio in the starless core phase. Thus, the deuterium fractionation ratio cannot be used for the index of the duration time of the starless core phase. Although several attempts to figure out the origin of the chemical diversity have been conducted so far, the conclusive evidence for the origin of the chemical diversity has not been obtained yet.

1.2.2 Envelope Scale Chemistry (10-100 au)

The advent of Atacama Large Millimeter/submillimeter Array (ALMA) enabled us to observe the thermal line emission of less abundant molecules at a sub-arcsecond resolution. It allowed us to study the chemical structures of the innermost envelope. The chemical structure around the protostar is found to be more complex than previously thought and is closely related to the physical structure. One notable result is the discovery of the centrifugal barrier. Sakai et al. (2014a) found that the CCH emission in the envelope gas shows the rotation motion in the outer part and suddenly disappears at a distance of 100 au from the protostar (Figure 1.7(a)). According to their result, this kinematic structure cannot be explained by the Keplerian motion, but be well explained by the simple ballistic infalling motion conserving angular momentum of the gas (Figure 1.7(c)). In this infalling-rotating motion, the gas cannot fall inward of a certain radius, because of the energy and the angular momentum conservation. They show that this position is the inner edge of the CCH emission, and name it as '*centrifugal barrier*' (Figure 1.8). Since this discovery, the model of this infalling-rotating envelope model has successfully been applied for several low-mass protostellar sources. (e.g. Sakai et al. 2016; Oya et al. 2016; 2017a) (see Chapter 4 for details of this model). Oya et al. (2016) reported the rise in gas kinetic temperature around the centrifugal barrier in IRAS 16293-2422. Based on the result, they point out the possibility that the gas may be stagnated in front of the centrifugal barrier. Indeed, Sakai et al. (2017) reported that the thickness of the envelope is increased by a factor of 2 around the radius of the centrifugal barrier in L1527. They suggest that the gas may stagnate in front of the centrifugal barrier and move toward the vertical directions perpendicular to the midplane.

What is important for the discovery of the centrifugal barrier is that it is not only a physical boundary between the envelope and the disk, but is also a boundary for the chemical structure. Sakai et al. (2014a; b) reported a drastic chemical change across the centrifugal barrier in L1527. The CCH and c-C_3H_2 lines trace the infalling-rotating envelope, while an SO line selectively highlights the centrifugal barrier. Furthermore, they detected a weak emission of CH_3OH coming from the centrifugal barrier and the disk component inside the centrifugal barrier. Such a drastic

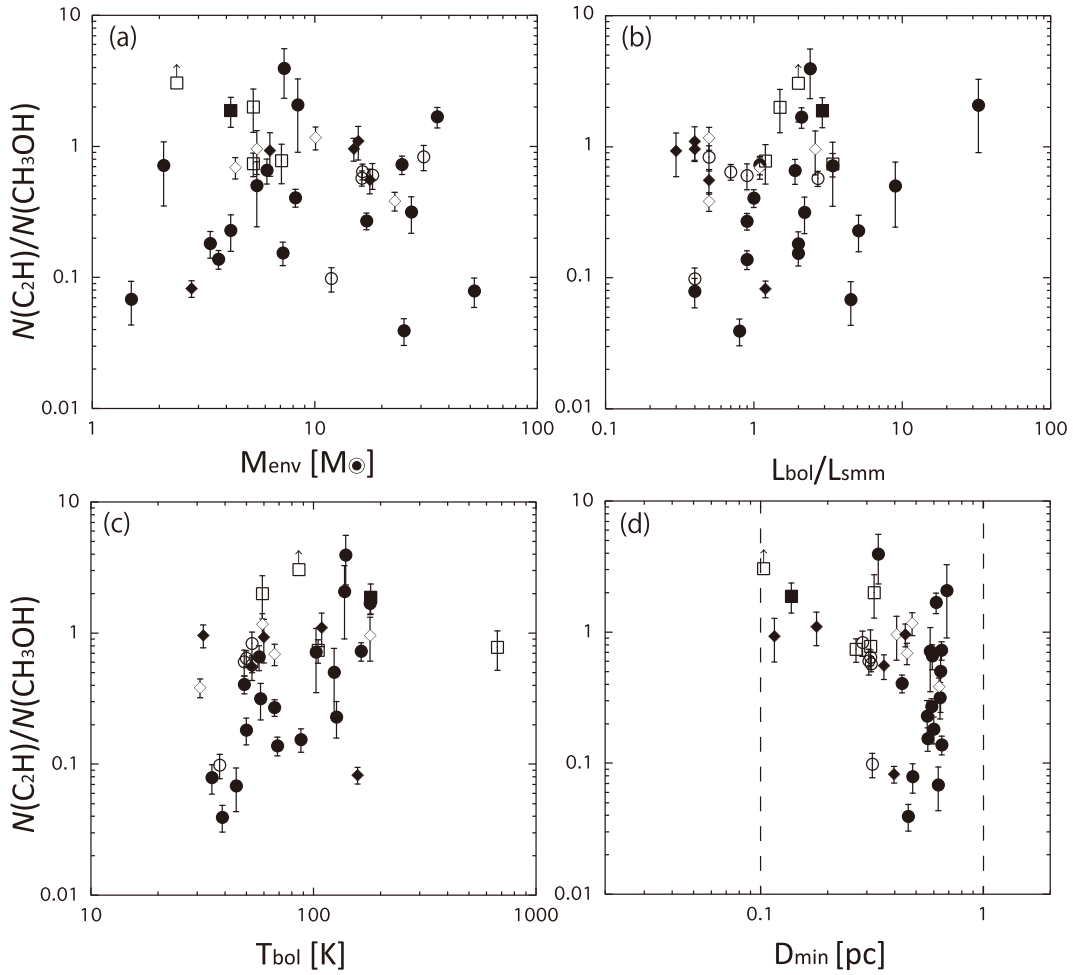

Figure 1.5: The correlation between the chemical diversity (CCH/CH_3OH) and physical parameters (envelope mass (a), the ratio of the bolometric luminosity to the submillimeter wavelength luminosity (b), bolometric temperature (c), and minimum projected distance to the cloud edge (d)) (Higuchi et al. 2018). They report that the sources with a short projected distance to the cloud edge tend to show a high CCH/CH_3OH ratio, suggesting the WCCC source may tend to be located in the cloud periphery or in the isolated cloud. On the other hand, they report that the CCH/CH_3OH ratio show no correlation with the evolutionary indicator (the ratio of the bolometric luminosity to the submillimeter wavelength luminosity $L_{\rm bol}/L_{\rm smm}$ and the bolometric temperature $T_{\rm bol}$).

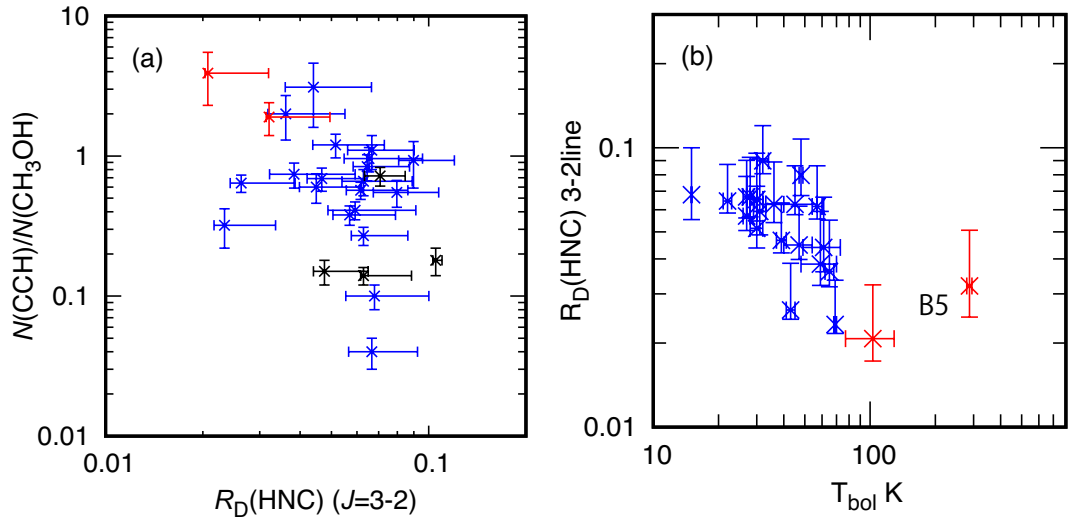

Figure 1.6: The results of the deuterium fractionation survey (Imai et al. 2018). (a, b) The correlation between the chemical diversity (CCH/CH_3OH) and the deuterium fractionation ratio (R_D(HNC)). Panel (a) represents the result for the deuterium fractionation ratio derived by the low excitation lines of DNC and $HN^{13}C$ (J=1-0), while panel (b) represents that derived by the high excitation lines (J=3-2). No clear correlation is found. (c, d) The correlation between the bolometric temperature of the protostar (T_{bol}) and the deuterium fractionation ratio. Panel (c) represents the result for the deuterium fractionation ratio derived by the low excitation lines of DNC and $HN^{13}C$ (J=1-0), while panel (d) represents that derived by the high excitation lines of DNC and $HN^{13}C$ (J=3-2). Negative correlation is confirmed in (c) and (d), suggesting the deuterium fractionation ratio decreases with the protostellar evolution.

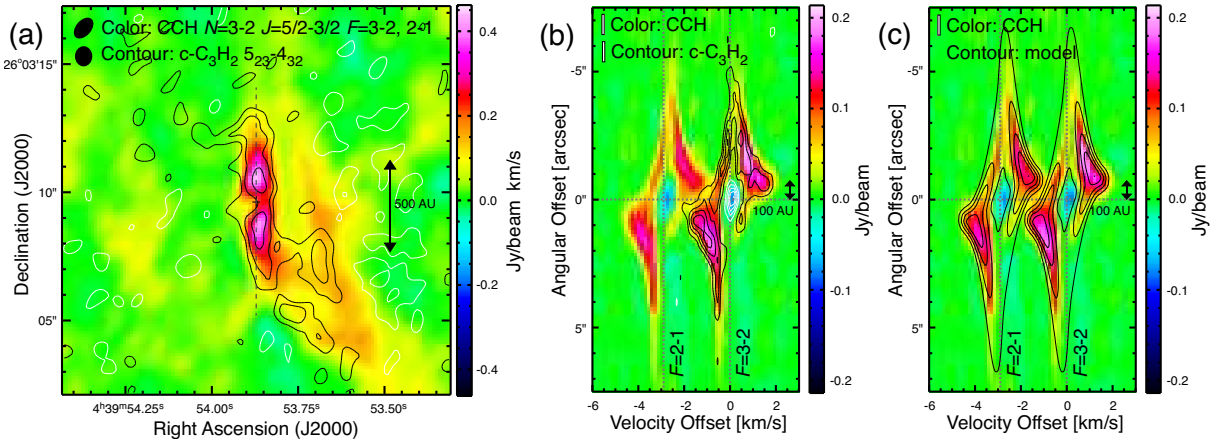

Figure 1.7: The distribution of the kinematic structure of CCH emission observed toward L1527 with ALMA (Sakai et al. 2014a). (a) The integrated intensity map of CCH. The distribution of the CCH line reveals a double-peaked structure elongated along the north-south direction (envelope direction), suggesting that CCH is absent in the vicinity of the protostar ($r < 100$ au). (b and c) The position velocity diagram of CCH along the south north direction (shown in a gray dashed line in panel a). The model of the infalling-rotating envelope is overlaid in the panel (c). The kinematic structure of the CCH is explained with the ballistic model of the infalling-rotating envelope where the angular momentum of the gas is conserved.

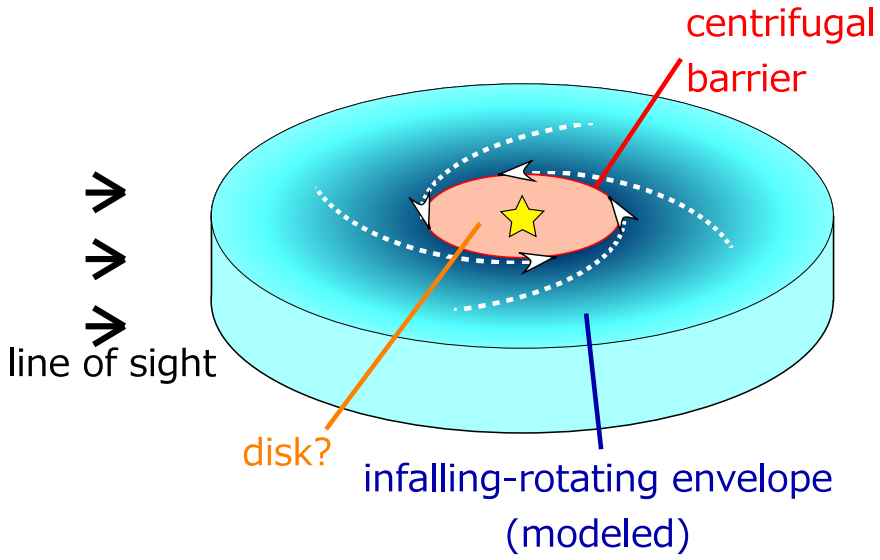

Figure 1.8: The schematic illustration of the model of the infalling-rotating envelope proposed by Sakai et al. (2014a).

chemical change across the centrifugal barrier is confirmed not only for WCCC sources, but also for hot corino sources. Oya et al. (2016) reported the similar drastic change across the centrifugal barrier toward the hot corino source IRAS 16293-2422. The OCS line traces the infalling-rotating envelope, while CH_3OH and $HCOOCH_3$ are concentrated around the centrifugal barrier. H_2CS emission comes from the disk component inside the centrifugal barrier as well as the envelope component, where the kinematic structure of the disk component is well explained by the Keplerian motion. They suggest that CH_3OH and $HCOOCH_3$ may be liberated by weak accretion shock in front of the centrifugal barrier and/or by protostellar heating. They also reported the increasing $HCOOCH_3/CH_3OH$ abundance ratio from the infalling-rotating envelope to centrifugal barrier, and to Keplerian disk, suggesting the formation of $HCOOCH_3$ across the centrifugal barrier through gas phase and/or grain surface reactions. Thus, the chemical structure has been found to be closely related to the physical structure around the protostar.

1.3 Motivation for the Isolated Sources

Thanks to ALMA, the physical and chemical structures of the envelope have been revealed by case studies of several representative protostellar sources in the Class 0 and I stages. It is also being revealed that their physical structures are essentially similar among the sources but their chemical structures are different. In spite of these efforts, the fundamental question on the origin of the chemical diversity has not been understood yet. One of the difficulties in tackling with this question is the different environments among the sources. As mentioned in Section 1.2.1, it has been proposed that the chemical feature of a protostellar source is affected by the activities of the nearby protostellar sources (*e.g.*, Buckle & Fuller 2002, Higuchi et al. 2010; 2014; Lindberg & Jørgensen 2012; Watanabe et al. 2012; Fukui et al. 2015; Spezzano et al. 2016a; 2016b). To overcome this situation, examining the simplest source without a protostellar activities of the other sources is useful. As such an ideal source, I focus on isolated protostellar sources and study their chemical characteristics together with the physical characteristics.

The isolated sources have been used as an ideal target for star-formation theory. Evans et al. (2015) verified the model of inside-out collapse core by observing the spectral line toward

a representative isolated source B335. They detected redshifted absorption features against continuum (inverse P-Cygni profile) in the HCN and HCO^+ lines. It had been known that the inverse P-Cygni profile would provide an indicator of matter in front moving inward toward the source center. However, it is not necessarily linked with the contraction motion toward a single star, because the effect of the foreground gas or outflow activities could also make such redshifted absorption features. Indeed, Di Francesco et al. (2001) detected the inverse P-Cygni profiles toward the protostellar core NGC 1333 IRAS 4A with interferometers. However, because of its rather complex region, there were suggestions that absorption arises from the foreground extended emission with a slight velocity offset which is resolved out in the observation rather than from an infalling motion in the envelope (Choi et al. 2004). Evans et al. (2015) thus employ the isolated source B335 to test the inside-out collapse model in order to exclude such environmental factors as much as possible. They concluded that the inverse P-Cygni profile seen in this source is the evidence of the infall motion toward the protostar.

In contrast to the intensive studies of the physical structure of the isolated sources (*e.g.*, Hirano et al. 1988; Evans et al. 2005; Launhardt et al. 2010; Shirley et al. 2011; Yen et al. 2015), the chemical characteristics of the isolated sources have been little understood or limited to some fundamental molecules. Thus, we need to study the chemical characteristics of the isolated sources to define the 'standard' chemical feature of the low-mass protostellar sources. Since most of the protostars are formed in molecular cloud complexes, the number of isolated sources are limited. Launhardt et al. (2010) conducted submillimeter and infrared observations toward 32 Bok globules, which were identified as candidates for globules with currently ongoing star formation, and studied their physical properties. According to their results, there are less than 10 candidates which have really isolated morphology and are close enough to us in order to study the innermost structure ($d < 400$ pc). Among the such target sources, B335 is one of the representative sources whose physical structure has been well studied (*e.g.,* Hirano et al. 1988; 1992; Chandler & Sargent 1993; Zhou et al. 1993; Wilner et al. 2000; Harvey et al. 2001). Hence, we first focus on the chemical characteristics of the isolated source B335, and then, extend this work to other isolated sources (CB68 and CB244).

1.4 Outline of This Thesis

This thesis consists of 10 chapters. After this introductory section (Chapter 1), basic theories of molecular line observations are summarized in Chapter 2. The fundamentals related to single-dish observations and interferometric observations are described in Chapter 3. The model used for the kinematic analysis of the envelope is discussed in Chapter 4. The observational results and analyses for the individual isolated sources are presented in Chapters 5-8. The chemical and physical characteristics of the representative isolated source B335 are shown in Chapters 5 and 6, and those of the other isolated sources CB68 and CB244 are presented in Chapters 7 and 8, respectively. Chapter 9 discuss the results for the three sources, and Chapter 10 finally concludes this thesis with future prospects.

Chapter 2

Basic Theory of Molecular Line Observations

2.1 Intensity

Intensity is defined as the energy flux I_ν of radiation coming from an unit solid angle through unit area per unit time and pre unit frequency, and its unit is J s^{-1} m^{-2} Hz^{-1} sr^{-1}. The energy dW of a radiation with intensity I_ν passing through a minute area $d\sigma$ coming from direction vector $d\boldsymbol{s}$ with a minute solid angle $d\Omega$ is written as:

$$dW = I_\nu(\boldsymbol{s}) \cos\theta d\Omega d\sigma d\nu. \tag{2.1}$$

Here, θ denotes the angle between the direction vector $\boldsymbol{s}$ and the direction normal to the minute area. On the other hand, the flux density S_ν is defined as the intensity integrated over a certain solid angle, and its unit is J s^{-1} m^{-2} Hz^{-1}.

$$S_\nu = \int_\Omega I_\nu(\boldsymbol{s}) d\Omega. \tag{2.2}$$

In the single dish observation, the antenna receives the radiation not only from the direction which the antenna is looking at, but also from other directions. How much radiation the antenna receives with the angular offset (θ, ϕ) is defined as the antenna beam pattern $(P(\theta, \phi))$. Normally, the beam pattern is normalized with the maximum signal intensity $P_{\rm max}$ as:

$$P_{\rm n}(\theta, \phi) = \frac{P(\theta, \phi)}{P_{\rm max}}. \tag{2.3}$$

Using the antenna beam pattern $P_n(\theta, \phi)$, the flux density received by the antenna is represented as:

$$S_\nu = \int_{\theta=0}^{\pi} \int_{\phi=-\pi}^{\pi} I_\nu(\theta, \phi) P_{\rm n}(\theta, \phi) \sin\theta \ d\theta \ d\phi. \tag{2.4}$$

Thus, the received flux density depends on the beam size and its pattern. Since the unit of the flux density, J s^{-1} m^{-2} Hz^{-1}, is usually too large, Jansky (Jy = 10^{-26} J s^{-1} m^{-2} Hz^{-1}) is often used in radio astronomy.

2.2 Brightness Temperature

Brightness temperature $T_{\rm b}$ is often substituted for the intensity I_ν. The intensity of the black body radiation of the temperature T at the frequency of ν is represented by the Plank equation:

$$I_\nu = \frac{2h\nu^3}{c^2}\frac{1}{\exp(\frac{h\nu}{k_{\rm B}T})-1}. \tag{2.5}$$

Since the intensity monotonously increases as increasing the temperature T, we can employ the temperature as the unit of the intensity I_ν. For the practical purpose, the linear conversion is used based on the Rayleigh-Jeans approximation:

$$I_\nu = \frac{2k_{\rm B}T\nu^2}{c^2} \tag{2.6}$$

$$T_{\rm B} = \frac{c^2}{2k_{\rm B}\nu^2}I_\nu = \frac{\lambda^2}{2k_{\rm B}}I_\nu, \tag{2.7}$$

where $\nu \ll k_{\rm B}T/h$ is assumed. In the radio observation, the above equation is employed for the conversion regardless of the applicability of the Rayleigh-Jeans approximation. In the case of thermal radiation, the brightness temperature provides a rough estimate on the actual temperature of the radiation source.

2.3 Radiative Transfer

When the radio waves propagate through an interstellar matter (*e.g.*, molecular cloud), its intensity varies due to absorption and emission by atoms, molecules, and dust particles. We here discuss how the intensity varies in the propagation. First, we define the x axis as the direction of propagation. The change in the intensity $\mathrm{d}I$ for the propagation of $\mathrm{d}x$ is represented as:

$$\frac{\mathrm{d}I}{\mathrm{d}x} = -\alpha I + j. \tag{2.8}$$

Here, j is the emissivity and α is the absorption coefficient. From now on, we consider that the cloud is homogeneous and α and j are independent of the position x, for simplicity. We define a new dimensionless variable τ as

$$\mathrm{d}\tau = \alpha\ \mathrm{d}x. \tag{2.9}$$

For the uniform cloud with a path length of L, $\tau = \alpha L$. Then, the equation is rewritten as:

$$\frac{\mathrm{d}I}{\mathrm{d}\tau} = -I + S, \tag{2.10}$$

where the source function S is defined as:

$$S = \frac{j}{\alpha}. \tag{2.11}$$

The equation gives the solution of

$$I = \exp(-\tau)\left[\int \exp(\tau)S\mathrm{d}\tau + C\right]. \tag{2.12}$$

For the optical depth τ of 0, the intensity should be the background radiation, $B(T_{\rm bg})$. With this boundary condition, we can get the relation that

$$I = \exp(-\tau)[\exp(\tau)S + B_\nu(T_{\rm bg}) - S]. \tag{2.13}$$

If we consider the hypothetical case that the cloud is completely enclosed with a black body at a temperature of T, the radiation will approach to the equilibrium of $I = B_\nu(T)$, after the sufficient time. This situation should be held for any τ, which gives the relation that

$$S = B_\nu(T). \tag{2.14}$$

This relation indicates that the absorption coefficient and the emissivity are not independent. Their relation is constrained only by the temperature. By replacing S with $B_\nu(T)$, we get the following relation:

$$I = B_\nu(T) + e^{-\tau}(B_\nu(T_{\rm bg}) - B_\nu(T)). \tag{2.15}$$

In usual observations, we measure the difference of the intensities between the source and the background. Hence, the difference is given as:

$$\Delta I = [B_\nu(T) - B_\nu(T_{\rm bg})](1 - e^{-\tau}). \tag{2.16}$$

The background intensity is usually observed toward the emission free region except for the cosmic microwave background. When $B_\nu(T)$ is approximated by the Rayleigh-Jeans equation, the intensity in the temperature scale is written as:

$$\Delta T = (T - T_{\rm bg})(1 - e^{-\tau}). \tag{2.17}$$

Here, we assume that $h\nu/k_{\rm B}T \ll 1$. This equation indicates that the emission is observed if $T - T_{\rm bg} > 0$, and the absorption is observed if $T - T_{\rm bg} < 0$.

2.4 Optical Depth and Column Density

The absorption coefficient α is a constant determined by the property of the matter. Now, we consider that radiation propagates in the matter with the two energy level system, and discuss how α is represented. Using the Einstein B coefficient, the energy absorbed in this matter by the transition from the level i to the level j in unit volume, in unit time, and from unit solid angle is written as:

$$h\nu n_i B_{ij} I/4\pi \cdot \phi(\nu). \tag{2.18}$$

Here, $\phi(\nu)$ represents the line shape shape function, and it is normalized as $\int \phi(\nu){\rm d}\nu = 1$. n_i is the number of molecules in the energy level of i. The lower and upper energy levels are represented as i and j, respectively. Similarly, the induced emission in unit volume, in unit time, and to unit solid angle is written as:

$$h\nu n_j B_{ji} I/4\pi \cdot \phi(\nu). \tag{2.19}$$

Using the above relations, the absorption coefficient α is represented as:

$$\alpha = \frac{h\nu}{4\pi}[n_i B_{ij} - n_j B_{ji}]\phi(\nu). \tag{2.20}$$

The Einstein B coefficients, B_{ij} and B_{ji}, are related with each other as:

$$g_i B_{ij} = g_j B_{ji}, \tag{2.21}$$

where g_i and g_j stand for the degeneracies of the lower and upper states, respectively. Using the relation between the Einstein A coefficient and the B coefficient as:

$$B_{ij} = \frac{c^2}{2h\nu^3} A_{ij}, \tag{2.22}$$

the absorption coefficient α is rewritten as:

$$\alpha = \frac{c^2}{8\pi\nu^2} A_{ji} n_j [\frac{n_i}{n_j}\frac{g_j}{g_i} - 1]\phi(\nu). \tag{2.23}$$

If we assume the Bolzman distribution for the two levels, the number of molecules (n_i and n_j) can be written as:

$$\frac{n_i g_j}{n_j g_i} = \exp(\frac{h\nu}{k_{\rm B} T_{\rm ex}}). \tag{2.24}$$

Here, $T_{\rm ex}$ represents the excitation temperature. The Einstein A coefficient is represented in terms of the intrinsic line intensity S and the dipole moment μ:

$$A_{ji} = \frac{64\pi^4\nu^3}{3hc^3}\mu_0^2\frac{S}{g_j}. \tag{2.25}$$

Then, the α is written as:

$$\alpha = \frac{8\pi^3\nu S\mu_0^2 n_j}{3hc\Delta\nu g_j}[\exp(\frac{h\nu}{k_{\rm B}T_{\rm ex}}) - 1]. \tag{2.26}$$

Here, the line shape function $\phi(\nu)$ is assumed to be $\frac{1}{\Delta\nu}$ ($\Delta\nu$: line width). This equation can be extended to the multi-energy level case as follows by using the velocity width of the line Δv and the partition function (U) of the molecule:

$$\alpha = \frac{8\pi^3 S\mu_0^2 n}{3h\Delta v U}[\exp(\frac{h\nu}{k_{\rm B}T_{\rm ex}}) - 1]\exp(-\frac{E_j}{k_{\rm B}T_{\rm ex}}), \tag{2.27}$$

where n denotes the total number of molecules. Here, we assume that the system is in the local thermodynamic equilibrium (LTE). In summary, the optical depth τ can be represented as:

$$\tau = \frac{8\pi^3 S\mu_0^2\ N}{3h\Delta v\ U}[\exp(\frac{h\nu}{k_{\rm B}T_{\rm ex}}) - 1]\exp(-\frac{E_j}{k_{\rm B}T_{\rm ex}}), \tag{2.28}$$

where N denotes the column density of the molecule ($N = nL$). Thus, we can derive the column density of the molecule by observing the molecular line emission. The relation between the column density and the observed brightness temperature is give as:

$$\begin{aligned}\Delta T &= \frac{h\nu}{k_{\rm B}}\left[\frac{1}{\exp(h\nu/k_{\rm B}T_{\rm ex}) - 1} - \frac{1}{\exp(h\nu/k_{\rm B}T_{\rm bg}) - 1}\right] \\ &\times \left[1 - \exp\left(-\frac{8\pi^3 S\mu_0^2\ N}{3h\Delta v\ U}(\exp(\frac{h\nu}{k_{\rm B}T_{\rm ex}}) - 1)\exp(-\frac{E_j}{k_{\rm B}T_{\rm ex}})\right)\right].\end{aligned} \tag{2.29}$$

We generally use the following approximation using the assumptions that $\tau \ll 1$, $\frac{h\nu}{k_{\rm B}T} \ll 1$, and $T_{\rm bg} \ll T_{\rm ex}$:

$$W = \frac{8\pi^3 S\mu_0^2\nu}{3k_{\rm B}T}\frac{N}{U}\exp(-\frac{E_j}{k_{\rm B}T_{\rm ex}}), \tag{2.30}$$

where W denotes the integrated intensity of the line ($W = \Delta v \cdot \Delta T$). If we observe the multiple lines of a single molecular species, we can extract the information on the excitation temperature and the column density in the LTE analysis.

Chapter 3

Instruments

3.1 Single-Dish Telescope

The single-dish telescope consists of a single aperture antenna to collect the faint emission from astronomical objects. Starting from molecular clouds are extremely cold ($\sim$ 10 K), molecules existing there only emit rotational transitions in the radio-wave region. Starting from the detection of fundamental molecular species such as NH_3, H_2O, H_2CO, and CO (*e.g.*, Cheung et al. 1968; 1969; Snyder et al. 1969; Wilson et al. 1970), rotational spectral lines of various molecules have been detected by ground-based single-dish radio telescopes. The basic techniques related to the single-dish observation are summarized here.

3.1.1 Components of the Single-Dish Telescope

The single-dish telescope has three major components: antenna, front end, and back end. The brief description of each component is given below.

Antenna

To collect a weak emission from astronomical objects, a radio telescope usually uses a main reflector with a paraboloidal shape. Since the spatial resolution of the beam is $\sim \lambda/D$ (D: diameter of the antenna aperture, λ: wavelength of the observation), a large antenna aperture is necessary to resolve the target source. The surface of the main reflector needs to have an accuracy much better than the observing wavelength λ. It should be typically better than $\lambda/20$. For an antenna with the aperture larger than 10 m (*e.g.*, IRAM 30 m and NRO 45m), it is difficult to maintain the paraboloidal shape of the antenna against the gravitational deformation. To overcome this effect, the main reflector is usually designed by the homologous deformation technique: the main reflector deforms depending on the elevation angle so as that it can keep the paraboloidal shape. If the position of the subreflector is appropriately set according to the deformation of the main reflector, the telescope performance is not degraded.

Front End

The radio signal collected by the main reflector is then conveyed to the receiver through the coupling optics. In the receiver, the signal is first converted to the intermediate frequency (IF) of a few GHz by a heterodyne mixer (here we consider the observation frequency of a few 100 GHz). The mixer is a non-linear device, which down-converts the frequency of the signal by the heterodyne mixing with the local oscillator signal (LO). The output IF signal includes information on two frequency bands: the upper side band (USB) and the lower side band (LSB).

The typical IF frequency range is 4-12 GHz, and hence, the frequency ranges from $\nu_{\rm LO}+4$ GHz to $\nu_{\rm LO}+12$ GHz for USB and from $\nu_{\rm LO}-12$ GHz to $\nu_{\rm LO}-4$ GHz for LSB are observed. Here $\nu_{\rm LO}$ denotes the LO frequency. If the receiver is sensitive to the sum of the USB and LSB, it is called a double-side-band receiver with the LO signals phase-shifted by 90°. If the receiver is sensitive to either of USB and LSB by using an input filter or by using two mixers, it is called a single-side-band receiver. The state-of-the-art mixer is 2SB mixer which outputs the USB and LSB signals simultaneously. This receiver is called as the side-band-separating receiver. The obtained IF signal is then amplified by an IF amplifier chain to the level necessary for the radio spectrometer.

Back End

The amplified IF signal is conveyed to a radio spectrometer. A digital spectrometer using an autocorrelator is the most popular back-end in these days. The IF signal is first digitized by a fast AD converter, followed by the autocorrelation as a function of the delay time. The spectrum is obtained by the Fourier transformation of the autocorrelation function. The sampling rate determines the instantaneous bandwidth, while the delay length determines the spectral resolution.

3.1.2 Observation with Single Dish Telescope

Gain Calibration

Responses of the receiver and the spectrometer show a frequency dependence. To calibrate this effect, we have to apply gain calibration by observing the black body radiation (absorber), whose temperature is known. We use cold and hot absorbers (COLD and HOT) in the calibration. By observing them, we calibrate the frequency dependence of the system as well as the intensity of target sources (Figure 3.1).

The observed output power (P) of the correlator is represented in a temperature scale by using linear interpolation of the output powers for COLD and HOT loads ($P_{\rm Hot}$, $P_{\rm Cold}$):

$$T = \frac{T_{\rm Hot} - T_{\rm Cold}}{P_{\rm Hot} - P_{\rm Cold}} P. \tag{3.1}$$

The noise temperature of the receiver system ($T_{\rm rec}$) is evaluated as:

$$T_{\rm rec} = \frac{T_{\rm Hot} - Y T_{\rm Cold}}{Y - 1}, \tag{3.2}$$

where

$$Y = \frac{P_{\rm Hot}}{P_{\rm Cold}}. \tag{3.3}$$

In the calibration process, we also observe the blank sky (SKY) in addition to the target sources. Systemic temperature is calculated by the signal intensity of SKY observation ($P_{\rm SKY}$) as:

$$T_{\rm sys} = \frac{T_{\rm Hot} - T_{\rm Cold}}{P_{\rm Hot} - P_{\rm Cold}} P_{\rm SKY}. \tag{3.4}$$

The radiation temperature of the sky ($T_{\rm sky}$) is also approximated as:

$$T_{\rm SKY} \simeq T_{\rm sys} - T_{\rm rec}. \tag{3.5}$$

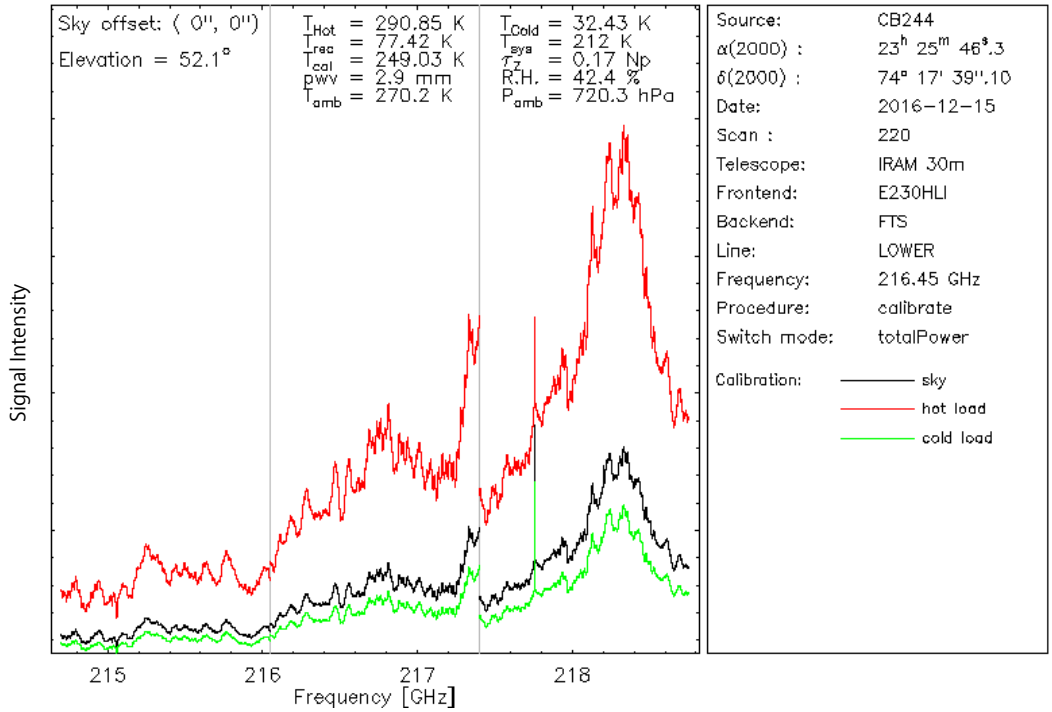

Figure 3.1: The example of the gain calibration in the IRAM 30 m observation. Red, green, and black lines indicate the signal intensity for the hot load, the cold load, and the SKY, respectively. The receiver has frequency dependence, and hence, the gain calibration is conducted for each frequency chank.

These values are calculated in the observation to assess the data quality (Figure 3.1). Using the signal intensities observed for the target source ($P_{\rm Source}$), the brightness temperature of the source ($\Delta T_{\rm source}$) is derived by taking a difference from the SKY observation as:

$$\Delta T_{\rm source} = \frac{P_{\rm Source} - P_{\rm SKY}}{P_{\rm Hot} - P_{\rm Cold}} \times (T_{\rm Hot} - T_{\rm Cold}). \tag{3.6}$$

Pointing

The direction of the antenna beam has to be maintained toward the source direction during the observation, because it is affected by strong wind and a change in the antenna temperature. For this purpose, we have to observe a bright point source whose coordinate is already known. This process should be conducted every 1 to 1.5 hours in normal weather conditions. Of course, the pointing should be conducted more often in the bad weather conditions. To minimize the effect of the distortion of the antenna by the elevation of the antenna, the pointing source should have a similar elevation angle as the target source. When the precipitable water vapor in the atmosphere (pwv) is high, the accuracy of the pointing becomes worse due to the refraction by water vapor. In that case, the pointing observation has to be be done in a lower frequency band.

3.1.3 IRAM 30 m

IRAM 30 m telescope is the one of the largest and sensitive radio telescope for millimeter wave observations (Figure 3.2). It is situated on Pico Veleta in the Spanish Sierra Nevada at an elevation of 2850 m. The average precipitable water vapor (pwv) at this site is 4.0 mm in the

Figure 3.2: Image of IRAM 30 m telescope.

winter condition, which realizes the average system temperature of 325 K in 1.2 mm band. It was constructed by the Institut de Radioastronomie Millimétrique (IRAM) in 1984. The parabolic dish is composed of 420 aluminium pannels with a surface precision of 55 μm, which is more than ten times smaller than the wavelength of its highest frequency band (375 GHz). The beam size at the 1.3 mm band is $9''.0$.

The heterodyne receiver EMIR (Eight MIxer Receiver) operates in the 3, 2, 1.3 and 0.9 mm atmospheric windows (Figure 3.3). All the EMIR bands are equipped with 2SB mixers that offer 8 GHz of instantaneous bandwidth for each sideband and each polarization. The Fast Fourier Transform Spectrometers (FTS) is connected to EMIR as the backend. The resolution of FTS is 200 kHz or 50 kHz. FTS provide 16 GHz of instantaneous bandwidth for each polarization at 200 kHz resolution, while it provide 7.2 GHz of instantaneous bandwidth for each polarization at 50 kHz resolution.

3.2 Interferometer

Interferometers employ a technique of the aperture synthesis, which produces an image of the target sources by combining signals of pairs of antennas. An essential part of the technique is described below.

3.2.1 Principles of Interferometers

In this Section, the basic principles of interferometers are described[1]. Now, we consider the situation that we observe a point source (marked with star in Figure 3.4) with two antennas (Antenna 1 and Antenna 2), for simplicity. $\boldsymbol{D}$ represents the relative position vector from Antenna 1 to Antenna 2, which is called baseline. $\boldsymbol{s}$ represents a unit vector from the center position of the antennas toward the source direction. There exists a geometric delay ($\tau_{\rm g}$) between Antenna 1 and Antenna 2 due to the optical path difference. Here, $\tau_{\rm g}$ is given as:

$$\tau_{\rm g} = \frac{1}{c}\boldsymbol{D}\cdot\boldsymbol{s}, \tag{3.7}$$

[1]Referenced literature of this Section: http://astro.sci.yamaguchi-u.ac.jp/jvn/reduction/SS2005text.pdf

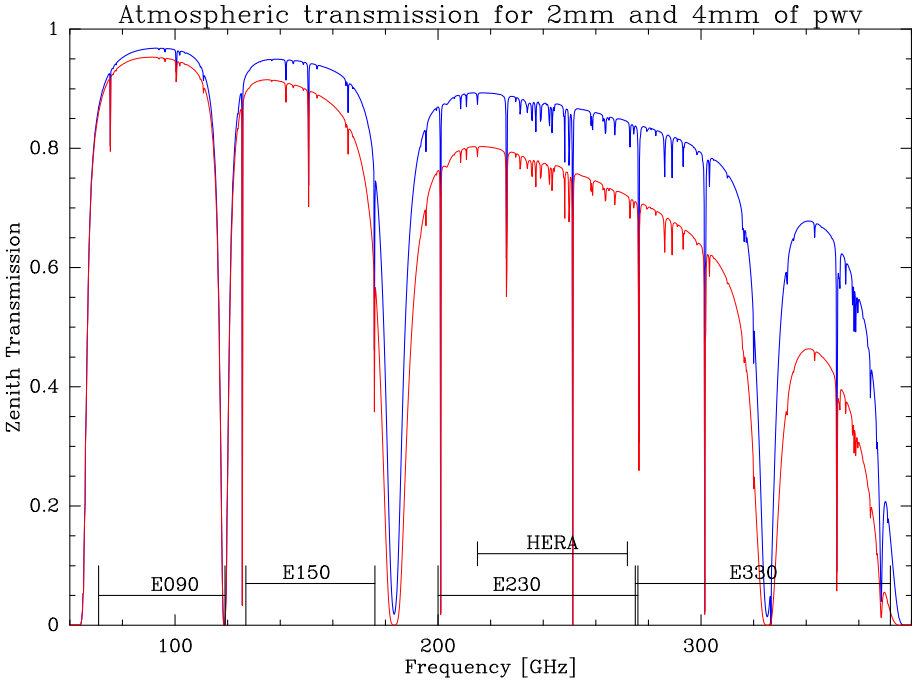

Figure 3.3: Atmospheric transmission at the IRAM 30 m site from 60 GHz to 400 GHz (http://www.iram.fr/GENERAL/calls/w16/30mCapabilities.pdf). The EMIR bands for 3, 2, 1.3 and 0.9 mm (E090, E150, E230, and E330) are marked.

where c denotes the speed of light. If we assume that the radiation is monochromatic at a frequency of ν_0, it is represented as $E(t) = E_0 \cos(2\pi\nu_0 t)$. Then, the signals received in each antenna are represented as follows:

$$V_1(t) = a_1 E_0 \exp(2\pi i \nu_0 t) \tag{3.8}$$

$$V_2(t) = a_2 E_0 \exp(2\pi i \nu_0 (t - \tau_{\rm g})). \tag{3.9}$$

Here, the coefficient $a_i (i = 1, 2)$ is a complex constant including the information on amplitude and phase, which are different between antennas. The cross correlation function $C(\tau)$ is derived as follows by using a correction of a delay τ_i:

$$\begin{aligned} C(\tau) &= \lim_{T\to\infty} \frac{1}{T} \int_{-T/2}^{T/2} V_1(t - \tau_{\rm i}) V_2^*(t - \tau) {\rm d}t \\ &= \lim_{T\to\infty} a_1 a_2^* \frac{1}{T} \int_{-T/2}^{T/2} E_0 \exp(2\pi i \nu_0 (t - \tau_{\rm i})) E_0^* \exp(-2\pi i \nu_0 (t - \tau - \tau_{\rm g})) {\rm d}t \qquad (3.10) \\ &= a_1 a_2^* |E_0|^2 \exp(2\pi i \nu_0 (\tau + \tau_{\rm g} - \tau_{\rm i})). \qquad (3.11) \end{aligned}$$

The cross correlation function, $C(\tau)$, is the output signal of the interferometer. The cross power spectrum $\hat{C}(\nu)$ is obtained by Fourier transformation of the cross correlation function:

$$\begin{aligned} \hat{C}(\nu) &= \int_{-\infty}^{\infty} C(\tau) \exp(-2\pi i \nu \tau) {\rm d}\tau \\ &= a_1 a_2^* |E_0|^2 \delta(\nu_0 - \nu) \exp(2\pi i \nu_0 (\tau_{\rm g} - \tau_{\rm i})). \qquad (3.12) \end{aligned}$$

Then, we consider the situation that the radiation from the source is represented as the function of ν, $\hat{E}(\nu)$. The radiation is written as:

$$E(t) = \int \hat{E}(\nu) \exp(2\pi i \nu t) {\rm d}\nu. \tag{3.13}$$

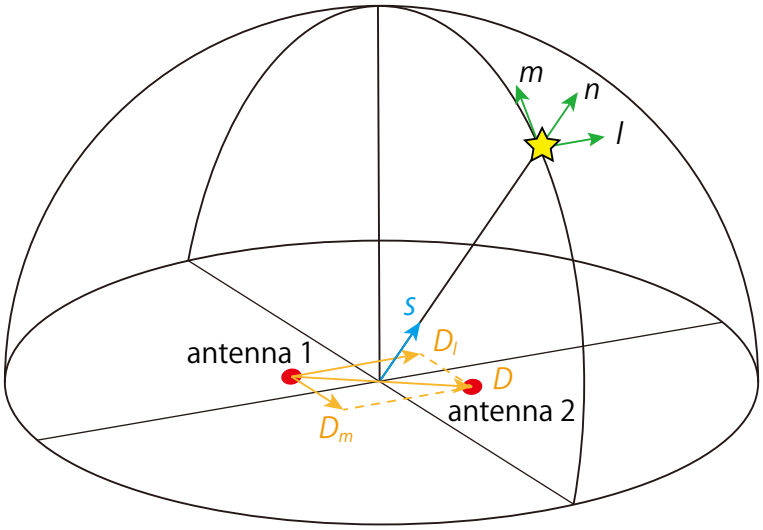

Figure 3.4: The schematic illustration of the assumed coordinate system of the plane of the sky and the observers.

Here, $\hat{E}$ is complex, and the phase depends on the frequency ν. Similar to the monochromatic radiation case, the received signal is written as:

$$V_1(t) = a_1 \int_{-\infty}^{\infty} \hat{E}(\nu) \exp(-2\pi i \nu t) \mathrm{d}\nu \tag{3.14}$$

$$V_2(t) = a_2 \int_{-\infty}^{\infty} \hat{E}(\nu) \exp(-2\pi i \nu (t - \tau_\mathrm{g})) \mathrm{d}\nu. \tag{3.15}$$

In this case, the cross correlation function is written as:

$$\begin{aligned} C(\tau) &= \lim_{T\to\infty} \frac{1}{T} \int_{-T/2}^{T/2} V_1(t - \tau_\mathrm{i}) V_2^*(t - \tau) \mathrm{d}t \\ &= a_1 a_2^* \lim_{T\to\infty} \frac{1}{T} \int_{-T/2}^{T/2} \mathrm{d}t E(t - \tau_\mathrm{i}) E^*(t - \tau_\mathrm{g} - \tau) \\ &= a_1 a_2^* \int_{-\infty}^{\infty} \mathrm{d}\nu \, |\hat{E}(\nu)|^2 \exp(2\pi i \nu (\tau + \tau_\mathrm{g} - \tau_\mathrm{i})). \end{aligned} \tag{3.16}$$

The cross power spectrum $\hat{C}(\nu)$ is written as:

$$\begin{aligned} \hat{C}(\nu) &= \int_{-\infty}^{\infty} \mathrm{d}\tau \, C(\tau) \exp(-2\pi i \nu \tau) \\ &= a_1 a_2^* |\hat{E}(\nu)|^2 \exp(2\pi i \nu (\tau_\mathrm{g} - \tau_\mathrm{i})). \end{aligned} \tag{3.17}$$

Here, we can see that the cross power spectrum is proportional to $|\hat{E}(\nu)|^2$.

Now, we consider the cases where the point source has an offset from the direction that the antennas are looking at. Defining an offset from the direction vector $\boldsymbol{s}$ for the direction of l as ψ, the differentiation of the phase $\Delta\phi$ is derived by using $\phi = 2\pi\nu(\tau_\mathrm{g} - \tau_\mathrm{i})$ as follows:

$$\begin{aligned} \Delta\phi &= \frac{\partial\phi}{\partial\psi} \Delta\psi \\ &= 2\pi \frac{D\cos\theta}{\lambda} \Delta\psi. \end{aligned} \tag{3.18}$$

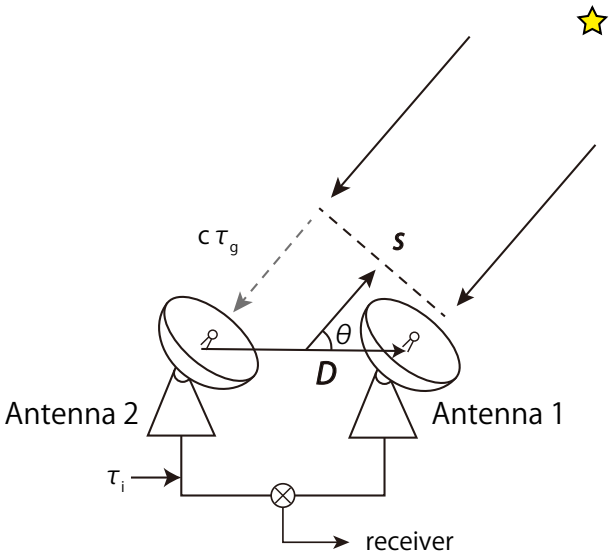

Figure 3.5: The schematic illustration of the array configuration.

To derive this equation, we employ the relation that

$$\begin{aligned} \frac{\partial \phi}{\partial \psi} &= 2\pi\nu \frac{\partial \tau_{\rm g}}{\partial \psi} \\ &= 2\pi \frac{1}{\lambda} \boldsymbol{D} \cdot \frac{\partial \boldsymbol{s}}{\partial \psi} \\ &= 2\pi \frac{D\cos\theta}{\lambda}. \end{aligned} \tag{3.19}$$

Hereafter, we call $D\cos\theta/\lambda$ as the spatial frequency and write it as u:

$$\Delta\phi = 2\pi u \Delta\psi. \tag{3.20}$$

We can thus derive the position of the radiation source from $\Delta\phi$.

Then, we consider that there are two radio sources whose positions are $l = l_1$ and l_2, where their radiation spectra are represented as $\hat{E}_1(\nu)$, and $\hat{E}_2(\nu)$, respectively. In this case, the intensity distribution in the plane of sky is written as:

$$I(\nu, \psi) = |\hat{E}_1(\nu)|^2 \delta(\psi - \psi_1) + |\hat{E}_2(\nu)|^2 \delta(\psi - \psi_2). \tag{3.21}$$

If we assume that the delay correction $\tau_{\rm i}$ is completely the same as $\tau_{\rm g}$ for the origin of $\psi = 0$, the phases in the cross power spectrum ϕ_1 and ϕ_2 are written as:

$$\phi_1 = 2\pi\nu\tau'_{\rm g1} = 2\pi u\psi_1 \quad (\tau'_{\rm g1} = \tau_{\rm g1} - \tau_{\rm i1}) \tag{3.22}$$

$$\phi_2 = 2\pi\nu\tau'_{\rm g2} = 2\pi u\psi_2 \quad (\tau'_{\rm g2} = \tau_{\rm g2} - \tau_{\rm i2}). \tag{3.23}$$

Using the Equations 3.16 and 3.17, the correlation function and the cross power spectrum is

written as follows as the super position of the radiation source.

$$\begin{aligned} C(\tau) &= a_1 a_2^* \int_{-\infty}^{\infty} \mathrm{d}\nu \left[|\hat{E}_1(\nu)|^2 \exp(2\pi i\nu(\tau + \tau'_{\mathrm{g}1})) + |\hat{E}_2(\nu)|^2 \exp(2\pi i\nu(\tau + \tau'_{\mathrm{g}2})) \right] \\ &= a_1 a_2^* \int_{-\infty}^{\infty} \mathrm{d}\nu \exp(2\pi i\nu\tau) \\ &\qquad \times \left[|\hat{E}_1(\nu)|^2 \exp(2\pi iu\psi_1)) + |\hat{E}_2(\nu)|^2 \exp(2\pi iu\psi_2) \right] \end{aligned} \tag{3.24}$$

$$\begin{aligned} \hat{C}(\nu) &= \int_{-\infty}^{\infty} \mathrm{d}\tau \; C(\tau) \exp(-2\pi i\nu\tau) \\ &= a_1 a_2^* \int_{-\infty}^{\infty} \mathrm{d}\tau \int_{-\infty}^{\infty} \mathrm{d}\nu' \exp(2\pi i(\nu' - \nu)\tau) \\ &\qquad \times \left[|\hat{E}_1(\nu')|^2 \exp(2\pi i\nu'(\tau'_{\mathrm{g}1})) + |\hat{E}_2(\nu)|^2 \exp(2\pi i\nu(\tau'_{\mathrm{g}2})) \right] \\ &= a_1 a_2^* \left[|\hat{E}_1(\nu)|^2 \exp(2\pi iu\psi_1)) + |\hat{E}_2(\nu)|^2 \exp(2\pi iu\psi_2) \right] \end{aligned} \tag{3.25}$$

In the same way, the cross power spectrum for the case of several radiation sources is written as:

$$\hat{C}(\nu) = a_1 a_2^* \sum_k |\hat{E}_k(\nu)|^2 \exp(2\pi iu\psi_k), \tag{3.26}$$

while that for the case of continuously distributed source is written as:

$$\begin{aligned} \hat{C}(\nu) &= a_1 a_2^* \int_{\mathrm{source}} \mathrm{d}\psi \; |\hat{E}(\nu, \psi)|^2 \exp(2\pi iu\psi) \\ &= a_1 a_2^* \int_{\mathrm{source}} \mathrm{d}\psi \; I(\nu, \psi) \exp(2\pi iu\psi). \end{aligned} \tag{3.27}$$

Here, the intensity distribution $I(\nu, \psi)$ is

$$I(\nu, \psi) = \int_{\mathrm{source}} \mathrm{d}\psi \; |\hat{E}(\nu, \psi)|^2. \tag{3.28}$$

In the Equation 3.27, $\hat{C}(\nu)$ is a function of not only ν but also ψ, and hence, we rewrite this as $V(\nu, \psi)$. $V(\nu, \psi)$ is called complex visibility, and holds information on the relation between the spatial frequency u and the amplitude and the phase. The intensity distribution $I(\nu, \psi)$ can be regarded as 0 outside the radiation source. Thus, $V(\nu, \psi)$ is written as:

$$V(\nu, u) = a_1 a_2^* \int_{-\infty}^{\infty} \mathrm{d}\psi \; I(\nu, \psi) \exp(2\pi iu\psi) \tag{3.29}$$

We can see that $V(\nu, \psi)$ is an inverse Fourier transform of $I(\nu, \psi)$. Using this, we can obtain the intensity distribution of $I(\nu, \psi)$ at a certain frequency ν by measuring $V(\nu, u)$. In the interferometric observation, we measure the visibility $V(\nu, u = D\cos\theta/\lambda)$ for various baselines $\boldsymbol{D}$ and retrieve the original intensity distributions.

In the above discussion, one dimensional baseline (u) is assumed. It can be extended to the two dimensional case (u and v), which is the case for the interferometric observation.

3.2.2 Observation with Interferometer

Flag

If a part of the data has large noise due to some reasons, they must be removed for the better analysis. This procedure is called '*Flag*'. The followings are several major instrumental reasons for flagging in the interferometric observation.

- Tracking
  Flux fluctuates due to the tracking error, and hence, the scans before and after the large pointing error should be flagged.

- Shadowing
  It is possible for foreground array elements to block the signal received by background antennas, especially for the source at low elevations. This effect is called "shadowing" and becomes prominent for compact configuration observations. The "shadowing" seriously compromises the sensitivity and imaging quality of observations. Therefore, the data from the shadowed antennas should be flagged.

- Doppler
  The effect of the doppler velocity shift due to the rotation of the earth is calculated for every a few seconds. If the change in the velocity shift exceeds the threshold within a subscan, that data should be flagged.

- Cable
  The cable inside the antenna may change in its shape, when the antenna direction largely changes due to the switching of targets. Hence, a large phase delay may happen, when we change the target source. The data before and after the large change in the cable delay should be flagged out.

Calibration

The output data from an interferometer suffer from amplitude variation and phase instability due to the atmospheric condition and the instrumental property even after flagging. Such effects are corrected by the phase and amplitude calibrations. The principle concept of the phase calibration is to make the phase for the original position set to 0. The variables which determine the phase in Equation 3.29 are $|a_i|$ and $\tau_{\rm i}$, and we can calibrate phase by applying the proper delay correction $\tau_{\rm i}$. The amplitude calibration corresponds to the correction of the a_i in Equation 3.29. There are mainly two types of the calibration for the interferometric observation, *i.e.*, the antenna-based calibration and the baseline-based calibration. The following description refers to the antenna-based calibration which is applied for our observations in this thesis.

- Phase Calibration
  The phase of the visibility function contains information on the source position. When the delay correction $\tau_{\rm i}$ is equal to the geometrical delay $\tau_{\rm g}$, the phase of the $\hat{C}(\nu)$ becomes 0 for the field center (*i.e.*, target source) regardless of the frequency ν (Equation 3.29). Here, we assume that the phase variation by the complex gain a is the same for the all antennas (*i.e.*, $a_1 = ra_2$ (r: real number). However, the observed phase actually suffers from the atmospheric delay (*e.g.*, different atmospheric conditions for different antennas) and the instrumental delay (*e.g.*, different length and temperature of the cables). In the phase calibration, these phase variations are corrected by modifying $\tau_{\rm i}$.

  Phase calibration is performed by using a well-known strong point source, because the source size should be much smaller than the synthesized beam size for accurate determination of the phase. Quasars are often used for the phase calibration. In the calibration, the phase for each antenna is calculated and apply the τ_i correction for each antenna. If the number of the antennas are n, we can make a correction of $n-1$ degrees of freedom for τ_i, and find a best solution to minimize the phase variation. The phase solution is searched for each baseline. The number of baselines is ${}_n\mathrm{C}_2$ which is larger than the number of the free parameters, and hence, we cannot make the variation zero. If some antennas have a

large phase variation, the data using these antennas must be flagged out, or we can have better solution by adjusting their weights in the calibration.

If the target source is bright enough, the phase calibration can be done using the target source itself. This procedure is called as '*self-calibration*'. When we perform the self-calibration, the information on the absolute coordinate is lost, unless the position of the target source is accurately known.

In addition, a water vapor radiometer (WVR) is used for compensating the short-term fluctuation of the phase delay due to the atmosphere. We can estimate the phase delay due to the water vapor by measuring the atmospheric water emission. In the cases of ALMA and NOEMA, a water vapor radiometer (WVR) is installed in each antenna for this purpose, and the time variation of the precipitable water vapor (pwv) is estimated. The temporal fluctuation of the delay is corrected by the measured pwv.

- Bandpass Calibration
  The frequency response of the interferometer is corrected by the bandpass calibration. The bandpass calibration is performed with a bright calibrator source, which has a known radio spectral index without spectral features. Bright quasars are typically used as a bandpass calibrator. The frequency response is almost stable over many hours, and nearly independent of the sky position of the radio source. Thus, the bandpass calibration is performed only at the start or end of the observation, or additionally just a few times during the observation. The bandpass calibrations typically take a half or an hour, because they require a good S/N ratio in each spectral channel of the correlator system. However, if the observation for other calibrations is performed toward a sufficiently bright source, it can also be used for the bandpass calibration.

- Flux Calibration
  In the flux calibration, the scaling factor from the observed amplitude to the absolute flux density is obtained by observing a flux calibrator. As a primary flux calibrator, Solar System objects are usually used. Based on the result, the flux densities of the secondary flux calibrators are monitored by the ALMA observatory and its recent value are accurately known. The temporal variation of the interferometer gain is corrected by observing the secondary flux calibrator. The accuracy of the flux calibration for Band 6 is 10 % for the ALMA Cycle 2 observation, 5 % for the Cycle 4 observation, and 10 % for the Cycle 6 observation.

CLEAN Method

CLEAN is a deconvolution method suggested by Högbom (1974), and is commonly used for the data reduction of interferometric observations. Due to the incompleteness of the *uv* plane of the observation, the observed image is usually different from the real distribution. The image directly derived from the Fourier transform of the visibility ('*dirty image*') suffers from the side lobes of the synthesized beam. The right panel of Figure 3.6 shows an example of the point spread function of the ALMA beam, which shows how point source emission will be observed with the uv-coverage of the observation (the left panel of Figure 3.6). The point spread function is extended as large as the synthesized beam size. Besides, weak negative and positive features appear, which are due to the side lobes of the beam. These features often make it difficult to distinguish whether the observed image is a real feature or an artificial one.

The main goal of the CLEAN method is to reduce the influence of the side lobes by replacing the point spread function of the observation with the ideal beam function without the side lobe component as the convolution function. To this end, the intensity distribution is modeled by a

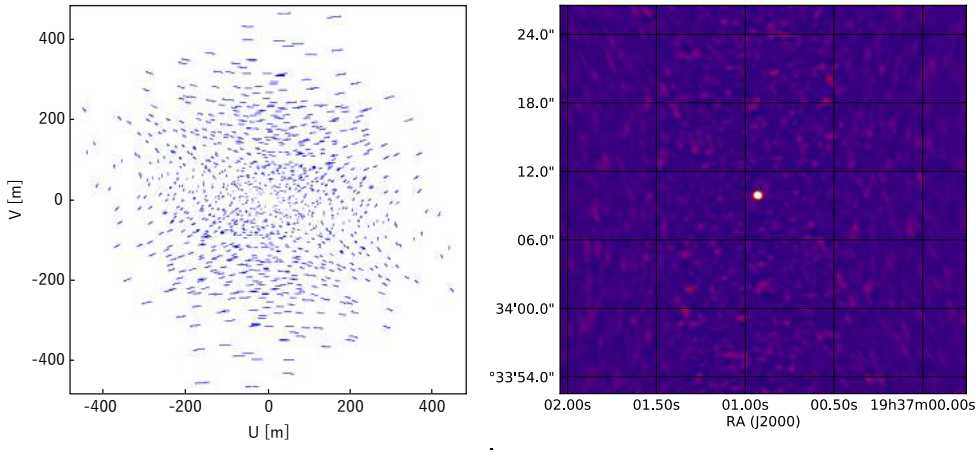

Figure 3.6: (*left*)The example of the uv coverage of the ALMA observation. (*right*) The point source function corresponding to the left uv coverage.

set of point sources. A point source is searched for from the intensity peak in a dirty map, and its convolved image with the synthesized beam is calculated. The convolved image, including its side lobe, is subtracted from the dirty image. This operation is repeated for specified times, or until the peak intensity in the residual image becomes lower than a specified threshold. Typically the threshold is set to be a few times noise level of the observation. With such procedure, the residual image includes emission, side lobe, and noise, which are much weaker than the first dirty image. Then, the modeled image is convolved by an ideal beam function ('*CLEAN beam*'). The CLEANed image is obtained by summing up the model convolved image and the residual image. The Gaussian beam having the same FWHM as that of the synthesized beam is usually used as the CLEAN beam.

Figure 3.7 shows an example of the application of CLEAN to the ALMA data. In the dirty image, the side lobe component appears periodically. Most of these components are removed by CLEAN (Figure 3.7 right panel). Figure 3.8 shows the total flux of the CLEAN components as a function of the number of the CLEAN cycles. In the left panel, the total flux of the CLEAN components gradually increases with the iteration of the CLEAN cycle, and finally saturate at a certain level, which indicates the residual reaches almost similar to the noise level of the observation. On the other hand, the total flux of the CLEAN components shows oscillation feature after some iterations of the CLEAN cycle in the right panel. This usually occurs when side lobe components are picked up as a real component. To avoid this situation, a mask is usually set for the CLEAN method, which defines the region of the real emission.

3.2.3 ALMA

Atacama Large Millimeter/submillimeter Array (ALMA) is the largest radio interferometer working in the millimeter- and submillimeter-wave regions, which is located at Chajnantor in the middle of the Atacama desert at 5000 m altitude (Figure 3.9). In spite of the strong penetration power of the radio wave, the water vapor in the atmosphere absorbs radio waves from the Universe. This is why the ALMA site is in one of the most dry and high altitude areas in the world. The precipitable water vapor (pwv) is typically below 0.5 mm at this site, and such a condition enables us to conduct good observations even at the high frequency band from 400 GHz to 1000 GHz. ALMA was constructed by the trilateral international partnership among East Asia, North America, and Europe. The construction was started in 2003, and the

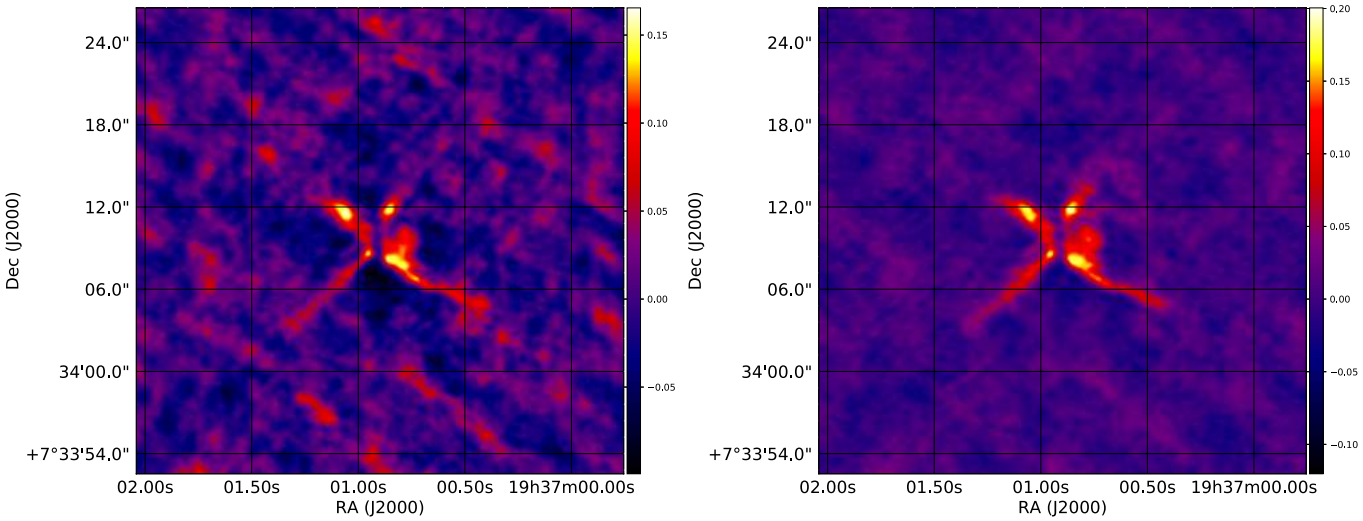

Figure 3.7: (*left*) The dirty map without the application of CLEAN. The emission is the spectral line of CCH observed for B335. (*right*) The CLEANed image of the left emission.

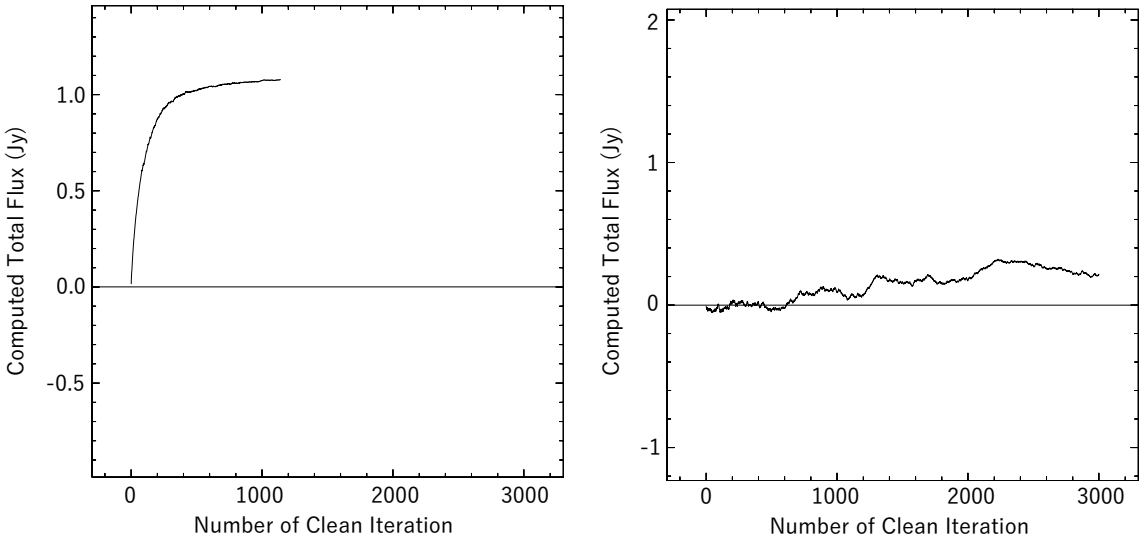

Figure 3.8: Examples of the CLEAN application. The total flux of the CLEAN components as a function of the number of the CLEAN cycles (NOEMA observation toward CB244) is shown. In the left panel, the total flux gradually increases and saturates around 1 Jy. This indicates that the peak intensity in the residual image becomes lower than the threshold. The iteration of CLEAN stops here. On the other hand, the total flux show oscillation feature, and the CLEAN iteration continues to 3000 times (the specified iteration time) in the right figure. This usually occurs when side lobe components are picked up as a real component.

Figure 3.9: Images of Atacama Large Millimeter/submillimeter Array (ALMA) (https://www.almaobservatory.org/en/home/) and NOthern Extended Millimeter Array (NOEMA) (https://www.iram-institute.org).

early science operation was started with the limited number of the array antennas in September 2011. The operation was started from 2012.

ALMA has 66 antennas which consists of fifty-four 12-meter diameter antennas (Main Arrays) and twelve 7-meter diameter antennas (Atacama Compact Array; ACA). They are distributed over the maximum distance of 18 km, and achieve a maximum angular resolution of $0''.01$ at the wavelength of 1 mm (300 GHz). This resolution corresponds to the linear-scale resolution of 1 au for the source at a distance of 100 pc (326 light years). ACA is implemented to fill the short baseline length in the observation, and it is located at the center of the array. In order to take the short baseline data, the diameter of the ACA antenna is 7 m, which is smaller than that of the main array (12 m). The 12 m and 7 m antennas have a surface accuracy better than 25 μm and 20 μm, respectively, which are about 50 times smaller than the wave-length at Band 6.

As mentioned above, the radio-wave observation is influenced by the absorption by water and oxygen molecules in the atmosphere, which makes it difficult to observe certain frequency ranges. The frequency ranges where radio wave can penetrate the atmosphere are called "Atmospheric Window". ALMA will cover all the atmospheric windows from 35 GHz to 950 GHz (Figure 3.10) with the 10 receiver bands (Band 1 to 10), as listed in Table 3.1. Now, we have 8 available bands for the observation, while 2 bands are not ready yet (December 2019).

3.2.4 NOEMA

NOthern Extended Millimeter Array (NOEMA) is the millimeter array in the Northern Hemisphere, which is situated on the Plateau de Bure at 2550 m altitude in the French Alps (Figure 3.9). The average pwv at this site is 3.0 mm in winter condition, which realizes the average systemic temperature of 180 K in the 1.3 mm band. NOEMA was constructed by the Institut de Radioastronomie Millimétrique (IRAM) as Plateau de Bure Interferometer (PdBI), and started its operation in 1988 with three antennas whose maximum baseline is 288 m.

NOEMA has 10 antennas with a diameter of 15 m which are arranged on the 'T' figured rail tracks. They are distributed over the maximum distance of 760 m (760 m in the east-west direction and 368 m in the north-south direction), which realizes the spatial resolution of $0''.4$ at 1.3 mm band. Advantage of the NOEMA interferometer is its strong spectroscopic capability. The total bandwidth of the low resolution baseband is 15.488 GHz with the spectral resolution of 2 MHz (Figure 3.11). The baseband is split into two sidebands (upper and lower side band),

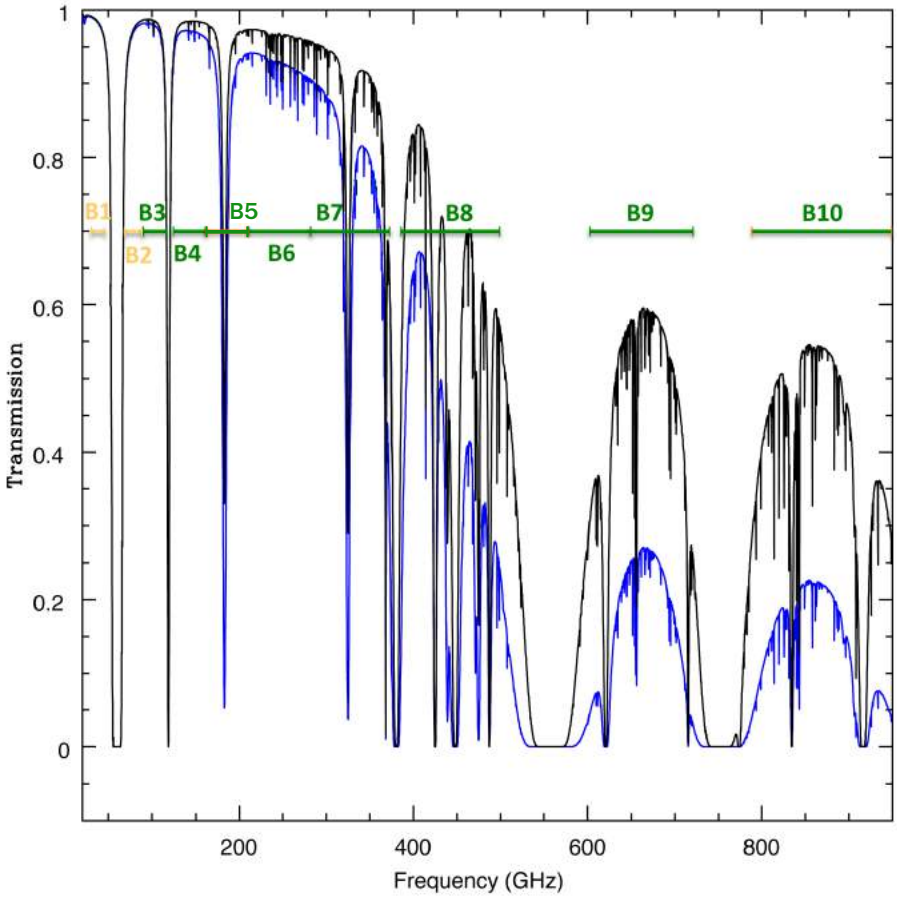

Figure 3.10: The transmission spectrum of the radio wave at Chajnantor (5000 m) (https://almascience.eso.org/documents-and-tools/cycle4/alma-early-science-primer). The frequency ranges of the 10 receiver bands installed on ALMA are shown with horizontal bars. Yellow indicates the band currently not in operation, and green indicates the band in operation.

Table 3.1: The list of ALMA Band

Band	Wavelength (mm)	Frequency (GHz)
1[a]	8.6 - 6	35 - 50
2[b]	4.6 - 3.3	65 - 90
3	3.6 - 2.6	84 -116
4	2.4 - 1.8	125 - 163
5	1.8 - 1.4	163 - 211
6	1.4 - 1.1	211 - 275
7	1.1 - 0.8	275 - 373
8	0.8 - 0.6	385 - 500
9	0.5 - 0.4	602 - 720
10	0.4 - 0.3	787 - 950

[a] Currently in preparation.
[b] Currently under development.

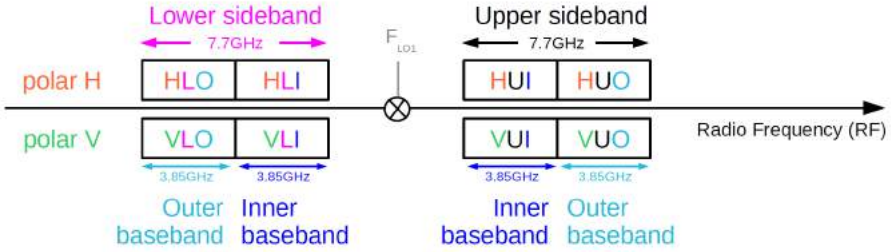

Figure 3.11: The schematic illustration of the baseband employed for the NOEMA observation (http://www.iram.fr/GENERAL/calls/w18/NOEMACapabilities.pdf).

and each sideband is composed of two adjacent basebands of 3.85 GHz width. Additionally, in total 64 high-resolution chunks are implemented in the baseband. Each chunk has a bandwidth of 64 MHz with a fixed spectral resolution of 62.5 kHz. The spectral windows composed by the sets of chunks cover the frequency range of 4.096 GHz in total. Among the atmospheric window, NOEMA covers 3 bands in the frequency range from 70 GHz to 276GHz. The frequency range of each band is 70.4 GHz to 119.87 GHz for Band 1, 127.00 GHz to 182.87 GHz for Band 2, 196.13 GHz to 276.00 GHz for Band 3.

Chapter 4

Kinematic Model of the Infalling-Rotating Envelope

Thanks to the high spatial resolution capability of ALMA, the kinematic structure of the innermost envelope around the protostar ($\sim$ a few 10 au) is now being revealed. One of the biggest discoveries brought by ALMA is the identification of the centrifugal barrier by Sakai et al. (2014a), as mentioned in Section 1.2.2. They reported that the kinematics of the flattened envelope around the protostar can be explained by the infalling-rotating gas motion. Oya et al. (2014) constructed the numerical model based on this idea, and revealed that a ballistic model of an infalling-rotating envelope well reproduced the observation. Since then, this model has been successfully applied to the several low-mass protostellar sources (e.g. Sakai et al. 2016; Oya et al. 2016; 2017a). In this Chapter, I describe the details of the model together with our new method to compare the observation data with the model data.

4.1 Configuration of the IRE Model

Figure 4.1 shows the schematic illustration of the 'infalling-rotating envelope' model (Oya 2017b). In this model, the gas is simply assumed to be falling and rotating under the gravity of the central protostar. The gas motion is approximated by the particle motion, where the effects of gas pressure, magnetic field, self gravity, and radiation from the protostar are ignored. Because of the energy and angular momentum conservation, the gas cannot fall inward of a certain radius. This radius is called as 'centrifugal barrier'. Assuming the velocity of a particle at the infinite distance to be 0, the radius of the centrifugal barrier ($r_{\rm CB}$) is written as:

$$r_{\rm CB} = \frac{j^2}{2GM}, \tag{4.1}$$

where G is the gravitational constant, M is the protostellar mass, and j is the specific angular momentum of the gas. Here all particles are assumed to have identical specific angular momentum. At the radius of the centrifugal barrier, all the kinetic energy is converted to the rotational energy. It is a half of the centrifugal radius ($r_{\rm CR}$), where the gravitational force and the centrifugal force are balanced:

$$r_{\rm CR} = \frac{j^2}{GM} = 2\ r_{\rm CB}. \tag{4.2}$$

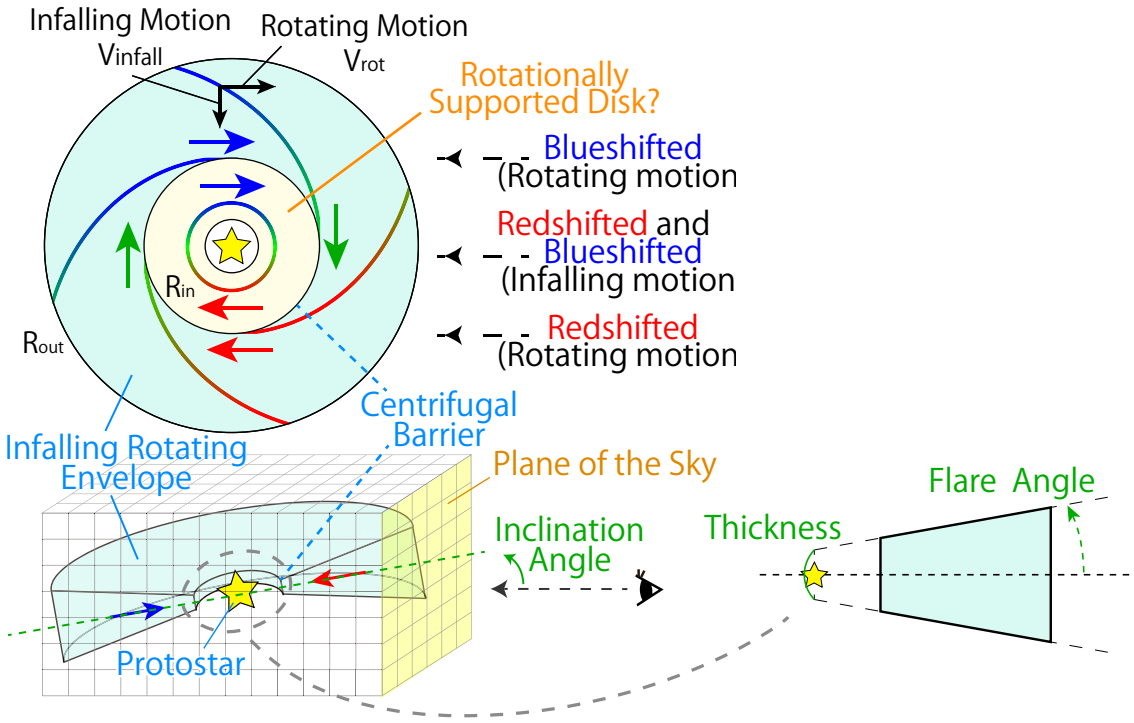

Figure 4.1: The schematic illustration of the infalling-rotating envelope model (Oya 2017b). The space and the velocity field are sectionalized into meshes.

The rotation velocity ($v_{\rm rot}$) and the infall velocity ($v_{\rm inf}$) of the gas at the distance of r from the protostar are represented as:

$$v_{\rm rot} = \frac{1}{r}\sqrt{2GMr_{\rm CB}} \tag{4.3}$$

$$v_{\rm inf} = \frac{1}{r}\sqrt{2GM(r - r_{\rm CB})}. \tag{4.4}$$

Thus, the velocity field is represented by M and $r_{\rm CB}$. In the model, the inclination angle and the position angle of the source can be chosen depending on the source.

The distribution of the molecular emission is assumed to have a flared-disk structure, which is specified by the following four parameters: the outer radius, the inner radius, the thickness of the envelope, the flare angle of the envelope (Figure 4.1). Here, 'flare' means that the thickness of the envelope linearly increases with the flare angle as an increasing radius on the midplane of the envelope. The value of the thickness represents the vertical thickness of the envelope at the protostellar position in the midplane (Figure 4.1).

In this model, the profile of the molecular distribution is assumed to have a power-law. Shu (1977), Ohashi et al. (1997), and Harvey et al. (2003) reported the H_2 density profile of $r^{-1.5}$ for a collapsing cloud. This power-law index can be used, if the fractional abundance of the molecule is constant over the envelope, and the excitation effect as well as the radiative transfer effect is ignored. These assumptions are employed in this thesis.

The spectral line is assumed to have an intrinsic Gaussian profile with a certain line width, and the emission is convolved with a Gaussian beam corresponding the synthesized beam. The intrinsic line width and the beam size are parameters of the model, depending on sources and the configurations of the observations.

Each particle has 6 dimensional information: three are for the position of the particle (x, y, and z) and the other three are for the velocity of the particle (v_x, v_y, and v_z). The 6

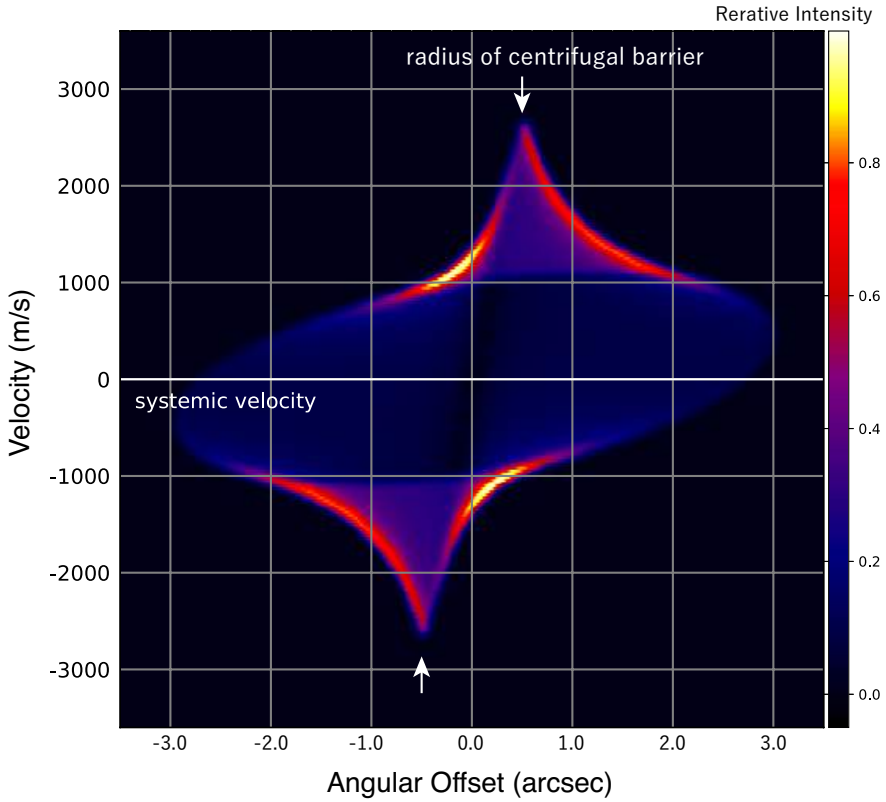

Figure 4.2: An example of the PV diagram of the IRE model. The position axis is along the disk/envelope direction, and the origin denotes the protostellar position.

dimensional parameter space are considered in the calculation, which is sectionalized into mesh for the numerical calculation (the same mesh sizes for x, y, and z ($\mathrm{d}x$) and for v_x, v_y, and v_z ($\mathrm{d}v$)). Hence, x, y, z, v_x, v_y, and v_z have discrete values. The mesh sizes for the position axis and the velocity axis can be changed according to the observations. $\mathrm{d}x$ and $\mathrm{d}v$ are unchanged over the parameter space.

Figure 4.2 shows an example of the model calculation. The kinematic structure of the rotation axis is represented in the position-velocity (PV) diagram (see also Figure 1.7 as an example of the observation). The horizontal axis denotes the position offset from the center of the source (*i.e.,* protostellar position), and the vertical axis denotes the velocity of the gas. Color indicates the intensity of the molecular emission. The model displays a typical feature of the infalling-rotating envelope. The position of the highest velocity component is different from that of the lowest velocity component. Such an inclined velocity structure in the PV diagram (*i.e.,* velocity gradient) is a typical feature of the rotation motion. The velocity of the particle becomes highest at the centrifugal barrier which is shown by white arrows in Figure 4.2.

4.2 Evaluation of the Similarity of the Observation and the Model

A quantitative evaluation of goodness of the fit between the observed PV image and the model PV image is not always straightforward. The difficulties of the fitting arise from the following reasons. First, we cannot directly compare the intensities of the observation and the model. This is because the intensity of the emission is affected by the distributions of the gas density,

the gas kinematic temperature, and the molecular abundance variation. Second, a fit of the model to the observed image tends to reproduce only the intense region in the case of the direct comparison of intensities, and does not account for the kinematic structure of the outer part of the envelope. Rather, the similarity of the outline shape of the PV diagram should be more important, because it reflects the whole kinematic structure of the envelope. Third, the model only reproduces the infalling-rotating structure of the envelope, and other structures such as an outflow activity, which may be contaminated, are ignored. These factors make it difficult to evaluate the accuracy of the PV fit, and hence, the fitting has conventionally been carried out by eye (e.g. Sakai et al. 2014b; Yen et al. 2015; Oya et al. 2016; Oya et al. 2017a; Imai et al. 2019).

The evaluation of the goodness of the PV fit is especially important in the case that no molecular emission traces the entire envelope structure from the outer region to the inner region. CB244 is the case for this situation (see Chapter 8). In this case, the emitting region of the molecular line differs from species and species, and the whole envelope structure can be extracted only by combining emissions of several molecular species. This situation makes the direct comparison of the observed data for each species and the modeled data more difficult. To overcome the above difficulties, we newly introduce the index of the goodness of the fit for the quantitative analysis.

4.2.1 Methodology

Our method consists of the following two processes: (1) evaluation of the signal detection probability of each pixel in the PV diagram and (2) introduction of the similarity function of the two images. Their details are discussed below.

First, we evaluate the signal detection probability of each pixel in the PV diagram for each molecule ($p_{i,\mathrm{mol}}$). The procedure is summarized by the schematic illustration in Figure 4.3. We introduce the signal detection probability, because we focus on the fitting of the outer shape of the PV diagram. As described above, the intensity of the emission itself is hard to be reproduced. Alternatively, we extract the information whether the emission is detected at a certain position and a certain velocity by setting a threshold to the intensity. For the numerical analysis, we use the sigmoid function ($\mathrm{sig}(I_{i,\mathrm{mol}}; I_{\mathrm{thres}}, b)$) (e.g. Basheer et al. 2000; Costarelli et al. 2013) as the probability calculation:

$$p_{i,\mathrm{mol}} = \mathrm{sig}(I_{i,\mathrm{mol}}; I_{\mathrm{thres}}, b) = \frac{1}{1 + \exp(-\frac{I_{i,\mathrm{mol}} - I_{\mathrm{thres}}}{b \times I_{\mathrm{thres}}})}. \tag{4.5}$$

Here, $I_{i,\mathrm{mol}}$ represents the observed intensity of the molecule at the pixel i in the PV diagram, I_{thres} represents the threshold intensity for the signal detection, and b is the coefficient which determines the smoothness of the boundary between detection and non-detection. Figure 4.4 shows an example of the application of the sigmoid function to the Gaussian distribution. The value of the sigmoid function represents how significantly the value of the Gaussian function exceeds the threshold. In this way, the outer boundary of the emission can be highlighted in the PV diagram by setting a certain threshold. In the analyses in this thesis, the threshold is set to be 30 % of the intensity peak for each molecular line, and b is set to be 0.2, where the signal detection probability for the zero emission is 0.67 %. The dependence of the result on these parameters will be discussed in each analysis of the source. I_{thres} should be determined so as that the probability distribution is not significantly affected by the noise of the observation.

Then, the signal detection probability at the pixel i is calculated as the maximum value of the probabilities for all the molecules in use:

$$p_i = \max(p_{i,\mathrm{mol}})\Big|_{\mathrm{mol}}. \tag{4.6}$$

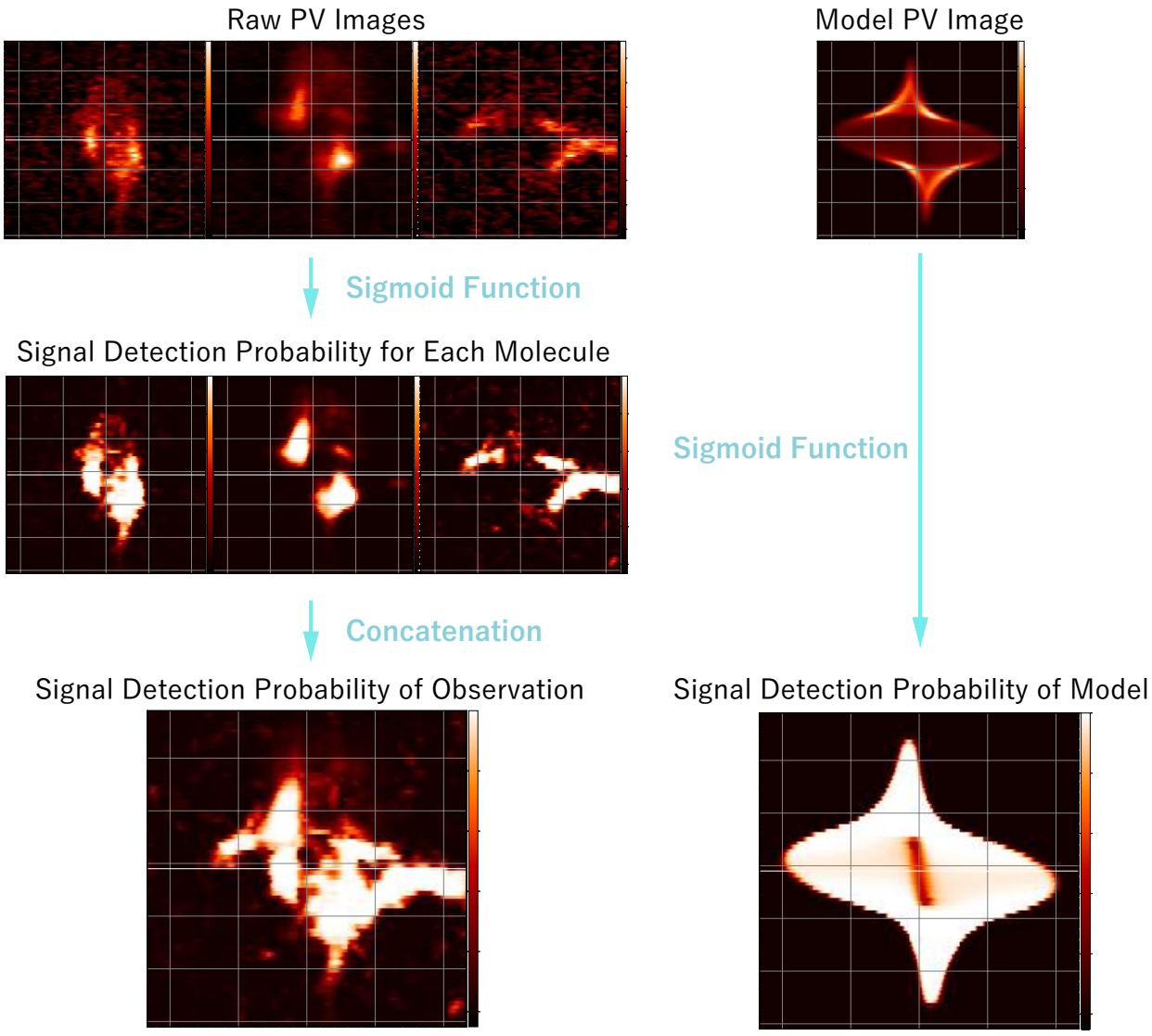

Figure 4.3: The schematic illustration of the procedure to obtain the signal detection probability distributions for the observation and the model. This is an example for the case of CB244 (Chapter 8).

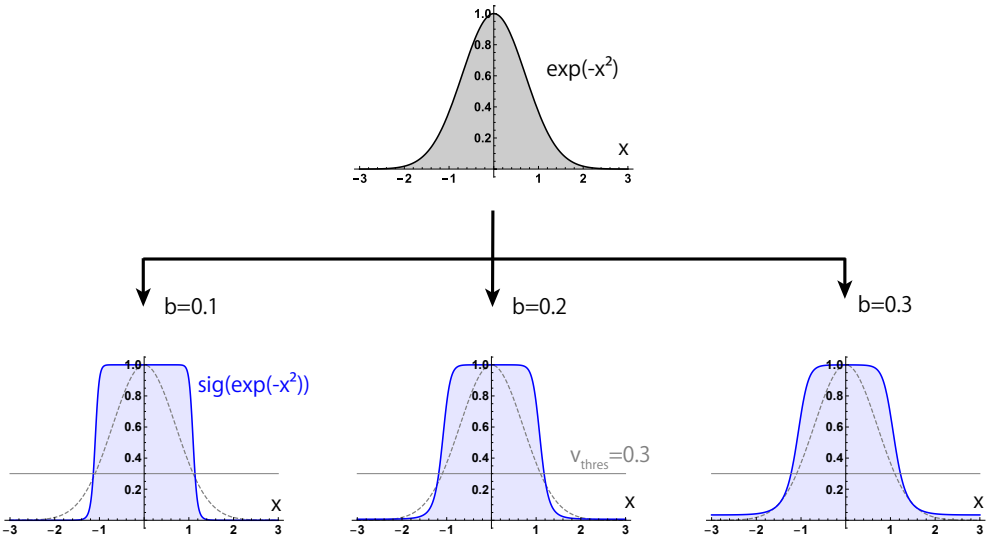

Figure 4.4: The example of the sigmoid function ($\mathrm{sig}(x; I_{\mathrm{thres}}, b)$) applied to the gaussian distribution. $\mathrm{sig}(x; I_{\mathrm{thres}}, b)$ is defined in Equation 4.6. In this example, I_{thres} is set to be 0.3 for the sigmoid function. b is changed to be 0.1, 0.2, and 0.3, which determines the smoothness of the boundary between signal detection and non-detection. For $b = 0.1$, the value of the sigmoid function is rapidly change across the I_{thres}, while it is more gentle for $b = 0.3$.

In the same way, the signal detection probability is calculated at the pixel i for the model (q_{i}) with the following equation:

$$q_i = \frac{1}{1 + \exp(-\frac{I_{i,\mathrm{model}} - I_{\mathrm{thres}}}{b \times I_{\mathrm{thres}}})}. \tag{4.7}$$

Here, we set the I_{thres} of 10 % of the maximum intensity of the model.

It should be noted that the values of I_{thres} for the observation and the model affect the shape of the outline of the PV diagram and the similarity calculation. In addition, b also affects the result, because it determines the sharpness of the boundary. In addition, the probability for zero emission is determined by this value, which change the effect of the noise emission. These values cannot be optimized by the observation dataset. The dependence of the results on these parameters will be discussed in each case of the analysis. However, these parameters do not significantly affect the result within 5-10 % variations for I_{thres} and ± 0.1 variation for b in general. For I_{thres}, a relative scale to the maximum intensity (30 %) is used instead of the noise level in order that the extent of the emission enclosed in the boundary is less influenced by the intensity of the line.

As the next step, we compare the probability distribution of the observation with that of the model. To evaluate the similarity, we use Kullback-Leibler divergence (KL divergence: $KL(p, q)$) (Kullback & Leibler 1951):

$$KL(p, q) = \sum_i \left(\tilde{p}_i \log \frac{\tilde{p}_i}{\tilde{q}_i} + \tilde{q}_i \log \frac{\tilde{q}_i}{\tilde{p}_i} \right) / \ 2. \tag{4.8}$$

Here, $\tilde{p}_i$ and $\tilde{q}_i$ are the normalized probabilities of p_i and q_i, respectively, where they are normalized as:

$$\sum_i \tilde{p}_i = 1, \sum_i \tilde{q}_i = 1. \tag{4.9}$$

There are several other indexes for the similarity calculation such as correlation function and inner product. However, these two indexes are more influenced by emission-free regions of the image, because the weighting is equal for each pixel regardless of the probability (intensity). On the other hand, the Kullback-Leibler divergence is less affected by the contribution of such no-emission regions. This index takes 0 or positive values, and smaller value suggests the similar probability distribution. For further verification, we confirm that the results based on the KL divergence is almost consistent with the those of the correlation function and the inner product in the analysis of this thesis. The detail comparison of the results based on these three indexes with the actual dataset is shown later in Section 4.2.3.

Figure 4.5 shows an example of optimization by the similarity calculation. $KL(p, q)$ is calculated for the observed PV image for CB244 with NOEMA (see Chapter 8 for detail). The black lines show how $KL(p, q)$ varies with the parameter variation. For instance, the value of $KL(p, q)$ becomes the lowest for the protostellar mass of 0.4 $M_{\odot}$ and increases as the mass increases or decreases from this value. Thus, the best parameter value can be estimated. The detailed description on the application of this method to individual sources presented in the analysis of each source.

4.2.2 Effect of Noise

Errors for $KL(p, q)$ due to the observation noise are difficult to be estimated, because they are derived in a non-analytic way. As one method for the estimation of the error of $KL(p, q)$, the mock PV images are employed as discussed below (Figure 4.6). First, we set an artificial threshold ($I_{\rm thres,out}$) for the PV diagram of each molecule to identify the 'emission-free' pixels whose intensities are below the threshold. Then, we artificially modify the intensity of the 'emission-free' pixels to zero. In other words, only emission is extracted and the noise in the emission free region below the threshold is removed to obtain the 'denoised' PV image. Then, we make a mock PV image for each molecular emission by adding artificial noise to the 'denoised' PV image. Here, the level of the artificial noise is the same as the rms noise of the observation. By applying the sigmoid function and concatenating the images for each molecule as discussed in Section 4.2.1, the signal detection probability is obtained for the 'denoised' images and mock images. We use the same parameter values for the sigmoid function as used in the analysis of the observation data ($I_{\rm thres} = 30$ % and $b = 0.2$). Although all of the noise are not eliminated from the raw PV image, the 'denoised' image can be virtually regarded as a noise-free one. Hence, the effect of the noise on $KL(p, q)$ is estimated by calculating the similarity between the 'denoised' image and mock image.

The derived similarity between the denoised image and the mock image ($KL_{\rm noise}$) can be regarded as the upper limit of the error due to the noise. Hence, we use $KL_{\rm noise}$ as the tolerance range in the optimization. For instance, if the similarity for the best fitted model is $KL_{\rm best}$, we estimate the uncertainty of the model parameter to be the range whose model similarity is between $KL_{\rm best}$ and $KL_{\rm best} + KL_{\rm noise}$. The tolerance range for the example shown in Section 4.2.1 is represented by the gray range in Figure 4.5.

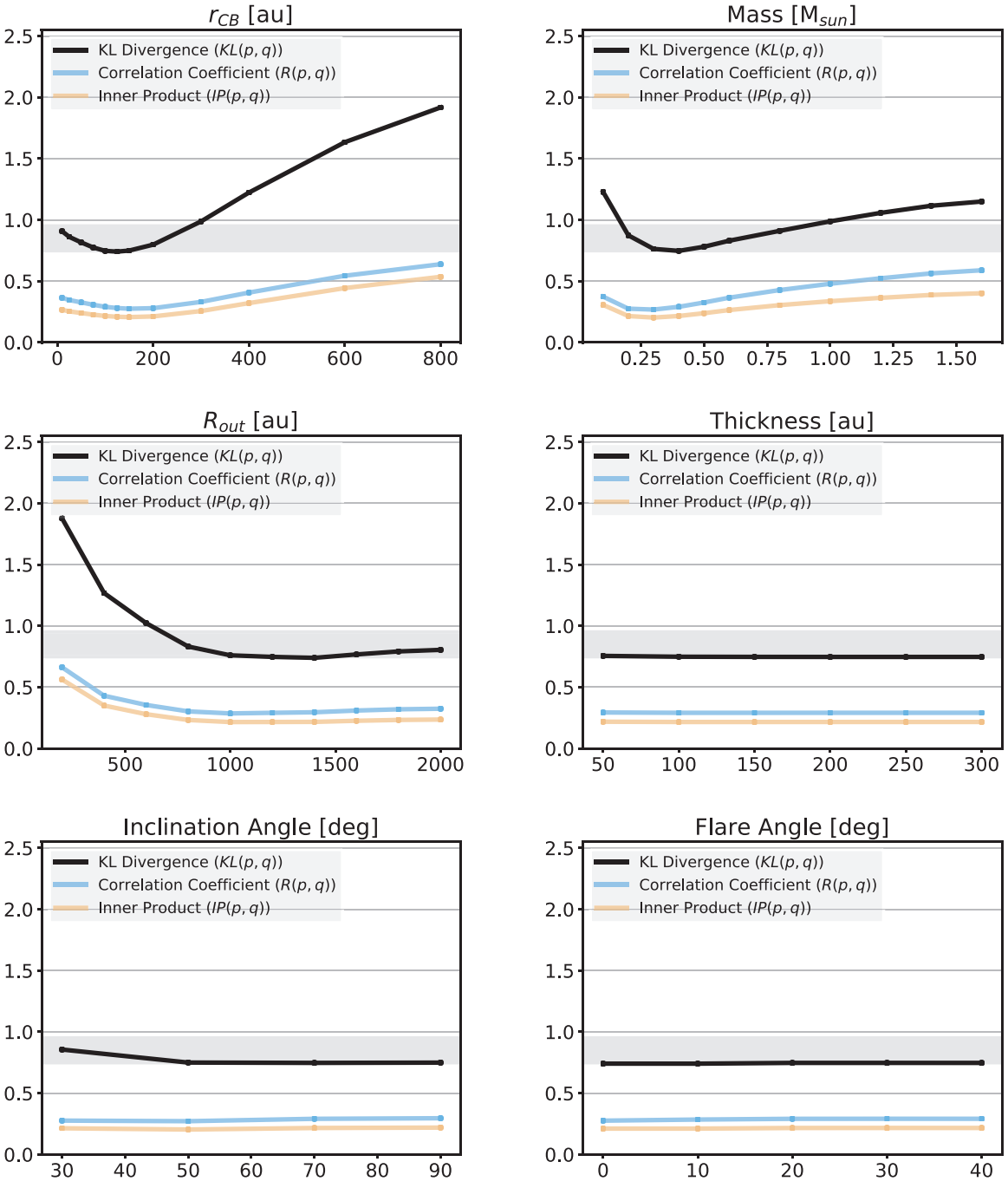

Figure 4.5: The results for the similarity indexes of the KL divergence (black), the correlation coefficient (blue), and the inner product (orange).

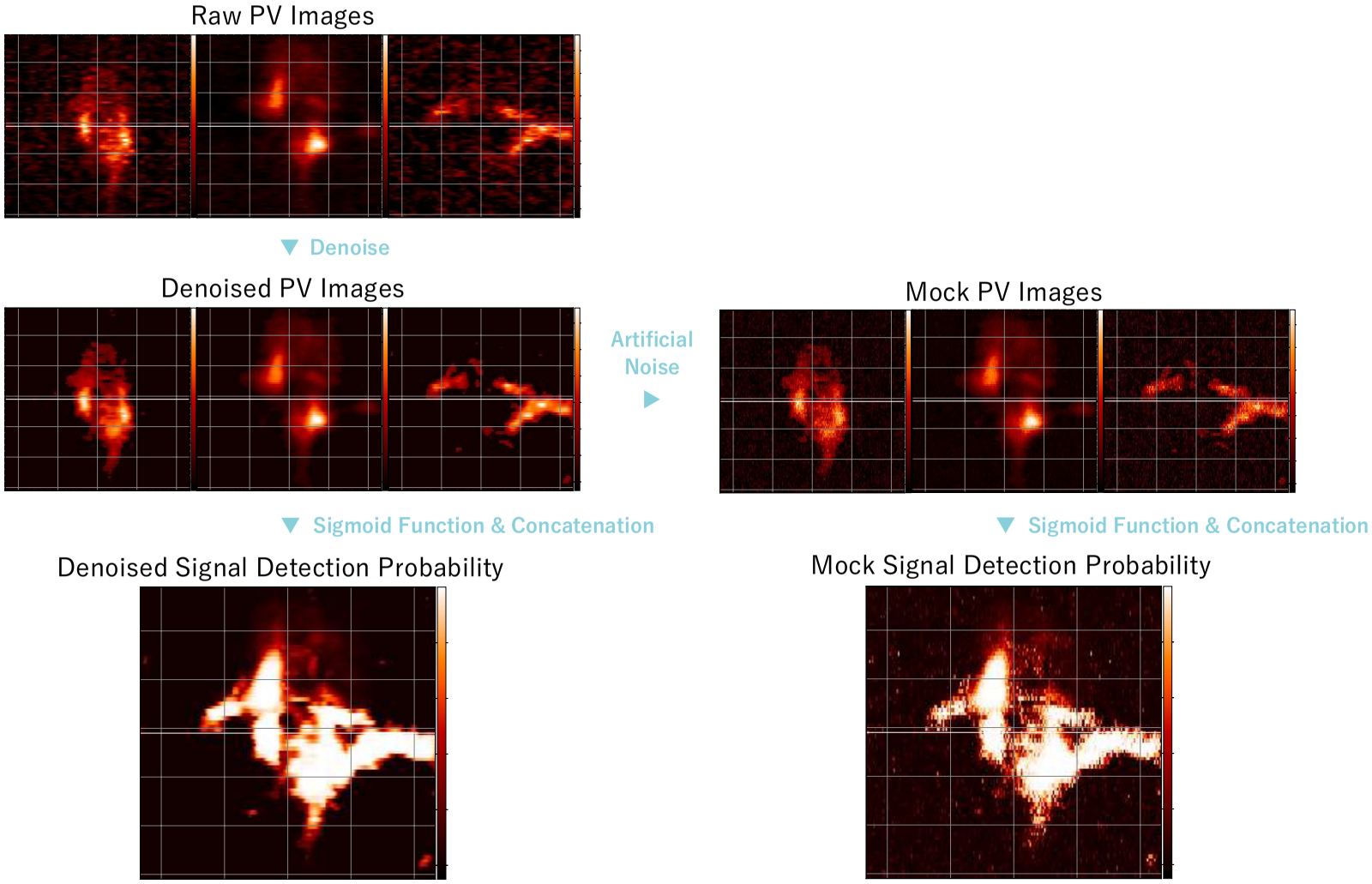

Figure 4.6: The schematic illustration of the producing the signal detection probability for the 'denoised' PV image and the mock PV image. The error of the $KL(p, q)$ is estimated from the similarity between their signal detection probability distributions.

4.2.3 Comparison of the Model Similarity Indexes

In Section 4.2.1, we introduce three indexes for the similarity calculation: the KL divergence, the correlation coefficient, and the inner product. Although we employ the result of the KL divergence in this thesis, we here show the results for the other two indexes.

First, the index of the correlation coefficient ($R(p, q)$) is calculated as follows:

$$R(p,q) = 1 - \frac{\sum_i (p_i - \bar{p})(q_i - \bar{q})}{((\sum_i (p_i - \bar{p})^2)(\sum_i (q_i - \bar{q})^2))^{\frac{1}{2}}}, \tag{4.10}$$

where $\bar{p}$ and $\bar{q}$ denote the averages of p_i and q_i. $R(p_i, q_i)$ is modified to take the minimum value of 0 by taking the difference from 1 for easy comparison with the KL divergence. As in the case of the KL divergence, a lower value represents the similar probability distributions.

Second, the index of the inner product (IP(p, q)) is calculated as follows:

$$\mathrm{IP}(p,q) = 1 - \frac{\sum_i p_i q_i}{\left((\sum_i p_i^2)(\sum_i q_i^2)\right)^{\frac{1}{2}}}. \tag{4.11}$$

As in the case of $R(p_i, q_i)$, IP(p, q) takes the minimum value of 0, and a lower value represents the similar probability distributions.

An example of the results for these two indexes are compared with that for the KL divergence in Figure 4.5. In the figure, the result for CB244 observation is shown (see Chapter 8). A similar trend among these indexes is seen for almost all of the parameter variations. Nevertheless, the value of KL divergence seems to change more sensitively to the parameter variation. This is because the KL divergence is less affected by no-emission region in the image, as noted in Section 4.2.1.

4.2.4 Application to the Previous Observation Data

The above method is applied to the low-mass protostellar source L1527, whose physical structure has been characterized well (*e.g.*, Sakai et al. 2014a; Sakai et al. 2014b; Oya et al. 2017b). Sakai et al. (2014b) and Oya et al. (2017b) applied the IRE model to the kinematic structure of the envelope traced by c-C_3H_2, and constrained the radius of the centrifugal barrier and the protostellar mass by the eye-based fitting. According to their result, the radius of the centrifugal barrier and the protostellar mass are estimated to be 100 ± 20 au and 0.18 ± 0.05 $M_\odot$, respectively. We apply our similarity estimation method to this source and compare the results with the previous ones.

We use the PV diagram of c-C_3H_2 along the envelope direction (south-north) (Figure 4.7). The results of KL divergence against the variation of the protostellar mass and the radius of the centrifugal barrier are shown in Figure 4.8. The KL divergence takes minimum value at the radius of the centrifugal barrier of 100 au and the protostellar mass of 0.22 $M_\odot$, and it monotonically increases as the parameter values are deviated from these values. Using the minimum value of the KL divergence, the centrifugal barrier and the protostellar mass are estimated to be 100^{+30}_{-30} au and $0.22^{+0.05}_{-0.04}$ $M_\odot$, respectively. The errors are estimated from the tolerance range calculated from the noise ($KL_{\mathrm{noise}} \sim 0.068$), which is shown in a gray range of Figure 4.8. The PV diagram of the best model is overlaid with the white contours in Figure 4.7. The radius of the centrifugal barrier is evaluated to be consistent with the previous result. On the other hand, our method gives slightly larger protostellar mass than the result of eye-based fitting. This can be ascribed to the weak emission of the redshifted component seen for the emission of c-C_3H_2. As shown in Figure 4.7, the redshifted emission is weak probably due to the absorption by the foreground infalling gas (inverse P-Cygni profile). The estimation of the

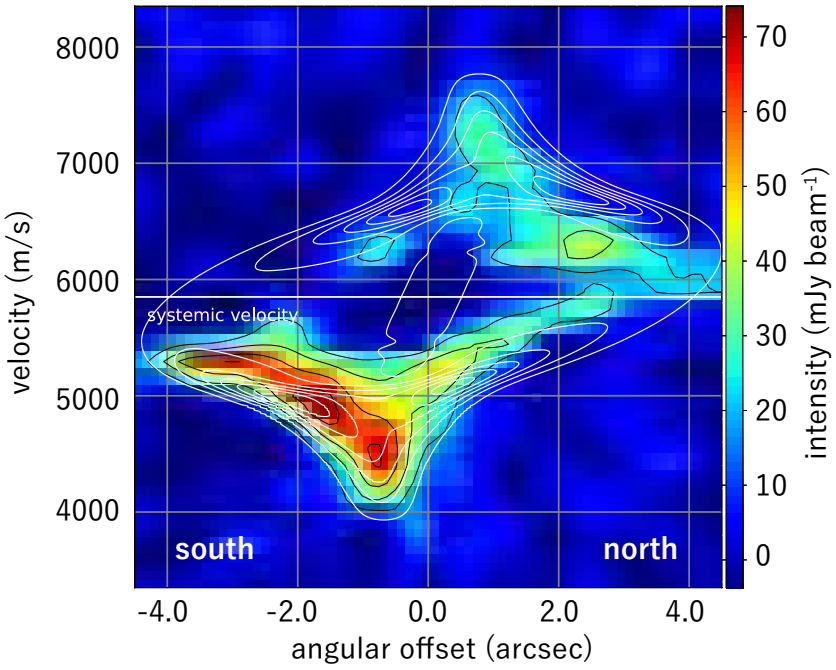

Figure 4.7: The PV diagram of c-C_3H_2 overlaid with the best IRE model searched by the KL divergence. The radius of the centrifugal barrier and the protostellar mass are 100 au and 0.25 $M_\odot$, respectively. We employ the outer radius of the envelope of 600 au, the thickness of the envelope of 30 au, and the flare angle of 10°. The inclination angle is taken from Oya et al. (2017b) ($i \sim 85°$). The contours of the model (white) represent 10, 35, 50, 65, 80, and 95 % of the intensity peak. The black contours show the 30, 50, 70, and 90 % of the intensity peak of c-C_3H_2 emission.

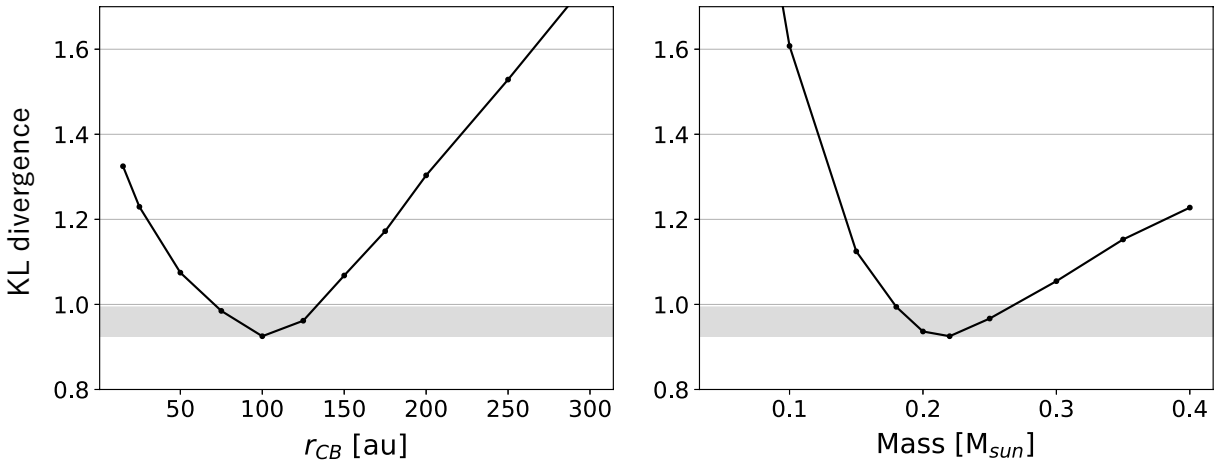

Figure 4.8: The result of the KL divergence calculated for the c-C_3H_2 emission in L1527. The radius of the centrifugal barrier and the mass of the protostar are varied.

protostellar mass is likely affected by such absorption effect of the emission. Nevertheless, the difference of the protostellar mass is within 1 σ between the previous eye-based fitting and our method. Thus, the KL divergence can be used as the similarity indicator of the observation and the model.

Chapter 5

Chemical Structure of B335

In this chapter, the first evidence of a hot corino in a Bok globule is described. This is based on the ALMA observations in the 1.2 mm band toward the low-mass Class 0 protostar IRAS 19347+0727 in B335. Saturated complex organic molecules (COMs), CH_3CHO, $HCOOCH_3$, and NH_2CHO, are detected in a compact region within a few 10 au around the protostar. Additionally, CH_3OCH_3, C_2H_5OH, C_2H_5CN, and CH_3COCH_3 are tentatively detected. Carbon-chain related molecules, CCH and c-C_3H_2, are also found in this source, whose distributions are extended over a few 100 au scale. On the other hand, sulfur-bearing molecules CS, SO, and SO_2, have both compact and extended components. Fractional abundances of the COMs relative to H_2 are found to be comparable to those in known hot corino sources.

5.1 Introduction

As described in Chapter 1, it has been established that chemical compositions of protostellar cores show significant diversity even among those in similar evolutionary stages (Class 0/I). Understanding of a total picture of the chemical diversity is a fundamental issue both for astrochemistry and star-formation studies. However, only a few hot corinos and only a few WCCC sources have so far been detected definitively, and hence, it is still essential to study chemical compositions of other protostars to unveil the total picture. In particular, it is important to study the chemical composition of a protostellar core in an isolated condition, which is thought to be free from various environmental effects caused by other protostars.

B335 is an ideal target for this purpose. It is a representative Bok globule (Keene et al. 1980), which harbors only one Class 0 low-mass protostar IRAS 19347+0727. Its distance and bolometric luminosity are reported to be 100 pc (Olofsson et al. 2009) and 0.72 $L_\odot$ (Evans et al. 2015), respectively. Figure 5.1 shows the images of B335 observed with optical, near infrared and radio observations (Launhardt et al. 2010). An opaque and roundish molecular cloud with an extent of 0.14 pc can be seen, which is isolated from the other clouds. The protostar drives a collimated outflow to the east-west direction. Hirano et al. (1988) reported that the east and west parts of the outflow traced by ^{12}CO have both redshifted and blueshifted components, suggesting that the outflow is almost along the plane of the sky (Figure 5.2). They report the inclination angle of the protostellar envelope system to be $\sim 80°$(nearly edge-on).

This source is regarded as the best "test-bed" for detailed studies of simple models of star-formation (*e.g.* Hirano et al. 1988; Hirano et al. 1992; Zhou et al. 1993; Chandler et al. 1993; Wilner et al. 2000; Harvey et al. 2001). Yen et al. (2015) conducted the ALMA observation at a resolution of $0''.34 \times 0''.28$, and reported that the protostar in B335 has no Keplerian disk with a radius of 10 au or larger. Evans et al. (2015) also reported on the basis of their ALMA observations that the HCN and HCO^+ lines show absorption features against continuum, which

are well reproduced by the model of inside-out collapse (Chapter 1). In addition to these physical studies, the chemical composition at a few 1000 au scale has been observed and modeled (Evans et al. 2015), where fundamental molecules such as CO, CN, HCO^+, HCN, HNC, N_2H^+, and H_2CO were studied. For full understandings of chemical evolution to the protoplanetary disk, the chemical composition in the closest vicinity of the protostar has to be explored in more detail. Here, the first chemical characterization of this source at a few 10 au scale with ALMA is described.

5.2 Observation

The 1.2 mm (250 GHz) observation (Band 6) of B335 was conducted with ALMA (Cycle 2) on May 18, 2015. In total, 37 antennas were used in the observation. The field center is α(J2000)=$19^{\rm h}37^{\rm m}0\overset{\rm s}{.}93$, δ(J2000)=$7°34'9\overset{''}{.}9$. Minimum and maximum baselines are 15 kλ and 444 kλ, respectively. A primary beam size is $23\overset{''}{.}6$, and a synthesized beam size is $0\overset{''}{.}58 \times 0\overset{''}{.}52$ (P.A. = 75°). Sixteen spectral windows were used whose bandwidth and channel spacing are 58.6 MHz and 61.027 kHz, respectively. The velocity resolution is 0.1404 km s^{-1}. On-source integration time was 34 minutes, which resulted in the rms noise of 3-7 mJy $beam^{-1}$. Titan was observed as a flux calibrator. J1955+1358 and J1751+0939 were observed as a phase calibrator and a bandpass calibrator respectively. Self-calibration was not applied for simplicity. The calibration accuracy is 10 %.

CASA was used for the data reduction. A continuum image was prepared by averaging line-free channels. Maps of the spectral line emission were obtained by CLEANing the dirty images with the Briggs robustness parameter of 0.5 after subtracting the continuum directly from the visibility data.

5.3 Results

5.3.1 Dust Continuum

Figure 5.3 shows the 1.2 mm continuum map. The peak position is determined by the Gaussian fit as: (α_{2000}, δ_{2000}) = ($19^{\rm h}37^{\rm m}0\overset{\rm s}{.}90$, $7°34'9\overset{''}{.}62$). The continuum emission consists of compact and extended components. A deconvolved size of the compact component of the continuum emission is $0\overset{''}{.}43 \times 0\overset{''}{.}28$ with the position angle of 23±15°. The extended component has a structure extended along the north-south direction which is perpendicular to the outflow direction (Hirano et al. 1988). The total integrated flux and peak flux are 92.8±2.1 mJy and 34.5 ± 0.5 mJy $beam^{-1}$, respectively. This total flux is consistent with the total continuum flux (compact + extended) of 87.5±2.8 mJy at 1.3 mm reported by Yen et al. (2015).

5.3.2 Detected Molecules and Their Distribution

Figure 5.4 shows the 16 spectral windows observed toward the continuum peak position. In this observation, B335 is found to be rich in molecular lines. Thirty-one spectral lines are assigned using the Cologne Database for Molecular Spectroscopy (CDMS) (Muller et al. 2005) and Jet Propulsion Laboratory (JPL) (Pickett et al. 1998) databases, while 5 lines are left unidentified. Here the systemic velocity is assumed to be 8.34 km s^{-1} (Yen et al. 2015). They are summarized in Table 5.1, as well as the line parameters obtained by the Gaussian fit. We use the detection threshold of 10 σ in the integrated intensity ($F_{\rm integ}$), while lines detected with the confidence level between 5 σ and 10 σ or lines which may be blended with other lines are represented as tentative detection. Here, σ is the error of the integrated intensity calculated by the rms

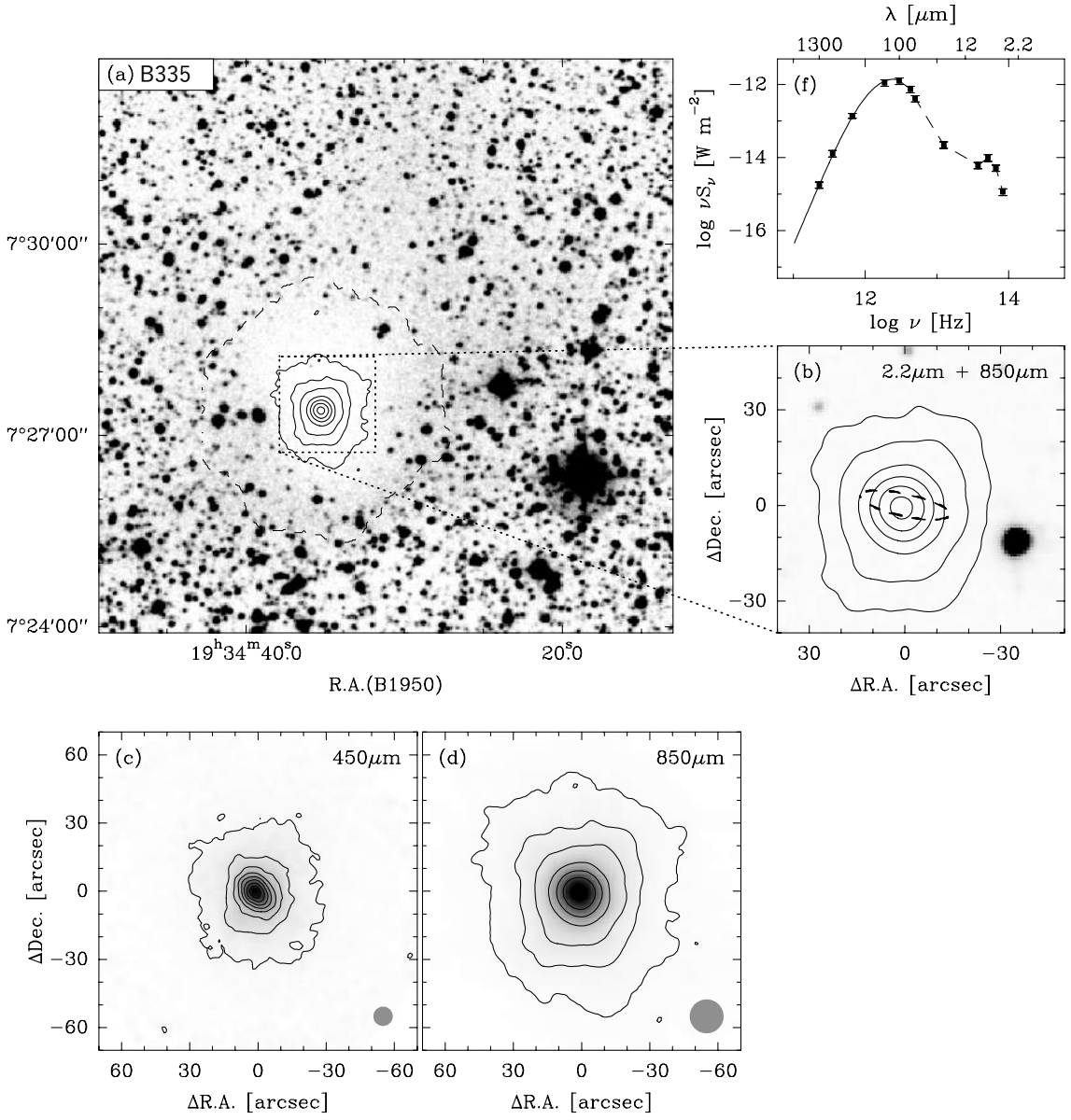

Figure 5.1: Large-scale images of B335 (Launhardt et al. 2010). (a) An optical image overlaid with contours of the 850 μm dust continuum emission. (b) A near infrared K-band image with 850 μm dust continuum contours. The IRAS source position is marked by a dashed ellipse. (c) The 450 μ dust continuum emission. (d) The 850 μm dust continuum emission. (f) SED of the protostellar core.

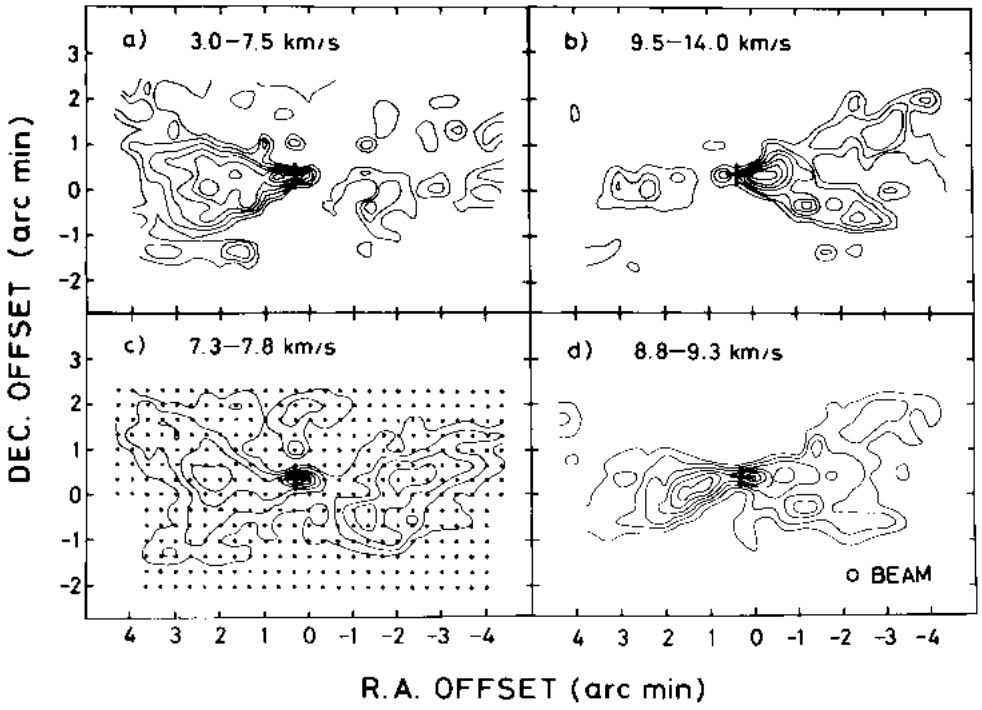

Figure 5.2: The integrated intensity maps of ^{12}CO emission at four velocity intervals: (a) 3.0-7.5 km s^{-1}; (b) 9.5.0-14.0 km s^{-1}; (c) 7.3-7.8 km s^{-1}; (d) 8.8-9.3 km s^{-1} (Hirano et al. 1988). The outflow structure is clearly seen.

noise. The most noteworthy result is the detection of CH_3CHO, $HCOOCH_3$, and NH_2CHO. Additionally, CH_3OCH_3, C_2H_5OH, C_2H_5CN, and CH_3COCH_3 are tentatively detected, each of which is identified only by a single faint feature. These saturated COMs are characteristic of hot corinos and hot cores of star-forming regions. This is the first detection of COMs in this source. In addition to saturated COMs, the carbon-chain molecule CCH and the carbon-chain related molecule c-C_3H_2 are also detected.

Spectral line profiles are different from molecule to molecule, as shown in Figure 5.4 and Table 5.1. Based on the FWHM width of the line (Δv), they are roughly classified into the following three categories:
(1) Broad lines ($\Delta v \gtrsim 5$ km s^{-1}): Twenty-one lines of the 11 molecular species including tentatively detected ones are classified in this group. They are mostly saturated COMs and related molecules (Table 5.1). They do not show absorption below the continuum emission level (*i.e.*, the baseline)
(2) Narrow lines ($\Delta v < 1.6$ km s^{-1}): CCH and c-C_3H_2 show the narrow line width with a double-peak structure due to absorption by the foreground gas. Five lines of these two species are classified into this category.
(3) Intermediate lines ($\Delta v \simeq 3.0$ km s^{-1}): Sulfur-bearing molecules such as SO, ^{34}SO, SO_2, $^{34}SO_2$ and CS belong to this category. These species have an intermediate line width between the first and second categories. Five lines of the above five species are classified into this category.

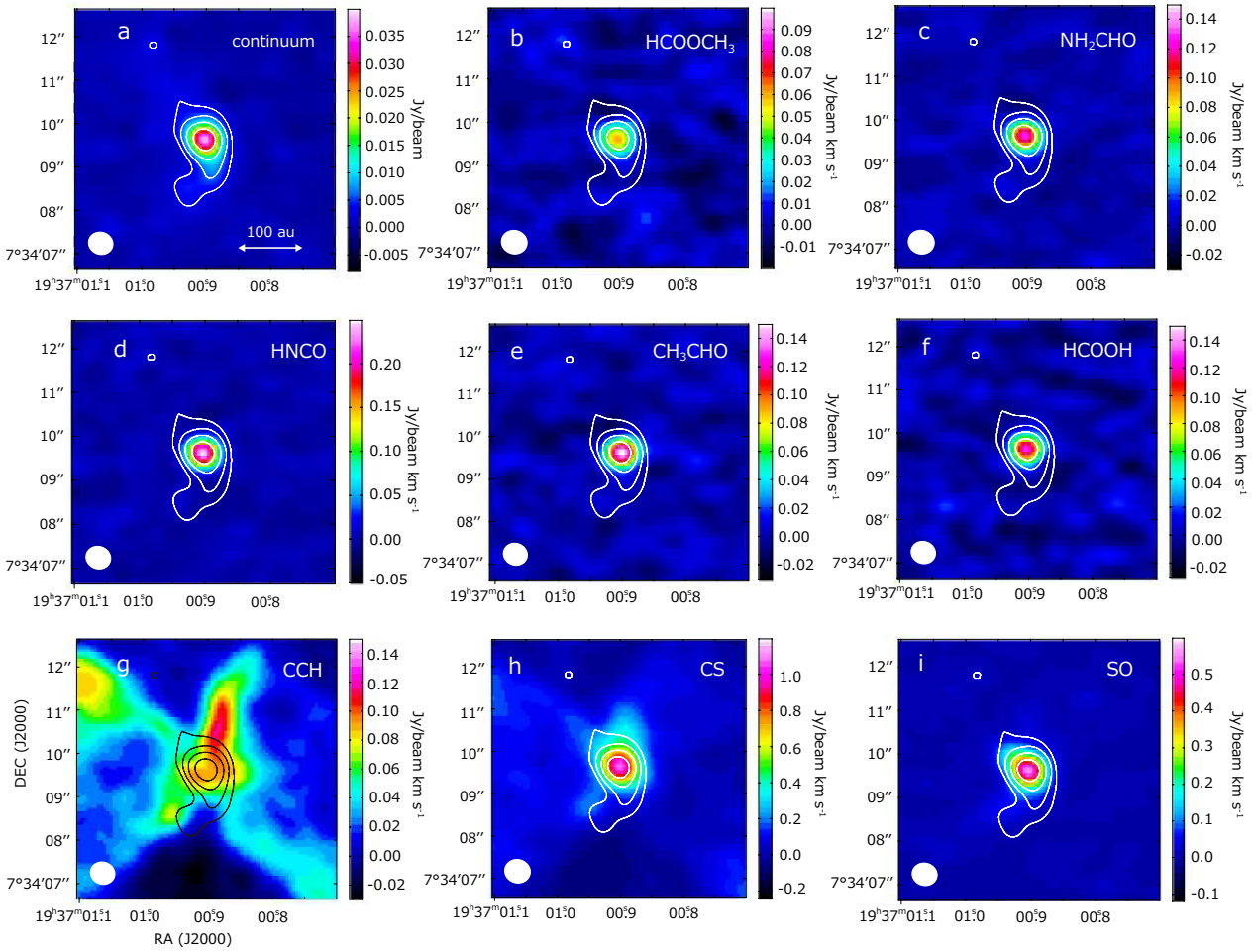

Figure 5.3: The continuum map and the moment 0 maps of $HCOOCH_3$ ($20_{5,16} - 19_{5,15}$), NH_2CHO ($12_{0,12} - 11_{0,11}$), HNCO ($12_{0,12} - 11_{0,11}$), CH_3CHO ($14_{1,14} - 13_{1,13}$ E), HCOOH ($12_{0,12} - 11_{0,11}$), CCH ($N = 3-2, J = 5/2-3/2, F = 3-2$), CS ($5-4$), and SO ($N_J = 6_7 - 5_6$). The contours represent the continuum flux of 10, 20, 40, 80 σ levels, where σ is 0.3 mJy beam^{-1}. Compared with the synthesized beam size shown in the bottom left in each figure, distributions of COMs are not resolved. The velocity range for integration is $5.06 - 11.67$ km s^{-1} for $HCOOCH_3$, $5.20 - 10.22$ km s^{-1} for NH_2CHO, $5.89 - 10.82$ km s^{-1} for HNCO, $5.03 - 11.62$ km s^{-1} for CH_3CHO, $2.85 - 13.66$ km s^{-1} for HCOOH, $7.02 - 9.46$ km s^{-1} for CCH, $6.28 - 10.54$ km s^{-1} for CS, and $6.69 - 9.27$ km s^{-1} for SO.

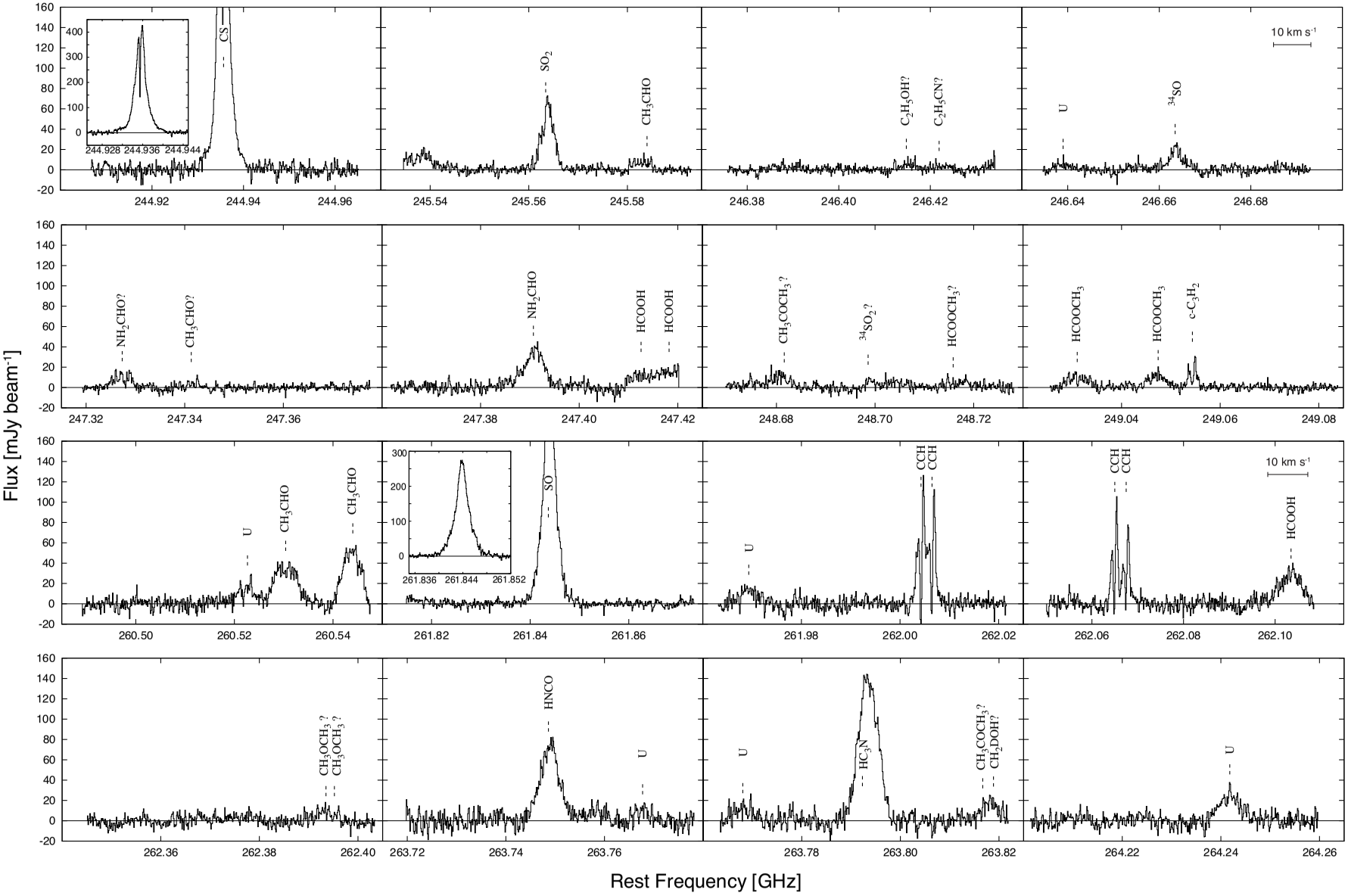

Figure 5.4: Spectrum toward the continuum peak of B335 observed with ALMA.

Figures 5.3(b-i) show moment 0 maps of $HCOOCH_3$, NH_2CHO, HNCO, CH_3CHO, HCOOH, CCH, CS, and SO. Molecular distributions are different among the above three categories. The moment 0 maps of the COM related lines ($HCOOCH_3$, NH_2CHO, HNCO, CH_3CHO, and HCOOH), which have broad line widths, reveal a compact distribution concentrated around the protostar (Figures 5.3(b-f)). They are not resolved with the synthesized beam of this observation ($0''.58 \times 0''.52$, P.A. $= 55°$): the deconvolved sizes of the emitting region (FWHM) for $HCOOCH_3$ and NH_2CHO are $(0''.42 \pm 0''.07) \times (0''.31 \pm 0''.08)$ and $(0''.42 \pm 0''.06) \times (0''.30 \pm 0''.07)$, respectively. According to the previous studies (Hirano et al. 1988), the outflow is extended along the east-west direction, and the protostellar disk/envelope system would have a nearly edge-on configuration with respect to the line-of-sight ($i \sim 80°$). Nevertheless, the rotation motion cannot be identified in the COMs spectrum in this observation. Hence, the broad line width of the COMs means that the COMs mainly exist in a structure whose distribution much smaller than the synthesized beam. Note that the rotation feature is detected in the COM lines at a higher angular resolution observation (Chapter 6).

On the other hand, the CCH emission, which shows the narrow line width, is extended over a few 100 au scale from the protostar (Figure 5.3g). Such an extended distribution is consistent with the self-absorption feature seen in the spectra (Figure 5.4). A part of the extended component would trace an outflow cavity wall, whose direction (east-west) is consistent with the previous studies (Hirano et al. 1988). Although this source harbors a hot corino, carbon-chain related species can be observed in the protostellar core at a scale of a few 100 au. This result suggests that the WCCC-like feature is also present in this source at the relatively larger scale ($\sim$ a few 100 au). Such hybrid type chemical characteristics (*i.e.*, hot corino chemistry and WCCC) are also reported in L483 (Oya et al. 2017a). The moment 0 maps of the sulfur-bearing molecules, showing the intermediate line width between COMs and carbon-chain molecule (CCH), reveal the compact distribution (Figures 5.3(h,i)), although a weak extended component can also be seen.

5.3.3 Derivation of Column Density and Fractional Abundance

The beam-averaged column densities of $HCOOCH_3$, CH_3OCH_3, CH_3CHO, NH_2CHO, HNCO, c-C_3H_2, SO_2, HC_3N, HCOOH, CH_3COCH_3, SO, and CS are derived toward the continuum peak, assuming the local thermodynamic equilibrium (LTE) and optically thin conditions (Chapter 2):

$$N(\mathrm{X}) = U(T)\frac{3k_\mathrm{B}W}{8\pi^3\nu S\mu^2}\exp\left(\frac{E_\mathrm{u}}{k_\mathrm{B}T}\right), \tag{5.1}$$

where $U(T)$ denotes the partition function of the molecule at the temperature T, W the integrated intensity, and E_u the upper state energy. Since a single line or multiple lines with similar upper state energies are observed in this study, the column densities are calculated for the excitation temperature of 100 K. This temperature is a typical excitation temperature of COMs in the hot corino source IRAS 16293-2422 (Richard et al. 2013; Jaber et al. 2014; Oya et al. 2016), and is also close to the mass-weighted dust temperature (Kauffmann et al. 2008) at a roughly $0''.5$ beam (111 K) reported for B335 by Evans et al. (2015). Although the detection of CH_3OCH_3 and CH_3COCH_3 is tentative in this study, their column densities are calculated for comparison with other sources. The results are shown in Table 5.2.

Table 5.1: Detected Molecular Lines

Molecule[a]	Transition	Frequency[b] GHz	E_u cm^{-1}	$S\mu^2$	F_{integ} mJy beam^{-1} km s^{-1}	I mJy beam^{-1}	Δv km s^{-1}	v_{LSR} km s^{-1}	rms mJy beam^{-1}	type[c]
CS[d]	5−4	244.935644	24.51	19.1	1301(4)	...	...	...	5.39	I
SO_2	$10_{3,7}$−$10_{2,8}$	245.563423	50.54	14.5	228(2)	61.1(14)	3.58(9)	7.77(4)	3.13	I
CH_3CHO[e]	$13_{0,13} - 12_{0,12}$ E $v_t = 1$	245.583105	199.84	163	39(2)	8.2(7)	4.6(5)	8.59(19)	3.13	B
C_2H_5OH?	$14_{3,11} - 13_{3,10}$	246.414762	108.23	21.3	30(2)	5.6(6)	5.3(7)	7.8(3)	3.17	B
C_2H_5CN?	$28_{2,27}$−$27_{2,26}$	246.421918	123.20	412	20(3)	3.5(4)	8(2)	7.1(8)	3.17	B
U-line		246.63899(19)	...	...	20(3)	5.5(6)	4.5(5)	...	3.74	
^{34}SO	6_5−5_4	246.663470	34.68	11.4	92(3)	20.1(9)	3.9(2)	8.17(8)	3.74	I
NH_2CHO?	$12_{0,12} - 11_{0,11}$ $v_{12} = 1$	247.327322	343.26	156	56(2)	10.8(8)	5.3(5)	8.82(18)	3.24	B
CH_3CHO?[f]	$14_{0,14}$−$13_{-1,13}$ E	247.341332	66.56	11.3	15.1(19)	...	...	...	3.24	B
NH_2CHO	$12_{0,12}$−$11_{0,11}$	247.390719	107.25	0.319	206(4)	35.9(7)	5.80(14)	8.12(6)	4.57	B
HCOOH[g]	11_8−10_8	247.412546	190.76	20.9	...	...	...	...	4.57	B
HCOOH[g]	11_7−10_7	247.418230	157.69	26.4	...	...	...	...	4.57	B
CH_3COCH_3[h]	$24_{2,23} - 23_{1,22}$ EE	248.681568	108.64	3050	52(3)	9.7(6)	7.5(5)	10.2(2)	3.78	B
$^{34}SO_2$?	$13_{1,13}$−$12_{0,12}$	248.698604	56.86	26.0	16(2)	7.4(8)	2.4(3)	7.69 (13)	3.78	I
$HCOOCH_3$?	$20_{3,14} - 19_{3,16}$ A $v_t = 1$	248.715840	223.01	102	25(3)	4.8(5)	7.6(10)	6.6(4)	2.97	B
$HCOOCH_3$	$20_{5,16}$−$19_{5,15}$ E	249.031002	98.39	49.8	60(2)	10.0(7)	5.7(5)	8.31(19)	2.97	B
$HCOOCH_3$	$20_{5,16}$−$19_{5,15}$ A	249.047428	98.39	49.3	56(2)	11.9(6)	5.0(3)	8.61(13)	2.97	B
c-C_3H_2[d]	$5_{2,3}$−$4_{3,2}$	249.054368	24.51	19.1	41.1(14)		...	...	2.97	N
U-line		260.5227(3)			67(3)	15.5(12)	5.2(9)	...	5.45	
CH_3CHO	$14_{1,14}$−$13_{1,13}$ E	260.530403	67.00	176	223(4)	37.0(9)	6.16(19)	8.37(7)	5.45	B
CH_3CHO	$14_{1,14}$−$13_{1,13}$ A	260.544020	66.95	176	265(4)	54.2(11)	4.80(12)	8.59(5)	5.45	B
SO	$N_J = 6_7$−5_6	261.843684	33.05	16.4	847(3)	245(3)	3.13(4)	8.09(2)	3.30	I
U-line	...	261.96932(16)	...	...	69(5)	13.5(11)	4.4(4)	...	5.65	
CCH[d]	$N = 3 - 2, J = 7/2 - 5/2, F = 4 - 3$	262.004260	17.48	2.29	136(3)	...	...	...	5.65	N
CCH[d]	$N = 3 - 2, J = 7/2 - 5/2, F = 3 - 2$	262.006482	17.48	1.71	129(2)		...	...	5.65	N
CCH[d]	$N = 3 - 2, J = 5/2 - 3/2, F = 3 - 2$	262.064986	17.49	1.63	100(3)	...	...	...	5.70	N
CCH[d]	$N = 3 - 2, J = 5/2 - 3/2, F = 2 - 1$	262.067469	17.49	1.07	89(3)	...	...	...	5.70	N
HCOOH	$12_{0,12}$−$11_{0,11}$	262.103480	57.53	24.2	190(5)	29.5(8)	6.4(2)	8.39(9)	5.70	B
CH_3OCH_3?[i]	$13_{5,8}$−$13_{4,9}$ EE	262.393513	82.02	148	44(3)	9.2(8)	5.2(6)	8.7(2)	5.12	B
CH_3OCH_3?[i]	$13_{5,8}$−$13_{4,9}$ AA	262.395111	82.02	108	44(3)	9.2(8)	5.2(6)	10.6(2)	5.12	B
HNCO	$12_{0,12}$−$11_{0,11}$	263.748625	57.19	30.0	389(6)	72.8(11)	5.19(9)	8.01(4)	7.65	B
U-line	...	263.7680(3)	...	...	72(5)	12.1(15)	5.3(7)	...	6.71	
HC_3N[j]	29−28	263.792308	132.00	404	763(6)	141.4(13)	5.17(6)	6.99(2)	6.71	B
CH_3COCH_3?[k]	$22_{6,17} - 21_{5,16}$ EA	263.816703	114.36	534	81(5)	4.5(3)	18.4(11)	6.66(13)	6.71	B
CH_2DOH?[k]	$2_{2,1} - 2_{1,2}$	263.818884	29.13	0.419	81(5)	4.5(3)	18.4(11)	9.14(13)	6.71	B
U-line	...	264.241808(9)	...	...	129(4)	24.3(9)	5.9(3)		6.03	

[a] Tentative detections are indicated by a question mark.
[b] Rest frequencies for the identified lines. Fitted rest frequencies assuming the v_{LSR} of 8.34 km s^{-1} for the unidentified lines.
[c] B: Broad line, I: Intermediate line, N: Narrow line. See section 3.2.
[d] I and Δv are not derived by the Gaussian fit due to the existence of the absorption feature.
[e] This line may be blended with the $20_{16,4} - 19_{16,3}$ E line of $HCOOCH_3$ (245.583970 GHz).
[f] I and Δv are not derived by the Gaussian fit because the line is too weak.
[g] F_{integ}, I and Δv are not derived by the Gaussian fit because of heavy blending. The K-doublet lines are also unresolved.
[h] This line is blended with the $24_{1,23} - 23_{2,22}$ EE line of CH_3COCH_3 (248.6815860 GHz).
[i] F_{integ}, I and Δv are values for the blended lines.
[j] This line is likely blended with the $5_{1,5} - 4_{2,4}$ A^+ $v_t = 1$ line of CH_3OH (263.7938560 GHz).
[k] These lines are blended with each other. Furthermore, these lines are blended with the $22_{6,17} - 21_{5,16}$ AE (263.8167120 GHz), $22_{5,17} - 21_{6,16}$ AE (263.8167120 GHz), and $22_{5,17} - 21_{6,16}$ EA (263.8167027 GHz) lines of CH_3COCH_3.

To derive the fractional abundances relative to H_2, the beam-averaged column density of H_2 are estimated by using the following equation (Ward et al. 2000):

$$N(\mathrm{H_2}) = \frac{F(\nu)N_\mathrm{A}}{\nu^3\kappa_\nu\Omega\rho(2h/c^2)}[\exp(h\nu/k_\mathrm{B}T_\mathrm{d}) - 1], \tag{5.2}$$

where ν denotes the frequency, $F(\nu)$ the peak integrated flux of dust continuum emission, κ_ν the mass absorption coefficient with respect to the gas mass, T_d the dust temperature, Ω the solid angle of the synthesized beam, ρ the average molecular weight (2.33) in the atomic mass unit, and N_A the Avogadro's number. The mass absorption coefficient at 1.2 mm is calculated to be 0.0068 cm^2 g^{-1} by using the average value of κ_ν at 850 μm (1.48×10^{-2}) with the β index of 2.38, which are reported for B335 by Shirley et al. (2011). Then, the beam-averaged column density of H_2 is derived to be $(9.41 \pm 0.13) \times 10^{23}$ cm^{-2} for the dust temperature of 100 K. Using the H_2 column density, the fractional abundances of the observed molecules relative to H_2 are evaluated, as summarized in Table 5.2. Here, the dust temperature is simply assumed to be equals to the gas temperature under the LTE condition. If the line-of-sight depth of the molecular distribution (L) were the same as the FWHM of the continuum peak ($L \simeq 1.1 \times 10^{15}$ cm), the H_2 density is roughly estimated to be $n(\mathrm{H_2}) \sim 9 \times 10^8$ cm^{-3}. Such a relatively high density justifies the LTE assumption employed in derivation of the column densities. In the following section, we discuss the abundances of the saturated COMs and their related species.

5.4 Discussion

In this observation, we detect the lines of CH_3CHO, $HCOOCH_3$, and NH_2CHO, and the tentatively detected lines of CH_3OCH_3, C_2H_5OH, C_2H_5CN, and CH_3COCH_3. These COM lines show a broad line width and a very compact distribution around the protostar. The fractional abundance of $HCOOCH_3$ relative to H_2 is evaluated to be 2.8×10^{-9}, which is comparable to that reported for the prototypical hot corino IRAS 16293-2422 (9×10^{-9}) (Jaber et al. 2014) and NGC 1333 IRAS 4A (1.4×10^{-9}) (Taquet et al. 2015). The fractional abundance of CH_3OCH_3 in B335 (2.0×10^{-9}) is lower than that reported for IRAS 16293-2422 (4×10^{-8}) (Jaber et al. 2014), but is slightly higher than that for NGC1333 IRAS 4A. Thus, B335 is confirmed to be rich in COMs. The $HCOOCH_3$ abundance is also comparable to that in the outflow shocked region L1157 B1 (Sugimura et al. 2011). On the other hand, the fractional abundances of $HCOOCH_3$ and CH_3OCH_3 in B335 are much higher than those found in the starless core L1689B ($10^{-10}-10^{-9}$) (Bacmann et al. 2012). This comparison indicates that the abundances of COMs are enhanced in the compact region near the protostar of B335, and hence, it is concluded that B335 harbors a hot corino.

Among the various COMs, NH_2CHO is proposed to be a key species in pre-biological evolution (Saladino et al. 2012). This molecule has been detected in hot corinos and hot cores in star forming regions (Bisschop et al. 2007; Adande et al. 2013; Kahane et al. 2013). It is reported that the abundance of NH_2CHO shows a good correlation with that of HNCO, implying that these two species are related to each other in their production mechanisms (López-Sepulcre et al. 2015). In B335, the NH_2CHO/HNCO ratio is 0.025, which is almost comparable to the range of the ratios found in star forming regions (0.03-0.25). Hence, the positive correlation between the abundances of these two species indeed holds in B335.

Detection of acetone (CH_3COCH_3) is tentative in this source. If the 248.682 GHz line originates from acetone, as in the case of NGC1333 IRAS 4A (López-Sepulcre et al. 2017), the fractional abundance of acetone in B335 is determined to be 5.0×10^{-10}. The acetone abundance is lower than the value reported toward the acetone peaks in Orion KL (hot core) ($(0.4-1.6) \times 10^{-8}$ by Friedel et al. 2005). According to the interferometric observations toward

Table 5.2: Column Densities and the Fractional Abundances Relative to H_2

Molecule	Column Density $/10^{14}$ cm^{-2}	Fractional Abundance $/10^{-10}$
$HCOOCH_3$[b,c]	26(3)	28(3)
CH_3CHO[d]	14(2)	14(2)
NH_2CHO	2.4(2)	2.6(2)
HNCO	96(10)	102(11)
HCOOH[e]	27(3)	28(3)
c-C_3H_2[f]	$> 0.80(8)$	$> 0.85(9)$
SO_2	16.9(17)	18.0(18)
SO	13.6(14)	14.4(15)
CS[f]	$> 5.4(5)$	$> 5.8(6)$
	Tentative Detection	
CH_3OCH_3	19(2)	20(2)
CH_3COCH_3[b]	4.7(5)	5.0(5)
C_2H_5OH	21(3)	23(3)
C_2H_5CN	0.96(15)	1.02(16)

[a] The excitation temperature is assumed to be 100 K.
[b] Derived from the $20_{5,16} - 19_{5,15}$ E line (249.031 GHz) and the $20_{5,16} - 19_{5,15}$ A line (249.047 GHz).
[c] The vibrationally excited states are not considered in the partition function.
[d] Derived from the $14_{1,14} - 13_{1,13}$ E line (260.530 GHz).
[e] Derived from the $12_{0,12} - 11_{0,11}$ line (262.103 GHz).
[f] The lower limit is estimated due to the absorption feature.

Orion KL by Friedel & Snyder (2008) and Peng et al. (2013), acetone shows different distribution from the other O-bearing COMs ($HCOOCH_3$ and CH_3OCH_3), and its distribution tends to be similar to the N-bearing COMs (C_2H_5CN). In B335, the distribution of acetone is similar to those of the other COMs, and we cannot find any specific trend in its distribution unlike the Orion KL case, probably because of the insufficient angular resolution in this study. Definitive identification of acetone in this source with multiple lines and its high resolution imaging are awaited.

So far, hot corino sources have been found in large cloud complexes with active star formation: *e.g.,* IRAS 16293-2422 is in the Ophiuchus molecular cloud complex (Cazaux et al. 2003), NGC1333 IRAS 4A, IRAS 4B, and IRAS 2A (Bottinelli et al. 2004; Sakai et al. 2006; Jørgensen et al. 2005) in the Perseus molecular cloud complex, Serpens SMM4 in the Serpens molecular cloud (Öberg et al. 2011), and HH212 in the Orion molecular cloud (Codella et al. 2016). In contrast, B335 is the first hot corino source identified in a Bok globule isolated from a large molecular cloud complex. It is generally thought that a star forming region in a molecular cloud complex would be affected by various activities of the other protostars in the same cloud complex. Likewise, the chemical composition of the protostellar core would also be affected by such environmental effects. However, B335 is thought to be almost free from them. Its chemical composition could be regarded as a 'standard' template for chemical compositions of isolated protostellar cores.

Table 5.3: Fractional Abundances of COMs

Molecule	B335[b]	IRAS 16293-2422[c]	IRAS 4A	IRAS 2A[d]
X(HCOOH)	2.8(3)	$\lesssim 0.3$	...	...
X(CH_3CHO)	1.4(2)	3	...	...
X($HCOOCH_3$)	2.8(3)	9	1.4[d]	13
X(CH_3OCH_3)	2.0(2)	40	0.85[d]	8.2
X(HNCO)	10.2(11)	...	0.8[e]	...
X(NH_2CHO)	0.26(2)	0.6	0.2[e]	2.3
X(C_2H_5OH)	2.3(3)	$\lesssim 5$	1.2[d]	10
X(C_2H_5CN)	0.102(16)	$\lesssim 0.2$	0.062[d]	0.24

[a] X represents the fractional abundance relative to H_2 in unit of 10^{-9}.
[b] The temperature is assumed to be 100 K.
[c] Taken from Jaber et al. (2014).
[d] Taken from Taquet et al. (2015).
[e] Taken from López-Sepulcre et al. (2015).

5.5 Summary

By the 1.2 mm band observation with ALMA, the chemical characteristics of the protostellar source in B335 are investigated at a 50 au scale. In total, 31 spectral lines including tentative ones are identified in this source. The main results are summarized below.

1. Saturated complex organic molecules (COMs) and their related molecules ($HCOOCH_3$, CH_3CHO, NH_2CHO, HNCO, HCOOH, CH_3OCH_3, CH_3COCH_3, C_2H_5OH, and C_2H_5CN) are detected. Their spectra show broad line widths ($\gtrsim$ 5 km s^{-1}), and their emissions are concentrated within a few 10 au around the protostar. Their fractional abundances relative to H_2 are as high as 10^{-10}-10^{-8} which is comparable to those in typical hot corino sources. Based on these results, we conclude that B335 harbors a hot corino.

2. Carbon-chain molecules and their related molecules (CCH and c-C_3H_2) are also bright in this source. Their spectra show narrow line widths ($<$ 1.6 km s^{-1}) and double-peak structures due to absorption by the foreground gas. The integrated intensity maps reveal that the emissions are extended to a few 100 au scale with association to the protostar, suggesting the WCCC feature at the outer part of the envelope. Thus, the chemical characteristics of B335 are concluded to be the hybrid type: hot corino chemistry and WCCC.

3. Sulfur bearing molecules (CS, SO, SO_2) are also detected in this source. They have intermediate line width between COMs and carbon-chain molecules, and their emissions have both compact and extended components.

Chapter 6

Physical Structure of B335

In this chapter, a kinematic structure of the innermost envelope of the low-mass Class 0 protostar IRAS 19347+0727 in B335 is investigated, based on the ALMA observation with the 0.″1 angular resolution. The target of the observation is complex organic molecule (COM) emission in the 1.2 mm band, which selectively traces a hot and dense part around the protostar, as shown in Chapter 5. The distribution of the COM emission is now resolved, and a clear velocity gradient is observed. Moreover, the direction of the gradient is found to be different from molecule to molecule. These features are well explained by the model of an infalling-rotating gas, but not by the model of a Keplerian motion. The protostellar mass and the radius of the centrifugal barrier are determined to be $0.05^{+0.03}_{-0.02}$ $M_{\odot}$ and < 4 au, respectively. The different directions of the velocity gradient observed for different COMs are interpreted as the different sizes of their distributions. In contrast to the COM emission, the SiO emission seems to trace a compact region at the closest vicinity of the protostar, that is a launching point of the outflow or a shocked region caused by the gas accretion onto the protostar. These results first reveal the transition zone from the infalling motion to the rotating motion in this representative isolated protostellar source.

6.1 Introduction

B335 is a representative Bok globule (Keene et al. 1980), which harbors the Class 0 low-mass protostar IRAS 19347+0727. According to Evans et al. (2015) and Yen et al. (2015), the gas motion at a scale of 100 au around the protostar is dominated by infall, and rotation motion has not clearly been detected even at a spatial resolution of 0.3″ ($\sim$ 30 au). Yen et al. (2015) reported the upper limit to the radius of the Keplerian disk to be 10 au and the protostellar mass of 0.05 $M_{\odot}$ with their observation of the $C^{18}O$ and SO emission. To determine the protostellar mass precisely, it is essential to resolve and characterize the rotation motion (e.g. infalling-rotating motion or Keplerian rotation).

To investigate the structure of such a compact region around the protostar, emission lines of complex organic molecules (COMs) can be a powerful tracer (Oya et al. 2016; Oya et al. 2017a). As described in Chapter 5, we investigated the chemical property of this source with ALMA with a 0.″5 beam. We detected a number of COMs in the vicinity of the protostar ($r \sim 10$ au), and revealed that B335 harbors a hot corino. This result means that we can study the innermost part around the protostar by use of these COM emissions without contaminations of the surrounding gas. We here report the kinematic structure of the innermost envelope of this source observed in the COM lines at the highest angular resolution ever made (10 au). Hereafter, we refer to organic molecules containing at least six atoms as COMs, and HCOOH as a COM related molecule in this Chapter.

Table 6.1: Specifications of the Observation

	Cycle 2	Cycle 4
Angular Resolution	$0\farcs58 \times 0\farcs52$	$0\farcs12 \times 0\farcs08$
Maximum Recoverable Size	$5\farcs0$	$0\farcs5$
Frequency Band	244-264 GHz	245-264 GHz
Frequency Resolution	61 kHz	122 kHz
On Source Integration Time	0.5 hours	2.6 hours
RMS Noise Level	3-7 mJy beam^{-1}	0.9 mJy beam^{-1}

Table 6.2: Parameters for Analyzed Lines

Molecule	Transition	Frequency GHz	$S\mu^2$ Debye^2	E_u cm^{-1}	I_{peak} mJy beam^{-1}	W[a] mJy beam^{-1} km s^{-1}	Catalog[b]
SiO	6-5	260.518009	57.6	30.42	18.2(9)	–	CDMS
CH_3CHO[b]	$14_{1,14}$-$13_{1,13}$ E	260.530403	13.9	67.00	22.7(9)	–	JPL
CH_3CHO[b]	$14_{1,14}$-$13_{1,13}$ A	260.544020	13.9	66.95	25.4(9)	–	JPL
CH_3OH	$12_{6,7}$-$13_{5,8}$ E	261.704409	8.5	250.05	33.0(9)	185.2(16)	CDMS
HCOOH	$12_{0,12}$-$11_{0,11}$	262.103481	24.2	57.53	21.8(9)	151.9(18)	CDMS

[a] Integrated intensity of the line.

[a] The catalog used for line identification. CDMS for the Cologne Database for Molecular Spectroscopy (Muller et al. 2005). JPL for the Jet Propulsion Laboratory (Pickett et al. 1998).

[b] These lines are contaminated with SiO emission.

6.2 Observation

We conducted the 1.2 mm (250 GHz) observation (Band 6) toward B335 with ALMA (Cycle 4) on July 29-August 17, 2017. In total, 46 antennas were used in the observation. The field center is α(J2000)=$19^h37^m0\fs902$, δ(J2000)=$7\arcdeg34\arcmin9\farcs64$. Minimum and maximum baselines are 18 kλ and 3100 kλ, respectively. The primary beam size is $23\farcs6$, and the synthesized beam size is $0\farcs12 \times 0\farcs08$ (P.A. = $-58.6\arcdeg$). We used 16 spectral windows whose bandwidth and channel spacing each are 117 MHz and 122 kHz, respectively. This channel spacing corresponds to a velocity resolution of 0.28 km s^{-1}. Some spectral windows overlap with those in the observation reported in Chapter 5; Imai et al. (2016). On-source integration time was 2 hours 39 minutes, which results in the rms noise of 0.9 mJy beam^{-1} at a nominal channel width of 0.28 km s^{-1}. J2148+0657 was observed as a flux calibrator. J1928+0848 and J2025+3343 were observed as a phase calibrator and a bandpass calibrator, respectively. The flux calibration accuracy is about 5 %. In Table 6.1, the specification of the Cycle 4 observation is compared with that of Cycle 2 observation used in Chapter 5.

CASA (Common Astronomy Software Applications) is used for data reduction and imaging. A continuum image was prepared by averaging line-free channels, resulting in rms noise of 88 μJy beam^{-1}. Maps of the spectral line emission were obtained by CLEANing the dirty images with the Briggs robustness parameter 0.5 after subtracting the continuum directly from the visibility data.

6.3 Results & Discussion

6.3.1 Detection of 10 au Scale Velocity Gradient

Figure 6.1 shows the spectrum observed toward the protostellar position derived by the Gaussian fit of the continuum image: (α_{2000}, δ_{2000}) = ($19^h37^m0\fs898$, $7\arcdeg34\arcmin9\farcs53$). The lines of various COMs

and their related species such as CH_3OH, CH_3CHO, $HCOOCH_3$, HCOOH, $CH_2(OH)CHO$, and CH_3COCH_3 are detected toward this position. Some lines of COMs and their related molecules show a double-peaked profile (Figure 6.1). Such a double-peaked profile can be a sign of rotation motion, because the double-peaked profile is seen regardless of the optical depth of the line.

We first focus on the emission line of CH_3OH ($2_{1,1} - 1_{0,1}$) (Table 6.2) and investigate its velocity structure. The CH_3OH line shows the most extended distribution ($r \sim 15$ au) of all the detected COMs and their related species (Figure 6.2(a)). Its emission peak almost coincides with the protostellar position. Figure 6.2(a) also shows the moment 1 map of the CH_3OH line. A clear velocity gradient is seen, which can be ascribed to the rotation motion at the innermost envelope. The bipolar outflow of this source extends along the east-west direction with significant overlapping of the blueshifted and redshifted components (Hirano et al. 1988). Thus, the envelope/disk component lies along the south-north direction. Its inclination angle is reported to be 80-87 degrees (90 degrees for edge-on) (Hirano et al. 1988; Stutz et al. 2008). If the rotation motion around the protostar is completely Keplerian (i.e., without radial velocity), the velocity gradient should be along the south-north direction regardless of the inclination. However, the observed velocity gradient is seen approximately along the northwest-southeast direction.

More interestingly, the direction of the velocity gradient is different from molecule to molecule. Figure 6.2(b) shows the moment 1 map of the HCOOH line ($12_{0,12} - 11_{0,11}$) (Table 6.2), whose distribution is more compact than the CH_3OH distribution. In this case, the velocity gradient is almost along the south-north direction, being consistent with the envelope/disk direction. Such a difference of the direction of the velocity gradient among molecules cannot be explained by the Keplerian motion. Rather, they can be interpreted as a different contribution of the infall motion in the infalling-rotating envelope. Indeed, the velocity gradient perpendicular to the disk direction appears, if the flattened envelope is slightly inclined. This is because the gas infalling toward the front and back sides will be spatially separated. Similar slant velocity gradients due to the infall motion are also reported for other low-mass protostellar sources (e.g., Ohashi et al. 1996; Saito et al. 1996; Momose et al. 1998; Oya et al. 2016). The contribution of the infall motion can be more conspicuous for CH_3OH whose distribution is more extended than that of HCOOH, because the infalling motion is dominant in the outer region. Thus the difference of the direction of the velocity gradient likely reflects different distributions of molecules in the infalling-rotating envelope.

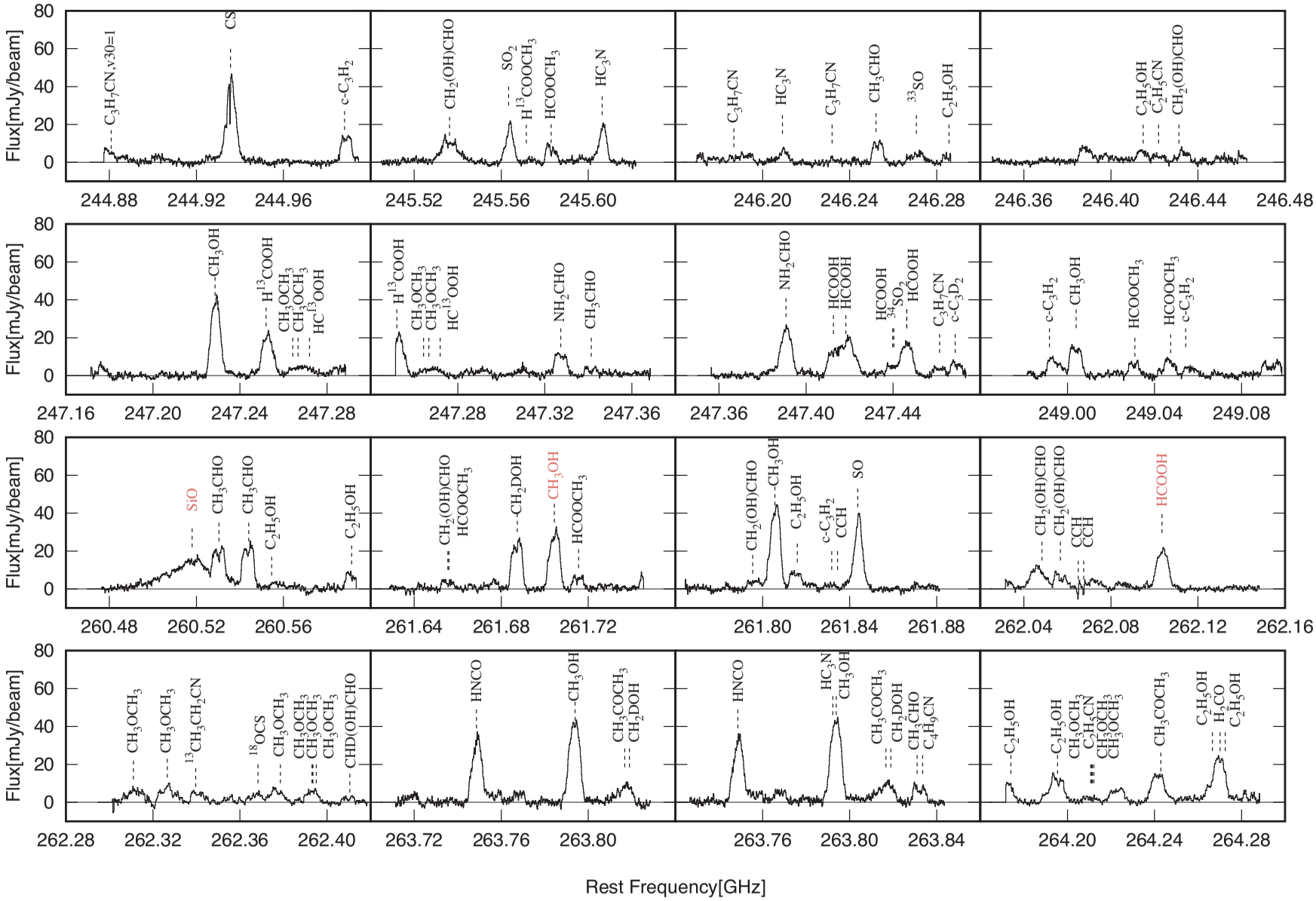

Figure 6.1: An overview of the observed spectrum toward the continuum peak position (α_{2000}, δ_{2000}) = ($19^{\rm h}37^{\rm m}0\overset{\rm s}{.}898$, $7^\circ34'9\overset{''}{.}53$). The lines analyzed in this thesis are shown in red.

6.3.2 Existence of CH_3OH and HCOOH in Infalling-Rotating Envelope

For more quantitative analyses of the kinematic structure, the position-velocity (PV) diagrams are prepared. Figure 6.2 shows the PV diagrams of the CH_3OH and HCOOH emissions along the south-north (disk) and east-west directions. Velocity gradients can be seen both for the south-north (disk) and east-west directions for the CH_3OH line. On the other hand, the emission is more compact and velocity gradient can be seen only for the south-north direction for the HCOOH line. These features are consistent with the moment 1 maps (Section 6.3.1).

To investigate the above features in more detail, we employ the ballistic model of the infalling-rotating envelope (IRE), where angular momentum and energy of the gas are conserved (see Chapter 4 for details of the model). This model has successfully been applied to the kinematic structure of the innermost envelope gas ($r \sim$ 10-100 au) for several low-mass protosteller sources (e.g., Sakai et al. 2014b; Oya et al. 2016). The beam size is considered in the model calculation. For simplicity, we assume that the emission intensity is proportional to $r^{-1.5}$ (e.g., Oya et al. 2016) and the envelope has constant thickness. It is verified that the result for the 25 au region around the protostar does not change significantly for the $r^{-0.5}$-$r^{-2.5}$ dependence. The result is not seriously affected by the envelope shape, either. We confirm that the result does not significantly change, even if the envelope thickness has a slope angle less than 45°. Since it is difficult to determine the inclination angle of the disk/envelope system from the present observation, the literature value of inclination angle of 80° is employed (Hirano et al. 1988). The results do not change significantly for the inclination angle of 60°-80°. However, the inclination angle of 90° does not account for the velocity gradient along the east-west direction seen in CH_3OH emission. Since infalling-rotating gas cannot fall inward of the centrifugal barrier (Oya et al. 2014), our model assumes no emission inside it.

The model calculation is conducted with the following four free parameters: (1) the radius of the centrifugal barrier ($r_{\rm CB}$), (2) the mass of the central protostar (M_*), (3) the outer radius of the envelope ($R_{\rm env}$), and (4) the full thickness of the envelope ($h_{\rm env}$). $r_{\rm CB}$ and M_* are the physical parameters specific to the source and independent of the molecular distributions. On the other hand, $R_{\rm env}$ and $h_{\rm env}$ reflect the distribution of the molecular line emission (i.e., molecular distribution). The parameter ranges which we inspected are as follows: 1-9 au at a step of 1 au for $r_{\rm CB}$, 0.01-0.12 $M_\odot$ at a step of 0.01 $M_\odot$ for M_*, 6-24 au at a step of 3 au for $R_{\rm env}$, 5-20 au at a step of 5 au for $h_{\rm env}$.

For CH_3OH, the PV diagrams are well explained with $r_{\rm CB}$ of 3 au, M_* of 0.04 $M_\odot$, $R_{\rm env}$ of 15 au, and $h_{\rm env}$ of 15 au. The results are overlaid in black contours in Figure 6.2. We use these values of $r_{\rm CB}$ and M_* as the fiducial values. Using these values, the PV diagram of HCOOH is also simulated. It is well explained with $R_{\rm env}$ of 6 au and $h_{\rm env}$ of 10 au. The smaller outer radius for HCOOH than for CH_3OH is consistent with the moment 0 maps (Figure 6.2). Thus, the different kinematic structure described in Section 6.3.1 is explained by the IRE model with the different emitting regions of the molecules. Note that the thickness of the emitting region ($h_{\rm env}$) may be slightly different between HCOOH and CH_3OH.

In contrast, a model of the Keplerian motion does not well explain the kinematic structure of CH_3OH, as shown in white contours in Figure 6.2. In this case, the counter velocity components (blueshifted in the northern part and redshifted in the southern part) cannot be reproduced. As shown in Figure 6.1, a clear redshifted peak of the CH_3OH emission is absent in the spectra, as seen in other COMs. This feature is also seen in the moment 1 map, where the redshifted component seems weakened at the northeast region. It could be due to asymmetric distribution of gas.

To constrain M_* and $r_{\rm CB}$, these values are varied from the fiducial ones, and the results are compared with the PV diagrams of CH_3OH (Figure 6.3). Here, the other parameters are fixed to the fiducial values. M_* mainly affects the velocity shift, because the velocity of the gas at a

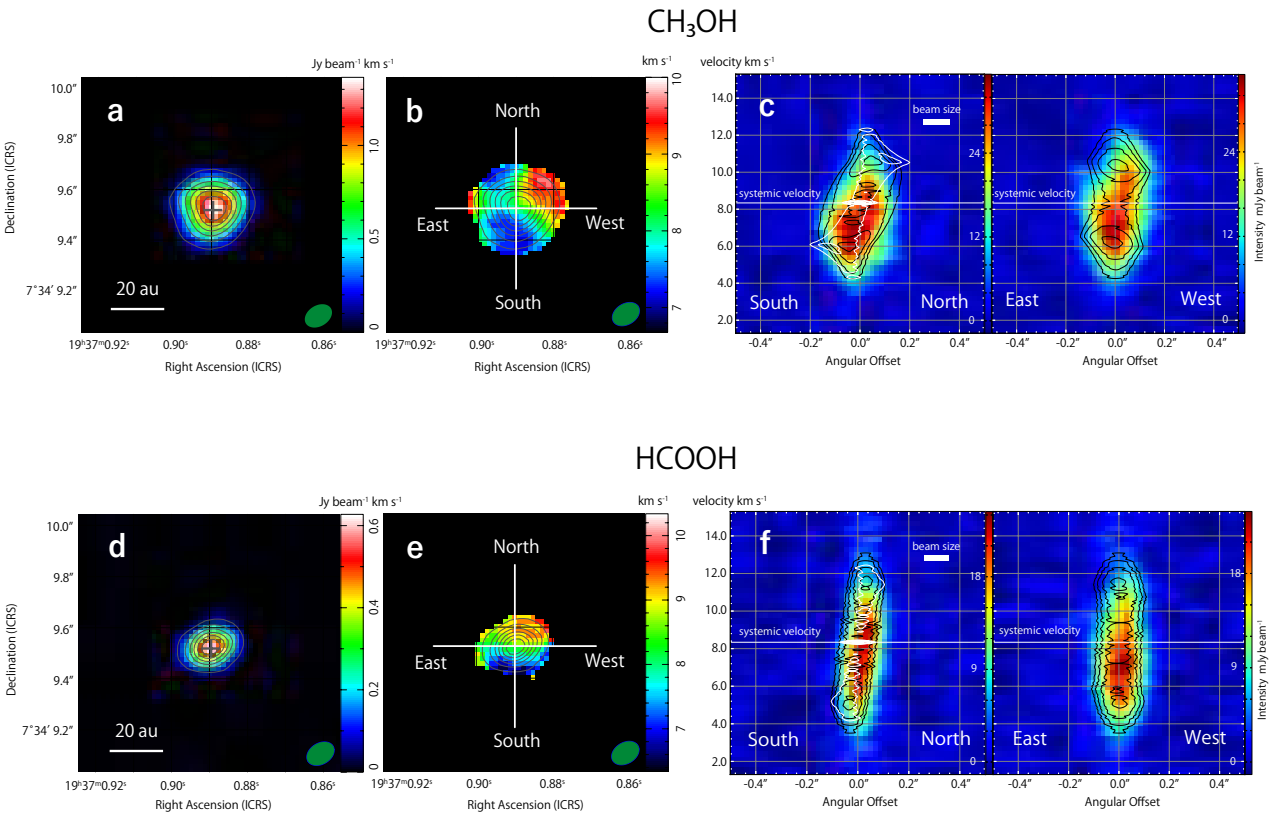

Figure 6.2: (*left two panels*) The integrated intensity maps (left) and the velocity maps (right) of CH_3OH and HCOOH emission. The contours in each panel represent the 10, 25, 40, 55, 70, and 85 % of the intensity peak of the integrated intensity map. The grey cross marks show the continuum peak position. The synthesized beam size is shown in the bottom right. (*right two panels*) Position-velocity diagrams of CH_3OH (c) and HCOOH (f) along the south-north (envelope/disk) and east-west (outflow) directions. The origin of the position axes is the continuum peak position. Black contours are the results of the IRE model with the parameters, $M_* = 0.04\ M_\odot$ and $r_{\rm cb} = 3$ au. The emitting regions are R_0 of 15 au and h_0 of 15 au for CH_3OH, and R_0 of 6 au and h_0 of 10 au for HCOOH. The contour levels denote 10, 20, 40, and 80 % of the intensity peak. White contours in the south-north direction panels show the fit by the Keplerian model, where a flatten disk is assumed. In this case, the protostellar mass is 0.10 $M_\odot$, and the outer radius and the thickness of the disk are 18 au and 20 au for CH_3OH and 9 au and 10 au for HCOOH, respectively. The contour levels are the same level as the IRE model case.

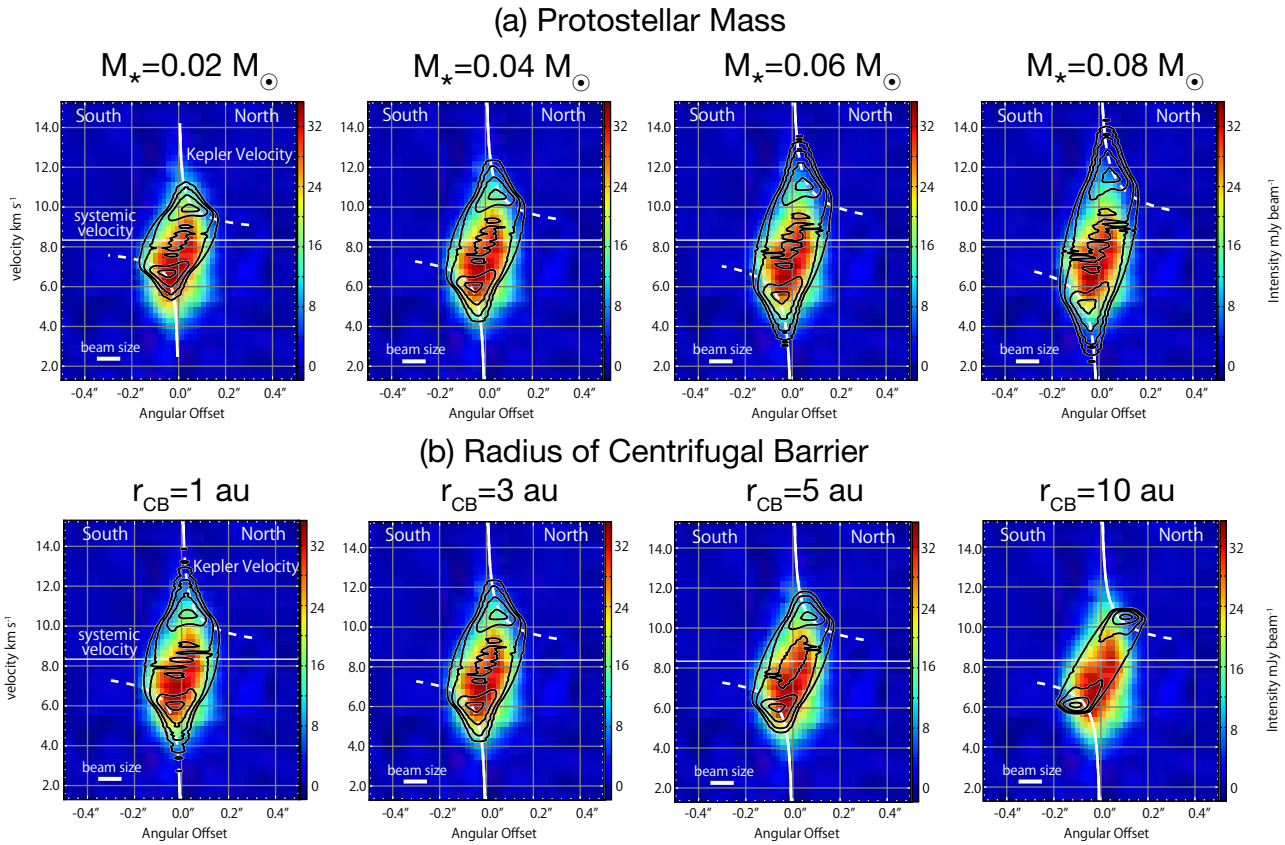

Figure 6.3: Position-velocity diagrams of CH_3OH along the south-north(disk) direction. The origin of the position axes is the continuum peak position. (a) Contours are the results of the IRE model for the protostellar mass of 0.02, 0.04, 0.06, 0.08 $M_\odot$, where $r_{\rm CB}$ is fixed to the fiducial value of 3 au. The other parameters are the same as those of Figure 6.2. The contour levels denote 10, 20, 40, and 80 % of the intensity peak. The maximum velocity of the Keplerian motion is shown in white lines. Solid and dotted parts denote the inside and the outside of the centrifugal barrier radius. (b) Contours are the results of the IRE model for the $r_{\rm CB}$ of 1, 3, 5, and 7 au, where M_* is fixed to the fiducial value 0.04 $M_\odot$. The other parameters are the same as those of Figure 6.2. The contour levels are the same as (a).

certain radius is roughly proportional to the $M_*^{1/2}$ in the IRE model. As shown in Figure 6.3(a), the protostellar mass is constrained to be in the range from 0.02 $M_\odot$ to 0.06 $M_\odot$. On the other hand, $r_{\rm CB}$ affects the degree of the slant feature in the PV diagram. The observed PV diagrams cannot be explained for $r_{\rm CB}$ larger than 5 au, as shown in Figure 6.3(b). The detailed accuracy of these parameter values are discussed in detail in Section 6.3.3.

6.3.3 Error Estimation of the Physical Parameters

To evaluate the model similarity, we calculate $KL(p, q)$ using the lines of CH_3OH and HCOOH. The definition of $KL(p, q)$ is described in Section 4.2. The signal detection probability for pixel i for the observation image (p_i) is derived as:

$$p_i = \max(p_{i,\rm mol})\Big|_{\rm mol=CH_3OH,\ HCOOH}. \tag{6.1}$$

Here, $p_{i,\mathrm{mol}}$ is calculated by using the sigmoid function as:

$$p_{i,\mathrm{mol}} = \mathrm{sig}(I_{i,\mathrm{mol}}; I_{\mathrm{thres}}, b) = \frac{1}{1+\exp(-\frac{I_{i,\mathrm{mol}}-I_{\mathrm{thres}}}{b\times I_{\mathrm{thres}}})}, \tag{6.2}$$

where I_{thres} and b are set to be 30 % of the intensity peak for each molecule and 0.2, respectively. The signal detection probability for pixel i for the model image (q_i) is derived as:

$$q_i = \frac{1}{1+\exp(-\frac{I_{i,\mathrm{model}}-I_{\mathrm{thres}}}{b\times I_{\mathrm{thres}}})}. \tag{6.3}$$

Here, I_{thres} is set to be 10 % of the maximum intensity of the mode.

The values of I_{thres} for the observation and the model affect the shape of the outline of the PV diagram and the similarity calculation (see Section 4.2). Since these values cannot be optimized by the observation dataset, the dependence of the following result on these parameters will be discussed later in this section. For I_{thres}, a relative scale to the maximum intensity (30 %) is used instead of the noise level in order that the extent of the emission enclosed in the boundary is less influenced by the intensity of the line, as noted in Section 4.2.

The ranges of the PV image used for the analysis are $\pm 0\farcs3$ from the continuum peak position along the envelope direction (P.A. = 290°) for the position axis and ± 5.0 km s^{-1} from the systemic velocity (8.34 km s^{-1}) for the velocity axis. The position angle of the envelope direction is optimized in order to better constrain the mass and the radius of the centrifugal barrier of the infalling-rotating motion. The pixel spacing for the position axis is set to $0\farcs018$ which is roughly five times smaller than the beam size. The pixel spacing for the velocity axis is 139.8 m s^{-1}, which is consistent with the velocity resolution of the observation. The PV image is recalculated from the data cube by interpolating the neighboring pixels both for the observation and the model. In total, the images contain 21060 pixels. We calculate the signal detection probability for each pixel by applying the sigmoid function. The calculated signal detection probability is compared with the observed PV diagrams in Figure 6.4. The signal detection probability well traces the outline of the PV diagrams of CH_3OH and HCOOH. Similarly, the signal detection probability for the model is also calculated. Using these probability distributions, we calculate $KL(p, q)$ for the model of the observation.

The KL divergence derived for the variation of the four free parameter is summarized in Figure 6.5. As for the r_{CB}, the KL divergence becomes the lowest around r_{CB} of < 3 and becomes larger as the r_{CB} increases from 3 au. This suggests that only the upper limit to the radius of the centrifugal barrier can be determined. This result is consistent with the result by the above eye-based fitting. The KL divergence for the variation of M_* is also shown in the upper right panel of Figure 6.5. In this case, the value becomes the smallest around the mass of 0.04-0.05 $M_\odot$. The value increases rapidly as the mass decreases from 0.03 $M_\odot$, while the increase is more gentle for the mass larger than 0.07 $M_\odot$. Again, this result is consistent with the above eye-based fitting. As for R_{out}, the value becomes the smallest for R_{out} of 12-15 au. The change in the KL divergence is not prominent for the variation of the thickness h_0. This is because we only fit the PV diagram along the direction of the envelope. Thus, the fitting result with $KL(p, q)$ seems consistent with the eye-based fitting (Section 6.3.2).

The value of the KL divergence has an uncertainty due to the noise of the observation. This effect is evaluated by calculating the similarity of the mock PV images based on the observation with and without the noise component (see Section 4.2.2 and Appendix A for details). By using this method, the tolerance range of the KL divergence in the optimization is estimated to be 0.04 above the minimum value of $KL(p, q)$.

Using the above tolerance range of the KL divergence, the uncertainties of the optimized parameters are evaluated. The tolerance range of the KL divergence is shown by the gray range

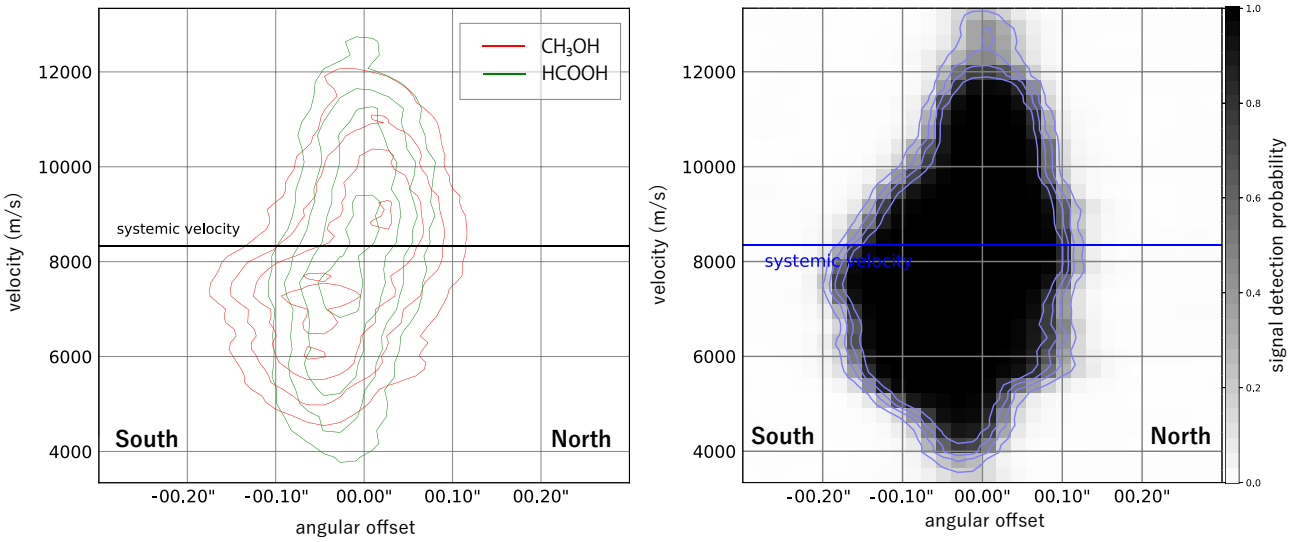

Figure 6.4: (*left*) The combined PV diagram of CH_3OH (red) and HCOOH (green). The contours represent the 30, 50, 70, and 90 % of the peak. (*right*) The probability distribution (p_i) calculated by using the sigmoid function to the combined PV diagram. The contours represent the signal probability of 0.2, 0.4, 0.6, and 0.8.

in Figure 6.5. The protostellar mass and the radius of the centrifugal barrier are evaluated to be $0.05^{+0.02}_{-0.015}$ $M_\odot$ and < 4 au, respectively. Here, the uncertainties of the parameters are estimated by the parameter range whose $KL(p, q)$ is in the gray range in Figure 6.5. However, the derived mass has an uncertainty due to the variation of $I_{\rm thres}$ for both observation and model, as discussed later. Their uncertainties are estimated to be ± 0.01 $M_\odot$. Including them, the uncertainty of the protostellar radius is estimated to be $0.05^{+0.03}_{-0.02}$ $M_\odot$. We can set only an upper limit to $r_{\rm CB}$ (4 au), because the synthesized beam size is $0''.1$ (10 au). These values are consistent with the eye-based fitting result (Section 6.3.2).

An interesting feature of this protostellar source is the remarkably small radius of the centrifugal barrier ($r_{\rm CB}$) (< 4 au). It is the smallest of those ever reported for low-mass sources, and smaller than the typical value (50-100 au) by an order of magnitude or more (Table 6.3). Since the gas motion outside the centrifugal barrier is explained by infall and rotation, the rotationally supported disk, if present, should be inside the centrifugal barrier at a scale of less than 4 au. This size is consistent with the previous estimate by Yen et al. (2015). Another explanation for the small radius of the centrifugal barrier is that the protostar is in a stage of the first core (Larson et al. 1969; Masunaga et al. 2000b) whose typical size is expected to be a few au. The complex organic molecules seen in this observation may be present in the infalling-rotating gas accreting onto the surface of the first core.

Here, we mention the effect of the assumed inclination angle on the error estimation (Figure 6.5). We find that the similarity index is almost independent of the inclination angle change from 50° to 90°. On the other hand, the KL divergence slightly increases as the inclination angle decreases below 50°, although the change is within the uncertainty. This result suggests that the source would have an edge-on disk configuration rather than face-on disk. However, we cannot determine the precise inclination angle from this analysis. The inclination angle does not significantly affect the optimization of the other free parameters used above discussion. We confirm that the flare angle of the envelope has little effect on the similarity index (Figure 6.5).

Finally, we show the dependence of $KL(p, q)$ on the variation of $I_{\rm thres}$ and b. In the present analysis, we set the $I_{\rm thres}$ of 30 % for the observation data, 10 % for the model data, and b of

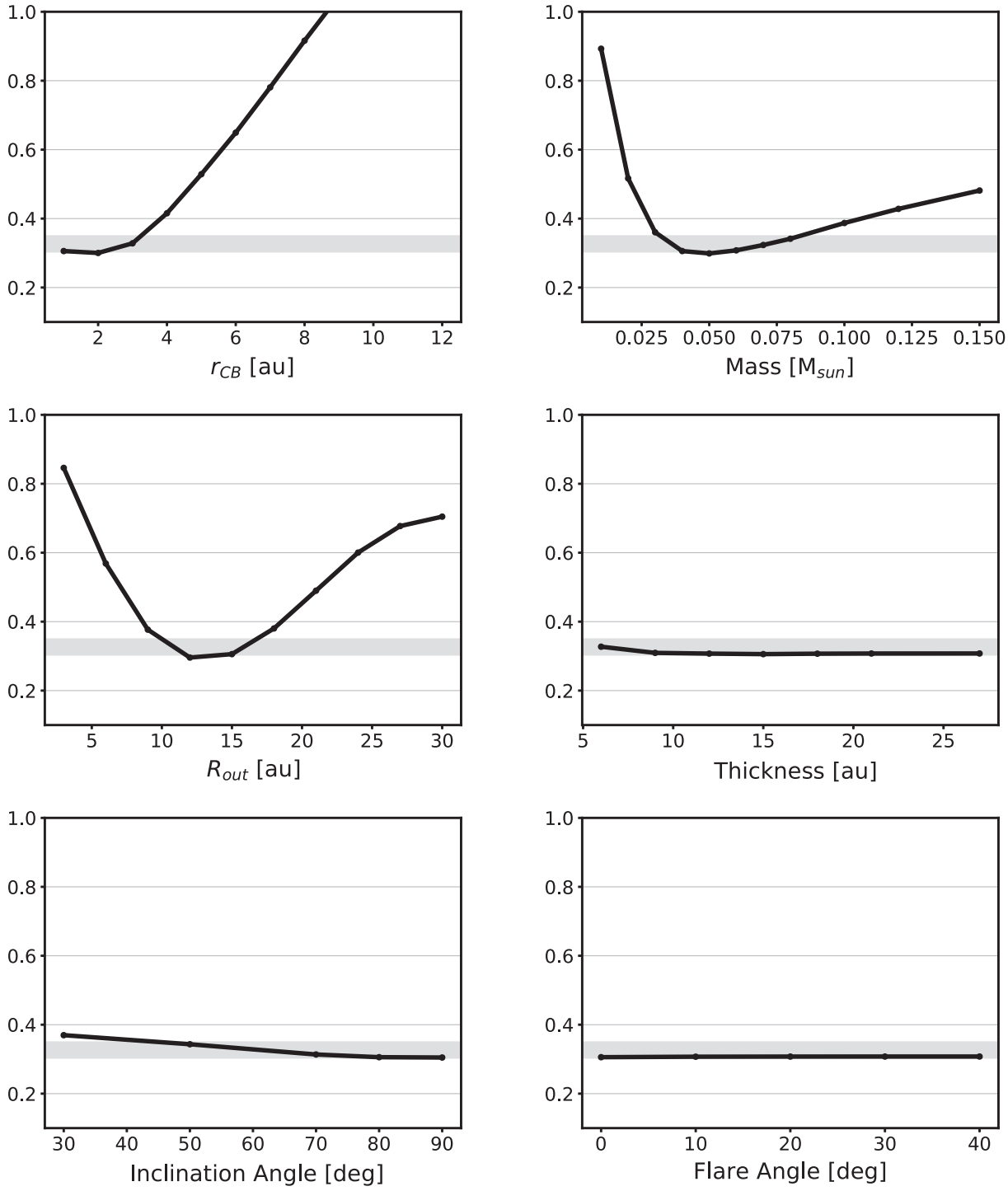

Figure 6.5: The KL divergence for variations of the radius of the centrifugal barrier, the mass of the protostar, the outer radius of the emitting region, the thickness of the emitting region, the inclination angle, and the flare angle. The gray area indicates the uncertainty for the KL divergence due to the observation noise.

Table 6.3: Comparison of $r_{\rm CB}$ among Low-Mass Sources

Source Name	Evolutionary Stage	Protostellar Mass ($M_\odot$)	Radius of the CB[b] (au)
B335	Class 0	$0.05^{+0.03}_{-0.02}$	< 4
L1527[c]	Class 0/I	0.18 ± 0.05	100±20
TMC 1A[d]	Class I	0.25 ± 0.05	50 ± 10
IRAS 16293-2422 Source A[c]	Class 0	0.75 ± 0.25	50 ± 10
IRAS 16293-2422 Source B[c]	Class 0	$0.4^{+0.4}_{-0.2}$	40 ± 10
L483[c]	Class 0	0.15 ± 0.05	100^{+100}_{-70}

[a] Centrifugal barrier.
[b] Taken from Oya et al. (2017b)
[c] Taken from Sakai et al. (2016)

0.2. We change these values and see how the result changes in Figure 6.6. The following cases are investigated: $I_{\rm thres}$ for the observation data of 20 % and 40 %, $I_{\rm thres}$ for the model data of 5 % and 20 %, and b of 0.1 and 0.3. In the investigation, only one of $I_{\rm thres}$ for the model and the observation and b is changed, while the others are remained to be unchanged. Overall, the basic shape of the dependence along with the parameters giving the minimum values does not significantly change within the above ranges. However, the mass showing the lowest $KL(p, q)$ value depends on the $I_{\rm thres}$ for both the observation and the model. The uncertainties of the mass due to their variations are derived to be ± 0.01 $M_\odot$ for both case. This is applied to the error of the mass estimation described above.

6.3.4 Different Distribution among COMs

As described in Section 6.3.2, the distribution of CH_3OH is extended over the area of 15 au in radius. Although the distribution of CH_3OH in B335 is much smaller compared with other hot corino sources (e.g., Oya et al. 2016), CH_3OH is extended well beyond the centrifugal barrier, and exist in the innermost part of the infalling-rotating envelope in B335. On the other hand, HCOOH shows even more compact distribution, as shown in Figure 6.2. Thus, the distributions of COMs and their related species seem different among molecular species. Since the upper state energy of the CH_3OH line is higher than that of HCOOH by a factor of 5, this difference cannot be explained by the excitation condition. Furthermore, the surface binding energy of HCOOH (5000 K) is almost comparable to that of CH_3OH (4930 K), and hence, the different distribution is not simply ascribed to the liberation process from grain mantle. Rather, it may reflect the difference of the formation process. Most of the COMs had been thought to be formed on the grain surface. However, Ceccarelli et al. (2017) reported that the detection of COMs in the cold environment is hard to be explained by the formation on the grain surface, because radicals are not mobile in the cold phase (<25-30 K). Alternatively, they propose the COM formation through gas-phase reactions triggered from the evaporation of CH_3OH from grain. Such a gas-phase contribution might cause the different distribution of COMs seen in B335.

6.3.5 SiO Emission Tracing the Inside of the Centrifugal Barrier

The SiO emission shows another interesting feature in B335. Its spectrum toward the protostellar position is shown in Figure 6.7. The SiO line emission is extended over a velocity range as large as 70 km s^{-1}, which is about ten times broader than those of typical COMs in B335. It has a compact distribution at the protostellar position without extended components. The

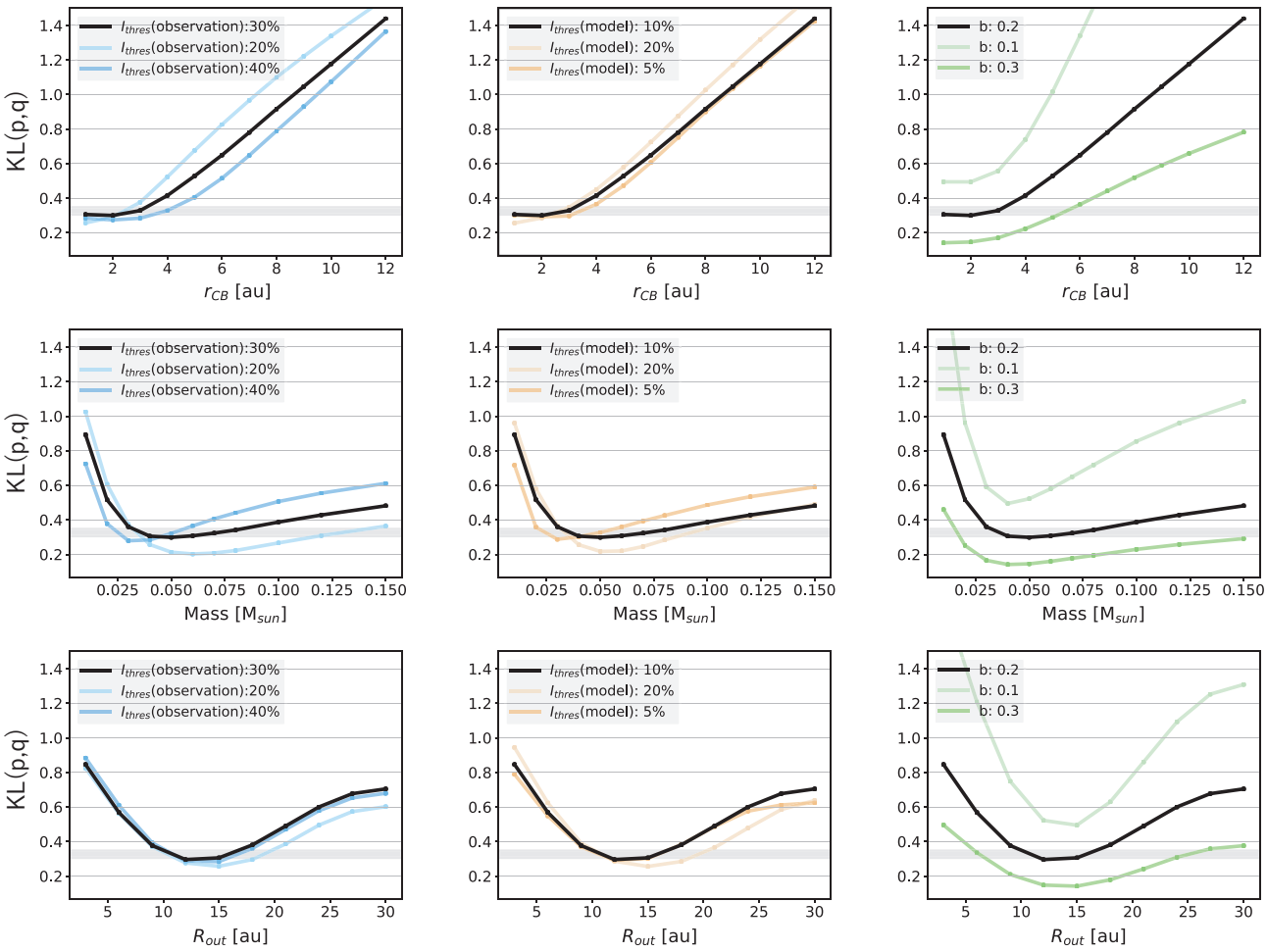

Figure 6.6: Examples of the dependence of the KL divergence on $I_{\rm thres}$ for the observation data (left column panels), that on $I_{\rm thres}$ for the model data (middle column panels), and that on b coefficient of sigmoid function (right column panels). The values used for the actual analysis are shown in black: $I_{\rm thres}$(observation)=30 %, $I_{\rm thres}$(model)=10 %, and b=0.2. The results for the $r_{\rm CB}$, M_*, and b are shown in the upper panels, the middle panels, and the bottom panels, repsectively

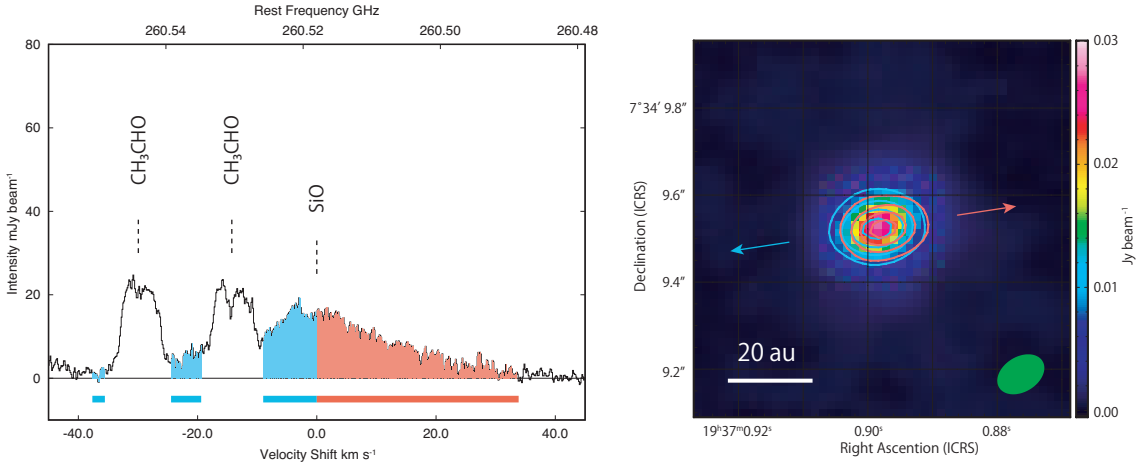

Figure 6.7: The spectrum of SiO (left panel). The line emission is extended over the velocity range as large as 70 km s^{-1}. The integrated intensity maps of the blueshifted and redshifted components (contours) are overlaid to the continuum image in the right panel. The contours denote 30, 50, 70, and 90 % of the integrated intensity peak. Since the blueshifted component is contaminated with the lines of CH_3CHO, the contaminated range is excluded in the integration. The integrated velocity range for the redshifted and blueshifted components are shown with red and blue in the spectrum, respectively. The blue and red arrows denotes the direction of blue- and redshifted outflow components, respectively (Yen et al. 2015).

integrated intensity maps of the redshifted and blueshifted components of SiO are overlaid in contours on the continuum image in Figure 6.7. Since the blueshifted component is heavily contaminated with the CH_3CHO emission, only non-contaminated channels are used for the integration. Both components are not spatially resolved with the synthesized beam. SiO usually traces outflow-shocked regions in low-mass protostellar sources (e.g., Mikami et al. 1992; Bachiller et al. 1997). In this source, spatial separation between the redshifted and blueshifted components is not definitely observed, although a marginal trend might be seen for the outflow direction; the east (blue)-west (red) direction. This trend is also recognized for the integration of the only high velocity component. Furthermore, the SiO emission including its high velocity component is not obviously elongated to the outflow direction. One possible explanation is that SiO traces the launching point of the outflow which is too compact to be resolved with a 0.″1 beam. Another possibility is that SiO traces the strong shock where the materials are accreting onto the protostar. If the energy conservation of the infalling gas without influence of radiation pressure is simply assumed, the emitting region of the highest velocity component of SiO is estimated to be 4 $R_\odot$ which is almost comparable to the size of photosphere (3 $R_\odot$ reported by Yen et al. 2015). Whichever the case is, SiO seems to trace the closest vicinity of the protostar inside the centrifugal barrier.

6.3.6 Summary

In the 1.2 mm band observation toward B335 with ALMA, a rotation structure at a scale of about 10 au is found in the CH_3OH and HCOOH lines, and its kinematic structure is discussed. The main results are summarized below.

1. The velocity gradient of HCOOH is almost along the disk direction, while that of CH_3OH is inclined to the outflow direction. These features can be explained by the infalling-

rotating envelope model with different molecular distributions. The different distribution may reflect the formation and destruction processes of these molecules.

2. The protostellar mass and the radius of the centrifugal barrier are derived to be $0.05^{+0.03}_{-0.02}$ $M_{\odot}$ and < 4 au, respectively. The radius of the centrifugal barrier is the smallest of previously known values for low-mass protostars.

3. SiO shows very broad lines and has a compact distribution at the protostellar position. It appears to reside in the closest vicinity of the protostar tracing the launching point of the outflow or gas accreting onto the protostar.

Chapter 7

Physical and Chemical Structures of CB68

In this chapter, chemical and physical structures of the envelope of the low-mass Class 0 protostar IRAS 16544-1604 in the Bok globule CB68 are described. The result is based on ALMA observation in the 1.2 and 1.3 mm band at a linear spatial resolution of 70-80 au. Five saturated complex organic molecules (COMs) CH_3OH, CH_3CHO, HCOOH, CH_3OCH_3, and NH_2CHO are detected. They are concentrated around the protostar and not resolved at the resolution of 70-80 au. The rotation temperature of the emitting region of COMs is derived to be 133 ± 14 K from the rotation diagram analysis of the CH_3OH lines. The fractional abundances of COMs relative to H_2 are roughly similar to those of B335, although relative abundances of COMs are slightly different. The detection of COMs in such a hot region in the vicinity of the protostar suggests that CB68 harbors a hot corino. In addition, extended emission lines of carbon-chain molecules associated with the protostar are detected, suggesting WCCC at a scale of 1000 au. These features are consistent with the hybrid chemical character (hot corino chemistry in the vicinity of the protostar and WCCC in the envelope around the protostar), which was found in B335. $C^{18}O$ traces from the outer part to the innermost part of the envelope, while CH_3OH and OCS mainly trace the innermost envelope. The kinematic structure of these lines is successfully explained by the infalling-rotating envelope model, and the protostellar mass and the radius of the centrifugal barrier are estimated to be $0.15^{+0.15}_{-0.07}$ $M_\odot$ and < 30 au, respectively.

7.1 Introduction

An isolated protostellar core without influences from nearby stars/protostars provide us with an ideal testbed of star formation theories. In this context, exploring the chemical and physical structures of the isolated source is of significant importance for understanding of the formation process of the protostellar sources. To this end, the chemical and physical feature of the representative isolated source B335 has been investigated with ALMA (Chapters 5 and 6; Imai et al. 2016; Imai et al. 2019). The chemical properties of B335 are characterized by rich existence of both carbon-chain molecules and complex organic molecules (COMs). In addition, it is revealed to have a remarkable small rotation structure ($\sim$ 10 au). Then, we now have an important question whether such a feature found in B335 can be seen in other isolated sources. With this motivation, chemical and physical diagnostics of another isolated source CB68 was carried out by using ALMA, and their results are described in this chapter.

CB68 is a slightly cometary-shaped Bok globule located in the outskirts of the ρ Oph dark cloud complex at a distance of $\sim$ 160 pc (Launhardt & Henning 1997) (Figure 7.1). The extent of the cloud is about 0.18 pc (Launhardt et al. 2010), and the mass of the core is reported to be

$\sim 0.9\ M_\odot$ (Bertrang et al. 2014). It harbors the Class 0 low-mass protostar IRAS 16544-1604. No near infrared (NIR) source is detected at 2.2 μm (Launhardt et al. 2010), indicating that the protostar is deeply embedded in the parent core. The protostar drives a collimated bipolar molecular outflow (Wu et al. 1996; Mardones et al. 1997; Vallée et al. 2000; Vallée & Jason 2007). Vallée et al. (2000) reported the outflow traced by the ^{12}CO line whose position angle is 142° (Figure 7.2). The protostar has the bolometric luminosity of 1.3 $L_\odot$ and the bolometric temperature of 50 K (Launhardt et al. 2010). In contrast, chemical and physical structures at a smaller scale (< 100 au) have little been understood.

7.2 Observation

The 1.2 and 1.3 mm observations (Band 6) toward CB68 were conducted with ALMA (Cycle 6) from 4 October, 2018 to 17 April, 2019. The field center is α(J2000)=$16^{\rm h}57^{\rm m}19\overset{\rm s}{.}643$, δ(J2000)=$-16°9'23\overset{''}{.}92$. These data are parts of the large program 'Fifty AU STudy of the chemistry in the disk/envelope system of solar-like protostars' (*FAUST*). The data used for this study consist of 2 frequency setups: 218-234 GHz (1.3 mm) and 245-260 GHz (1.2 mm). The details of the observations are summarized below.

Setup for 1.3 mm Observation

The minimum and maximum baselines are 6 kλ and 750 kλ, respectively. The primary beam size is $23\overset{''}{.}6$, and the synthesized beam size is $0\overset{''}{.}48 \times 0\overset{''}{.}38$ (P.A. = 297°). ACA is employed in the observation, and the maximum recoverable size is $26\overset{''}{.}9$. In total, 13 spectral windows are used. One spectral window has low velocity resolution whose bandwidth and channel spacing are 1875 MHz and 0.977 MHz, respectively (continuum setup). The other twelve spectral windows have high velocity resolution whose bandwidth and channel spacing each are 58.6 MHz and 141 kHz, respectively. The channel spacing for the high resolution windows corresponds to a velocity resolution of 0.18-0.20 km s^{-1}. The achieved rms noise is 2.5 mJy beam^{-1} at a nominal channel width of 0.18-0.20 km s^{-1}. J1733-1304 is observed as a flux and phase calibrator. J1751+0939 and J1924-2914 are observed as a bandpass calibrator. The flux calibration accuracy is about 5 %. We employed a new calibration process which overcomes the problem found in the original calibration pipeline. Self-calibration was applied by using the continuum data.

Setup for 1.2 mm Observation

The minimum and maximum baselines are 8 kλ and 500 kλ, respectively. The primary beam size is $23\overset{''}{.}6$, and the synthesized beam size is $0\overset{''}{.}50 \times 0\overset{''}{.}43$ (P.A. = 276°). In total, 13 spectral windows are used. One spectral window has low velocity resolution whose bandwidth and channel spacing are 1875 MHz and 0.977 MHz, respectively. The other twelve spectral windows have high velocity resolution whose bandwidth and channel spacing each are 58.6 MHz and 141 kHz, respectively. The channel spacing for the high resolution windows corresponds to a velocity resolution of 0.16-0.17 km s^{-1}. The achieved rms noise is 3.0 mJy beam^{-1} at a nominal channel width of 0.16-0.17 km s^{-1}. J1733-1304 is observed as a flux and phase calibrator. J1517-2422 and J2056-4714 are observed a bandpass calibrator. The flux calibration accuracy is about 5 %. In this setup, we also employed the new calibration process mentioned above. Self-calibration was applied by using the continuum data.

CASA (Common Astronomy Software Applications) was used for data reduction and imaging. A continuum image was prepared by averaging line-free channels, resulting in the rms noise of 88 μJy beam^{-1}. Maps of the spectral line emission were obtained by CLEANing the dirty

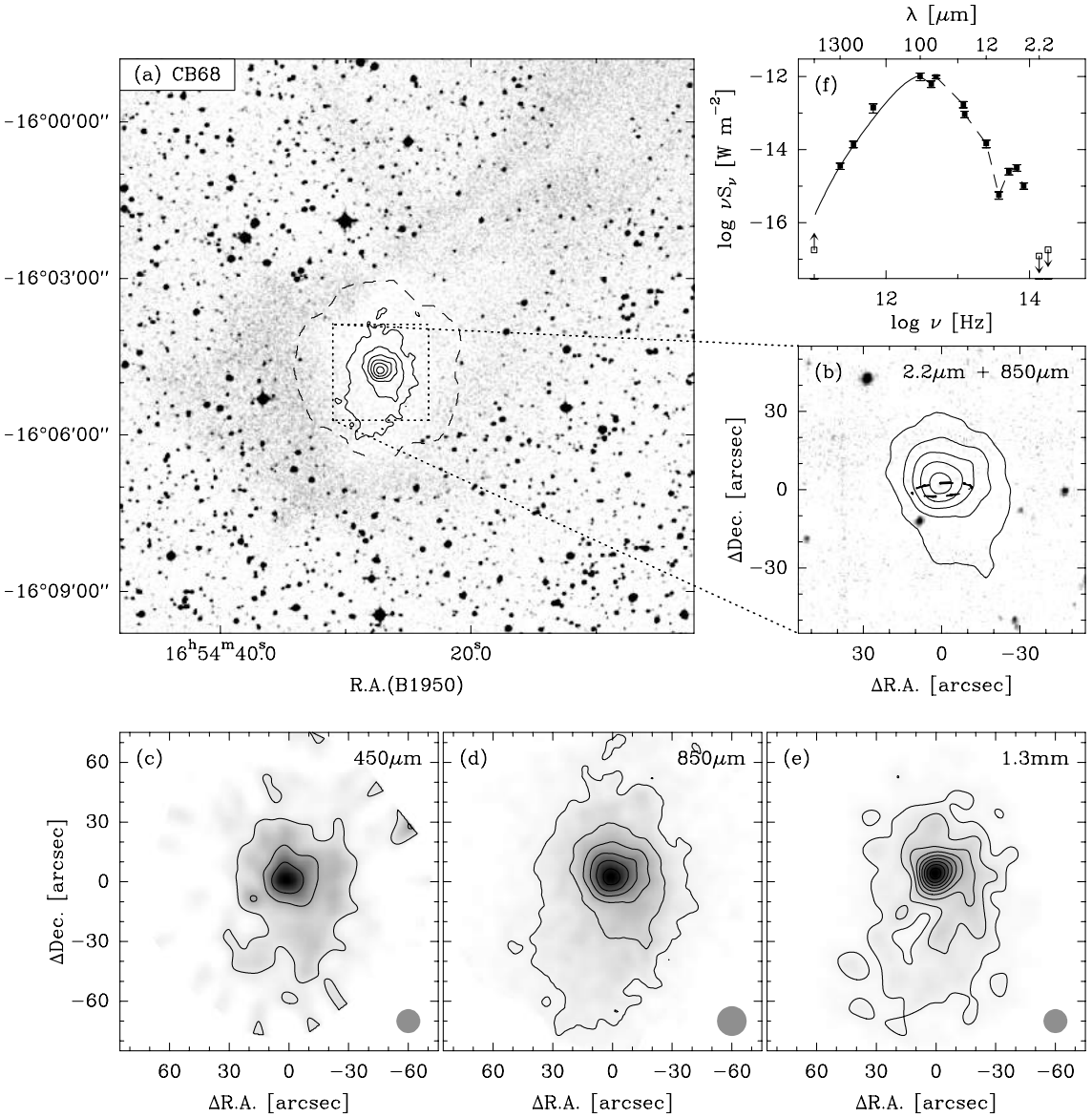

Figure 7.1: Images of CB68 (Launhardt et al. 2010). (a) Optical image overlaid with contours of the 850 μm dust continuum emission. (b) Near infrared K-band image with the 850 μm dust continuum contours. The IRAS source position is marked by a dashed ellipse. (c) The 450 μ dust continuum emission. (d) The 850 μm dust continuum emission. (e) The 1.3 mm dust continuum emission. (f) SED of the protostellar core.

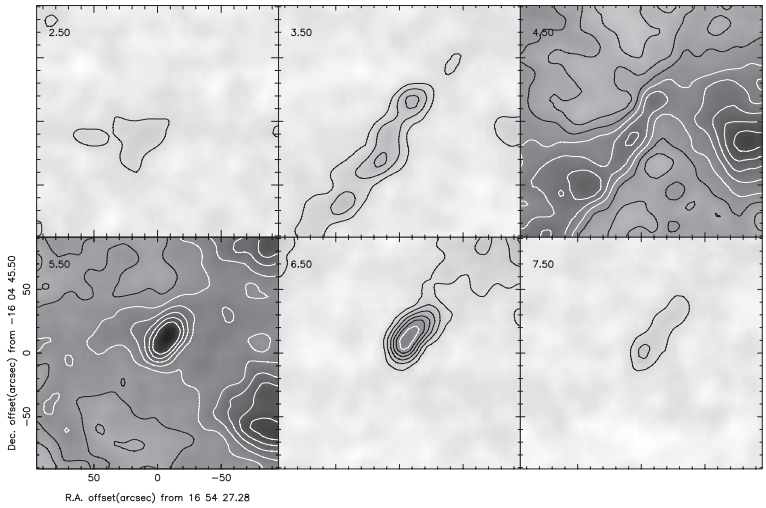

Figure 7.2: Velocity channel maps of the ^{12}CO line (J=3-2) for the velocity of 2.5, 3.5, 4.5, 5.5, 6.5, and 7.5 km s^{-1} (Vallée et al. 2000). A collimated bipolar outflow extends along the position angle of 142°.

images with the Briggs robustness parameter of 0.2 after subtracting the continuum directly from the visibility data.

7.3 Results & Discussion

7.3.1 Distributions

Figure 7.3 shows the 1.3 mm continuum map. The peak position is determined by the Gaussian fit as: (α_{2000}, δ_{2000}) = ($16^{\rm h}57^{\rm m}19\overset{\rm s}{.}647$, -16°9′23$\overset{\prime\prime}{.}$94). The integrated flux and peak flux are 53 ± 3 mJy and 42 ± 2 mJy beam^{-1}, respectively. The peak intensity corresponds to the brightness temperature of 7.8 ± 0.4 K, indicating that the dust is not so optically thick at the 1.3 mm and 1.2 mm bands at the present resolution. We simply assume that the effect of the dust opacity is negligible for the molecular line emission in the following analyses and discussions.

Figures 7.4 and 7.5 show the spectrum toward the protostellar position at a scale of synthesized beam size (∼0$\overset{\prime\prime}{.}$4-0$\overset{\prime\prime}{.}$5; 70-80 au) for the 1.2 mm and 1.3 mm bands, respectively. In total, 57 molecular lines are identified using the Cologne Database for Molecular Spectroscopy (CDMS) (Muller et al. 2005) and Jet Propulsion Laboratory (JPL) (Pickett et al. 1998) databases. Carriers of the lines are labeled in Figures 7.4 and 7.5. The detection rate of the molecular lines is 11 GHz^{-1}.

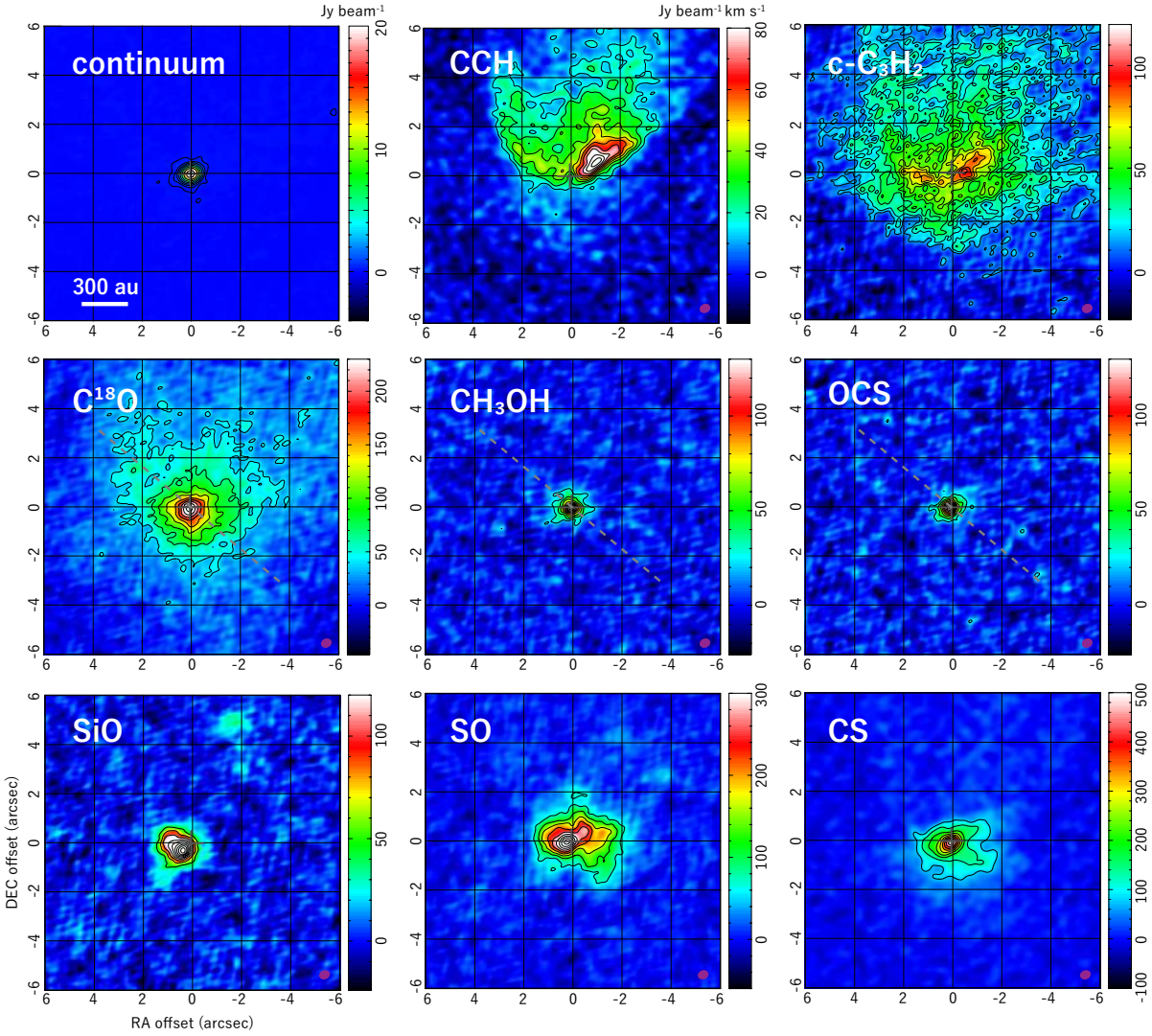

Figure 7.3: The 1.3 mm continuum map and the moment 0 maps of CCH, c-C_3H_2, $C^{18}O$, CH_3OH, OCS, SiO, SO, and CS. The gray cross marks represent the protostellar position. The dashed lines in the panels of $C^{18}O$, CH_3OH, and OCS indicate the direction of the envelope (P.A.=230°) (Section 7.3.3).

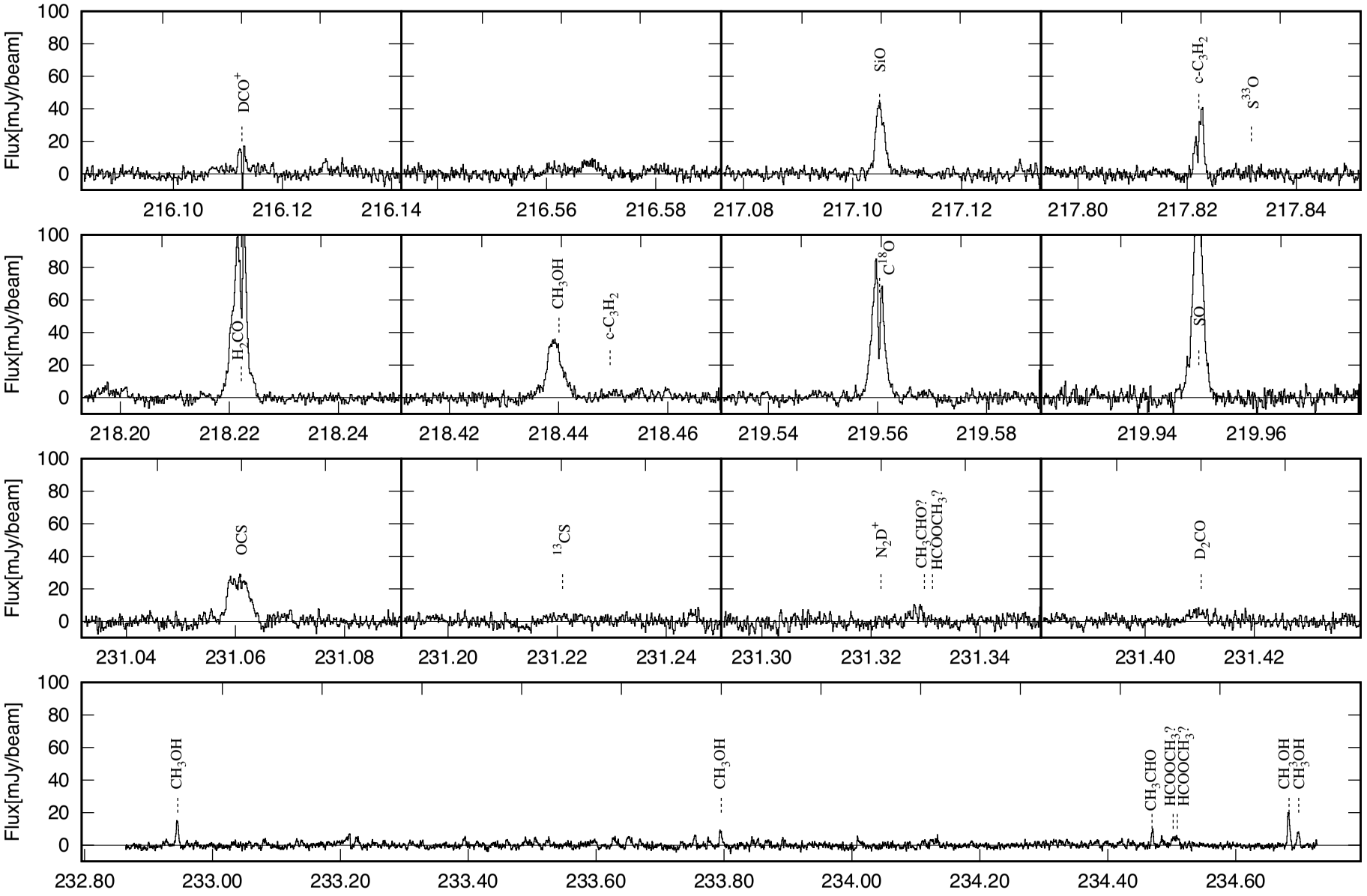

Figure 7.4: The spectrum observed toward the continuum peak ((α_{2000}, δ_{2000}) = ($16^{\rm h}57^{\rm m}19\overset{\rm s}{.}647$, -16°9′23″.94)) of CB68 in the 1.3 mm band.

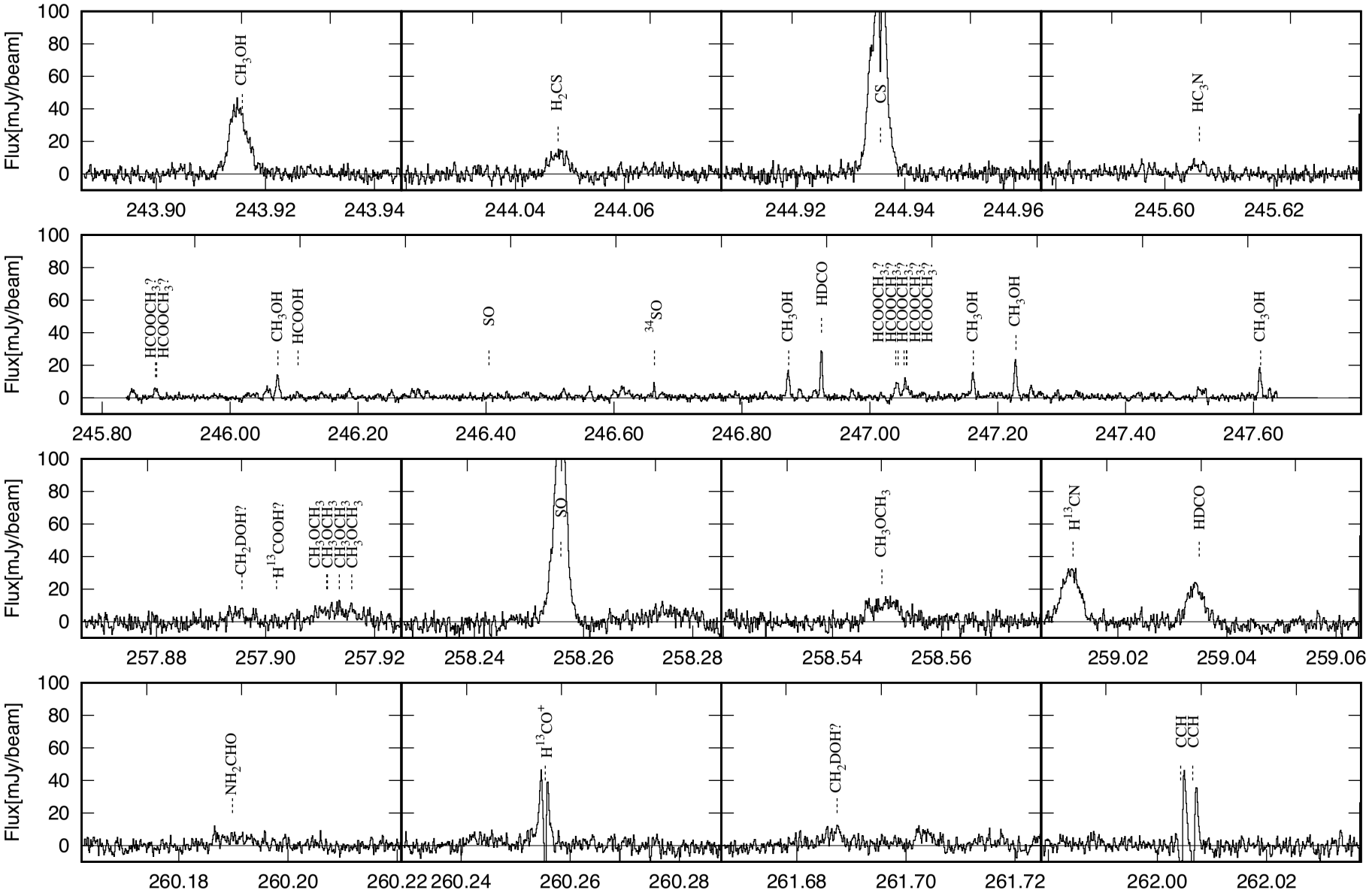

Figure 7.5: The spectrum observed toward the continuum peak ((α_{2000}, δ_{2000}) = ($16^{\rm h}57^{\rm m}19\overset{\rm s}{.}647$, -16°9′23.″94)) of CB68 in the 1.2 mm band.

Bright emissions of carbon-chain molecules (CCH and c-C_3H_2) are detected. In addition, bright emissions of CH_3OH are also detected in this source. Figure 7.3 shows the moment 0 maps of CCH, c-C_3H_2, $C^{18}O$, CH_3OH, OCS, SiO, SO, and CS. The CCH and c-C_3H_2 distributions are extended and elongated to the north direction. Since the outflow blows along the southeast-northwest direction in this source (Wu et al. 1996), the extended emission of carbon-chain molecules likely traces the outflow cavity. In addition, c-C_3H_2 has a bright emission with association to the protostar. These features suggests that CB68 has a WCCC feature on a scale of 1000 au. On the other hand, CH_3OH is concentrated around the protostar on a scale of 100 au. These features are similar to those found in B335. Although COM lines are not as bright as those in B335, 7 lines of 4 COM species in addition to CH_3OH are detected in this source. We used the 10 σ confidence level in the integrated intensity for the detection threshold, while lines whose integrated intensities are between 5 σ and 10 σ are noted as tentative detections. Here, σ is the error of the integrated intensity calculated from the rms noise. The detected lines are listed in Table 7.2. The detected species are CH_3CHO, CH_3OCH_3, NH_2CHO, and HCOOH, although the detection of CH_3CHO, NH_2CHO, and HCOOH are tentative. Among the 9 species of COMs and their related species detected in B335, $HCOOCH_3$, CH_3COCH_3, HNCO, C_2H_5OH, and C_2H_5CN are not detected in CB68. Here, we refer to organic molecules containing at least six atoms as COMs, and HCOOH and HNCO as COM related molecules in this chapter. The moment 0 maps of COMs are shown in Figure 7.6. Overall, their integrated intensities are weak, and detection is marginal just above the criteria for tentative detection (5 σ). Their distributions are compact around the protostar and their emission is not resolved with the synthesized beam ($\sim$ 0.″4-0.″5; $\sim$70-80 au).

7.3.2 COM abundance

First, the column density and the rotation temperature of CH_3OH at the continuum peak are derived by the rotation diagram analysis (Figure 7.7). The lines used for the derivation are listed in Table 7.1. Since the line shape of the CH_3OH line is slightly different between that observed at the high velocity resolution and that observed at the low velocity resolution, only the lines for low velocity resolution are used. The rotation temperature and the column density are derived to be 133 ± 14 K and $(4.56 \pm 0.04) \times 10^{16}$ cm^{-2}, respectively.

The beam-averaged column densities of the detected COMs and their related molecules except for CH_3OH are derived by using the following equation (Chapter 2):

$$N(\mathrm{X}) = U(T)\ \frac{3k_\mathrm{B}W}{8\pi^3\nu S\mu^2} \exp\left(\frac{E_\mathrm{u}}{k_\mathrm{B}T}\right), \tag{7.1}$$

where $U(T)$ denotes the partition function of the molecules at the excitation temperature T, W is the integrated intensity, ν is the frequency of the line, and E_u is the upper state energy. Here, we assume the local thermal equilibrium (LTE) condition. Considering the excitation temperature of CH_3OH line (133 K), the excitation temperature T is assumed to be 133 K. This temperature is comparable to a typical excitation temperature for COMs in the hot corino sources (Richard et al. 2013; Jaber et al. 2014; Oya et al. 2016; Chapter 5; Imai et al. 2016). An error of the integrated intensity W_err is calculated by using the rms noise σ_rms as:

$$W_\mathrm{err} = \sigma_\mathrm{rms} \times \sqrt{\Delta v_\mathrm{int} \times \Delta v_\mathrm{res}}, \tag{7.2}$$

where Δv_int and Δv_res are the velocity width used for integration and the velocity resolution of the observation (0.16-0.20 km s^{-1}), respectively. The errors of the column densities are derived by using W_err. The results are shown in Table 7.3.

We derive the upper limits to the column densities of COMs detected in B335 but not detected in CB68. We use the most intense lines at 100 K, which are included in our frequency

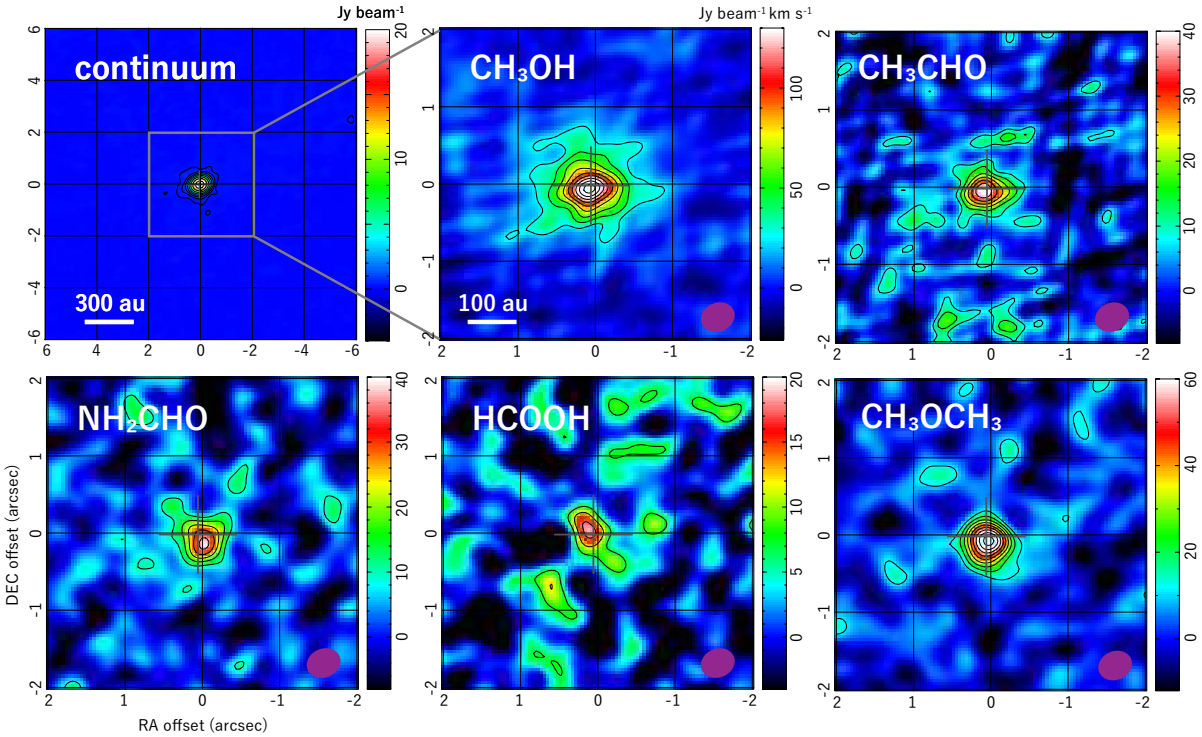

Figure 7.6: The 1.3 mm continuum map and the moment 0 maps of detected COMs (CH_3OH, CH_3CHO, NH_2CHO, HCOOH, and CH_3OCH_3). The gray cross marks represent the protostellar position.

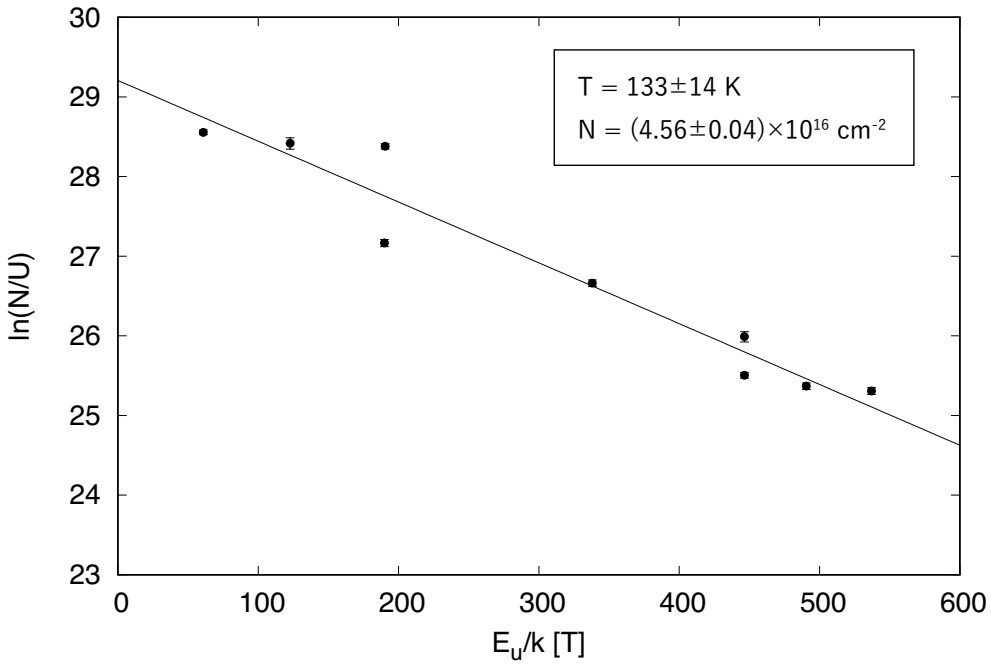

Figure 7.7: The rotation diagram of CH_3OH. Detected lines are marked by points with error bars. A solid line indicates the result of the single temperature fit.

Table 7.1: Parameters of the CH_3OH Lines for Rotation Diagram Analysis.

Molecule	Transition	Frequency[a] GHz	$S\mu^2$[a] Debye^2	E_u[a] cm^{-1}	W mJy beam^{-1} km s^{-1}	I_{peak} mJy beam^{-1}
CH_3OH	10_{-3}-11_{-2}E2	232.945797	12.14	132.31	86(4)	14.9(10)
CH_3OH	18_3^--17_4^-	233.795666	21.87	310.39	48(3)	8.5(10)
CH_3OH	4_2^--5_1^-	234.683370	4.48	132.37	109(4)	18.9(10)
CH_3OH	5_{-4}-6_{-3}E2	234.698519	1.85	85.30	47(3)	7.8(10)
CH_3OH	20_3^--20_2^+	246.074605	78.03	373.26	102(4)	14.1(11)
CH_3OH	19_3^--19_2^+	246.873301	73.68	341.02	103(4)	16.7(11)
CH_3OH	16_2-15_3E1	247.16195	19.32	235.02	99(4)	12.1(11)
CH_3OH	4_2^+-5_1^+	247.228587	4.34	42.34	148(5)	23.3(11)
CH_3OH	18_3^--18_2^+	247.610918	69.43	310.39	112(4)	16.3(11)

[a] Frequencies, $S\mu^2$, and E_u are taken from CDMS.

Table 7.2: Parameters for Analyzed Lines

Molecule	Transition	Frequency GHz	$S\mu^2$ Debye^2	E_u cm^{-1}	W mJy beam^{-1} km s^{-1}	I_{peak}[a] mJy beam^{-1}	v_{center}[b] km s^{-1}
CH_3CHO	$3_{3,1}$-$3_{2,2}$	234.4692610	1.94	17.96	25(3)	6.0(10)	4.01
HCOOH	$11_{2,10}$-$10_{2,9}$	246.1060870	10.56	58.20	12(2)	3.6(11)	6.35
CH_3OCH_3[c]	$11_{1,14}$-$13_{0,13}$EA	258.5487751	29.64	56.25	67(3)	10(3)	–
CH_3OCH_3[c]	$11_{1,14}$-$13_{0,13}$AE	258.5487753	44.46	56.25	67(3)	10(3)	–
CH_3OCH_3[c]	$11_{1,14}$-$13_{0,13}$EE	258.5490190	118.57	56.24	67(3)	10(3)	–
CH_3OCH_3[c]	$11_{1,14}$-$13_{0,13}$AA	258.5492628	74.11	56.24	67(3)	10(3)	–
NH_2CHO	$12_{2,10}$-$11_{2,9}$	260.1898482	488.94	64.19	19(3)	8(3)	5.21

Line parameters are taken from JPL .

[a] Peak intensity of the line.

[b] The velocity center of the lines is calculated to be the weighted average velocity (moment 1), because the lines cannot be fitted by Gaussian function.

[c] These lines are blended with each other. The maximum intensity is calculated as one blended line.

setup but not detected in the observation. An upper limit to the integrated intensity W_{limit} is calculated by using the rms noise σ_{rms} as:

$$W_{limit} = \sigma_{rms} \times \sqrt{\Delta v \times \Delta v_{res}}, \tag{7.3}$$

where Δv and Δv_{res} are the line width and the velocity resolution of the observation, respectively. The line width is assumed to be 3.14 km s^{-1}. This is the average line width of the detected COMs in this observation. The derived upper limit is also listed in Table 7.3.

To reveal the dependence of the derived column densities on the assumed excitation temperature, the column densities are also calculated for the excitation temperature of 100 K and 150 K. The dependence of the column density on the excitation temperature is within a factor of 2 for the above temperature range. These results are also given in Table 7.3.

To derive the fractional abundances relative to H_2, the beam-averaged H_2 column density is estimated from the continuum flux by using Equation 5.1 in Chapter 5. The mass absorption coefficient employed here is the same as that used for B335 (0.0068 cm^2 g^{-1}) (Chapter 5; Imai et al. 2016). The column density of H_2 is derived to be $(2.42 \pm 0.12) \times 10^{24}$ cm^{-2} for the dust temperature of 133 K. It is $(3.26 \pm 0.16) \times 10^{24}$ cm^{-2} and $(2.13 \pm 0.11) \times 10^{24}$ cm^{-2} for the dust temperature of 100 K and 150 K, respectively. The dust temperature is simply assumed to be 133 K for the derivation of the fractional abundances of molecules.

The fractional abundances of COMs and their related species relative to H_2 are compared with those of B335 in Table 7.4. The abundance of CH_3CHO is higher than that in B335, while HCOOH, CH_3OCH_3, and NH_2CHO is less abundant in CB68 by about a factor of 4-20. $HCOOCH_3$ and C_2H5OH are less abundant in CB68 than B335, while the upper limits

Table 7.3: Column Densities of COMs

Molecule	Column Density[a]/ 10^{14} cm^{-2}		
	T =100 K	T=133 K	T =150 K
CH_3OH[a]	...	456(4)	...
CH_3CHO	88(9)	140(15)	178(18)
HCOOH	1.6(3)	1.8(4)	2.0(4)
CH_3OCH_3	10.6(5)	12.9(6)	14.2(7)
NH_2CHO	0.31(4)	0.36(5)	0.39(6)
non-detected molecules			
$HCOOCH_3$[b]	< 14	< 21	< 25
CH_3COCH_3[b]	< 13	< 14	< 16
C_2H_5OH[b]	< 2.8	< 3.8	< 4.3
C_2H_5CN[b]	< 290	< 410	< 480

[a] The column density is derived by the rotation diagram analysis. The rotation temperature is derived to be 133 ± 14 K.
[b] Upper limit to the column densities are derived for non-detected molecules.

to the abundances of CH_3COCH_3 and C_2H_5CN in CB68 are not lower than B335. Thus, the composition of COMs is different from B335. Nevertheless, the existence of several COMs in the hot region around the protostar suggests that CB68 should harbor a hot corino.

7.3.3 Envelope Kinematics

Figure 7.8 shows the position velocity (PV) diagrams of the $C^{18}O$, CH_3OH, and OCS along the position angle of 230° (shown in dashed line in Figure 7.6). This direction is perpendicular to the outflow direction observed with the ^{12}CO line (Vallee et al. 2000). The zero offset of the position axis denotes the protostellar position. A diamond shape structure and a marginal velocity gradient can be confirmed for the $C^{18}O$ line. The diamond shape structure is a typical feature of the infalling-rotating envelope (Chapter 4). Hence, we set this direction as the disk/envelope direction in this Chapter. The PV diagram of $C^{18}O$ has a counter velocity component so that the kinematic structure is difficult to be explained by a Keplerian motion. To compare the kinematic structures of the above molecules, the combined PV image is prepared, where the PV diagrams of $C^{18}O$, CH_3OH, and OCS are overlaid in the same panel (Figure 7.9). Although the distributions of CH_3OH and OCS are not well resolved, the kinematic structure of CH_3OH looks similar to that of OCS. Since $C^{18}O$ emission also has the component similar to that observed for CH_3OH and OCS, CH_3OH and OCS most likely trace only the inner part of the envelope. In contrast, $C^{18}O$ seems to trace an entire envelope.

We try to fit the kinematic structures of $C^{18}O$, CH_3OH, and OCS with the model of infalling-rotating envelope (Chapter 4). This model has been successfully applied for the 10 to a few 100 au scale envelope structures of the low-mass protostellar sources (e.g., Sakai et al. (2014); Oya et al. 2016; Oya et al. 2017a; Imai et al. 2019; Imai et al. in prep). The fitting is conducted with the following four free parameters: (1) the radius of the centrifugal barrier ($r_{\rm CB}$), (2) the mass of the central protostar (M_*), (3) the outer radius of the emitting region in the envelope (R_0), and (4) the full thickness of the envelope (h_0). $r_{\rm CB}$ and M_* are the physical parameters specific to the source and independent of the molecular distributions. We assume the flare angle of the envelope of 10° and the inclination angle of 70° (nearly edge-on disk). We confirm that the result does not significantly change for the flare angle of between 0° and 30° and the inclination

Table 7.4: COM Abundances in CB68 and B335

Molecule	CB68 Fractional Abundance[a] /10^{-10}	B335 Fractional Abundance[b,c] /10^{-10}
CH_3CHO	58(7)	14(2)
HCOOH	0.75(16)	28(3)
CH_3OCH_3	5.3(4)	20(2)
NH_2CHO	0.15(2)	2.6(2)
	non-detected molecules	
$HCOOCH_3$	< 8.7	28(3)
CH_3COCH_3	< 5.8	5.0(5)
C_2H_5OH	< 1.6	23(3)
C_2H_5CN	< 170	1.02(16)

[a] Fractional abundance relative to H_2 derived by assuming the excitation temperature and the dust temperature of 133 K.
[b] Fractional abundance relative to H_2 derived by assuming the excitation temperature and the dust temperature of 100 K.
[c] Chapter 5 (Imai et al. 2016).

angle of between 50° and 90°. The dependence on the flare angle and the inclination angle will be discussed in Section 7.3.4. The left panel of Figure 7.10 shows the result of the model calculation overlaid on the PV diagram of $C^{18}O$. The velocity structure including the counter velocity component seems to be reproduced with the following parameters: (1) r_{CB} of 2 au, (2) M_* of 0.15, (3) R_{out} of 600 au, (4) h_0 of 100 au. We set these values as the fiducial values, and discuss their errors in the following sections. The right panel of Figure 7.10 shows the result of the model calculation overlaid on the combined PV image. The kinematic structures of the CH_3OH and OCS are also explained by the model.

7.3.4 Evaluation of the Model Parameters

To evaluate the model similarity, we apply the comparison method described in Chapter 4 by using the $C^{18}O$, CH_3OH, and OCS lines. In this case, the signal detection probability for pixel i is derived as:

$$p_i = \max(p_{i,\mathrm{mol}})\Big|_{\mathrm{mol}=C^{18}O,CH_3OH,OCS}. \tag{7.4}$$

Here, $p_{i,\mathrm{mol}}$ is calculated by using the sigmoid function as:

$$p_{i,\mathrm{mol}} = \mathrm{sig}(I_{i,\mathrm{mol}}; I_{\mathrm{thres}}, b) = \frac{1}{1+\exp(-\frac{I_{i,\mathrm{mol}}-I_{\mathrm{thres}}}{b\times I_{\mathrm{thres}}})}, \tag{7.5}$$

where I_{thres} and b are set to be 30 % of the intensity peak for each molecule and 0.2, respectively. The signal detection probability for pixel i for the model image (q_i) is derived as:

$$p_{i,\mathrm{mol}} = \mathrm{sig}(I_{i,\mathrm{model}}; I_{\mathrm{thres}}, b) = \frac{1}{1+\exp(-\frac{I_{i,\mathrm{model}}-I_{\mathrm{thres}}}{b\times I_{\mathrm{thres}}})}. \tag{7.6}$$

We use the same values of I_{thres} for the observation and the model and b as those used in the analysis of B335 (Chapter 6). As in the case of B335 (Chapter 6), the dependence of the following result on I_{thres} and b is discussed later in this Section.

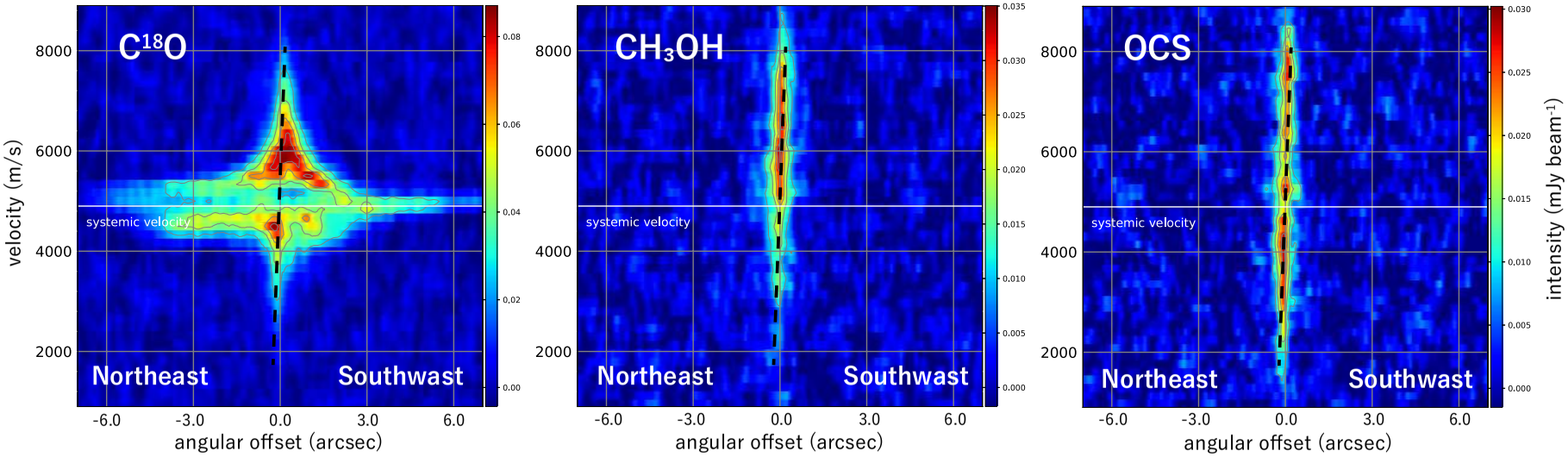

Figure 7.8: The PV diagrams of the $C^{18}O$, CH_3OH, and OCS along the envelope direction (shown in dashed line in Figure 7.3). The contours represent 30, 50, 70, and 90 % of the intensity peak.

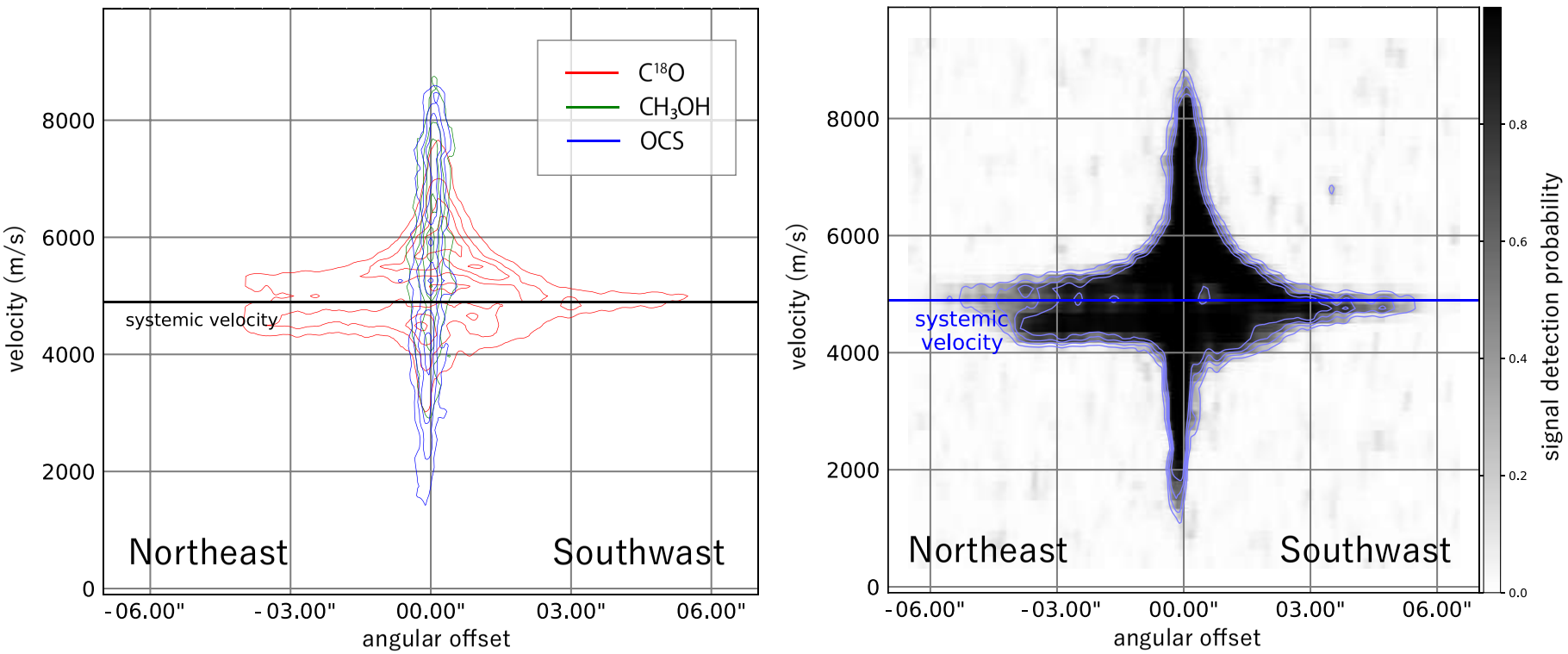

Figure 7.9: (*left*)The combined PV image of the $C^{18}O$ (red), CH_3OH (green), and OCS (blue) emissions. The contours represent 30, 50, 70, and 90 % of the intensity peak. (*right*) The probability distribution (p_i) calculated by using the sigmoid function to the combined PV diagram. It is confirmed that the probability distribution reasonably depicts the outline of the combined PV diagram. The contours represent the signal probability of 0.2, 0.4, 0.6, and 0.8.

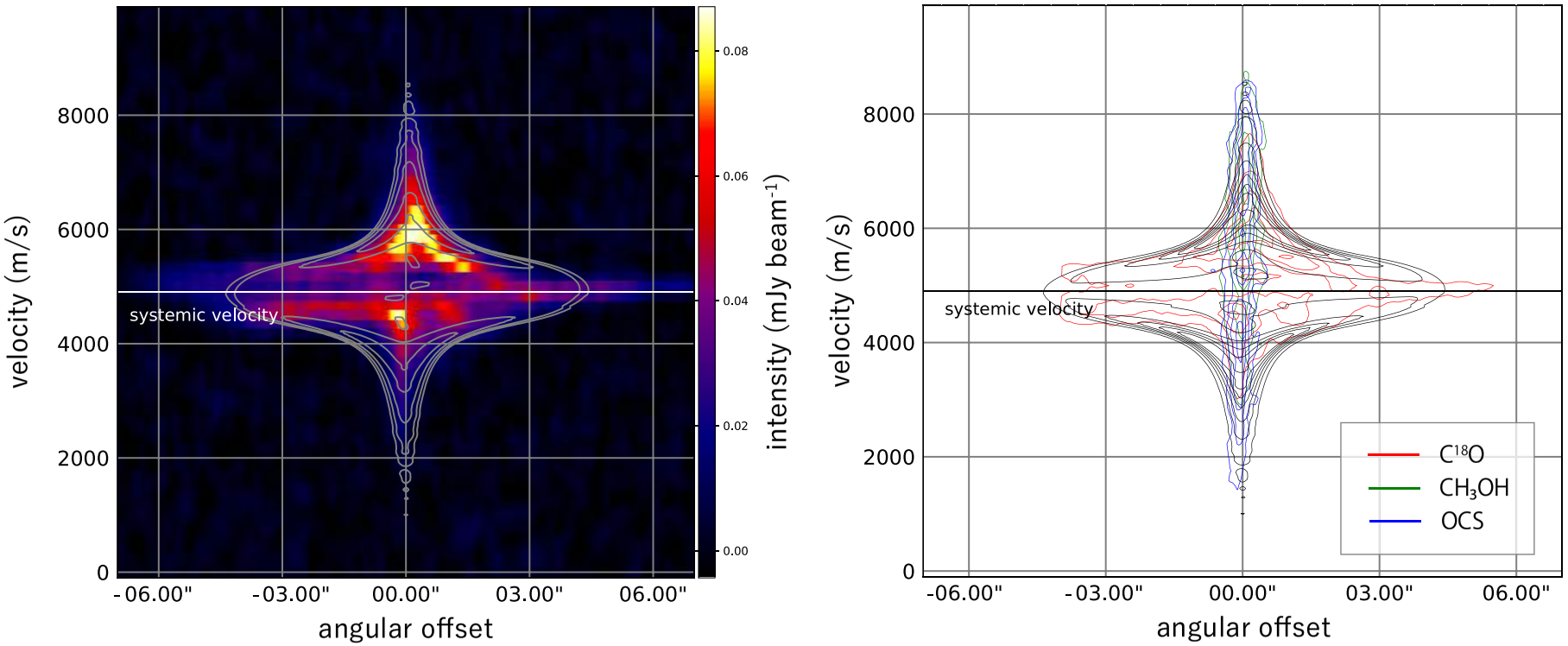

Figure 7.10: (*left*) The PV diagram of $C^{18}O$ overlaid with the IRE model. The contours of the model (gray) represent 10, 35, 50, 65, 80 and 95 % of the intensity peak. (*right*) The PV diagrams of $C^{18}O$, CH_3OH, and OCS overlaid with the IRE model. The contour levels for the model (gray) are the same as the left panel. The red, green, and blue contours represent the PV diagrams for $C^{18}O$, CH_3OH, and OCS, respectively. The contours of the observed PV diagrams (red, green, and blue) represent 30, 50, 70, and 90 % of the intensity peak.

The ranges of the PV image used for the analysis are $\pm 6\farcs5$ from the continuum peak position along the envelope direction (P.A. = 290°) for the position axis and ± 4.5 km s^{-1} from the systemic velocity (4.9 km s^{-1}) for the velocity axis. The pixel spacing for the position axis is set to $0\farcs040$ which is roughly ten times smaller than the beam size. The pixel spacing for the velocity axis is 167.5 m s^{-1}, which corresponds to the velocity resolution of the observation. The PV image is recalculated from the data cube by interpolating the neighboring pixels both for the observation and the model. In total, the images contain 17604 pixels each. The signal detection probability for each pixel is calculated by applying the sigmoid function. Similarly, the signal detection probability for the model is also calculated. Using these probability distributions, we calculate the $KL(p, q)$ for the model of the observation.

Figure 7.11 represents the IRE model results for variations of the model parameters: $r_{\rm CB}$, $R_{\rm out}$, and M_*. The parameter variations are 1, 2, and 50 au for $r_{\rm CB}$, 0.02, 0.15, and 0.75 $M_\odot$ for M_*, and 400, 600, 1200 au for $R_{\rm out}$. The KL divergence for each model is also shown on top right of each panel in Figure 7.11. The middle panels show the results for fiducial one (Section 7.3.3). In the eye-based fitting, the result for $r_{\rm CB}$ of 1 and 2 au seems better than that for 50 au. This is consistent with the result of the KL divergence. Actually, $KL(p, q)$ for $r_{\rm CB}$ of 1 and 2 au are smaller than that for 50 au. The result of the variations for the other parameters are also consistent with the goodness of the fit judged by eye. Thus, the KL divergence can provide a quantitative evaluation of the goodness of the fit in this case.

The KL divergence derived for the variation of the four free parameters is summarized in Figure 7.12. As for the $r_{\rm CB}$, the KL divergence becomes the lowest around $r_{\rm CB}$ of < 10 and becomes larger as the $r_{\rm CB}$ increases from 30 au. This suggests that only the upper limit to the radius of the centrifugal barrier can be determined. This is reasonable, because the beam size of the observation is 70-80 au. The KL divergence for the variation of M_* is also shown in the upper right panel of Figure 8.10. In this case, the value becomes the smallest around the mass of 0.15 $M_\odot$. The value increases rapidly as the mass decreases from 0.1 $M_\odot$, while the increase is more gentle for the mass larger than 0.3 $M_\odot$. As for $R_{\rm out}$, the KL divergence becomes the smallest for $R_{\rm out}$ of ~ 600 au. The change in the KL divergence is not prominent for the variation of the thickness h_0, because we only fit the PV diagram along the direction of the envelope.

The KL divergence has an uncertainty due to the noise of the observation. We evaluate this effect by calculating the similarity of the mock PV images based on the observation with and without the noise component (see Section 4.2.2 for detail), as in the case of B335 described in Section 6.3.3. By using the method, the tolerance range of the KL divergence is estimated to be 0.12 above the minimum value of the $KL(p, q)$ (see Appendix A).

Using the above tolerance range of the KL divergence, the uncertainties of the optimized parameters are evaluated. The tolerance range is shown by the gray range in Figure 7.12. The protostellar mass and the radius of the centrifugal barrier are thus evaluated to be $0.15^{+0.15}_{-0.07}$ $M_\odot$ and < 30 au, respectively.

Here, we note the result for the variation of the inclination angle (Figure 7.12). It is confirmed that the similarity index does not significantly change for the inclination angle from 50° to 90°. On the other hand, the KL divergence slightly increases as the inclination angle decreases below 50°, although its difference is within the uncertainty. This result suggests that the source would have an edge-on disk configuration rather than a face-on one. However, the precise inclination angle cannot be determined from this analysis. It should be noted that the inclination angle does not significantly affect the optimization of the other free parameters. It is also confirmed that the flare angle of the envelope has little effect on the similarity index (Figure 7.12).

Finally, we show the dependence of the $KL(p, q)$ on the variation of $I_{\rm thres}$ and b. In the present analysis, we set the $I_{\rm thres}$ of 30 % for the observation data, 10 % for the model data, and

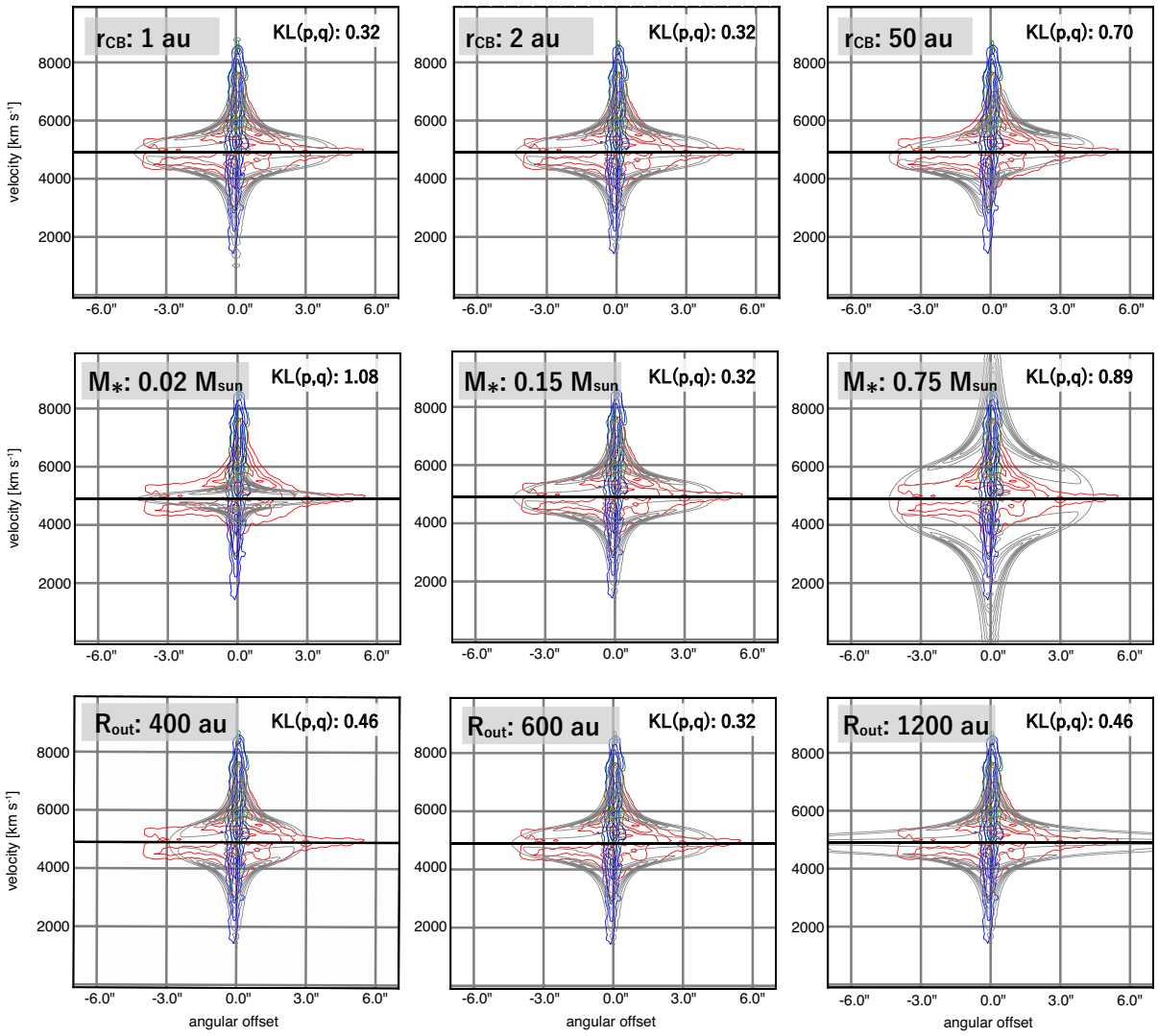

Figure 7.11: The comparison with the model (gray) and combined PV image of $C^{18}O$ (red), CH_3OH (green), and OCS(blue). The parameters are 1, 2, 50 au for $r_{\rm CB}$, 0.02, 0.15, and 0.75 $M_\odot$ for M_*, and 400, 600, and 1200 au for $R_{\rm out}$. The results for the fiducial values are shown in the middle panels. The KL divergence is shown on the top right corner. The contours for the model represent 10, 25, 40, 55, 70, and 85 % of the peak, while those for the molecules represent 30, 50, 70, and 90 % of the peak.

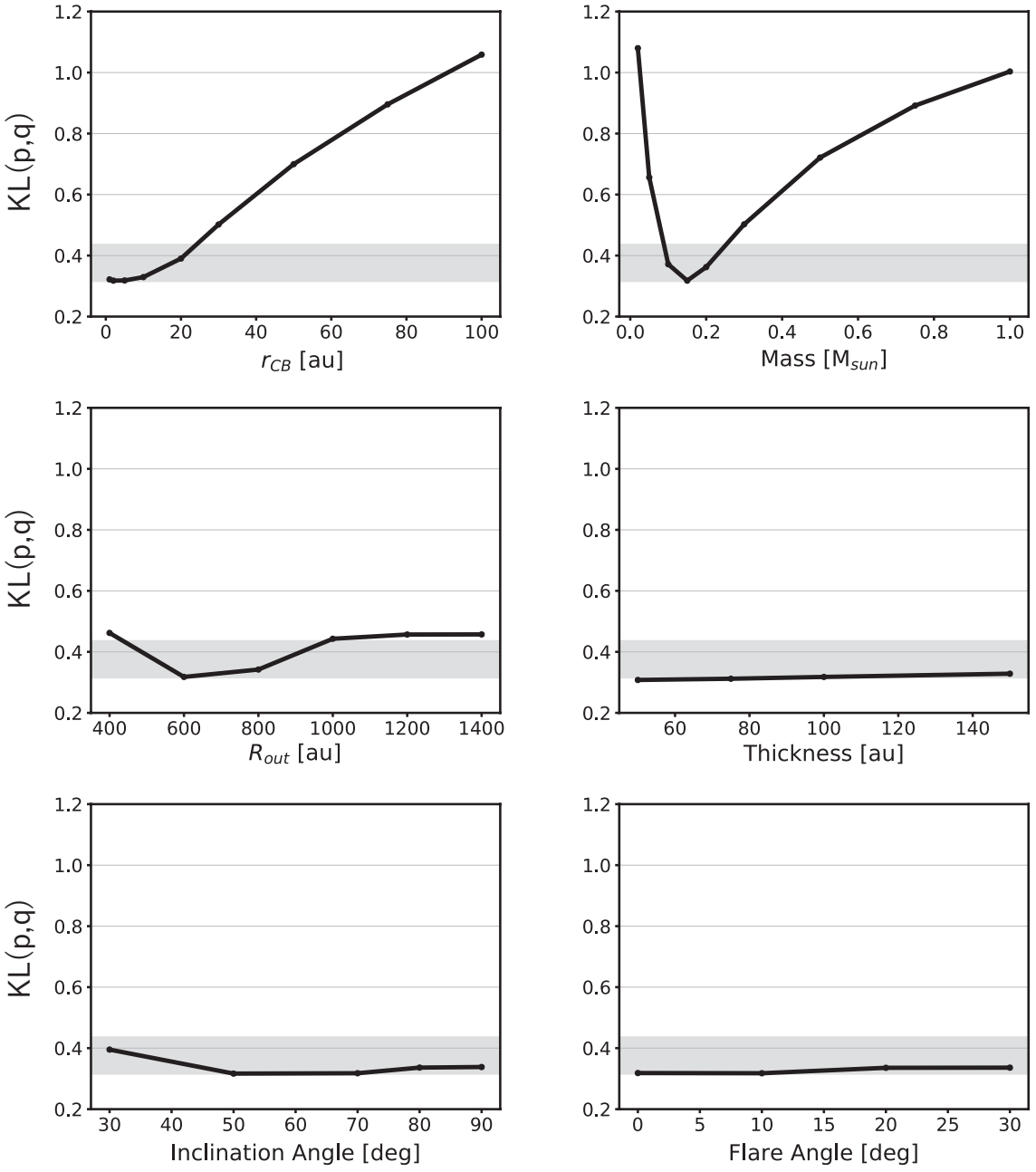

Figure 7.12: The result of KL divergence with the variations of the radius of centrifugal barrier, the mass of the protostar, the outer radius of the emitting region, the thickness of the emitting region, the inclination angle, and the flare angle. The gray area indicates the uncertainty for the KL divergence due to the observation noise.

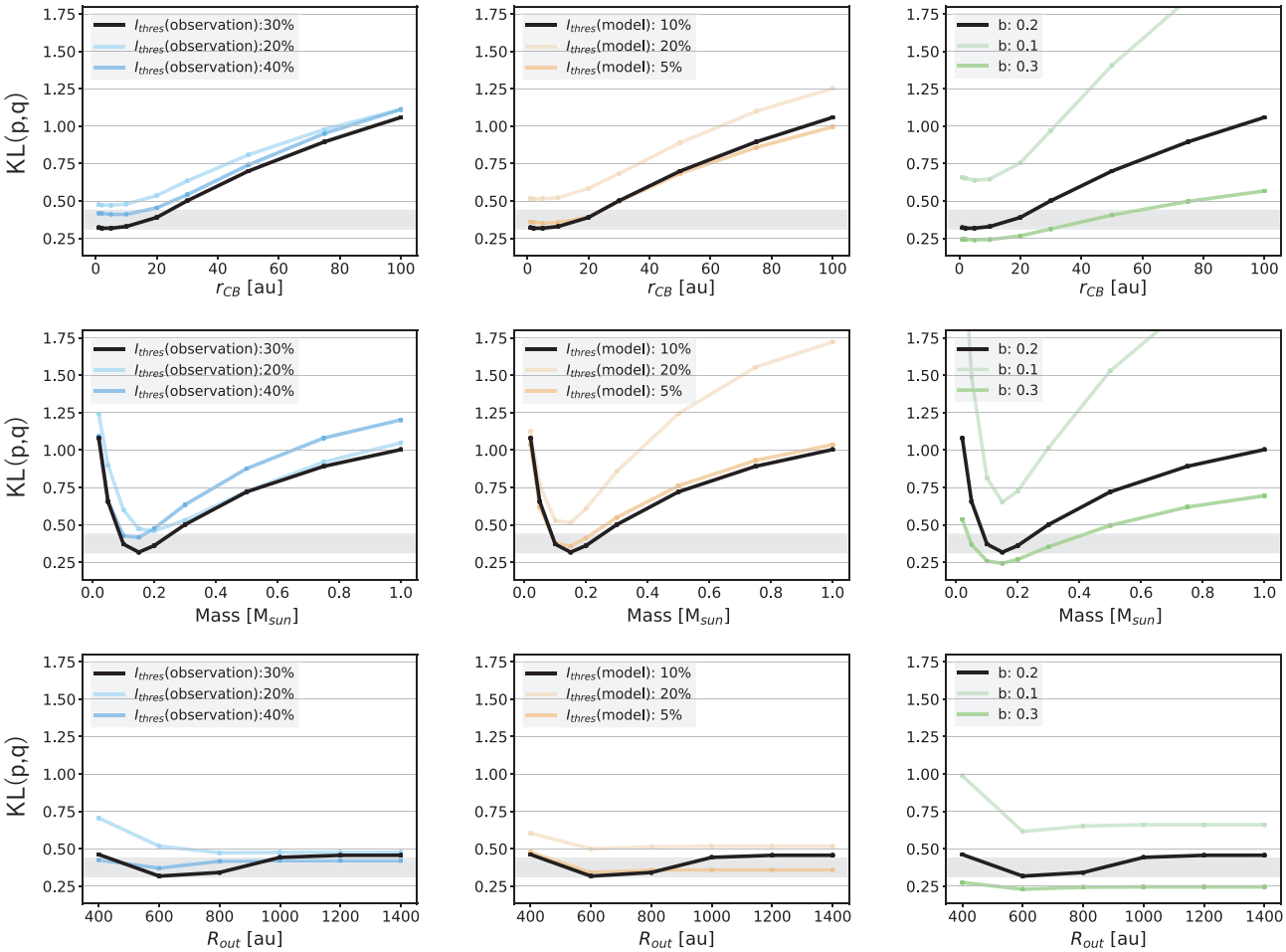

Figure 7.13: Examples of the dependence of the KL divergence on $I_{\rm thres}$ for the observation data (left column panels), $I_{\rm thres}$ for the model data (middle column panels), b coefficient of sigmoid function (right column panels). The values used for the analysis in this thesis are shown in black ($I_{\rm thres}$(observation)=30 %, $I_{\rm thres}$(model)=10 %, b=0.2). The results for $r_{\rm CB}$, M_*, and Rout are shown in the upper, middle, and bottom panels, respectively.

b of 0.2. We change these values and see how the result changes in Figure 7.13. The following cases are investigated: $I_{\rm thres}$ for the observation data of 20 % and 40 %, $I_{\rm thres}$ for the model data of 5 % and 20 %, and b of 0.1 and 0.3. Here, only one of $I_{\rm thres}$ for the model and the observation and b is changed, while the others are remained to be unchanged. Overall, the basic shape of the dependence along with the parameters giving the minimum values does not significantly change within the above ranges.

7.3.5 Summary

The 1.2 and 1.3 mm band observations of CB68 were conducted with ALMA to characterize the chemical and physical structures of the protostellar envelope. The main results are summarized below.

1. Carbon-chain molecules CCH and c-C_3H_2 are detected in the envelope at a scale of 1000 au. Thus, CB68 reveals WCCC on a scale of 1000 au. Although their emissions are elongated to the the outflow direction, only the north component of the outflow is traced by CCH, and the structure of the outflow cavity is not clearly seen for c-C_3H_2.

2. Several saturated organic molecules (COMs) are detected in the vicinity of the protostar on a scale less than the beam size (∼70-80 au). The rotation temperature of CH_3OH is derived to be 133 ± 14 K by the rotation diagram analysis. The fractional abundances of COMs relative to H_2 are less abundant than those of B335 except for the CH_3CHO. The existence of COMs near the protostar indicates that CB68 harbors hot corino.

3. The hybrid type chemical characteristics (hot corino chemistry and WCCC) is confirmed in the protostellar envelope in CB68. This resembles the case of B335.

4. The whole envelope structure is traced by $C^{18}O$, while only the innermost part of the envelope is traced by CH_3OH and OCS. These molecules show a marginal velocity gradient perpendicular to the outflow (disk/envelope direction). The position velocity diagram along the disk/envelope direction is well explained by the infalling-rotating envelope model. The protostellar mass and the radius of the centrifugal barrier are estimated to be $0.15^{+0.15}_{-0.07}$ $M_\odot$ and < 30 au, respectively.

Chapter 8

Physical and Chemical Structures of CB244

In this chapter, chemical and physical structures of the envelope of the low-mass Class 0/I protostar IRAS 23238+7401 in the Bok globule CB244 are presented. This is based on our NOEMA observations in the 1.2 mm band at a linear spatial resolution of 100 au. This source is found to be deficient in molecular lines, and only 11 lines of 8 molecular species are detected in the bandwidth of 4 GHz. No saturated complex organic molecule (COM) except for CH_3OH is detected, while carbon-chain molecules are detected in the envelope. Thus, warm carbon-chain chemistry (WCCC) is seen in this source, while hot corino chemistry is not evident. The chemical characteristics of CB244 seems different from that of the other isolated sources B335 and CB68 showing both WCCC and hot corino chemistry. This result suggests that the chemical properties are different among the isolated sources. In CB244, the main tracers of the envelope are CS, SO, and $H^{13}CO^+$. Although their distributions are different from one another, concatenation of their kinematic structures provides the kinematic structure of the infalling-rotating envelope. From the rotating motion of the envelope, the protostellar mass and the radius of the centrifugal barrier are estimated to be $0.4^{+0.6}_{-0.2}$ $M_\odot$ and < 300 au by the infalling-rotating envelope model.

8.1 Introduction

CB244 is a Bok globule with an approximate extent of about 0.46 pc and is in a relatively isolated condition (Figure 8.1). It harbors the Class 0/I low-mass protostar IRAS 23238+7401 whose bolometric temperature is 62 K (Stutz et al. 2010). It also accompanies a starless core separated from the protostar by 90″ ($\sim$ 18000 au) (Figure 8.1). However, no influences from other protostars (e.g. UV radiation and the outflow) are recognized. The protostar has a bolometric luminosity of 1.5 $L_\odot$ (Stutz et al. 2010), and drives a bipolar molecular outflow (Terebey et al. 1989; Yun et al. 1994). Yun et al. (1994) reported the moderately collimated outflow along the position angle of 225° in the ^{12}CO (J=1−0) line (Figure 8.2). Since this source is in the northern hemisphere and is relatively close to the Sun (200 pc: Hilton et al. 1995) compared with the other isolated sources, a 100 au scale structure can be investigated with the Nothern Extended Millimeter Array (NOEMA) interferometer. Among the list of Bok globules summarized by Launhardt et al. (2010), this is only one source with isolated morphology which is located within 200 pc and observable with the NOEMA interferometer. No interferometric observations have been reported for this source so far, and hence, its detailed chemical and physical structures are little understood.

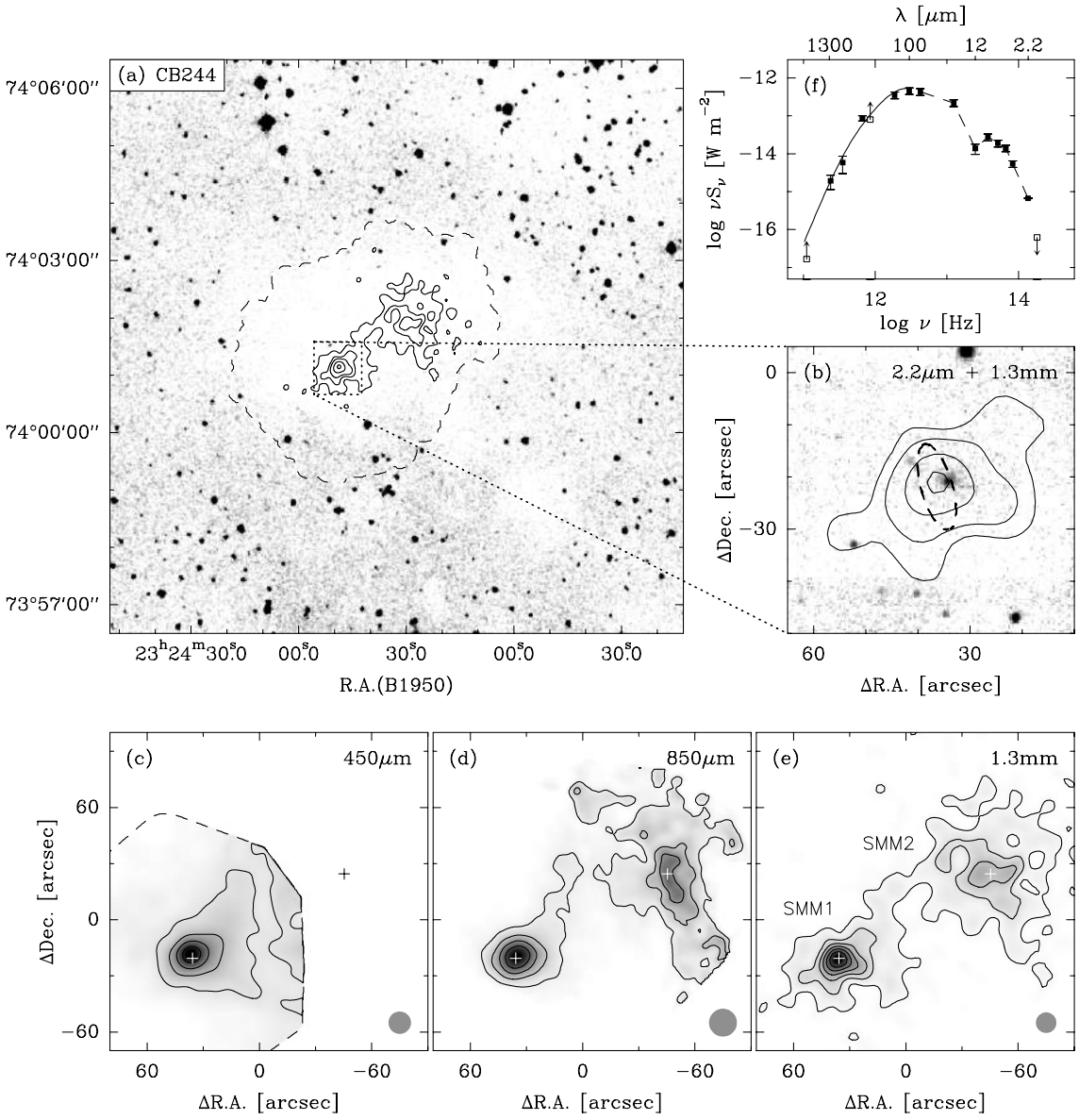

Figure 8.1: Images of CB244 (Launhardt et al. 2010). (a) Optical image overlaid with contours of the 1.3 mm dust continuum emission. (b) Near infrared K-band image with the 1.3 mm dust continuum contours. The IRAS source position is marked by a dashed ellipse. (c) The 450 μ dust continuum emission. (d) The 850 μm dust continuum emission. (e) The 1.3 mm dust continuum emission. (f) SED of the protostellar core.

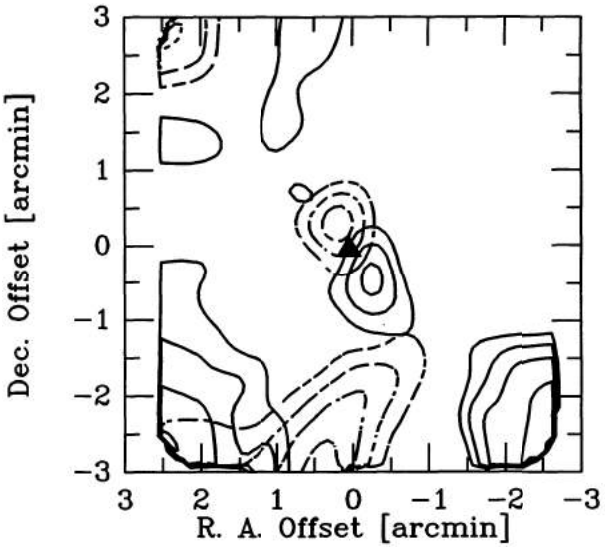

Figure 8.2: Contour plot of the blueshifted (solid lines) and redshifted (dashed lines) components of the ^{12}CO (J=1-0) line emission (Yun et al. 1994). A moderately collimated outflow can be seen with the position angle of 225°.

8.2 Observation

The 1.2 mm (247 GHz) observation toward CB244 was conducted with NOEMA on 2019 January 21−March 5. In total, 10 antennas were used in the observation. The field center is (α_{2000}, δ_{2000}) = ($23^{\rm h}25^{\rm m}46\overset{\rm s}{.}30$, 74°17′39″.10). Minimum and maximum baselines are 26 kλ and 630 kλ, respectively. The half-power beam size is 50″, and the synthesized beam size is 0″.65 × 0″.50 (P.A. = 91°). As for the correlator mode, 4 low-resolution basebands are used whose spectral resolution and band width are 2.0 MHz and 15 GHz, respectively. Twenty-five high-resolution spectral windows are also used whose spectral resolution and total band width are 62.5 kHz and 4.0 GHz, respectively. The frequency ranges of the basebands are 243.0-250.5 GHz and 258.5-266.0 GHz. The spectral windows are implemented in these frequency ranges. The channel spacing of the high-resolution spectral windows corresponds to a velocity resolution of 76 m s^{-1}. On-source integration time was 10.2 hours, which resulted in the rms noise ($\sigma_{\rm spw}$) of 8 mJy beam^{-1} at a nominal channel width for the high-resolution spectral windows (76 m s^{-1}). MWC349 and 0016+731 were observed as a flux calibrator, while 0016+731 and J0011+707 were observed as a phase and bandpass calibrator, respectively. The flux calibration accuracy is about 10 %.

ASTRO, a GILDAS package developed by IRAM, was used for data reduction and imaging. A continuum image was prepared by averaging line-free channels for each base band. Maps of the spectral line emissions in high-resolution spectral windows were obtained by CLEANing the dirty images after subtracting the continuum directly from the visibility data. Self-calibration was not applied for simplicity.

8.3 Results

8.3.1 Distributions

Figure 8.3 (upper-left) shows the 1.2 mm continuum map. The peak position is determined by the Gaussian fit as: (α_{2000}, δ_{2000}) = ($23^{\rm h}25^{\rm m}46\overset{\rm s}{.}656$, 74°17′38″.412). The continuum image shows

slight elongation to the direction of the position angle of 298°± 11°. The integrated flux and peak flux are 59.1±4.0 mJy and 26.9±1.3 mJy beam^{-1}, respectively. The peak intensity corresponds to the brightness temperature of 1.79±0.07 K, indicating that the dust is not optically very thick at the present resolution. Therefore the effect of the dust opacity is assumed to be negligible for the molecular line emissions in the following analyses and discussions.

The beam averaged spectra toward the protostellar position are shown in Figure 8.4. The molecular emission is not necessarily concentrated around the protostar in this source, and hence, we cannot determine the criteria of the detection by the spectra taken toward the protostellar position. Instead, we use the peak integrated intensity in the moment 0 map (Figure 8.3) as the criteria of the detection. The peak integrated intensity of 10 σ is used for the detection threshold, while lines whose peak integrated intensity is between 5 σ and 10 σ is represented as tentative detection. In total, 11 molecular lines of 8 species (CS, SO, $H^{13}CO^+$, CCH, HCN, c-C_3H_2, SiO, and CH_3OH) are detected or tentatively detected, as listed in Table 8.1. CH_3OH and c-C_3H_2 are the tentatively detected lines. No complex organic molecules (COMs) except for CH_3OH are detected in this source. Hereafter, we refer to organic molecules containing at least six atoms as COMs, while HNCO and HCOOH are called as COM related species in this Chapter.

Overall, the emissions of the detected molecules tend to be elongated to the east-west direction, as shown in the moment 0 maps (Figure 8.3). However, their emitting regions are different from molecule to molecule. For example, SO is concentrated around the protostar, while $H^{13}CO^+$ is extended over about 1000 au from the protostar. Furthermore, the asymmetric distribution with respect to the protostar can be seen for almost all molecular emissions. The west part is generally brighter than the east part. A similar feature can be seen in the continuum emission. The distribution of the continuum emission is slightly elongated to the west direction but not very much to the east direction. These features indicate that the envelope likely lies along the east-west direction, and the gas is more abundant in the west part of the envelope.

8.3.2 Velocity Gradient Revealed by Molecular Emissions

Figure 8.5 shows the PV diagrams of CS, SO, $H^{13}CO^+$, CCH, and HCN along the position angle of 290°. In CS, SO, $H^{13}CO^+$, the emissions are redshifted for the east side, while they are blueshifted for the west side. Thus, a clear velocity gradient is detected for these species. The velocity gradient is the largest along the above position angle. Since this direction is almost consistent with the direction of the continuum elongation (P.A. = 298°), this velocity gradient is most likely interpreted as a rotating motion of the envelope. An arc-like structure is seen in the northeast-southwest direction for CCH (highlighted by white dashed lines in Figure 8.3), which can be regarded as a part of an outflow cavity. In fact, this direction is consistent with the ^{12}CO outflow reported by Yun et al. (1994). This direction is not exactly perpendicular to the direction of the continuum elongation and the velocity gradient. However, we here employ the direction of P.A.=290° as the direction of the envelope based on the continuum elongation and the velocity gradient as the envelope direction, because the whole structure of the outflow cavity is unclear in this source. The envelope direction will be discussed in more detail in Section 8.4.2.

The kinematic structures look different from molecule to molecule. $H^{13}CO^+$ traces the most extended structure and disappears at the inner envelope. SO seems to trace an innermost part of the envelope with the extent of about 400 au (= 2″), while CS seems to trace an intermediate region between them. It should be noted that none of them shows a clear diamond shape structure in the PV diagram which is a typical feature of the infalling-rotating envelope (Chapter 4; Sakai et al. 2014b; Oya et al. 2014). In other words, none of them traces the whole envelope structure. Rather, each molecule would trace a part of the rotating envelope. Since the emission of the east component is weaker than that of the west component, the center position

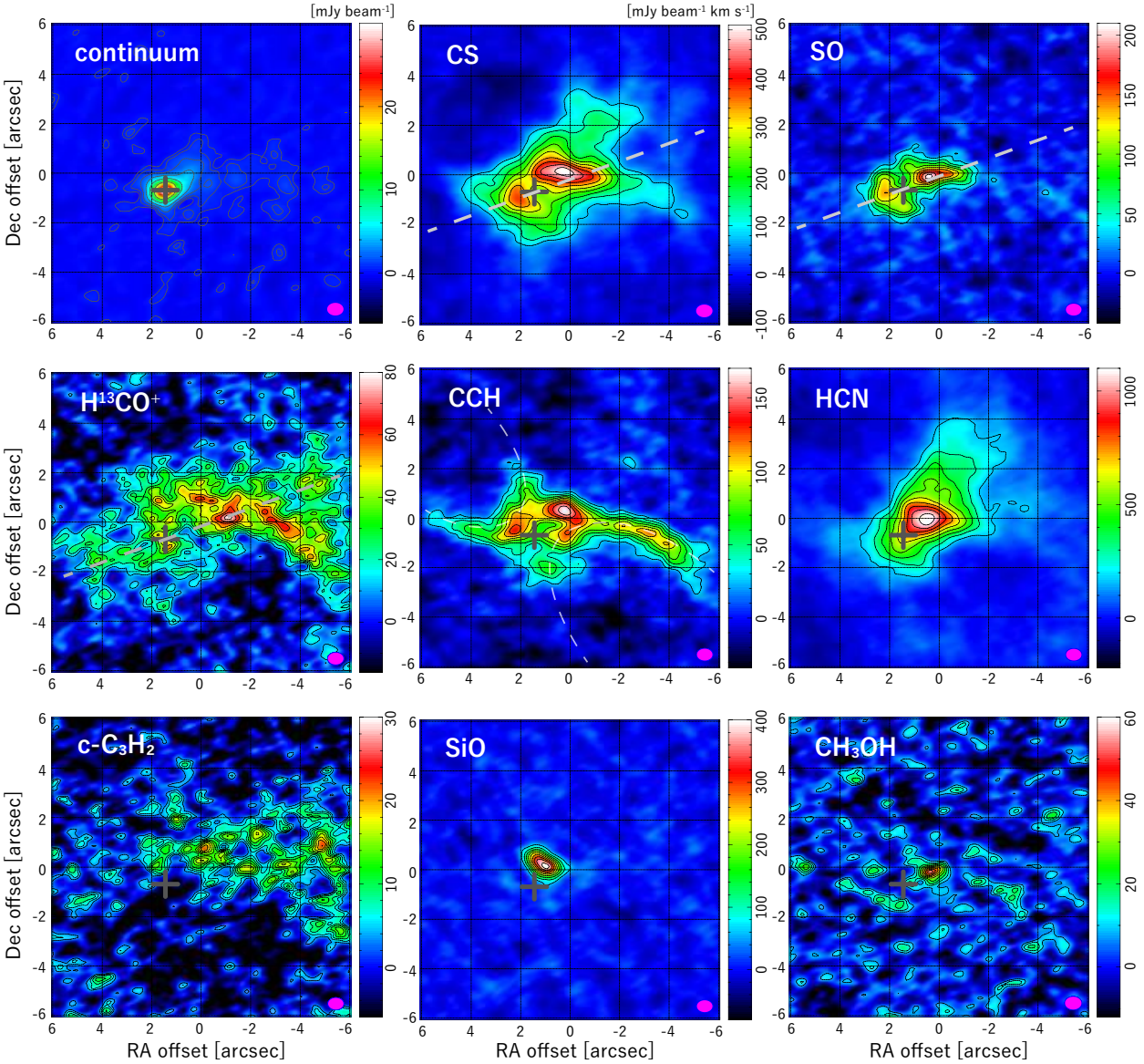

Figure 8.3: Continuum image and the moment 0 maps of SO, $H^{13}CO^+$, CS, HCN, c-C_3H_2, CCH, SiO, and CH_3OH. The cross mark indicates the protostellar position, whereas the origin of the coordinates is the field center of the observation ((α_{2000}, δ_{2000}) = ($23^h25^m46\overset{s}{.}30$, $74°17'39\overset{''}{.}10$)). Dashed lines in the panels of CS, SO, and $H^{13}CO^+$ represents the envelope direction (P.A.=290°). An arc-like structure seen for CCH emission is highlighted by white dashed lines.

of the rotation motion could be different from the protostellar position in the PV diagram. However, the rotation center is assumed to be the protostellar position, because the molecular emission likely traces only a part of the envelope.

8.4 Discussion

8.4.1 Chemical Composition

Only 11 molecular lines of 8 species are detected at the bandwidth of 4 GHz in this observation. Although they are observed with the almost same sensitivity ($\sim$ 5-10 mJy beam^{-1}), the detection rate of the molecular lines is different from that of B335. The rate for CB244 is 2.5 GHz^{-1}, while those for B335 and CB68 are 33 GHz^{-1} and 11 GHz^{-1}, respectively (Chapter 5; Imai et al. 2016 and Chapter 7). Thus, CB244 seems deficient in molecular lines in comparison with B335 and CB68.

Carbon-chain related molecules (CCH and c-C_3H_2) are detected in CB244 as well as B335 and CB68. CCH seems to reside in the relatively inner part of the envelope around the protostar in addition to the outflow cavity, while c-C_3H_2 mainly exists in the extended part of the envelope. Both of them are deficient in the closest vicinity of the protostar. On the other hand, COMs except for CH_3OH are not detected in CB244, while a variety of them are detected in B335.

The upper limits to the beam-averaged column densities of COMs and their related molecules are derived by using the Equation 5.1 in Chapter 5. Here, we assume the local thermal equilibrium (LTE) condition and the excitation temperature T of 100 K. This temperature is a typical excitation temperature for COMs in the hot corino sources (Richard et al. 2013; Jaber et al. 2014; Oya et al. 2016) and is the same as the that employed for the derivation of the COM abundances in B335 (Chapter 5; Imai et al. 2016). We use the most intense lines at 100 K, which are included in our frequency setup but not detected in the observation. An upper limit to the integrated intensity W is calculated by using the rms noise $\sigma_{\rm rms}$ as:

$$W = \sigma_{\rm rms} \times \sqrt{\Delta v \times \Delta v_{\rm res}}, \tag{8.1}$$

where Δv and $\Delta v_{\rm res}$ are the line width and the velocity resolution of the observation, respectively. The line width is assumed to be 4 km s^{-1}. This is equal to the line width of SO, which gives the broadest line in the present observation. This assumption could be justified, because COMs, if exist, would reside in the innermost and hot region around the protostar. $\sigma_{\rm rms}$ and $\Delta v_{\rm res}$ are set to be 1.4 mJy beam^{-1}, and 2.4 km s^{-1}, which is the rms noise and the velocity resolution for the low resolution baseband setup, respectively. The derived upper limits to the column densities are listed in Table 8.2. In order to examine the effect of the assumed excitation temperature, they are also evaluated for the excitation temperature of 50 K and 150 K, which are also listed in Table 8.2.

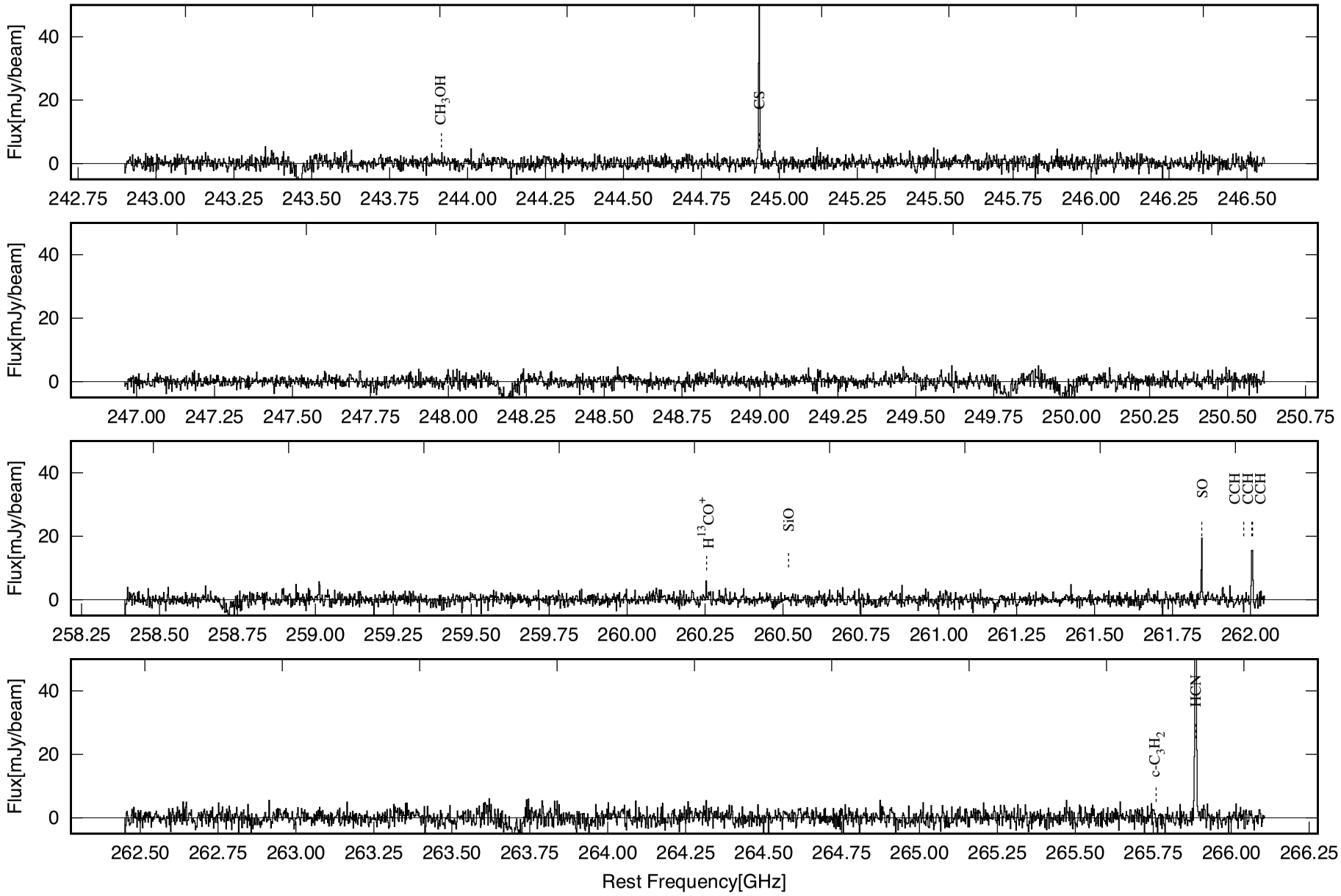

Figure 8.4: The spectrum observed toward the continuum peak ($(\alpha_{2000}, \delta_{2000}) = (23^{\rm h}25^{\rm m}46\overset{\rm s}{.}656, 74°17'38\overset{''}{.}412)$) of CB244 in the 1.2 mm band.

Table 8.1: Parameters for Analyzed Lines

Molecule	Transition	Frequency GHz	$S\mu^2$ Debye^2	E_u cm^{-1}	W_{peak}[a] mJy beam^{-1} km s^{-1}
CH_3OH	$5_{1,4}$-$4_{1,3}$	243.915788	15.5	34.52	54(7)
CS	5,0-4,0	244.935557	19.2	16.34	511(10)
$H^{13}CO^+$	3-2	260.255339	45.6	17.36	79(7)
SiO	6-5	260.518009	57.6	30.42	405(11)
SO	6,7-5,6	261.843721	16.4	24.32	213(10)
CCH[b]	N=3−2,J=7/2−5/2,F=4−3	262.004260	2.3	17.48	166(7)
CCH[b]	N=3−2,J=7/2−5/2,F=3−2	262.006482	1.7	17.48	166(7)
CCH[c]	N=3−2,J=5/2−3/2,F=3−2	262.064986	2.3	17.48	144(11)
CCH[c]	N=3−2,J=5/2−3/2,F=2−1	262.067469	1.7	17.48	144(11)
c-C_3H_2	$4_{4,1}$−$3_{3,0}$	265.759481	89.8	22.39	24(4)
HCN	3-2	265.886434	80.2	17.74	1122(18)

Parameters are taken from CDMS (Muller et al. 2005).

[a] Peak integrated intensity of the line in the moment 0 map. The error is estimated by the rms noise of the moment 0 map.

[b] These lines are blended with each other. The peak integrated intensity represent the sum up of these lines.

[c] These lines are blended with each other. The peak integrated intensity represent the sum up of these lines.

To derive the fractional abundances relative to H_2, the beam-averaged H_2 column density is estimated from the continuum flux by using Equation 5.2 in Chapter 5. The mass absorption coefficient employed here is the same as that used for B335 and CB68 (0.0068 cm^2 g^{-1}) (Shirley et al. 2011). The column density of H_2 is derived to be $(7.0 \pm 0.3) \times 10^{23}$ cm^{-2} for the dust temperature of 100 K. It is $(1.48 \pm 0.07) \times 10^{24}$ cm^{-2} and $(4.6 \pm 0.2) \times 10^{23}$ cm^{-2} for the dust temperature of 50 and 150 K, respectively. The dust temperature is simply assumed to be 100 K for the derivation of the fractional abundances of molecules.

The fractional abundances of COMs and their related species relative to H_2 are compared with those of B335 in Table 8.3. Overall, the upper limits to the COM abundances in CB244 are lower than the abundances in B335. $HCOOCH_3$, CH_3CHO, and HNCO are abundant in B335. The upper limit to these molecules in CB244 is lower than those in B335 by 1-2 orders of magnitude. Although the linear scale of the beam size for CB244 is about twice larger than that for B335, the difference of the abundance by 1-2 orders of magnitude cannot be explained by the beam dilution effect. Thus, COMs are deficient in CB244.

Carbon-chain molecules and their related molecules are regarded as the key molecules of warm carbon-chain chemistry (WCCC) (Sakai et al. 2008; Sakai et al. 2009; Sakai et al. 2010a), while the existence of COMs is regarded as the main feature of the hot corino chemistry Cazaux et al. (2003); Bottinelli et al. (2004), Kuan et al. (2004). Thus, only the WCCC-like feature is confirmed, while hot corino chemistry is not evident in CB244. Such a chemical characteristics are rather similar to that of the WCCC source such as L1527 (Sakai et al. 2008) than the hybrid type source (WCCC and hot corino chemistsry) such as B335 and L483 (Imai et al. 2016; Oya et al. 2017a). This suggests that the chemical characteristics are different even among the isolated sources.

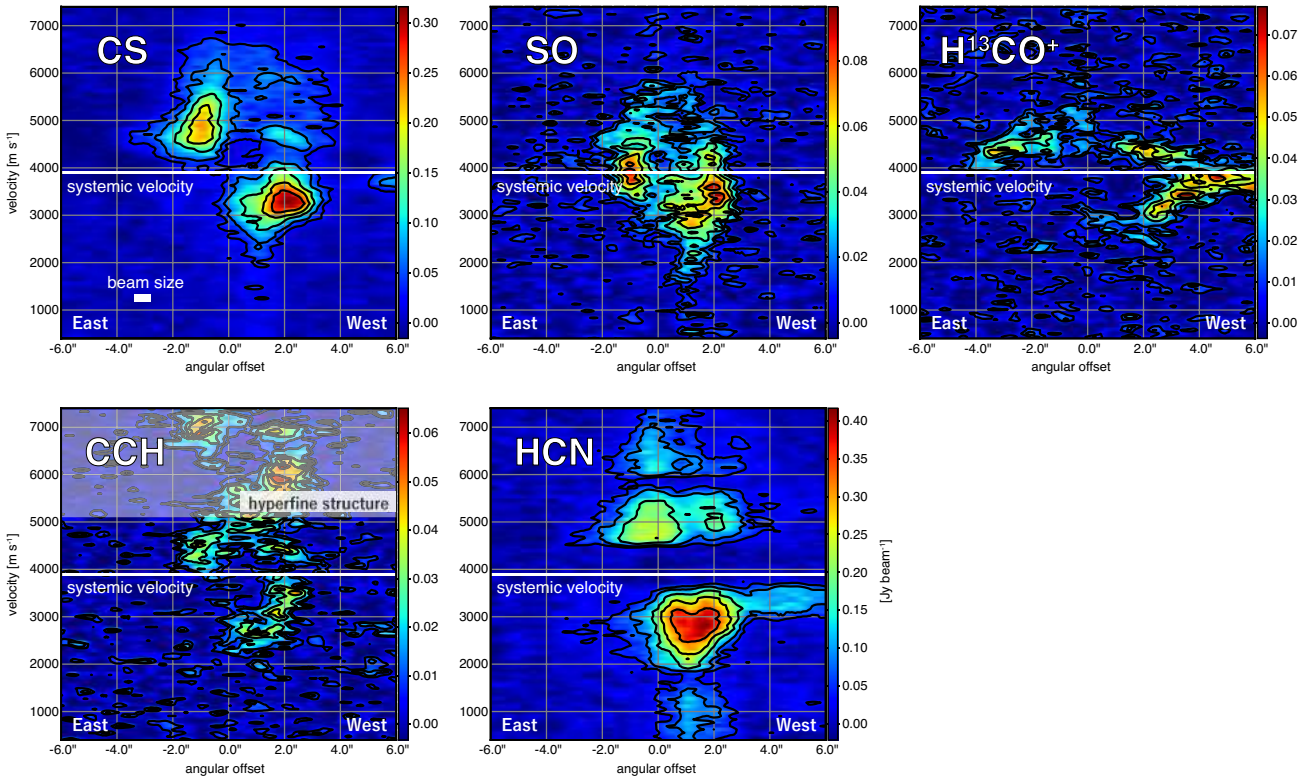

Figure 8.5: PV diagrams of the CS, SO, $H^{13}CO^+$, CCH, and HCN lines along the position angle of 290°. Zero offset represents the protostellar position. A velocity gradient can be seen for CS, SO, $H^{13}CO^+$, and HCN.

Table 8.2: Beam Averaged Column Density of COMs in CB244

Molecule	Column Density / 10^{14} cm^{-2}		
	T =50 K	T =100 K	T =150 K
$HCOOCH_3$	< 2.5	< 2.1	< 2.7
CH_3CHO	< 0.21	< 0.32	< 0.43
NH_2CHO	< 0.054	< 0.072	< 0.095
HNCO	< 0.13	< 0.16	< 0.22
HCOOH	< 0.40	< 0.45	< 0.54
CH_3OCH_3	< 1.6	< 3.3	< 5.4
CH_3COCH_3	< 5.6	< 6.7	< 9.2
C_2H_5OH	< 1.2	< 3.2	< 5.7
C_2H_5CN	< 1.4	< 2.5	< 4.0

Table 8.3: COM Abundances in CB244 and B335

Molecule	CB244 Fractional Abundance[a] $/10^{-10}$	B335 Fractional Abundance[a,b] $/10^{-10}$
$HCOOCH_3$	< 3.0	28(3)
CH_3CHO	< 0.42	14(2)
NH_2CHO	< 0.10	2.6(2)
HNCO	< 0.22	102(11)
HCOOH	< 0.65	28(3)
CH_3OCH_3	< 4.7	20(2)
CH_3COCH_3	< 9.6	5.0(5)
C_2H_5OH	< 4.5	23(3)
C_2H_5CN	< 3.6	1.02(16)

[a] Fractional abundance relative to H_2 derived by assuming the excitation temperature and the dust temperature of 100 K.
[b] Taken from Imai et al. (2016).

8.4.2 Envelope Kinematics

To figure out the rotation structure of the envelope in more detail, we first attempt to fit the PV diagrams of the SO, CS, and $H^{13}CO^+$ emission along the position angle of 290° with the ballistic model of the infalling-rotating envelope (IRE) (Chapter 4; Oya et al. 2017a; Sakai et al. 2014b). The following five free parameters are optimized to reproduce the velocity structure of the PV diagram. (1) the radius of the centrifugal barrier ($r_{\rm CB}$); (2) the mass of the central protostar (M_*); (3) the outer radius of the emitting region in the envelope ($R_{\rm out}$); (4) the vertical thickness of the emitting region in the envelope (h_0); (5) the inner radius of the emitting region in the envelope ($R_{\rm in}$). Here, we assume that the emission intensity is proportional to $r^{-1.5}$, and its distribution is symmetric about the rotation axis. A slight flared disk is assumed, where the thickness of the envelope increases with the angle of 10° along the midplane of the envelope. The thickness (h_0) represents the vertical thickness of the envelope at the protostellar position in the midplane. We also assume the inclination angle of 70° (nearly edge-on disk). We confirm that the result does not significantly change for the flare angle of between 0° and 40° and the inclination angle of between 50° and 90°, because we only fit the disk/envelope direction. The dependence on the flare angle and the inclination angle will be discussed in Section 8.4.3. The model distribution is convolved by the observation beam. In the optimization, we use the same values of $r_{\rm CB}$ and M_* for all molecules.

A typical result is shown in the upper panels of Figure 8.6. Only a part of the structure can be reproduced, but the whole kinematic structure is not reproduced by the model. The fitting is not successful in spite of a search for a wide range of the parameters. We also try to fit the PV diagrams by the Keplerian model, where the inclination angle of the source and the emission profile are assumed to be the same as those for the IRE model. Again, the fitting is not successful. In particular, the counter velocity component cannot be reproduced with the Keplerian model (Figure 8.6 lower pannels).

Thus, the kinematic structure of each molecule cannot be reproduced well by the IRE model nor Keplerian model. This is mainly because the PV diagram of each molecular line only represents some parts of the whole structure of the disk/envelope system. Considering this situation, we attempt to reveal the overall structure of the envelope, by preparing the combined PV diagram of SO, CS, and $H^{13}CO^+$. Figure 8.7 shows the combined PV diagram of SO, CS

and $H^{13}CO^+$ along 6 directions from the position angle of 200° with the intervals of 30°. CCH and HCN are excluded, because their emissions suffer from the hyperfine splittings and self-absorption. Interestingly, a diamond shape structure appears for the position angle from 260°to 320°, which can be interpreted as the infalling-rotating motion. This position angle is consistent with the direction along which the velocity gradient is the largest. Thus, we confirm the position angle of 290° as the envelope direction.

We try to fit the outer shape of the combined PV diagram with the IRE model. In the fitting, we set $R_{\rm in}$ to be equal to $r_{\rm CB}$, assuming that the combined PV diagram traces the whole envelope structure. Then fitting was carried out for the four parameters ((1)-(4)). The left panel of Figure 8.8 shows the result of the model calculation overlaid on the combined PV diagram. This time, the fitting to the whole velocity structure including the counter velocity component seems reasonable with the following parameters: (1) $r_{\rm CB}$ of 100 au, (2) M_* of 0.40 $M_\odot$, (3) $R_{\rm out}$ of 1200 au, and (4) h_0 of 150 au. We therefore set these values as the fiducial values, and discuss their accuracy in the following sections.

We here note the chemical differentiation within the envelope. The SO, CS, and $H^{13}CO^+$ lines are found to trace different parts of the infalling-rotating envelope. Such a feature in the infalling-rotating envelope is scarcely reported in other protostellar cores, although a drastic chemical change across the centrifugal barrier due to accretion shocks has been reported for several sources (Sakai et al. 2014b; Oya et al. 2016; Oya et al. 2017a). The present result suggests that the distributions of molecules can be no longer rotationally symmetric in CB244. The mechanism to drive such a chemical structure in the envelope is left for the future work. It should be noted that a similar anisotropic structure of the envelope is also reported for B335, although it is not so prominent as CB244. In the case of B335, the distributions of COMs differ from each other in the envelope, but they are reproduced by the IRE model with different sizes of the emitting region. Nevertheless, the redshifted emission of the particular part of the envelope is weakened. This feature could be ascribed to the asymmetric distribution of molecules or the infalling motion (Chapter 6).

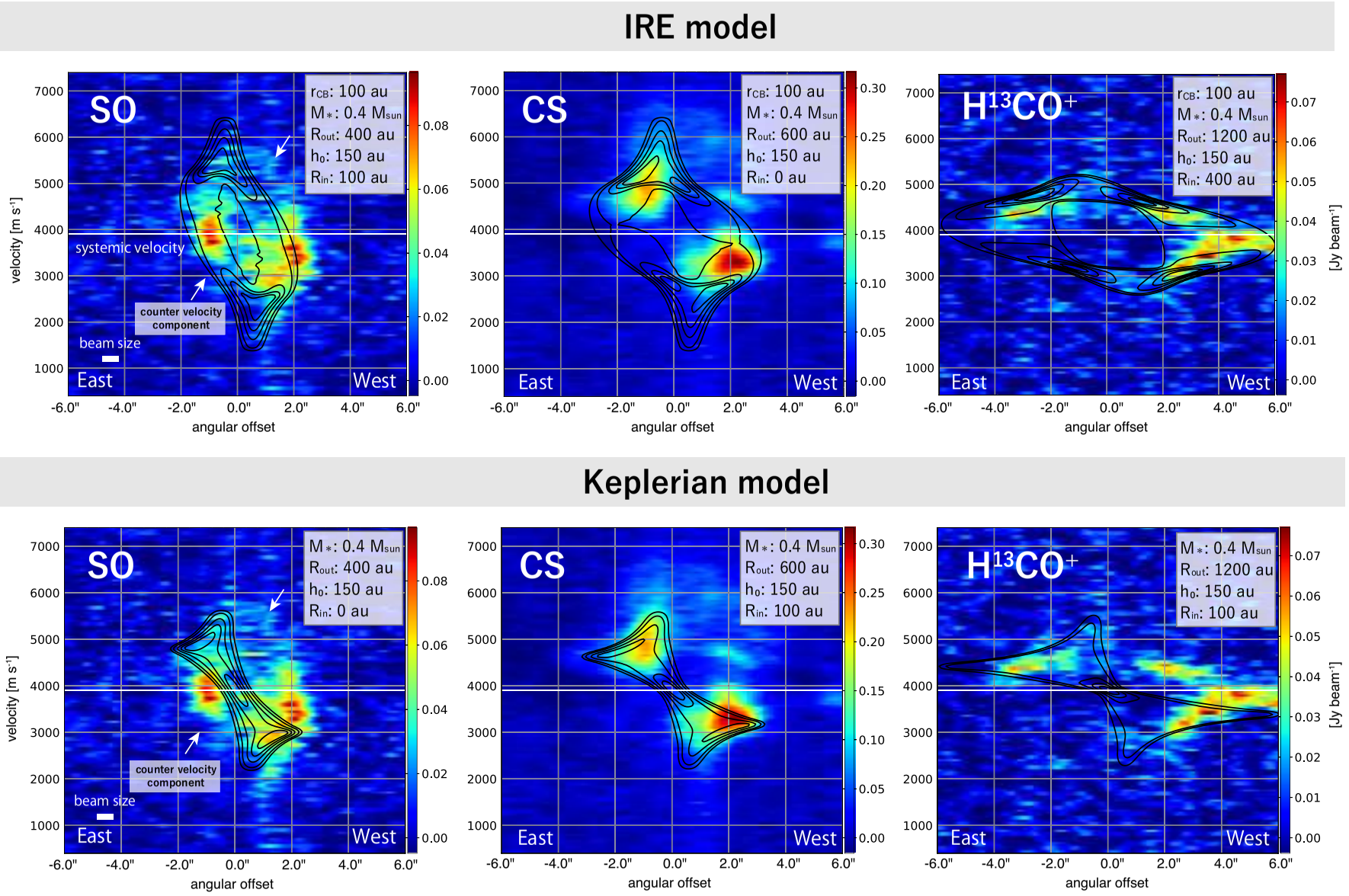

Figure 8.6: Fitting results for the PV diagrams of SO, CS, and $H^{13}CO^+$ by the IRE and Keplerian models. Examples of the model results are shown in black contours. The upper panels show the results for the IRE model, and the lower panels show the results for the Keplerian model. The contours represent the 10, 20, 40, 60, and 80 % of the model peak intensity.

8.4.3 Evaluation of the Model Parameters

To evaluate the goodness of the fit, $KL(p, q)$ is calculated by using the lines of SO, CS and $H^{13}CO^+$, as discussed in Section 4.2. The calculation method is the same as the cases of B335 and CB68 (Sections 6.3.3 and Appendix A) We set the $I_{\rm thres}$ of 30 % and 10 % of the maximum intensity for the observation data and the model data, as in the case of B335 and CB68.

The ranges of the PV image used for the analysis are $\pm 7\farcs0$ from the continuum peak position along the envelope direction (P.A. = 290°) for the position axis and ± 3.0 km s^{-1} from the systemic velocity (3.9 km s^{-1}) for the velocity axis. The pixel spacing for the position axis is set to $0\farcs066$ which is roughly ten times smaller than the beam size. The pixel spacing for the velocity axis is 76.45 m s^{-1}, which corresponds to the velocity resolution of the observation. The PV image is recalculated from the data cube by interpolating the neighboring pixels both for the observation and the model. In total, the images contain 7130 pixels each. The signal detection probability for each pixel is calculated by applying the sigmoid function (Chapter 4). The right panel of Figure 8.8 shows the result of the probability calculation applied for the observed dataset. The outer shape of the PV image of the observation is successfully revealed in the image. Similarly, the signal detection probability for the model is also calculated. Using these probability distributions, $KL(p, q)$ is evaluated.

Figure 8.9 represents the IRE model results for some combination of the model parameters: $r_{\rm CB}$, $R_{\rm out}$, and M_*. The parameter variations are 25, 100, and 400 au for $r_{\rm CB}$, 0.1, 0.4, and 1.6 $M_\odot$ for M_*, and 600, 1200, 1800 au for $R_{\rm out}$. The result of the KL divergence for each model are also shown on top right of each panel in Figure 8.9. In this figure, the middle panels show the fiducial ones (Section 8.4.2). In the eye-based fitting, the results for the $r_{\rm CB}$ of 25 and 100 au seems better than that for 400 au. This is consistent with the result of the KL divergence. Actually, the KL divergences for 25 and 100 au are smaller than that for 400 au. The results of the variations for the other parameters are also consistent with the goodness of the fit judged by eye.

The KL divergences derived for the variation of the four free parameter are summarized in Figure 8.10. As for the $r_{\rm CB}$, the KL divergence becomes the lowest around $r_{\rm CB}$ of < 100 and becomes larger as the $r_{\rm CB}$ increases from 200 au. This suggests that only the upper limit to the radius of the centrifugal barrier can be determined. This is reasonable, because 100 au almost corresponds to the beam size of the observation. The KL divergence for the variation of M_* is also shown in the upper right panel of Figure 8.10. In this case, the value becomes the smallest around the mass of 0.4 $M_\odot$. The KL divergence increases rapidly as the mass decreases from 0.4 $M_\odot$, while the increase is more gentle for the mass larger than 0.4 $M_\odot$. As for $R_{\rm out}$, the KL divergence becomes the smallest for $R_{\rm out}$ of > 1000 au. In this case, the increase is more steep for the smaller value of $R_{\rm out}$. The change in the KL divergence is not prominent for the variation of the thickness h_0. This is because we only fit the PV diagram along the direction of the envelope.

Overall, the KL divergence is useful to find the best set of the model parameters in this source as in the case of B335 and CB68. We also point out that $KL(p, q)$ changes more sensitively for the case that model reproduces only a part of the observation, while the change is more gentle for the case that the signal distribution of the model is larger than that of observation. For example, the change in $KL(p, q)$ is more gentle for $R_{\rm out}$ of > 1200 au and M_* of $> 0.4 M_\odot$, as mentioned above. In these cases, the signal distribution of the model is indeed larger than that of the observation [1].

[1] A part of this reason is that the signal distribution of the model exceeds the image size included for the calculation. Another reason for the gentle increase of $KL(p, q)$ for $R_{\rm out}$ is the asymmetric molecular distribution. Since the emission profile is different between the east and the west part of the envelope, the KL divergence almost stays constant.

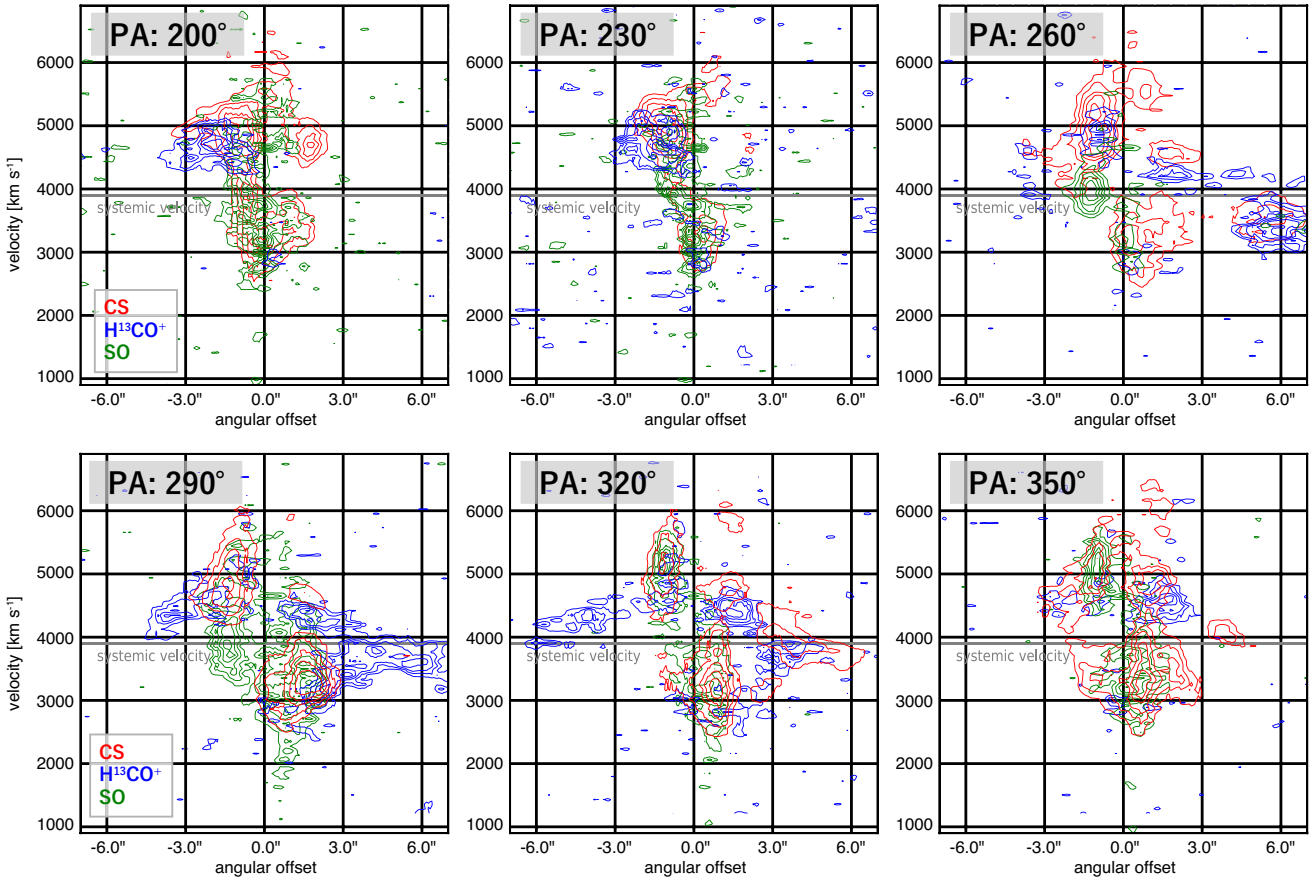

Figure 8.7: The PV diagrams of CS, $H^{13}CO^+$, and SO overlaid in the same panel. The position angles for the position axis is taken from 200° to 350° with the 30° interval. The contours for each molecule represent 25, 40, 55, 70, and 85 % of the peak.

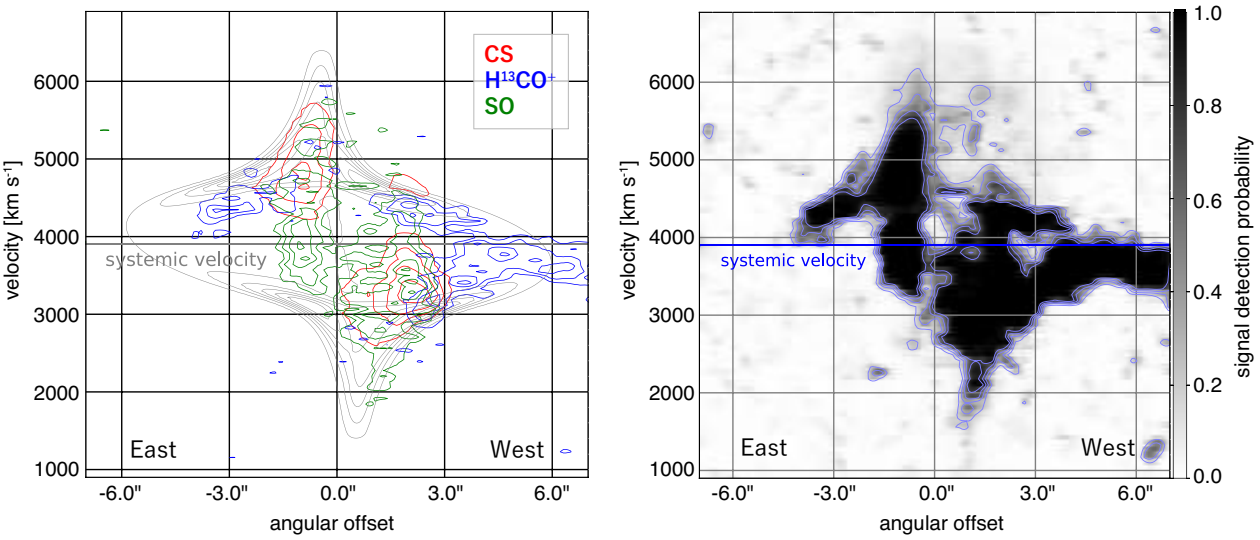

Figure 8.8: (*left*) The combined PV diagrams of CS (red), $H^{13}CO^+$ (blue), and SO (green) overlaid with the IRE model (black contours) for the fiducial values. The contours for the model represent the 10, 25, 40, 55, 70, and 85 % of the peak, while those for the molecules represents the 30, 50, 70, and 90 % of the peak. (*right*) The probability distribution (p_i) calculated by using the sigmoid function to the combined PV diagram. It is confirmed that the probability distribution reasonably depicts the outer shape of the combined PV diagram. The contours represent the signal probability of 0.2, 0.4, 0.6, and 0.8.

The KL divergence has an uncertainty due to the noise of the observation. We evaluate this effect by preparing the mock PV images based on the observation with and without the noise component, as described in Section 4.2.2. The details of the calculation are described in Appendix A. By using the method, the tolerance range of the KL divergence is estimated to be 0.21 above the minimum value of $KL(p, q)$.

Using the above tolerance range of the KL divergence, the uncertainty of the optimized parameters are evaluated. The tolerance range of the KL divergence is shown by the gray range in Figure 8.10. The protostellar mass and the radius of the centrifugal barrier are evaluated to be $0.4^{+0.6}_{-0.2}$ $M_\odot$ and < 300 au, respectively. Here, the uncertainties of the parameters are estimated by the parameter range whose $KL(p, q)$ is in the gray range in Figure 8.10.

Here, we mention the result for the variation of the inclination angle (Figure 8.10 lower left panel). It is confirmed that the KL divergence does not significantly change for the inclination angle from 50° to 90°. On the other hand, the KL divergence slightly increases as the inclination angle decreases below 50°, although its difference is within the uncertainty. This result suggests that the disk may be edge-on rather than face-on. However, the precise inclination angle cannot be determined from this analysis. It should be noted that the inclination angle does not significantly affect the optimization of the other free parameters used above discussion. It is also confirmed that the flare angle of the envelope has little effect on the KL divergence (Figure 8.10 lower right panel).

In the present analysis, we set the $I_{\rm thres}$ of 30 % for the observation data, 10 % for the model data, and b of 0.2. We change these values and see how the result changes in Figure 8.11. $I_{\rm thres}$ for the observation data is changed to 20 % and 40 %, $I_{\rm thres}$ for the model data is changed to 5 % and 20 %, b is changed to 0.1 and 0.3. Only one of $I_{\rm thres}$ for the model and the observation and b is changed, while the others are remained to be unchanged. Overall, the value of $KL(p, q)$ does not significantly change with the variation of $I_{\rm thres}$ from the value used in the above analysis

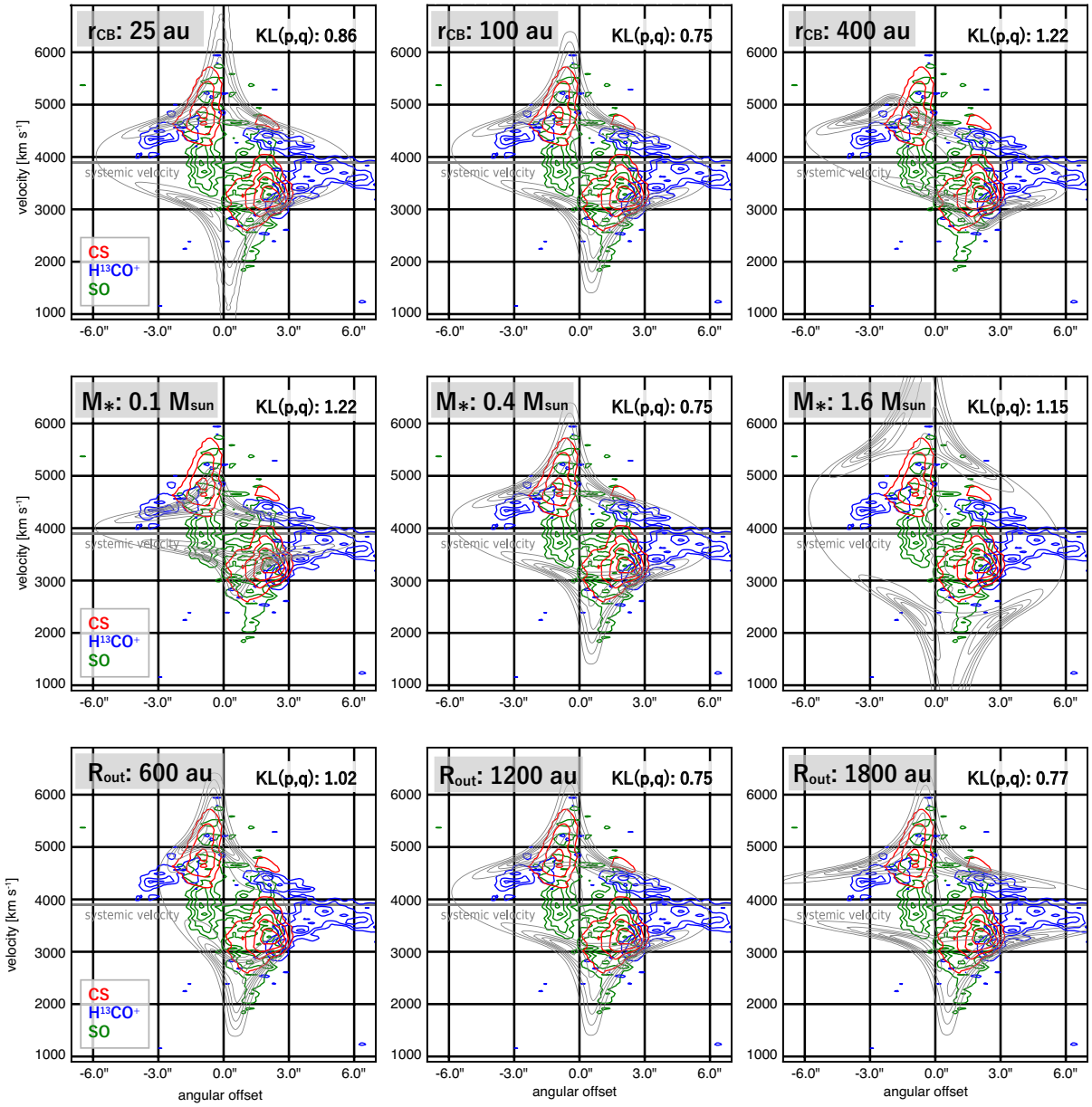

Figure 8.9: The comparison with the model (gray) and combined PV diagrams of CS (red), $H^{13}CO^+$ (blue), and SO (green). The parameters are 25, 100, and 400 au for $r_{\rm CB}$, 0.1, 0.4, and 1.6 $M_\odot$ for M_*, and 600, 1200, and 1800 au for $R_{\rm out}$. The results for the fiducial values are shown in the middle panels. The $KL(p,q)$ divergence is shown on the top right corner. The contours for the model represent 10, 25, 40, 55, 70, and 85 % of the peak, while those for the molecules represent 30, 50, 70, and 90 % of the peak.

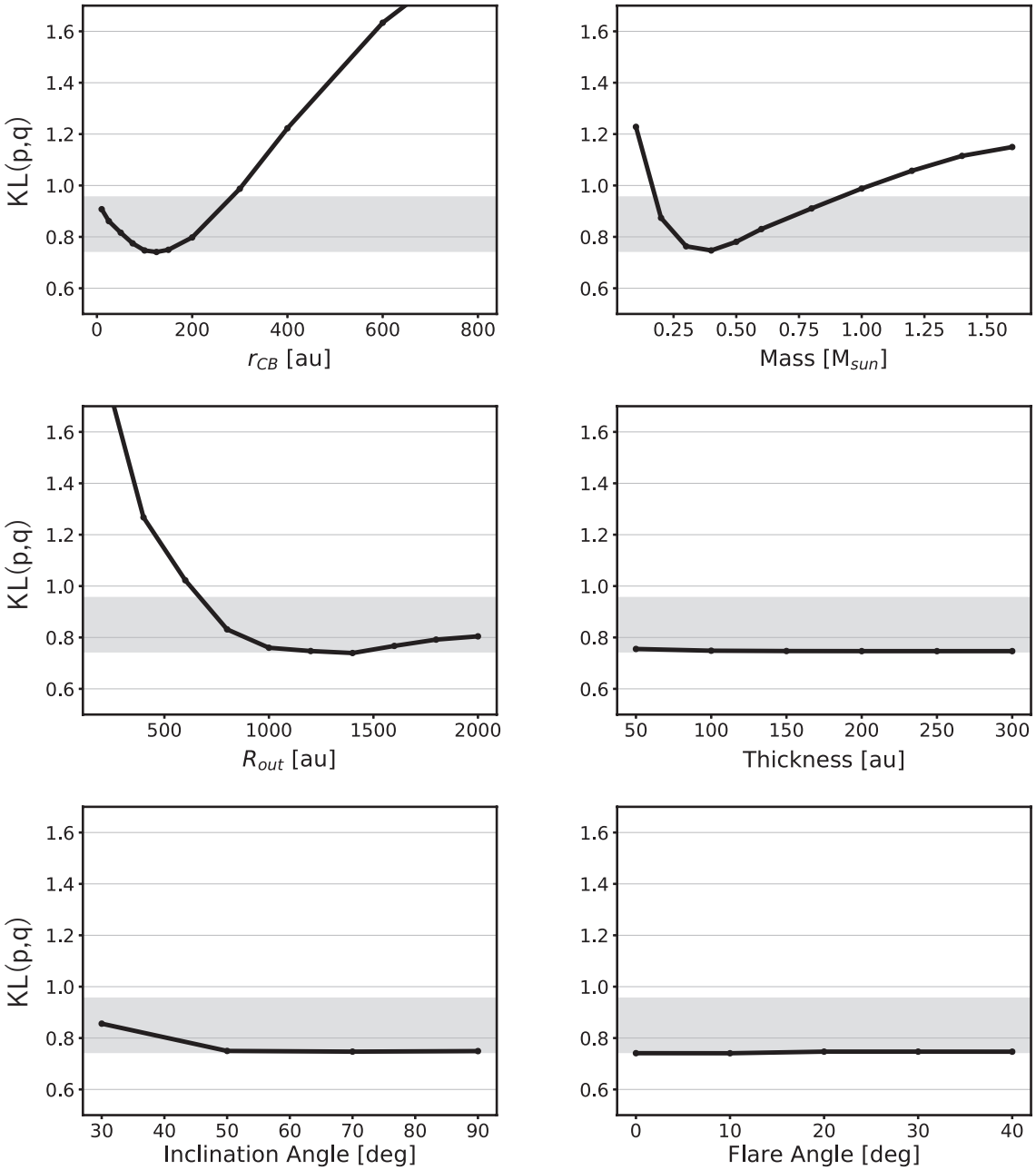

Figure 8.10: The result of KL divergence with variation of the radius of centrifugal barrier, and the mass of the protostar, the outer radius of the emitting region, the thickness of the emitting region, the inclination angle, and the flare angle. The gray area indicates the uncertainty for the KL divergence due to the observation noise.

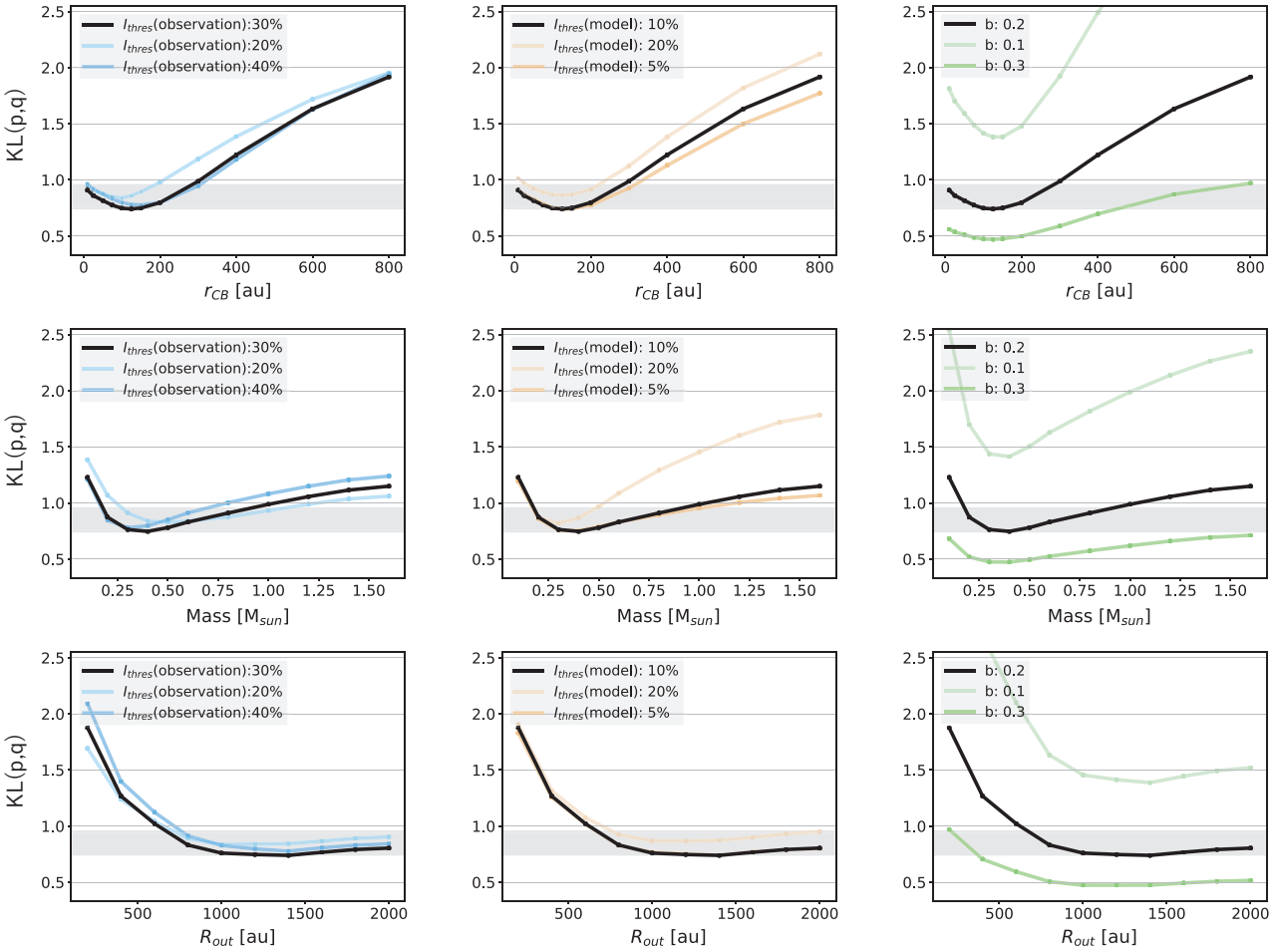

Figure 8.11: Examples of dependence of the KL divergence on $I_{\rm thres}$ for the observation data (left column panels), $I_{\rm thres}$ for the model data (middle column panels), b coefficient of sigmoid function (right column panels). The values used for the analysis in this thesis is shown in black ($I_{\rm thres}$(observation)=30 %, $I_{\rm thres}$(model)=10 %, b=0.2). The results for $r_{\rm CB}$ are shown in upper panels, the results for M_* are shown in middle panels, and the results for $r_{\rm out}$ are shown in bottom panels.

(black line in Figure 10), while the deviation is fairly large in the case of $I_{\rm thres}$ for the model of 20 %. The KL divergence significantly changes from the original value for the variation of b, because it determines the value for the zero-emission region which is not zero in the signal detection probability as noted in Section 8.4.3. Nevertheless, the basic shape of the dependence along with the parameters giving the minimum values does not significantly differ from the original value within the above parameter range.

8.4.4 Diversity of Isolated Sources

We have discussed the chemical and physical features of the isolated source CB244 and have compared them with the case of the representative isolated source B335 and CB68. One important result is that the chemical and physical feature is found to be different from source to source. A caveat for this result should be noted here. CB244 accompanies a starless core located at 18000 au apart from it, and hence, it cannot be regarded as a "truly isolated" source. Although the influences of other protostellar activities can be excluded for this source, the existence of the

starless core in the cloud may affect the formation process of the protostar. For example, the asymmetric infall of the gas to the protostar may affect the kinematic structure of the collapsing core. In fact, the gas distribution in CB244 is revealed to be asymmetric: the gas seems more abundant in the west direction, which is the direction to the starless core. The asymmetric structure of the protostellar envelope, which is less prominent for B335, may be ascribed to such an asymmetric environment. Another factor which can cause the diversity in isolated source is the external pressure caused by anisotropic UV radiation field, which can cause the variation of the time scale to form the protostar in the cloud (Watanabe et al. 2012; Lindberg et al. 2015). The mechanism responsible for the variation of the different physical and chemical conditions is left for future studies.

8.5 Summary

The 1.2 mm band observation toward CB244 was conducted with NOEMA. CB244 is revealed to be deficient in molecular lines: 11 lines of CH_3OH, CS, $H^{13}CO^+$, SiO, SO, CCH, c-C_3H_2, and HCN are detected. The main results are summarized below.

1. Carbon-chain molecules CCH and c-C_3H_2 are detected in the envelope, while no COMs except for CH_3OH are detected. The upper limit to the fractional abundances of COMs are lower than the fractional abundances in B335. Thus, only WCCC like feature is confirmed, while hot corino chemistry is not evident in CB244. The chemical characteristics of this source are thus different from the hybrid-type chemical characteristics (WCCC and hot corino chemistry) found in B335 and CB68.

2. The direction of the velocity gradient (P.A.=290°) is consistent with the direction of the continuum elongation. A feature of the infalling-rotating envelope is confirmed for the PV diagram along this direction. Although the distributions of the molecular lines are different from one another, the combined PV diagram is successfully reproduced by our model of the infalling-rotating envelope. The protostellar mass and the radius of the centrifugal barrier are thus evaluated to be $0.4^{+0.6}_{-0.2}$ $M_\odot$ and < 300 au, respectively.

Chapter 9

Discussion

In this thesis, physical and chemical diagnostics of three isolated low-mass protostellar sources, B335, CB68, and CB244, have been conducted with the state-of-the-art millimeter interferometers, ALMA and NOEMA, at a linear spatial resolution resolving their envelope structure. The main results are summarized below.

9.1 Comparison among the Isolated Sources

9.1.1 Physical Structure

The physical structures of the three sources on a disk/envelope scale ($<$ 100 au) are characterized for the first time by our observations. Rotation motion is resolved for the three sources, and it is explained by the infalling-rotating model (Chapter 4). The protostellar mass (M_*) and the radius of the centrifugal barrier ($r_{\rm CB}$) of B335, CB68, and CB244 are summarized in Table 9.1. The radius of the centrifugal barrier is estimated to be $<$4, $<$30, and $<$300 au for B335, CB68, and CB244, respectively. Mass of the protostar is derived to be $0.05^{+0.03}_{-0.02}$, $0.15^{+0.15}_{-0.07}$, and $0.4^{+0.6}_{-0.2}$ $M_\odot$ for B335, CB68, and CB244, respectively. These values are the best-fit ones by using the KL divergence.

The upper limit to the specific angular moment (j) is also derived by using the following equation:

$$j = \sqrt{2GM_* r_{\rm CB}}, \tag{9.1}$$

where G is the gravitational constant. It is calculated to be $<$0.9, $<$4, and $<$22 for B335, CB68, and CB244. Although only the upper limits are obtained for $r_{\rm CB}$ and j, the values of CB244 could be larger than those of B335 and CB68 by about one order of magnitude. Since the environmental effects such as external UV radiation or outflow from nearby sources can be excluded in the isolated sources, such a physical difference may arise from the different structures of their individual parent molecular cloud cores. For example, the parent core has a small and round shape (*i.e.*, small aspect ratio) for B335 and CB68, while a flattened structure is seen for CB244 (Table 9.1). Moreover, CB244 harbors a starless core in addition to the protostellar core inside the cloud. Thus, CB244 has a different cloud structure from those of B335 and CB68. Although the sample is small at the present stage, the shape of the parent core may affect the rotation structure of the protostellar source born there.

According to Goodman et al. (1993), the specific angular momentum of cloud cores roughly scales as $R^{1.5}$, where R denotes their FWHM diameters. This empirical relation is obtained from the survey observation of NH_3, $C^{18}O$, and CS toward many cloud cores ($\sim$ 40). Since the size of the parent cloud core of CB244 is larger than those of B335 and CB68, a larger specific angular

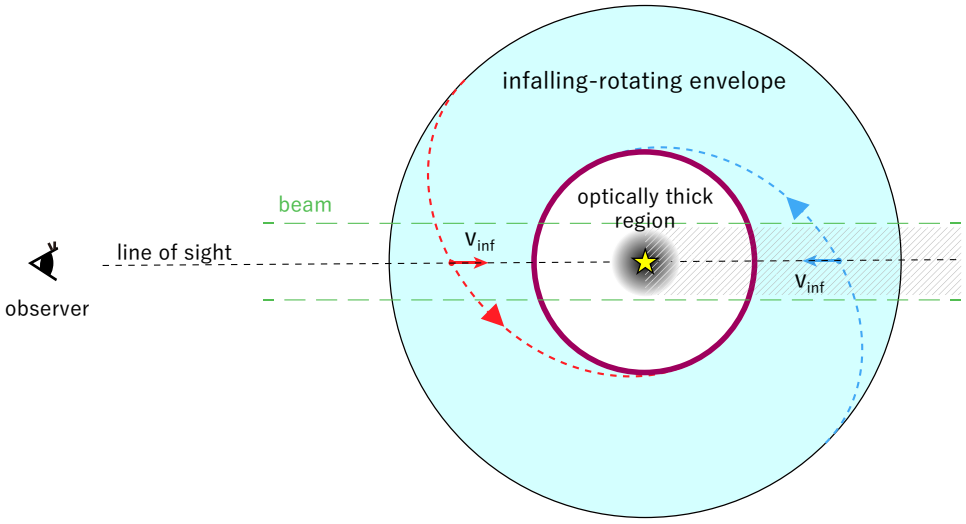

Figure 9.1: A possible scenario to explain the asymmetric velocity structure seen in B335 and CB68. If the dust is optically thick in the vicinity of the protostar, the backside gas moving to the observer will be shielded by the dust, when they are observed at similar spatial resolution as optically thick region. It can explain the weakened blueshifted emission detected in CB68. The gray hatch in the figure shows that the emissions coming from this area can be shielded in the vicinity of the protostar.

momentum is expected for CB244. This qualitative consideration seems consistent with the observational trend for the radius of the centrifugal barrier and the specific angular momentum.

We here note that the asymmetric gas distribution is revealed for the observed sources. The most apparent asymmetry is seen in the distributions of molecules in CB244. The molecular distributions in the envelope are not symmetric around the protostellar position. Most of the molecules are distributed in the west part of the envelope, and their individual kinematic structures are not explained by the simple IRE model if a symmetric distribution are assumed. Such an asymmetric structure may be related to the large radius of the centrifugal barrier in CB244. On the other hand, asymmetry of the gas kinematics between blueshifted and redshifted components are seen in B335 and CB68 (Chapters 6 and 7). The redshifted components of COM emissions are weakened in B335, which can be ascribed to the absorption due to the foreground infalling gas toward protostars. On the other hand, the blueshifted components are weakened in the vicinity of the protostar in CB68. This feature cannot be explained by the absorption due to the foreground infalling gas. Therefore, the asymmetric emission likely originate from the asymmetric gas distributions around the protostar. This indicates that the whole infalling-rotating envelope is not filled with the gas, although the radial profile is assumed in the IRE model. Alternative interpretation is the affect of the dust opacity as depicted by a schematic illustration in Figure 9.1. If the dust in the vicinity of the protostar is optically thick, the backward gas moving frontward (i.e., blueshifted emission) can be shielded by the dust. In this case, the blueshifted emission will be weakened. Such a feature can be detected in our observations because the closest vicinity of the protostar is now resolved with ALMA.

9.1.2 Chemical Characteristics

In addition to the physical structures, the chemical characteristics are also revealed for the three sources. COMs are detected toward B335 and CB68, suggesting hot corino chemistry in these sources (Table 9.2). Nine species of COMs are detected toward B335, and four species in

Table 9.1: Physical and Chemical Features of the Isolated Sources and Cloud Morphology

Source	Evolutionary Stage	Chemistry[a]	$L_{\rm bol}$[b] ($L_\odot$)	Protostellar Mass ($M_\odot$)	Radius of the CB[c](au)	$j^{\rm d}/10^{-4}$ (km s^{-1} pc)	Cloud Size[e] (pc)	Aspect Ratio of Cloud Core[e]
B335	Class 0	HC+WCCC	0.72	$0.05^{+0.03}_{-0.02}$	< 4	< 0.9	0.14	1.2
CB68	Class 0	HC+WCCC	1.3	$0.15^{+0.15}_{-0.07}$	< 30	< 4	0.18	1.3
CB244	Class 0/I	WCCC	1.5	$0.4^{+0.6}_{-0.2}$	< 300	< 22	0.46	2.0

[a] 'HC' denotes the hot corino chemistry.
[b] Bolometric luminosity of the protostar.
[c] Centrifugal barrier.
[d] The specific angular momentum.
[e] Taken from Launhardt et al. (2010). A cloud size is determined with the optical image by taking a root mean square of length of major and minor axis (Clemens & Barvainis 1988). The aspect ratio is the ratio of the lengths of the major and minor axis.

addition to CH_3OH are detected toward CB68. Among the detected COMs in CB68, CH_3CHO is more abundant in CB68, while HCOOH, CH_3OCH_3, and NH_2CHO are more abundant in B335. Thus, the composition of COMs are slightly different between B335 and CB68. The upper limit to the fractional abundances of COMs in CB244 is clearly lower than those in B335 and CB68. The hot corino chemistry is not prominent in CB244.

Carbon-chain molecules are detected toward the three sources. The extent of their emission is as large as 1000 au with association to the protostar as well as the outflow cavity. These results indicates that the WCCC feature is seen in the three sources. Thus, the hybrid chemical characteristics (hot corino chemistry and WCCC) are identified in B335 and CB68, while WCCC feature is identified in CB244.

The hybrid chemical characteristics are predicted in the chemical model calculation of a collapsing protostellar core by Aikawa et al. (2008) (Figure 9.2). In their model, the result of a one-dimensional radiation-hydrodynamics calculation (Masunaga & Inutsuka 2000a) is employed as a physical structure of the core. The chemical network is the gas-grain model developed by Garrod & Harbst (2006), which includes the gas-phase and grain-surface reactions (6309 reactions in total). According to their result, WCCC occurs in the outer region of a protostellar core (100- a few 1000 au scale), triggered by the evaporation of CH_4 ($T > 25$ K). Indeed, the gas-phase abundances of carbon-chain molecules are enhanced there. At the same time, the model predicts the enhancement of COMs in the vicinity of the protostar (< 100 au; $T > 100$ K). This picture seems consistent with the hybrid character revealed for B335 and CB68. The hybrid chemical character has not been recognized so far except for IRAS18148-0440 in L483 (Oya et al. 2017a). Hence the results for B335 and CB68 stand for a definitive evidence of the existence of the hybrid source.

The physical and chemical structures of the protostellar envelope in B335, CB68, and CB244 are summarized in Figure 9.3. Overall, B335 and CB68 seem to have similar physical and chemical structures to each other (*i.e.*, the small radius of the centrifugal barrier and the hybrid chemical characteristics), as discussed above. They also have similar morphology of their parent molecular clouds. On the other hand, CB244 shows only the WCCC feature and has a kinematic structure and a morphology of the parent molecular cloud which are different from those of B335 and CB68. Since B335, CB68, and CB244 are in a similar evolutionary stage, the chemical difference cannot be ascribed to the evolutionary stage of the protostar. Rather, the different chemical characteristics seen in CB244 may be related to the different physical structure and/or morphology of its parent cloud core. Such physical and morphological differences may cause different chemical compositions of the surface of dust grains in the past cold phase before the onset of star formation.

As described in Section 1.2.1, it is proposed that the difference between hot corino chemistry

Table 9.2: Fractional Abundances of COMs relative to H_2 (10^{-9})

Molecule	B335[a]	CB68[b]	CB244[a]	I16293[c]	IRAS 4A	IRAS 2A[d]
HCOOH	2.8(3)	0.075(16)	< 0.065	$\lesssim 0.3$	...	...
CH_3CHO	1.4(2)	5.8(7)	< 0.042	3	...	...
$HCOOCH_3$	2.8(3)	< 0.87	< 0.30	9	1.4[d]	13
CH_3OCH_3	2.0(2)	0.53(4)	< 0.47	40	0.85[d]	8.2
HNCO	10.2(11)	...	< 0.022	...	0.8[e]	...
NH_2CHO	0.26(2)	0.015(2)	< 0.010	0.6	0.2[e]	2.3
C_2H_5OH	2.3(3)	< 0.16	< 0.45	$\lesssim 5$	1.2[d]	10
C_2H_5CN	0.102(16)	< 17	< 0.36	$\lesssim 0.2$	0.062[d]	0.24

[a] The temperature is assumed to be 100 K.
[b] The temperature is assumed to be 133 K.
[c] IRAS 16293-2422. Taken from Jaber et al. (2014). Although this source is a binary, the components are not resolved in their observation.
[d] Taken from Taquet et al. (2015).
[e] Taken from López-Sepulcre et al. (2015).

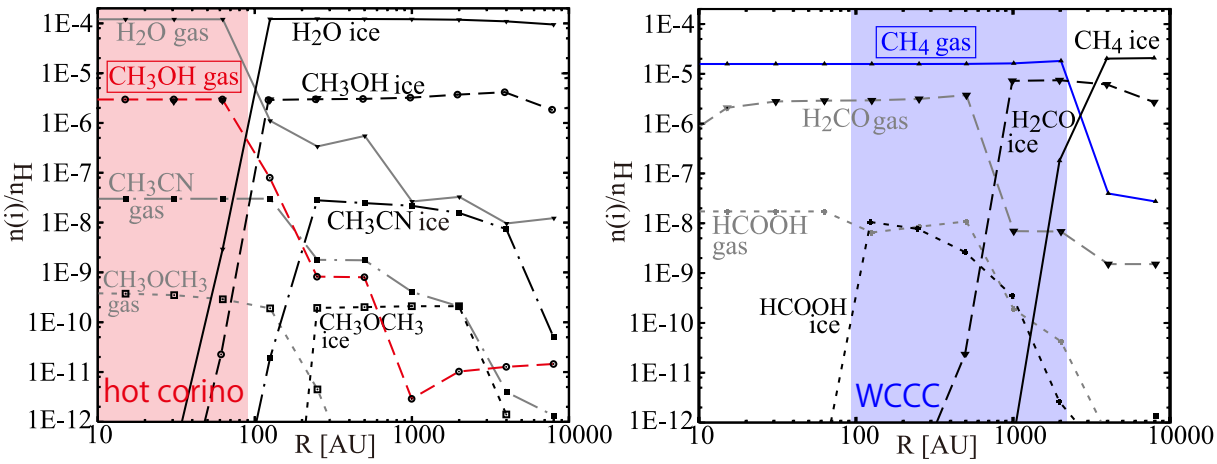

Figure 9.2: Radial distributions of molecules in the protostellar core after 10^5 year from the onset of star formation by the chemical model calculation (Aikawa et al. 2008). The total mass is 3.852 $M_\odot$. COMs (CH_3OH, CH_3OCH_3 and CH_3CN) are distributed in the vicinity of the protostar (hot corino chemistry) ($r < 100$ au), while the CH_4 is evaporated in to the gas phase in the region from 100 to a few 1000 au. COMs are evaporated from dust grains in the hot region near the protostar. On the other hand, evaporation of CH_4 in the warm region triggers efficient production of carbon-chain molecules including CCH (WCCC).

and WCCC could originate from the difference of the major form of carbon depleted on the dust grain. If the duration time of starless core phase is long enough, most of the C atoms are converted to CO, and then, they are depleted onto the dust grain. CH_3OH will be formed from CO through hydrogenation on the dust surface, and it will trigger hot corino chemistry after evaporation to the gas phase in the hot region ($T > 100$ K). On the other hand, if the duration time of the starless core phase is as short as a free fall time ($\sim 10^5$ yr), C atoms are directly depleted onto the dust grain and CH_4 is formed through hydrogenation on the dust surface. This will lead to WCCC after the evaporation of CH_4 in the warm region (> 25 K). If this scenario is the case, the intermediate chemical composition of the dust surface (C and CO) can explain the existence of the hybrid chemical characteristics seen in B335 and CB68. On the other hand, only the WCCC feature is detected in CB244. This might suggest that C atoms would have been directly depleted onto the dust grain before they are converted to CO in CB244. The C to CO conversion starts when the H_2 density becomes high enough to shield the external UV radiation ($n(H_2) \sim 10^4$ cm^{-3}), and its time scale is roughly estimated to be 10^5 years (*e.g.*, Yamamoto 2017). On the other hand, the depletion time scale is reported to be inversely proportional to the H_2 density ($\sim 10^9/n(H_2)$ yr) (*e.g.*, Caselli et al. 1999). If the average density of the core at the starless phase is higher in CB244 than B335 and CB68, it might have shorten the depletion time scale, which leads to the direct depletion of C atoms onto the dust grain. The different morphology of the parent molecular cloud might cause the different H_2 density profile at the starless phase in CB244. However, further details of physical processes for the shorter time scale are uncertain, which are left for future study.

Another possibility for the non-detection of hot corino chemistry in CB244 is the different temperature distribution around the protostar at the present stage. Hot corino chemistry is thought to appear in the hot region ($T > 100$ K). If the size of such a hot region is small, hot corino chemistry will hardly be detected due to the beam dilution effect. The non-detection of hot corino chemistry in CB244 might be ascribed to such a temperature structure difference. As shown in Table 9.2, the upper limit to the fractional abundances of COMs in CB244 are smaller than those in B335 by 1-2 orders of magnitude. Considering the COM distributions of a few 10 au in B335, the upper limit to the size of hot corino in CB244 is roughly estimated to be a few au, if we assume the same fractional abundances of COMs between B335 and CB244. Here, we simply assume that H_2 density is constant within the beam size. To test whether hot corino chemistry really exists at such a small region in CB244, higher angular resolution observations are necessary.

9.2 Comparison with Other Protostellar Sources

We compare the physical and chemical characteristics of the isolated sources with those of other low-mass protostellar sources reported so far. The physical parameters and chemical characteristics are summarized in Table 9.3. B335 and CB68 are found to have a smaller radius of the centrifugal barrier than the other sources. CB244 has a radius of the centrifugal barrier comparable to the previously observed sources, if the radius of the centrifugal barrier is not different from the upper limit by an order of magnitude or more. Figure 9.4 shows a correlation diagram between r_{CB} and the protostellar mass. Since r_{CB} is inversely proportional to the protostellar mass and proportional to the square of the specific angular momentum, the anti-correlatioin is expected for r_{CB} and the protostellar mass as far as the specific angular momentum is constant. However, there is no such anti-correlation between the protostellar mass and r_{CB} (Figure 9.4).

The fractional abundances of COMs relative to H_2 are compared with previously known hot corino sources in Table 9.2. Since hot corino sources have so far been detected in large

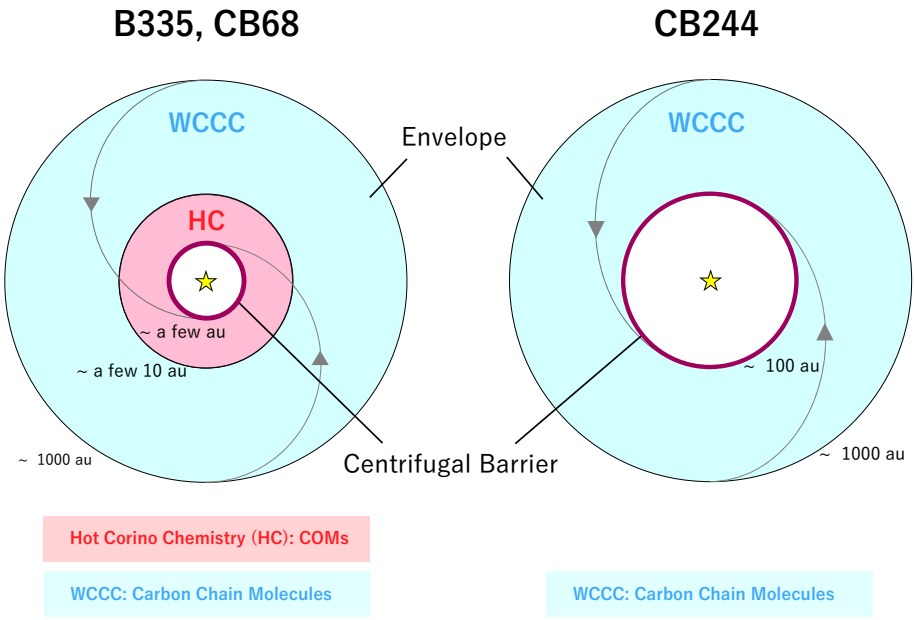

Figure 9.3: A rough sketch of the physical and chemical structures of the protostellar envelopes of B335, CB68, and CB244.

molecular cloud complex (*e.g.*, Perseus molecular cloud complex), the detection of hot corino chemistry in isolated sources is noteworthy. The COM abundances seem different from source to source. Even between B335 and CB68, which would have a similar physical condition, the COM abundances show some differences, if we closely look at them. This result may indicate that the COM abundances are sensitive to the physical condition and the evolution history of each source. Systematic observations will be necessary to solve its origin.

Nevertheless, we find an important hint. A relation between the radius of the centrifugal barrier and the chemical characteristics are not obtained in the previously observed sources, as reported by Oya et al. (2017b). Now, we could see the trend that hot corino chemistry appears for the sources having a small radius of the centrifugal barrier in the isolated sources.

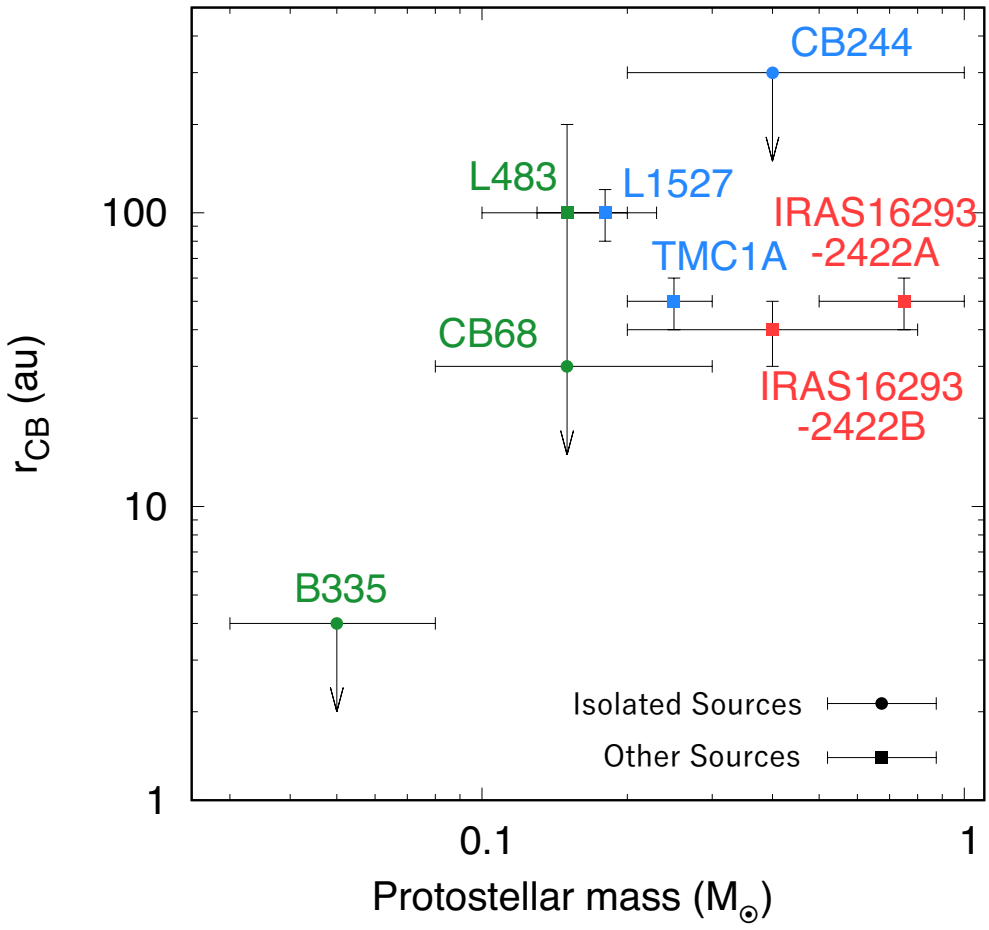

Figure 9.4: The comparison of the protostellar mass and the radius of the centrifugal barrier ($r_{\rm CB}$) among low-mass protostellar sources. The sources whose chemical characteristics are WCCC, hot corino chemistry, and the hybrid type are shown in blue, red, and green, respectively. The isolated sources are marked with circle, while the other sources are marked with square.

Table 9.3: Physical and Chemical Features of the Low-Mass Sources

Source Name	Evolutionary Stage	Chemistry[a]	Protostellar Mass ($M_\odot$)	Radius of the CB[b] (au)	j[c] (10^{-4} km s^{-1} pc)
		Isolated Sources			
B335	Class 0	HC+WCCC	$0.05^{+0.03}_{-0.02}$	< 4	< 0.9
CB68	Class 0	HC+WCCC	$0.15^{+0.15}_{-0.07}$	< 30	< 4
CB244	Class 0/I	WCCC	$0.4^{+0.6}_{-0.2}$	< 300	< 22
		Other Sources			
L1527[d]	Class 0/I	WCCC	0.18 ± 0.05	100 ± 20	9 ± 1
TMC 1A[e]	Class I	WCCC	0.25 ± 0.05	50 ± 10	7 ± 1
IRAS 16293-2422 Source A[c]	Class 0	HC	0.75 ± 0.25	50 ± 10	13 ± 2
IRAS 16293-2422 Source B[c]	Class 0	HC	$0.4^{+0.4}_{-0.2}$	40 ± 10	8^{+4}_{-2}
L483[d]	Class 0	HC+WCCC	0.15 ± 0.05	100^{+100}_{-70}	8^{+4}_{-3}

[a] HC denotes the hot corino chemistry.
[b] Centrifugal barrier.
[c] Specific angular momentum of the envelope gas derived from the protostellar mass and the radius of the centrifugal barrier.
[d] Taken from Oya et al. (2017b)
[e] Taken from Sakai et al. (2016)

Chapter 10

Conclusion and Future Prospect

I started this study with the aim to reveal the origin of the chemical diversity of the envelope of low-mass protostellar sources. Since the origin of the diversity would be the environmental effect, it is important to discriminate one effect from the others. With this in mind, we picked up three isolated sources (B335, CB68, and CB244) to study physical and chemical structures of the protostellar sources without influences of other protostellar activities. The physical and chemical structures of the three isolated sources are revealed by this study, and the following implications toward the above goal is obtained.

1. Although star-formation activities of isolated sources are not very active, various molecular lines are observed in their envelopes. In particular, we discover the COMs in the isolated star forming region for the first time.

2. The infalling-rotating envelope and the centrifugal barrier are the common occurrences among the isolated sources as well as the others studied previously. The chemical change around the centrifugal barrier is also seen in the envelope of the isolated sources.

3. The physical and chemical diversities seen in isolated sources suggest the possibility that the physical and chemical variation of the protostellar sources can emerge even without apparent environmental effects such as star-formation activities of nearby sources.

4. A possible link can be seen between the shape of the parent molecular cloud and the physical and chemical structures of the protostellar envelope. The different cloud size and morphology and/or the existence of starless core in CB244 may be ascribed to the different chemical characteristics from the other two sources (B335 and CB68).

The latter two implications suggest the marginal relation between physical structure and chemical structure based on the three examples of the isolated sources. A statistical study of the isolated sources is necessary to step forward.

In the present analysis, rotation motion is explained by the infalling-rotating envelope model. However, the Keplerian disk is thought to be formed inside the centrifugal barrier, as reported by Oya et al. (2017a). B335 and CB68 have remarkably small radius of the centrifugal barrier ($\sim$ a few au), and now we have a key question whether a Keplerian disk can really be formed in such a small region. As Yen et al. (2015) suggests, the small Keplerian disk in B335 might be due to the young age of the protostar. If the disk structures are really formed in B335, it means that the disk is formed in an infant stage. The same thing can be also applied to CB68. Since the protostellar disk is a place where planets will be formed in the future, the chemical structure of this region will give us important information on the initial condition of the planet-forming region. In this relation, Okoda et al. (2018) recently reported the Keplerian disk structure around an infant protostar.

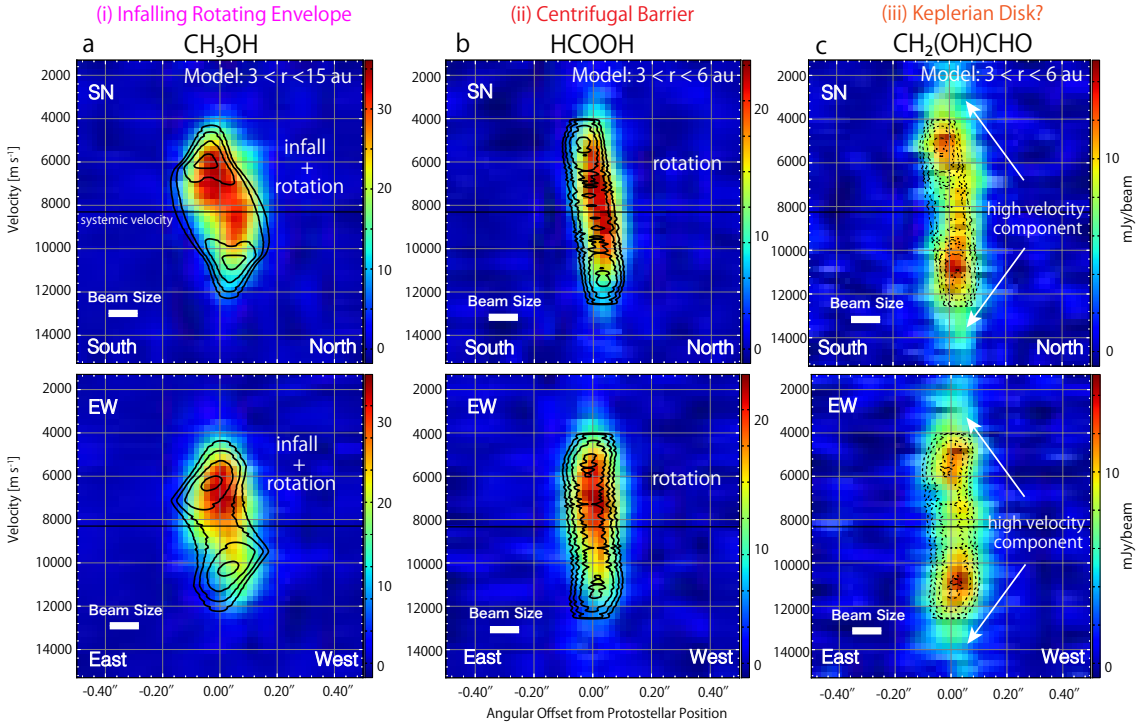

Figure 10.1: Examples of the PV diagram (upper: disk/envelope direction, lower: outflow direction) overlaid with the IRE model ($M = 0.04\ M_{\odot}$, $r_{\rm CB}$=3 au). The distribution of CH_3OH is assumed to be $3 < r < 15$ au in its model, while those of HCOOH and $CH_2(OH)CHO$ are assumed to be $3 < r < 6$ au. Most of the complex organic molecules are explained by the IRE model as (a) and (b). However, the large velocity width of $CH_2(OH)CHO$ cannot be reproduced with the IRE model (c), which suggests that the molecule is likely distributed inside the centrifugal barrier (disk).

A hint for the existence of Keplerian disk is obtained in the observation of B335. As discussed in Chapter 6, CH_3OH and HCOOH are detected in the infalling-rotating envelope in this source. The line widths of these molecules are around 6 km s^{-1}. However, other complex organic molecules $CH_2(OH)CHO$, CH_3OCH_3, and CH_3COCH_3 are found to have more broad line widths ($>$ 10 kms $^{-1}$) (Figure 10.1). Since CH_3OH and HCOOH trace around the centrifugal barrier where velocity shift becomes the largest in the infalling-rotating envelope, this line width cannot be explained by envelope structure. Rather, they seems to trace structure inside the centrifugal barrier as illustrated in Figure 10.2. In fact, they have very compact distribution which is not resolved with the linear resolution of 10 au, and the velocity gradients are less clear than CH_3OH and HCOOH, probably because their distributions are too compact to resolve the rotation motion. As shown in orange in Figure 10.1, the gas inside the centrifugal barrier seems to have high velocity component as traced by $CH_2(OH)CHO$. This may be an indication of the disk component.

In the last decades, the statistical studies of chemical characteristics of low-mass protostellar sources have been conducted by single dish telescopes as described in Chapter 1. However, the recent interferometric observations reveal the chemical structure around the protostar is much more complex than ever thought, as shown in this thesis. Thus, the statistical studies with the interferometers are important. As an example of such studies 'PErseus ALMA CHEmical Survey' (PEACHES) is now in progress by Sakai and her collaborators. On the other hand, the high dust opacity in the vicinity of the protostar makes it difficult to probe the structure of such a

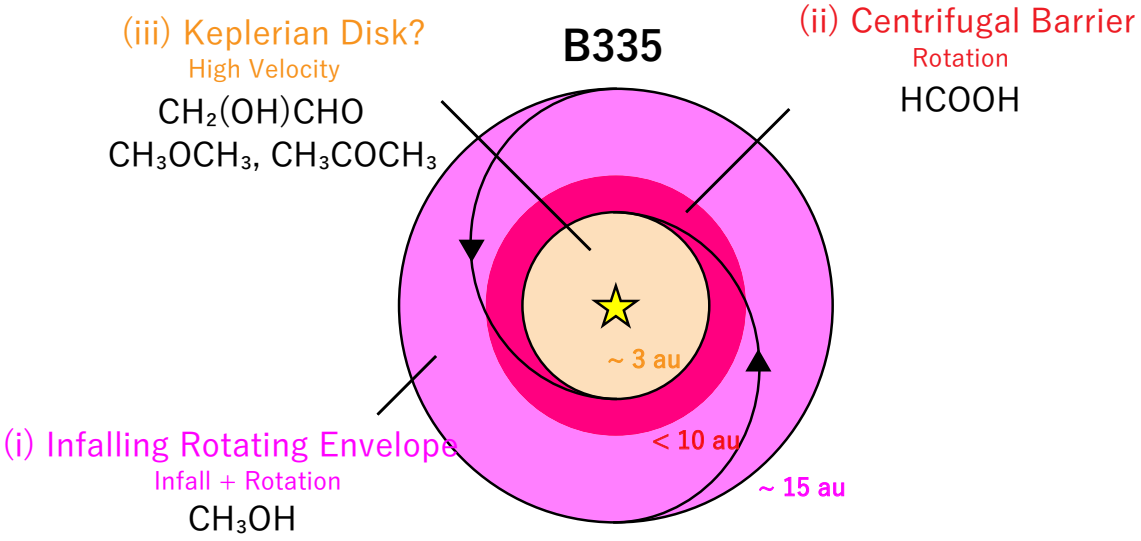

Figure 10.2: The schematic illustration of the distribution of the complex organic molecules. CH_3OH resides in the infalling-rotating envelope, while HCOOH resides around the centrifugal barrier. $CH_2(OH)CHO$ most likely exist in the Keplerian disk, because their high velocity component cannot be reproduced by the IRE model.

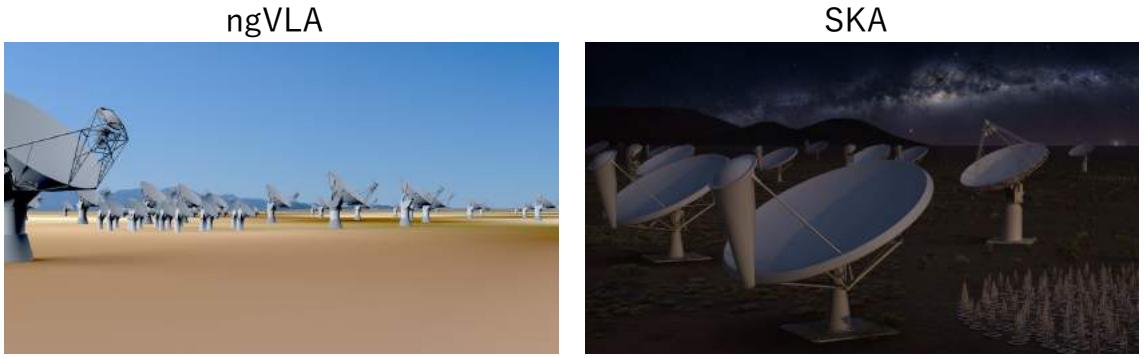

Figure 10.3: The imaginary figures of the ngVLA (Next Generation Very Large Array) (https://ngvla.nrao.edu) and SKA (Square Kilometer Array) (https://japan.skatelescope.org/ska-project/).

compact region with ALMA, as presented in Section 9.1.1. To overcome this difficulties, the lower frequency observations with high sensitivity are waited. For this purpose, new interferometric observations at a lower bands are now being planned such as Next Generation Very Large Array (ngVLA) and Square Kilometer Array (SKA) (Figure 10.3).

Finally, I also note the expediency of the similarity index introduced in the model optimization. As discussed in the analysis, the similarity index, the KL divergence, can be used to search for the best parameters to explain the observations with a consistency of the eye-based fitting. This method can successfully be applied to all the observed sources in this thesis. Although the error of $KL(p, q)$ cannot be determined in the statistical way, the uncertainty calculated by the mock image can be temporary used to determine the acceptable range of the fitting. Such a quantification of the goodness of the model and the observation is useful for future studies.

Acknowledgement

The author is grateful to Prof. Satoshi Yamamoto for his invaluable advise and suggestions. The author is in indebted to Dr. Nami Sakai for her valuable discussions and for providing the ALMA data used in this thesis. The author acknowledges PI and co-PIs of the large program *FAUST* (Drs. Satoshi Yamamoto, Cecilia Ceccarelli, Claire Chandler, Claudio Codella, and Nami Sakai) for providing the ALMA data used in this thesis. In particular, the author thanks Dr. Claire Chandler for applying the re-normalization and the self-calibration on the data of CB68. The author thanks Drs. Hiroya Yamaguchi, Yasushi Suto, Masaki Ando, Masami Ouchi, and Hideko Nomura for their valuable comments and suggestions as reviewers of this thesis. The author also thanks Drs. Yoko Oya and Yoshimasa Watanabe for their kind collaborations. The author is grateful to Drs. Cecilia Ceccarelli, Bertrand Lefloch, and Ana López-Sepulcre, for their collaborations and suggestions. The author is also grateful to Drs. Yuri Aikawa,. Aya Higuchi, Yichen Zhang, Emmanuel Caux, Charlotte Vastel, Claudine Kahane, Takeshi Sakai, Tomoya Hirota, and all the members in Yamamoto Group of Deparment of Physics, The University of Tokyo for their great supports and discussion.

This thesis makes use of the following ALMA data sets: ADS/JAO.ALMA#2013.1.01102.S, ADS/JAO.ALMA#2016.1.01376.S, ADS/JAO.ALMA#2018.1.01205.L and IRAM NOEMA data set: project ID W18AL001. ALMA is a partnership of ESO (representing its member states), NSF (USA) and NINS (Japan), together with NRC (Canada), NSC and ASIAA (Taiwan), and KASI (Republic of Korea), in cooperation with the Republic of Chile. The Joint ALMA Observatory is operated by ESO, AUI/NRAO, and NAOJ. IRAM is supported by INSU/CNRS (France), MPG (Germany) and IGN (Spain). This study is supported by Grant-in-Aids from Ministry of Education, Culture, Sports, Science, and Technologies of Japan (25400223, 25108005, 18H05222, and JP18J11010). The authors acknowledge the financial support by JSPS and MAEE under the Japan-France integrated action programme (SAKURA: 25765VC).

Appendix A

Error Estimate of $KL(p, q)$

The error of $KL(p, q)$ due to the noise is derived by using the mock PV images, as described in Section 4.2. We calculate the KL divergence between the mock PV images with and without the noise components for three different values of $I_{\rm thres,out}$, which are 1 $\sigma_{\rm rms}$, 2 $\sigma_{\rm rms}$, and 3 $\sigma_{\rm rms}$. Here, $\sigma_{\rm rms}$ is the rms noise of the observation. The noise is less removed from the raw PV image for the lower value of $I_{\rm thres,out}$, while the real emission can be artificially removed from the raw PV image for the higher value of $I_{\rm thres,out}$. The effect for the higher value of $I_{\rm thres,out}$ is serious especially for the weak line (*e.g.*, $H^{13}CO^+$ in CB244). The KL divergence calculated here has an uncertainty due to the variation of the artificial noise. We assess the uncertainty by the statistics of the 100 mock PV images. The calculation for each source is described below.

The error of $KL(p, q)$ due to the noise is calculated for B335 by using the rms noise level of 0.9 mJy beam^{-1}. $KL(p, q)$ between the mock PV images with and without the noise components is calculated to be 0.04 for all cases of the above $I_{\rm thres,out}$ variations (1 $\sigma_{\rm rms}$, 2 $\sigma_{\rm rms}$, and 3 $\sigma_{\rm rms}$). This $KL(p, q)$ value is employed as the tolerance range in the optimization of the model in B335 (Section 6.3.3). The uncertainty due to the variation of the artificial noise is confirmed to be about 10 % (Figure A.1).

The error of $KL(p, q)$ due to the noise is calculated for CB68 by using the rms noise level of 2.5 mJy beam^{-1}. $KL(p, q)$ between the mock PV images with and without the noise components is calculated to be 0.12, 0.11, and 0.11 for $I_{\rm thres,out}$ of 1 $\sigma_{\rm rms}$, 2 $\sigma_{\rm rms}$, and 3 $\sigma_{\rm rms}$, respectively. The $KL(p, q)$ value for $I_{\rm thres,out}$ of 2 $\sigma_{\rm rms}$ (0.11) is employed as the tolerance range in the optimization. This $KL(p, q)$ value is employed as the tolerance range in the optimization of the model in CB68 (Section 7.3.4). The uncertainty due to the variation of the artificial noise is confirmed to be about 6 % (Figure A.1).

The error of $KL(p, q)$ due to the noise is calculated for CB244 by using the rms noise level of 8 mJy beam^{-1}. $KL(p, q)$ between the mock PV images with and without the noise components is calculated to be 0.22, 0.20, and 0.20 for $I_{\rm thres,out}$ of 1 $\sigma_{\rm rms}$, 2 $\sigma_{\rm rms}$, and 3 $\sigma_{\rm rms}$, respectively. The $KL(p, q)$ value for $I_{\rm thres,out}$ of 2 $\sigma_{\rm rms}$ (0.20) is employed as the tolerance range in the optimization. This $KL(p, q)$ value is employed as the tolerance range in the optimization of the model in CB244 (Section 8.4.3). The uncertainty due to the variation of the artificial noise is confirmed to be about 10 % (Figure A.1).

We here note that the error of $KL(p, q)$ is smaller for B335 than those for CB68 and CB244. This is because the signal to noise ratios of the observed molecular emissions are higher in B335.

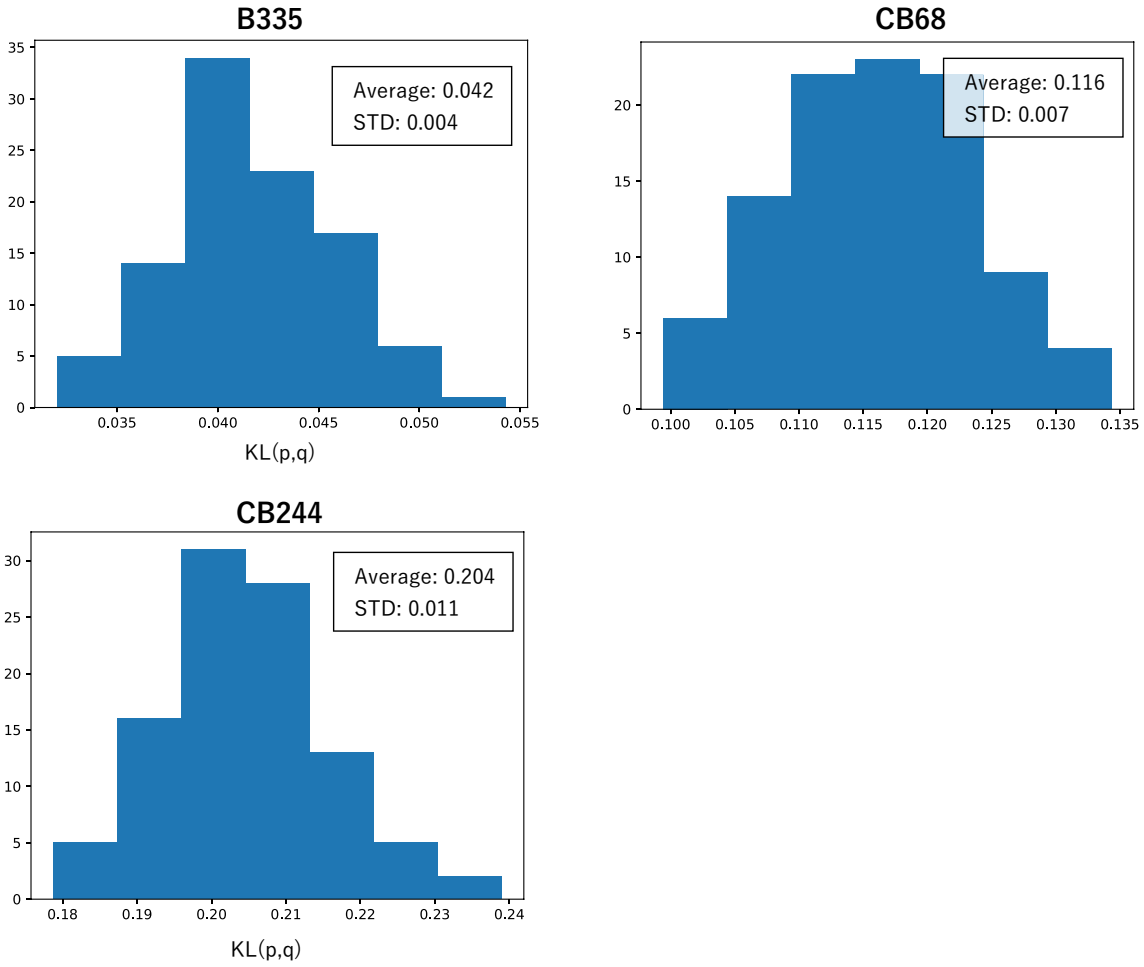

Figure A.1: The histograms of the result of similarity calculation between observed PV image and 100 mock PV images calculated for B335, CB68, and CB244. The average and the standard deviation (STD) of the KL divergences for 100 mock PV images are shown in top right of each panel.

Bibliography

[1] Adande, G. R., Woolf N. J., & Ziurys, L. M. 2013 Astrobiology, 13, 439

[2] Aikawa, Y., Wakelam, V., Garrod, R. T., & Herbst, E. 2008, ApJ, 674, 993

[3] Andre, P., Ward-Thompson, D., & Barsony, M. 1993, ApJ, 406, 122

[4] Andre, P., Ward-Thompson, D., & Barsony, M. 2000, Protostars and Planets IV, 59

[5] Bachiller, R. 1996, ARA&A, 34, 111

[6] Bachiller, R., & Pérez Gutiérrez, M. 1997, ApJL, 487, L93

[7] Bacmann, A., Taquet, V., Faure, A., Kahane, C., & Ceccarelli, C.bacmann 2012, A&A, 541, L12

[8] Balucani, N., Ceccarelli, C., & Taquet, V. 2015, MNRAS, 449, L16

[9] Bertrang, G., Wolf, S., & Das, H. S. 2014, A&A, 565, A94

[10] Basheer, I. A., Hajmeer, M. 2000, Journal of Microbiological Methods, 43, 3

[11] Benson, P. J., & Myers, P. C. 1989, ApJS, 71, 89

[12] Bisschop, S. E., Jørgensen, J. K., van Dishoeck, E. F., & de Wachter, E. B. M. 2007, A&A, 465, 913

[13] Blake, G. A., van Dishoeck, E. F., Jansen, D. J., et al. 1994, ApJ, 428, 680

[14] Bottinelli, S., Ceccarelli, C., Neri, R., et al. 2004, ApJ, 617, L69

[15] Buckle, J. V., & Fuller, G. A. 2002, A&A, 381, 77

[16] Caselli, P., Walmsley, C. M., Tafalla, M., Dore, L., & Myers, P. C. 1999, ApJL, 523, L165

[17] Caux, E., Kahane, C., Castets, A., et al. 2011, A&A, 532, A23

[18] Cazaux, S., Tielens, A. G. G. M., Ceccarelli, C., et al. 2003, ApJ, 593, L41

[19] Ceccarelli, C., Caselli, P., Fontani, F., et al. 2017, ApJ, 850, 176

[20] Chandler, C. J. & Sargent, A. I. 1993, ApJ, 414, L29

[21] Chen, H., Myers, P. C., Ladd, E. F., & Wood, D. O. S. 1995, ApJ, 445, 377

[22] Cheung, A. C., Rank, D. M., Townes, C. H., et al. 1968, PRL, 21, 1701

[23] Cheung, A. C., Rank, D. M., Townes, C. H., et al. 1969, Nature, 221, 626

[24] Choi, M., Kamazaki, T., Tatematsu, K., & Panis, J.-F. 2004, ApJ, 617, 1157

[25] Clemens, D. P., & Barvainis, R. 1988, ApJS, 68, 257

[26] Codella, C., Ceccarelli, C., Cabrit, S., et al. 2016, A&A, 586, L3

[27] Costarelli, D., Spigler, R. 2013, Neural Networks, 44, 101

[28] Di Francesco, J., Myers, P. C., Wilner, D. J., et al. 2001, ApJ, 562, 770

[29] Evans, N. J., II, Di Francesco, J., Lee, J., et al. 2015, ApJ, 814, 22

[30] Evans, N. J., II, Dunham, M. M., Jørgensen, J. K., et al. 2009, ApJS, 181, 321

[31] Evans, N. J., II, Lee, J.-E., Rawlings, J. M. C., & Choi, M. 2005, Apj, 626, 919

[32] Friedel, D. N., Snyder, L. E., Remijan, A. J., & Turner, B.E. 2005, ApJ, 632, L95

[33] Friedel, D. N. & Snyder, L. E. 2008, ApJ, 672, 962

[34] Fukui, Y., Harada, R., Tokuda, K., et al. 2015, ApJL, 807, L4

[35] Garrod, R. T., & Herbst, E. 2006, A&A, 457, 927

[36] Goodman, A. A., Benson, P. J., Fuller, G. A., et al. 1993, ApJ, 406, 528

[37] Harvey, D. W. A., Wilner, D. J., Lada, C. J., et al. 2001, ApJ, 563, 903

[38] Harvey, D. W. A., Wilner, D. J., Myers, P. C., et al. 2003, ApJ, 596, 383

[39] Hayashi, C. 1961, PASJ, 13, 450

[40] Henyey, L. G., Lelevier, R., & Levée, R. D. 1955, PASP, 67, 154

[41] Higuchi, A. E., Chibueze, J. O., Habe, A., et al. 2014, AJ, 147, 141

[42] Higuchi, A. E., Kurono, Y., Saito, M., et al. 2010, ApJ, 719, 1813

[43] Higuchi, A. E., Sakai, N., Watanabe, Y., et al. 2018, ApJS, 236, 52

[44] Hilton, J., & Lahulla, J. F. 1995, A&AS, 113, 325

[45] Hirano, N., Kameya, O., Nakayama, M., & Takakubo, K. 1988, ApJ, 327, L69

[46] Hirano, N., Kameya, O., Kasuga, T., & Umemoto, T. 1992, ApJ, 390, L85

[47] Hirota, T., Bushimata, T., Choi, Y. K., et al. 2008, PASJ, 60, 37

[48] Hirota, T., Ikeda, M., & Yamamoto, S. 2001, ApJ, 547, 814

[49] Högbom , J. A. 1974, A&AS, 15, 417,

[50] Howe, D. A., Millar, T. J., Schilke, P., & Walmsley, C. M. 1994, MNRAS, 267, 59

[51] Imai, M., Oya, Y., Sakai, N., et al. 2019, ApJL, 873, L21

[52] Imai, M., Sakai, N., López-Sepulcre, A., et al. 2018, ApJ, 869, 51

[53] Imai, M., Sakai, N., Oya, Y., et al. 2016, ApJL, 830, L37

[54] Jaber, A. A., Ceccarelli, C., Kahane, C., & Caux, E. 2014, ApJ, 791, 29

[55] Jeans, J. H. 1902, Philosophical Transactions of the Royal Society of London Series A, 199, 1

[56] Jørgensen, J. K., Bourke, T. L., Myers, P. C., et al. 2005, Apj, 632, 973

[57] Jørgensen, J. K., Bourke, T. L., Nguyen Luong, Q., & Takakuwa, S. 2011, A&A, 534, A100

[58] Kahane, C., Ceccarelli, C., Faure, A., & Caux, E. 2013, ApJ, 763, L38

[59] Kauffmann, J., Bertoldi, F., Bourke, T. L., Evans, N. J., II, & Lee, C. W. 2008, A&A, 487, 993

[60] Keene, J., Hildebrand, R.H., Whitcomb, S. E., & Harper, D. A. 1980, ApJ, 240, L43

[61] Kuan, Y., Huang, H., Charnley, S. B., et al. 2004, ApJ, 616, L27

[62] Kullback, S., Leibler, R. A. 1951, Ann. Math. Statist., 22, 79

[63] Larson, R. B. 1969, MNRAS, 145, 271

[64] Launhardt, R., & Henning, T. 1997, A&A, 326, 329

[65] Launhardt, R., Nutter, D., Ward-Thompson, D., et al. 2010, ApJS, 188, 139

[66] Lindberg, J. E., & Jørgensen, J. K. 2012, A&A, 548, A24

[67] Lindberg, J. E., Jørgensen, J. K., Watanabe, Y., et al. 2015, A&A, 584, A28

[68] López-Sepulcre, A., Jaber, A. A., Mendoza, E., et al. 2015, MNRAS, 449, 2438

[69] López-Sepulcre, A., Sakai, N., Neri, R., et al. 2017, A&A, 606, A121

[70] Machida, M. N., Tomisaka, K., & Matsumoto, T. 2004, MNRAS, 348, L1

[71] Mardones, D., Myers, P. C., Tafalla, M., et al. 1997, ApJ, 489, 719

[72] Masunaga, H., & Inutsuka, S.-. ichiro . 2000, ApJ, 531, 350

[73] Masunaga, H., & Inutsuka, S.-i. 2000, ApJ, 536, 406

[74] Masunaga, H., Miyama, S. M., & Inutsuka, S.-. ichiro . 1998, ApJ, 495, 346

[75] McGuire, B. A. 2018, ApJS, 239, 17

[76] Mikami, H., Umemoto, T., Yamamoto, S., & Saito, S. 1992, ApJL, 392, L87

[77] Momose, M., Ohashi, N., Kawabe, R., Nakano, T., & Hayashi, M. 1998, ApJ, 504, 314

[78] Müller, H. S. P., Schlöder, F., Stutzki, J., & Winnewisser, G. 2005, JMoSt, 742, 215

[79] Myers, P. C., & Ladd, E. F. 1993, ApJL, 413, L47

[80] Öberg, K., van der Marel, N., Kristensen, L. E., & van Dishoeck, E. F. 2011, ApJ, 740, 14

[81] Ohashi, N., Hayashi, M., Ho, P. T. P., Momose, M., & Hirano, N. 1996, ApJ, 466, 957

[82] Ohashi, N., Hayashi, M., Ho, P. T. P., et al. 1997, ApJ, 488, 317

[83] Okoda, Y., Oya, Y., Sakai, N., et al. 2018, ApJL, 864, L25

[84] Olofsson, S. & Olofsson, G. 2009, A&A, 498, 455

[85] Oya, Y., Sakai, N., López-Sepulcre, A., et al. 2016, ApJ, 824, 88

[86] Oya, Y., Sakai, N., Sakai, T., et al. 2014, ApJ, 795, 152

[87] Oya, Y., Sakai, N., Watanabe, Y., et al. 2017, ApJ, 837, 174

[88] Oya, Y. 2017, PhD thesis

[89] Peng, T.-C., Despois, D., Brouillet, N., et al. 2013, A&A, 554, A78

[90] Pickett, H. M., Poynter, R. L., Cohen, E. A., et al. 1998, JQSRT, 60, 883

[91] Prodanović, T., Steigman, G., & Fields, B. D. 2010, MNRAS, 406, 1108

[92] Richard, C., Margulès, L., Caux, E., et al. 2013, A&A, 552, A117

[93] Saito, M., Kawabe, R., Kitamura, Y., & Sunada, K. 1996, ApJ, 473, 464

[94] Sakai, N., Oya, Y., Higuchi, A. E., et al. 2017, MNRAS, 467, L76

[95] Sakai, N., Oya, Y., López-Sepulcre, A., et al. 2016, ApJL, 820, L34

[96] Sakai, N., Oya, Y., Sakai, T., et al. 2014, ApJL, 791, L38

[97] Sakai, N., Sakai, T., Hirota, T., Burton, M., & Yamamoto, S. 2009, ApJ, 697, 769

[98] Sakai, N., Sakai, T., Hirota, T., & Yamamoto, S. 2008, ApJ, 672, 371

[99] Sakai, N., Sakai, T., Hirota, T., & Yamamoto, S. 2010, ApJ, 722, 1633

[100] Sakai, N., Sakai, T., Hirota, T., et al. 2014, Natur, 507, 78

[101] Sakai, N., Sakai, T., & Yamamoto, S. 2006, PASJ, 58, L15

[102] Sakai, N. & Yamamoto, S. 2013, Chem. Rev., 113, 8981

[103] Saladino, R., Botta, G., Pino, S., Costanzo, G., & Di Mauro, E. 2012, Chem. Soc. Rev., 41, 5526

[104] Shirley, Y. L., Huard, T. L., Pontoppidan, K. M., et al. 2011, ApJ, 728, 143

[105] Shu, F. H. 1977, ApJ, 214, 488

[106] Snyder, L. E., Buhl, D., Zuckerman, B., et al. 1969, PhRvL, 22, 679

[107] Sonneborn, G., Tripp, T. M., Ferlet, R., et al. 2000, ApJ, 545, 277

[108] Spergel, D. N., Bean, R., Doré, O., et al. 2007, ApJS, 170, 377

[109] Spezzano, S., Bizzocchi, L., Caselli, P., et al. 2016, A&A, 592, L11

[110] Spezzano, S., Gupta, H., Brünken, S., et al. 2016, A&A, 586, A110

[111] Stutz, A., Launhardt, R., Linz, H., et al. 2010, A&A, 518, L87

[112] Stutz, A. M., Rubin, M., Werner, M. W., et al. 2008, ApJ, 687, 389

[113] Sugimura, M., Yamaguchi, T., Sakai, T., et al. 2011, PASJ, 63, 459

[114] Suzuki, H., Yamamoto, S., Ohishi, M., et al. 1992, ApJ, 392, 551

[115] Taquet V., López-Sepulcre, A., Ceccarelli, C., et al. 2015, ApJ, 804, 81

[116] Terebey, S., Vogel, S. N., & Myers, P. C. 1989, ApJ, 340, 472

[117] Tielens, A. G. G. M., & Hollenbach, D. 1985, ApJ, 291, 722

[118] Tomisaka, K. 2000, ApJL, 528, L41

[119] Tomisaka, K. 2002, ApJ, 575, 306

[120] Vallée, J. P., Bastien, P., & Greaves, J. S. 2000, ApJ, 542, 352

[121] Vallée, J. P., & Fiege, J. D. 2007, AJ, 134, 628

[122] van Dishoeck, E. F., Blake, G. A., Jansen, D. J., & Groesbeck, T. D. 1995, ApJ, 447, 760

[123] Ward-Thompson, D., Zylka, R., Mezger, P. G., & Sievers, A. W. 2000, A&A, 335, 1122

[124] Watanbe, Y., Sakai, N., Lindberg, J. E., et al. 2012, ApJ, 745, 126

[125] Wilner, D. J., Myers, P. C., Mardones, D., & Tafalla, M. 2000, ApJ, 544, L69

[126] Wilson, R. W., Jefferts, K. B., & Penzias, A. A. 1970, ApJL, 161, L43

[127] Wood, D. O. S., & Churchwell, E. 1989, ApJS, 69, 831

[128] Woodruff, H. C., Eberhardt, M., Driebe, T., et al. 2004, A&A, 421, 703

[129] Wu, Y., Huang, M., & He, J. 1996, A&AS, 115, 283

[130] Yamamoto, S. 2017, 'Introduction to Astrochemistry' Springer, (Berlin, Heidelberg), Chapter 5

[131] Yen, H., Takakuwa, S., Koch, P. M., et al. 2015, ApJ, 812, 129

[132] Yun, J. L., & Clemens, D. P. 1994, ApJS, 92, 145

[133] Zhou, S., Evans, N. J., II, Koempe, C., & Walmsley, C. M. 1993, ApJ, 404, 232

[134] Zinnecker, H., & Yorke, H. W. 2007, ARA&A, 45, 481